

**Phase Evolution in Manganese-Germanium System
During Mechanical Alloying**

by

Vamsi Madhukar Meka

**A thesis submitted in partial fulfillment
of the requirements for the degree of
Master of Science in Engineering
(Mechanical Engineering)
in the University of Michigan–Dearborn
2017**

Master Thesis Committee:

Assistant Professor Tanjore V. Jayaraman, Chair

Professor Pravansu Mohanty

Associate Professor German Reyes-Villanueva

ACKNOWLEDGEMENTS

I would like to extend my deepest gratitude towards my thesis advisor, Prof. Tanjore V. Jayaraman, for his continual support, encouragement, and expert guidance throughout the research work. This opportunity to work with him has enhanced my technical, ethical, and soft skills. I would also like to thank Prof. Pravansu Mohanty and Prof. German Reyes-Villanueva for sparing their time to evaluate my thesis and for being a part of the thesis committee.

I would like to thank the Mechanical Engineering Department, College of Engineering and Computer Science at the University of Michigan in Dearborn for their support in completing my thesis and the Department of Material Science and Engineering at The University of Michigan at Ann Arbor for providing access to some of their equipment.

I would also like to thank Tim Chambers, Chris Cristian, Ying Qi, and Erik Kirk for their assistance with equipment and safety training and, special thanks to Cory Sayle from Ann Arbor for opening the laboratory door every time we were early.

Lastly, I would like to thank my family Mr. Vijaya Bhaskar Meka, Ms. Naga Mani Meka, Ms. Pranathi, friends, and the close ones for supporting me throughout this journey.

ABSTRACT

In this thesis work, the phase evolution during the synthesis of metastable binary germanides of Mn-Ge system was investigated. A thorough literature review on the various metallic germanides was performed. Attempts were made to synthesize various metastable manganese germanides by mechanical alloying. The phase evolution during the synthesis was investigated by x-ray diffraction and scanning electron microscopy.

Powders of MnGe (an equiatomic metastable phase of Mn-Ge system) were successfully synthesized. The structural characterization revealed the lattice parameter and the particle size to be 0.4798 ± 0.0008 nm and $\sim 1-3$ μm , respectively. The magnetic characterization showed that MnGe was paramagnetic at room temperature, antiferromagnetic at sub-ambient temperatures with Neel temperature estimated as ~ 162 K, and the magnetization (at 1 Tesla) was estimated to be ~ 3 emu/g. In the case of MnGe, based on the phase evolution, attempts were made to reduce the synthesis time by varying appropriate processing parameters. During the synthesis of Ge-rich metastable manganese-germanides, the evolution of the respective phases (Mn_3Ge_5 , MnGe_2 , and MnGe_4) was always accompanied with MnGe.

The metastable MnGe synthesized (in powder form), in this work, at ambient temperature and pressure conditions had a considerably high yield and reproducibility, unlike in the past synthesized by high-pressure/high-temperature technique (in bulk form) and thin-film deposition technique (thin film) available in the literature. Future study would involve the synthesis of other metastable compound by isolating MnGe during their evolution.

TABLE OF CONTENTS

ACKNOWLEDGEMENTS.....	ii
ABSTRACT.....	iii
LIST OF FIGURES	vi
LIST OF TABLES.....	xiv
CHAPTER 1. INTRODUCTION.....	1
1.1. Diluted Magnetic Semiconductors.....	1
1.2. Non-Equilibrium Processing.....	2
CHAPTER 2. LITERATURE REVIEW AND BACKGROUND.....	5
2.1. Metallic Germanides	5
2.2. Transition metal Germanides	7
2.3. Rare Earth Germanides	54
2.4. Rare Earth-Transition Metal Germanides	65
2.5. Mechanical Alloying.....	72
2.5.1. Type of Mill.....	73
2.5.2. Milling Container.....	75
2.5.3. Milling Speed.....	76
2.5.4. Milling Time	76
2.5.5. Type, Size and Size Distribution of Grinding Medium.....	76
2.5.6. Ball to Powder Ratio.....	77
2.5.7. Extent to Which the Vial Is Filled	77
2.5.8. Milling Atmosphere.....	78
2.5.9. Process Control Agent	78
2.5.10. Temperature of Milling.....	79
2.6. Contaminations in Mechanical Alloying.....	79
2.6.1. Contamination from Milling Tools.....	79
2.6.2. Contamination from Atmosphere	80
2.6.3. Contamination from Process Control Agents	80
2.7. Key Points from Literature Review:	81
CHAPTER 3. MOTIVATION.....	83
CHAPTER 4. EXPERIMENTAL PROCEDURE.....	84

4.1. Material Synthesis	84
4.2. Materials Characterization	87
CHAPTER 5. RESULTS AND DISCUSSIONS	89
5.1. Phase evolution during the synthesis of MnGe	89
5.1.1. Adopting the Prevalent Technique.....	89
5.1.2. Adopting the Ideal Technique.....	92
5.1.3. Magnetization of MnGe	118
5.1.4. Synthesis Process Comparison:	118
5.2. Process Optimization for synthesis of MnGe.....	119
5.2.1. Using ideal technique with intermediate addition of stearic acid	119
5.2.2. Using Ideal technique, with increased ball to powder ratio.....	124
5.2.3. Synthesis of MnGe by alloying powders in atmosphere.	126
5.2.4. Study of Effect of Different Types of PCA's	128
5.3. Phase evolution during the synthesis of Mn ₃ Ge ₅	130
5.4. Phase evolution during the synthesis of MnGe ₂	131
5.4.1. Adopting Ideal alloying technique.....	131
5.4.2. Adopting prevalent alloying technique.....	132
5.5. Phase evolution during the synthesis of MnGe ₄	135
CHAPTER 6. CONCLUSION	136
REFERENCES	138

LIST OF FIGURES

Figure 1 The basic concept of "energize and quench" to synthesize non-equilibrium materials [1].....	2
Figure 2 Periodic Table with metals, rare-earths, and transition metals highlighted	5
Figure 3 Temperature dependence a) electrical resistivity and b) thermoelectric power measured from 500 to 90K of SrGe _{5.6} [9]	6
Figure 4 Electrical resistivity vs. temperature for a) α -MoGe ₂ and β -MoGe ₂ and b) α -WGe ₂ and β -WGe ₂ [11].....	10
Figure 5 Mn-Ge phase diagram [13].....	10
Figure 6 Belt type apparatus arrangement [12].....	11
Figure 7 Temperature dependence of a) electrical resistivity and b) thermoelectric power of Mn ₃ Ge ₅ [9].....	12
Figure 8 Temperature dependence of a) electrical resistivity and b) thermoelectric power of MnGe [10].....	13
Figure 9 Temperature dependence of magnetic susceptibility and reciprocal magnetic susceptibility of MnGe [14]	13
Figure 10 Temperature dependence of a) electrical resistivity and b) thermoelectric power of CoGe [10].....	14
Figure 11 Temperature dependence of magnetic susceptibility and reciprocal of magnetic susceptibility of CoGe with B20 structure [14]	15
Figure 12 Effective moment per first-row transition metal atom as a function of the number of electron in the outer shell of B20 germanides [14].....	16
Figure 13 Magnetic field dependence of magnetization of MnGe ₄ [2]	18
Figure 14 Temperature dependence of a) electrical resistivity and b) magnetization as well as the reciprocal magnetic susceptibility of MnGe ₄ [2]	18
Figure 15 Temperature dependence of electrical resistivity of CoGe ₄ [23].....	19
Figure 16 Ni-Ge phase diagram [24]	20

Figure 17 Temperature dependence of a) electrical resistivity and b) thermoelectric power of NiGe ₂ [33]	21
Figure 18 XRD spectra of (a) 10 nm Ni germanide Ge, (b) 10 nm Ni silicide Si and (c) 10 nm Ni germanosilicide Si _{0.75} Ge _{0.25} by RTA method and in-situ annealing method at 400 °C [27]	22
Figure 19 Sheet resistance of 10 nm Ni on Si, Si _{0.75} Ge _{0.25} and Ge using a rapid thermal annealing and an in-situ annealing method at 400 °C, respectively [35]	23
Figure 20 Raman spectra of (a) 10nm Ni on Ge and (b) 10nm Ni on Si annealed at 400 °C by RTA and the in-situ annealing [27]	23
Figure 21 Magnetic measurements using a SQUID magnetometer. Magnetic fields are applied in the plane along the (100) direction. a) Temperature dependence of the saturation magnetization measured at 2 T. The inset shows extrapolated matrix signal at low temperature after subtracting the nanocolumns magnetic signal, b) ZFC_FC measurement carried out at 0.01 T. Both curves superimpose. Inset: ZFC_FC curves after 15 min annealing at 650 °C, c) Magnetization loops at 5, 100 and 400 K, after subtracting the diamagnetic contribution from the substrate. The inset demonstrates the easier saturation in-plane at 250 K. d) Coercive field (μ_0H_C) and remnant magnetization (M_r/M_s) versus temperature. μ_0H_C and M_r/M_s are given with a precision of the order of 10% [28]	26
Figure 22 Temperature dependence of magnetic susceptibility of a) CoGe and b) MnGe (samples A and B are from different preparations) [11]	28
Figure 23 a) Magnetization curves of MnGe at different temperatures and b) The magnetic T-H diagram of MnGe [11]	29
Figure 24 Temperature dependence of the specific heat of MnGe and CoGe [29]	29
Figure 25 Temperature-dependent (FC and ZFC) magnetization data for the Fe ₃ Ge ₂ nanocrystals, indicating ferromagnetic behavior with a T _c of ~265 K. Consistent with this, the inset shows a plot of M vs H, which indicates magnetic hysteresis at 5 K but not at 300 K [30]	31
Figure 26 X-ray diffraction patterns of the 20Ge/80Mn film system: (a) initial sample, (b) sample annealed at 250 °C, (c) 350 °C, and (d) 500 °C [31]	33
Figure 27 Annealing temperature dependences of (a) saturation magnetization M _S , and (b) resistance R of the 20Ge/80Mn bilayer. The top of the figure shows the temperature boundaries of the existence of the 20Ge/80Mn film system and the Mn ₅ Ge ₃ and Mn ₅ Ge ₃ C _x O _y phases [31]	33
Figure 28 Temperature dependences of saturation magnetization M _S measured in a magnetic field of 0.5 T for the 20Ge/80Mn film system after annealing at (a) 250 °C, (b) 350 °C, and (c) 500 °C. Insets show in-plane M–H hysteresis loops for Mn ₅ Ge ₃ and Mn ₅ Ge ₃ C _x O _y phases [31]	35

Figure 29 Relative concentration of Mn, Ge, C, and O in 20Ge/80Mn films as a function of sputtering time [31].....	36
Figure 30 Powder X-ray diffraction patterns and Rietveld refinements of Cr ₅ B ₃ -type Ta ₅ Si ₃ . The TaSi ₂ impurity is indicated with arrows [7].....	37
Figure 31 Powder X-ray diffraction patterns and Rietveld refinements of Cr ₅ B ₃ -type Ta ₅ Ge ₃ . The Ta impurity is indicated with an arrow [7]	38
Figure 32 Magnetization vs. temperature for Ta ₅ Si ₃ and Ta ₅ Ge ₃ [7].....	39
Figure 33 Electrical resistivity of the Ta ₅ Si ₃ and Ta ₅ Ge ₃ samples [7].....	40
Figure 34 XRD patterns of the Ni–67 at.% Ge powder blend milled for different times. While the Ni and Ge peaks are seen in the unmilled powder (0 h), the formation of a solid solution started to occur on milling for 1 h. Simultaneously, the equilibrium NiGe intermetallic also started to form, and its amount increased with milling time. On milling the powder for 10 h, a new metastable phase, identified as the metastable NiGe ₂ phase, started to form. An almost homogeneous NiGe ₂ phase had formed on milling the powder for 60 h [6]	41
Figure 35 Variation of the lattice parameter of the Ni(Ge) solid solution with Ge content based on ref [6]	42
Figure 36 XRD pattern of the Ni–67 at.% Ge powder blend milled for 10 h showing the formation of the equilibrium NiGe intermetallic phase. Note that a small amount of Ge, and even a smaller amount of NiGe ₂ , are also present in the powder at this stage [6].....	43
Figure 37 XRD patterns of the Ni–67 at.% Ge powder blend milled for 60 h showing an almost homogeneous formation of the metastable NiGe ₂ phase [6]	43
Figure 38 SEM images and EDS spectra of the Ni–67 at. % Ge powder blend milled for (a and b) 0 h, (c and d) 5 h and (e and f) 60 h. Whereas Ni and Ge are present in the unmilled powder (0 h), the powder contains predominantly the equilibrium NiGe phase on milling the powder for 5 h, and the metastable NiGe ₂ phase on milling for 60 h [6]	45
Figure 39 RHEED images of a 7x7 reconstructed Si(111) surface shown for in-plane directions of 112 and 110, respectively [43]	46
Figure 40 RHEED patterns measured along the 110 and 112 in-plane directions of the ~40 nm FeGe film, respectively [43]	47
Figure 41 XRD scan of the FeGe film. Single-phase, single crystal FeGe is shown amongst the Si substrate peaks [43]	48
Figure 42 RHEED for MnGe thin film grown on FeGe buffer layers is shown along the 110 and 112 directions respectively [43]	48
Figure 43 XRD for a ~40 nm thick MnGe film. The MnGe(111) peak is shown alongside the ~5 nm FeGe buffer layer [43]	49

Figure 44 RHEED patterns are shown for the final topmost layers in a [MnGe/FeGe] ₈ superlattice for FeGe 110 (111) and CrGe 110 (111), respectively [43].....	50
Figure 45 XRD for the superlattice structure shows a single (111) peak. Inset: a weak satellite peak (arrow) due to superlattice structure is observed [43].....	50
Figure 46 RHEED for the CrGe thin film grown on FeGe buffer layers is shown along the 110 and 112 directions respectively [43].....	51
Figure 47 XRD for a ~30 nm thick CrGe film. The CrGe(111) peak is shown alongside the ~5 nm FeGe buffer layer [43]	51
Figure 48 RHEED patterns are shown for the final topmost layers in a [CrGe/FeGe] ₁₀ superlattice for FeGe 110 (111) and CrGe 110 (111), respectively [43].....	52
Figure 49 XRD for the superlattice structure shows a single (111) peak. Inset: satellite peaks (arrows) are observed due to the superlattice structure [43].....	52
Figure 50 RHEED and XRD characterization of a three-component superlattice [CrGe/MnGe/FeGe] ₈ . (a-c) RHEED patterns are shown for the topmost layers FeGe, MnGe, and CrGe layers, respectively. The patterns are measured along the 110 in-plane directions of the films. Qualitatively, the RHEED images are very similar to each layer. (d) XRD scan of the trilayer superlattice shows a single (111) peak with satellite peaks from the superlattice structure (arrows in the inset) [43].....	53
Figure 51 Temperature dependence of magnetic susceptibility of a) PrGe ₅ and b) NdGe ₅ c) SmGe ₅ and d) CeGe ₅ [46].....	55
Figure 52 X-ray powder diffraction patterns of La Ge samples: (a) 5 GPa, 500 °C; (b) 12 GPa, 1100 °C; (c) 10 GPa, 850 °C. Cross marks show diffractions from LaGe ₂ . Filled and open circles show XRD patterns of LaGe ₅ and LaGe ₃ , respectively [47].....	57
Figure 53 Temperature dependence of the electrical resistivity for LaGe ₃ for (a) wide temperature range and (b) lower temperature range [47]	58
Figure 54 Temperature dependence of the magnetic susceptibility of LaGe ₃ [47].....	58
Figure 55 Field cooled magnetization data gathered under an applied field of 500 Oe for the REBiGe compounds with structures I and II [48]	60
Figure 56 Field cooled magnetization data gather under an applied field of 500 Oe for the REBiGe compounds with structure II [48]	61
Figure 57 Field-cooled magnetic susceptibility versus temperature of RE _{5-x} Ca _x Ge ₃ (RE = Ce–Nd and Gd–Er). The insets show the temperature dependence of the inverse magnetic susceptibility [50].....	64
Figure 58 Magnetic data for RECr _{0.3} Ge ₂ (RE = Gd–Er). The left panels show the zero-field-cooled dc magnetic susceptibility and its inverse as a function of temperature (with the insets highlighting low-temperature transitions in the ac magnetic susceptibility), and the right panels	

show isothermal magnetization curves at various temperatures. The field-cooled susceptibility is also shown in the case of $\text{ErCr}_{0.3}\text{Ge}_2$ [51]	67
Figure 59 Temperature dependence of a) electrical resistivity and b) Magnetic susceptibility of SmPtGe_2 [52]	69
Figure 60 Plots of (a) electrical resistivity, (b) magnetic susceptibility and its inverse as a function of temperature, and (c) magnetization as a function of the field at 2 and 300K for $\text{La}_{2.1}\text{MnGe}_{2.2}$ [54]	71
Figure 61 Schematic of collision as the main event of energy transfer [55]	72
Figure 62 Particles getting trapped between the grinding media [3]	72
Figure 63 SPEX 8000 mixer/mill [1].....	74
Figure 64 Vial of a Shaker ball mill and the shaking direction [1].....	74
Figure 65 Influence of vacuum and nitrogen environments on the change in average lattice parameter of Fe [57].....	80
Figure 66 Elemental powders a) Manganese with 99.99% purity and b) Germanium with 99.999% purity.....	84
Figure 67 SPEX Sample Prep 8000D high energy ball mill.....	85
Figure 68 SPEX 8007 Stainless steel vial.....	85
Figure 69 Components of vial and the stainless-steel balls spread out beside a Dollar coin for size reference	85
Figure 70 Samples after alloying are stored inside the bigger and smaller Glass vials as shown in left and right images respectively	86
Figure 71 Rigaku Miniflex powder X-ray diffractometer	87
Figure 72 Philips XL30 SEM and EDAX setup	88
Figure 73 Quantum design's vibrating sample magnetometer setup	88
Figure 74 XRD Pattern of all the samples synthesized with intermediate addition of PCA and removal of sample.....	91
Figure 75 XRD pattern of sample S24 analyzed in JADE 2016 software package showing oxidation	91
Figure 76 Temperature variation observed on the outside walls of the vial recorded every 3 hours during the alloying process	94

Figure 77 XRD patterns of sample alloyed for 3 hours compared with S0, i.e., just blended sample in stoichiometric ratio	95
Figure 78 XRD patterns of samples alloyed for 3 hours and 9 hours compared with S0, i.e., just blended sample in stoichiometric ratio	96
Figure 79 XRD patterns of all the samples obtained at different hours of alloying without the intermittent addition of PCA or removal of the sample.....	97
Figure 80 XRD patterns of all the samples obtained at different hours of alloying stacked one over the other	97
Figure 81 XRD of all the samples in the 2- θ range of 25-30 degree showing shift in Ge peak	98
Figure 82 XRD of all the samples in the 2- θ range of 41-44 ° showing shift in Mn peak	99
Figure 83 XRD pattern of sample alloyed for 30 hours continuously with MnGe peaks indexed.	100
Figure 84 XRD pattern of sample alloyed for 30 hours continuously, analyzed in JADE 2016 software package showing 100% MnGe phase	101
Figure 85 XRD patterns of Samples obtained from two different runs after 30 hours of alloying	102
Figure 86 XRD patterns of Samples obtained from two different runs after 30 hours of alloying stacked one over the other to show similarity.....	102
Figure 87 XRD pattern comparison between sample S30 and S36.....	103
Figure 88 XRD pattern comparison between sample S30 and S36 stacked one over the other to show stability	103
Figure 89 SEM images of sample alloyed for 30 hours are shown on the left and those of sample alloyed for 36 hours are shown on the right	105
Figure 90 EDAX analysis of the sample S30 and the inset shows the corresponding image of the sample at 20 μm /1352x magnification.....	106
Figure 91 EDAX analysis of the sample alloyed for 36 hours and the inset shows corresponding image at 20 μm /1312x magnification	107
Figure 92 Particle size (μm) distribution in sample alloyed for 30 hours.....	108
Figure 93 Particle size (μm) distribution in sample alloyed for 36 hours.....	109
Figure 94 Change in Magnetic moment with applied field in MnGe	110

Figure 95 Change in Zero field and field cooled magnetization with temperature in sample alloyed for 9 hours	111
Figure 96 Change in Zero field and field cooled magnetization with temperature in sample alloyed for 12 hours	111
Figure 97 Change in Zero field and field cooled magnetization with temperature in sample alloyed for 15 hours	112
Figure 98 Change in Zero field and field cooled magnetization with temperature in sample alloyed for 18 hours	112
Figure 99 Change in Zero field and field cooled magnetization with temperature in sample alloyed for 24 hours	113
Figure 100 Change in Zero field and field cooled magnetization with temperature in sample alloyed for 30 hours	114
Figure 101 Change in Zero field and field cooled magnetization with temperature in sample alloyed for 30 hours for reproducibility check	114
Figure 102 Change in Zero field and field cooled magnetization with temperature in sample alloyed for 36 hours	115
Figure 103 Change in magnetization with temperature in sample alloyed for 30 hours	116
Figure 104 Change in magnetization with temperature in sample alloyed for 36 hours	116
Figure 105 Change in magnetization with an increase in temperature in sample alloyed for 30 hours.....	117
Figure 106 Change in magnetization with decrease in temperature in sample alloyed for 30 hours.....	117
Figure 107 XRD patterns comparison between 24 hour alloyed samples using different alloying techniques	120
Figure 108 XRD patterns of 24 hour alloyed samples stacked one over the other.....	121
Figure 109 XRD patterns comparison between 30 hour alloyed samples using different alloying techniques	122
Figure 110 XRD patterns of 30-hour alloyed samples stacked one over the other	122
Figure 111 XRD patterns comparison between 30-hour alloyed samples using different alloying techniques	123
Figure 112 XRD patterns of 30-hour alloyed samples stacked one over the other	124

Figure 113 XRD Pattern of 24 hours alloyed sample with high ball to powder ratio showing pure MnGe phase	125
Figure 114 XRD patterns comparison between 30 hours alloyed sample with ~8:1 B/P and 24 hours alloyed sample with ~15:1 B/P	125
Figure 115 Change in Zero field and field cooled magnetization with temperature in sample alloyed for 24 hours with high ball to powder ratio.....	126
Figure 116 XRD pattern of sample alloyed in air for 30 hours using 8:1 B/P	127
Figure 117 XRD pattern comparison between sample alloyed for 30 hours in air with those alloyed for 18 hours and 24 hours in argon atmosphere.....	127
Figure 118 XRD pattern comparison of sample alloyed for 3 hours using different PCA's .	129
Figure 119 XRD pattern comparison of all the samples obtained during the synthesis process of Mn ₃ Ge ₅	130
Figure 120 XRD pattern of sample during the attempt to synthesize MnGe ₂ alloyed for 36 hours	131
Figure 121 XRD pattern of sample ~MnFeGe ₂ alloyed for 150 hours with 10:1 B/P.....	133
Figure 122 XRD pattern of sample alloyed for 150 hours analyzed in JADE software package	133
Figure 123 EDAX analysis of the sample alloyed for 150 hours	134
Figure 124 The magnetization versus applied magnetic field measurement performed on sample alloyed for 150 hours showing a hysteresis loop.....	134
Figure 125 XRD pattern of the sample alloyed for 30 hours during the attempt to synthesize MnGe ₄	135

LIST OF TABLES

Table 1 Departure from equilibrium achieved in various processes [3].	3
Table 2 Attributes of mechanical alloying [3].	4
Table 3 Preparation conditions and crystal type of Rare-Earth Disilicides, Digermanides, and Transition-metal silicides and germanides [10].	8
Table 6 Chemical compositions of Mn_3Ge_5 [12].	12
Table 7 Crystallographic parameters of Mn_3Ge_5 [12].	12
Table 13 Crystallographic data for the Ta_5Si_3 and Ta_5Ge_3 samples determined from the powder X-ray diffraction [7].	38
Table 15 Crystal structures and lattice parameters of stable and metastable phases in the Ni–Ge system [6].	44
Table 17 Magnetic properties of $LaGe_5$ -type compounds [45].	56
Table 18 Magnetic parameter of $RE[Bi_xGe_{1-x}]_2$ [48].	61
Table 19 Summary of magnetic data for $RECr_{0.3}Ge_2$ ($RE = Gd-Er$) [51].	68
Table 20 Table showing number of impacts for a different number of balls and the resultant values of kinetic energy [4].	75
Table 21 Amount of H_2 , O_2 and C percentage in each process control agent which could lead to contamination [57].	81
Table 22 Table of parameters used in the Prevalent technique.	90
Table 23 Table of parameters used in the mechanical alloying process without intermediate removal of sample or addition of PCA.	93
Table 24 Lattice parameter calculation of the obtained sample using Cohen's method	104
Table 26 Table summarising the magnetization values of different MnGe samples measures at 10,000 Oe applied field.	118
Table 25 Alloying parameters during synthesis of $MnGe_2$.	132

CHAPTER 1. INTRODUCTION

1.1. Diluted Magnetic Semiconductors

Dilute magnetic semiconductors (DMS) are semiconductors that are doped with transition metals consisting of unpaired d electrons. These materials have achieved a great interest due to their potential application in magnetoelectronic devices, solid-state devices and in spintronics [1]. Spintronics is considered as an approach towards the improvement of electronic devices by offering simultaneous control over electric and magnetic properties, i.e., simultaneous control over intrinsic spin of the electron and its associated magnetic moment alongside its charge. For such applications, transition metal silicides and germanides have been widely investigated as they exhibit a variety of magnetic and electric properties that could be exploited according to the requirement.

Silicon-based semiconductors/technology have been in use for a long time, and Germanium base is the best system that can easily replace this mainstream silicon technology. Not all but most germanium based systems have similarities in structure to their corresponding silicon-based systems. Germanides of transition metals exist in various compositionally diverse binary phases such as TGe, T₂Ge, T₃Ge, T₅Ge₃, T₁₁Ge₈, TGe₂ and TGe₄ (T – Transition metal) [2].

From the experimental results which show a significant change in Curie temperature with change in concentration of Mn in Mn_xGe_{1-x} and the p-type semiconducting property of the same, reported by Park et al. [3], Ge-Mn system seems promising in allowing simultaneous control over magnetic and electric properties as discussed above. This lead to many experimentations and studies on magnetic properties of this system [4][5][6][7][8]. Although many have tried to synthesize metastable phases of Mn-Ge system, they were synthesized under high temperature and high-pressure synthesis techniques [9][10][2][11], by relatively low-temperature molecular beam epitaxy growth technique [12][13][3], or by doping Mn into Ge crystals [14] and all of these techniques have their limitations and practical difficulties. In most of the cases, yield was low or a high pressure and high-temperature synthesis technique

were used for the synthesis of MnGe [10] and MnGe₄ [2] in which the temperature and pressure conditions were too high which could lead to degradation of Ge.

Current work involves investigation of the phase evolution during the synthesis of metastable MnGe phases at room temperature and pressure using mechanochemical processing technique (a non-equilibrium processing technique), i.e., by mechanically inducing solid state reactions. This technique has been used previously to synthesize many intermetallic compounds [15][16][17][18] including a metastable phase of Ni-Ge system under room temperature and pressure [19].

1.2. Non-Equilibrium Processing

Research for development of materials with improved properties has been increasing through increasing with increase in demand for advanced materials designed specifically for demanding applications. These advanced materials are designed by controlling the structure such that they are tailored specifically to obtain a set of properties [1]. Non-equilibrium processing techniques such as rapid solidification from the liquid state, vapor deposition, plasma processing, mechanical alloying (MA), as well as irradiation/Ion implantation, can produce/synthesize such materials with unique and improvised properties. The basic process underlying in these techniques is to synthesize materials in a non-equilibrium state by ‘energizing and quenching’ as shown in **Figure 1** below.

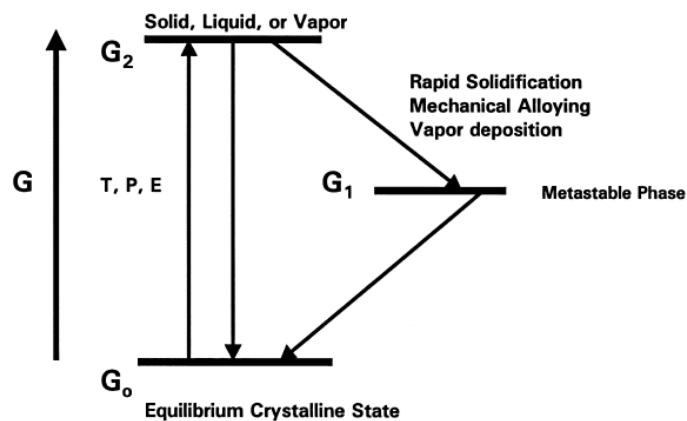


Figure 1 The basic concept of "energize and quench" to synthesize non-equilibrium materials [1]

The energizing process involves exciting the material to a non-equilibrium state by external dynamical force such as melting, evaporating, irradiation, application of pressure or storing of mechanical energy by plastic deformation (as in MA) [2]. The material is then

quenched to configurationally frozen state which if necessary can then be used for subsequent heat treatment. These techniques have been widely used and are rapidly developing to erase or minimize material limitations on many applications using new and improved materials.

The feasibility of synthesizing a metastable structure using a certain synthesis technique can be evaluated by determining/estimating the departure from equilibrium [1] which determines that maximum energy that can store in excess than that in an equilibrium state. This far from equilibrium processing shows significant departures from equilibrium. The departure values for various processes are shown in **Table 1 below**.

Table 1 Departure from equilibrium achieved in various processes [3]

Process	Maximum departure from equilibrium (KJ mol ⁻¹)
Solid state quench	16 ^a
Quench from liquid (rapid solidification)	24 ^b
Condensation from vapor	160 ^c
Irradiation / Ion implantation	30 ^d
Mechanical cold work	1 ^e
Mechanical Alloying	30 ^d
^a Assuming disordering of an ordered intermetallic (not ordered to MP) (6 KJ mol ⁻¹) and a supersaturated solid solution (10 KJ mol ⁻¹)	
^b Assuming disordering of an ordered intermetallic (not ordered to MP) (6 kJ mol ⁻¹), amorphous phase formation (8 kJ mol ⁻¹) and a supersaturated solid solution (10 kJ mol ⁻¹).	
^c Assuming a supercooled vapor transforms to a solid (160 kJ mol ⁻¹).	
^d Assuming a strongly ordered intermetallic (ordered to MP) disorders (12 kJ mol ⁻¹) and becomes amorphous (8 kJ mol ⁻¹), and is a supersaturated solid solution (10 kJ mol ⁻¹)	
^e Assuming 10 ¹⁶ dislocations m ⁻² (2 kJ mol ⁻¹).	
MP, melting point.	

The departure from equilibrium in MA is highest, second to condensation from vapor and compared to rapid solidification technique; it has larger departures. This departure from equilibrium in mechanical alloying leads to following attributes shown in **Table 2 below**:

Table 2 Attributes of mechanical alloying [3]

1. Production of a fine dispersion of second phase particles
2. Extension of solubility limits
3. Refinement of the matrix microstructure down to the nanometre range
4. Synthesis of novel crystalline phases
5. Development of amorphous (glassy) phases
6. Possibility of alloying of difficult-to-alloy elements
7. Inducement of chemical reactions at low temperatures
8. Scalable process

Mechanical alloying (MA) of all the other non-equilibrium processing techniques is an inexpensive, dry and high energy ball milling process that is capable of producing composite metal alloy powders with controlled and extremely fine microstructure[4]. A wide range of alloys including ODS alloys; ceramics, intermetallics, amorphous materials, solid-state solutions including supersaturated solid solutions, metastable crystalline and quasi-crystalline phases including nanocrystalline structures have been developed using Mechanical alloying technique [1]. This method has become common in industries for the production of such materials [5]. This technique was first developed and used by John Benjamin and his colleagues in 1966 at Paul D. Merica Research Laboratory of the International Nickel Company (INCO). MA has currently been shown that it can be used to synthesize a range of equilibrium as well as non-equilibrium alloy phases ranging from homogenized elemental to pre-alloyed powders. One thought that ought to be avoided is a possible contamination from the milling media which was reported previously [6].

CHAPTER 2. LITERATURE REVIEW AND BACKGROUND

Many metallic Germanides have been studied and synthesised so far including Transition metal germanides, rare-earth metal germanides and rare-earth transition metal germanides as they exhibit wide array of intriguing properties including but not limited to High thermal stability (limited to some transition metals) and oxidation resistance (limited to some transition metals) useful in Thermoelectric power generation at high temperatures [7] along with variety of electric and magnetic properties which in turn are used in semiconductor applications [6] and Spintronics applications like GMR technology [8]. Some of these are mentioned below in the literature.

Legend:
 ■ Metals
 ■ Transition metals
 ■ Rare earth metals

Example element:
 atomic # → 29
 atomic symbol → Cu
 English element name → copper
 ← ions commonly formed
 ← atomic mass (rounded) 63.55

1 1s	1 IA H hydrogen 1.008	2 IIA He helium 4.003											18 VIII A																																			
2 2s	3 Li lithium 6.941	4 Be beryllium 9.012											13 III A B boron 10.81	14 IVA C carbon 12.01	15 VA N nitrogen 14.01	16 VIA O oxygen 16.00	17 VII A F fluorine 19.00	18 Ne neon 20.18																														
3 3s	11 Na sodium 22.99	12 Mg magnesium 24.31	3 III B Al aluminum 26.98	4 IV B Si silicon 28.09	5 VB P phosphorus 30.97	6 VIB S sulfur 32.07	7 VIIB Cl chlorine 35.45	8 VIII B Ar argon 39.95	9 VIII B K potassium 39.10	10 VIII B Ca calcium 40.08	11 IB Sc scandium 44.96	12 IIB Ti titanium 47.87	13 IIIB V vanadium 50.94	14 IIIB Cr chromium 52.00	15 IIIB Mn manganese 54.94	16 IIIB Fe iron 55.85	17 IIIB Co cobalt 58.93	18 IIIB Ni nickel 58.69	19 IIIB Cu copper 63.55	20 IIIB Zn zinc 65.41																												
4 4s	19 K potassium 39.10	20 Ca calcium 40.08	21 3d Sc scandium 44.96	22 3d Ti titanium 47.87	23 3d V vanadium 50.94	24 3d Cr chromium 52.00	25 3d Mn manganese 54.94	26 3d Fe iron 55.85	27 3d Co cobalt 58.93	28 3d Ni nickel 58.69	29 3d Cu copper 63.55	30 3d Zn zinc 65.41	31 4p Ga gallium 69.72	32 4p Ge germanium 72.64	33 4p As arsenic 74.92	34 4p Se selenium 78.96	35 4p Br bromine 79.90	36 4p Kr krypton 83.80	37 5s Rb rubidium 85.47	38 5s Sr strontium 87.62	39 4d Y yttrium 88.91	40 4d Zr zirconium 91.22	41 4d Nb niobium 92.91	42 4d Mo molybdenum 95.94	43 4d Tc technetium 98	44 4d Ru ruthenium 101.1	45 4d Rh rhodium 102.9	46 4d Pd palladium 106.4	47 4d Ag silver 107.9	48 4d Cd cadmium 112.4	49 5p In indium 114.8	50 5p Sn tin 118.7	51 5p Sb antimony 121.8	52 5p Te tellurium 127.6	53 5p I iodine 126.9	54 5p Xe xenon 131.3												
5 5s	37 Rb rubidium 85.47	38 Sr strontium 87.62	39 4d Y yttrium 88.91	40 4d Zr zirconium 91.22	41 4d Nb niobium 92.91	42 4d Mo molybdenum 95.94	43 4d Tc technetium 98	44 4d Ru ruthenium 101.1	45 4d Rh rhodium 102.9	46 4d Pd palladium 106.4	47 4d Ag silver 107.9	48 4d Cd cadmium 112.4	49 5p In indium 114.8	50 5p Sn tin 118.7	51 5p Sb antimony 121.8	52 5p Te tellurium 127.6	53 5p I iodine 126.9	54 5p Xe xenon 131.3	55 6s Cs cesium 132.9	56 6s Ba barium 137.3	57 4f La lanthanum 138.9	58 4f Ce cerium 140.1	59 4f Pr praseodymium 140.9	60 4f Nd neodymium 144.2	61 4f Pm promethium 145	62 4f Sm samarium 150.4	63 4f Eu europium 152.0	64 4f Gd gadolinium 157.3	65 4f Tb terbium 158.9	66 4f Dy dysprosium 162.5	67 4f Ho holmium 164.9	68 4f Er erbium 167.3	69 4f Tm thulium 168.9	70 4f Yb ytterbium 173.0														
6 6s	55 Cs cesium 132.9	56 Ba barium 137.3	57 4f La lanthanum 138.9	58 4f Ce cerium 140.1	59 4f Pr praseodymium 140.9	60 4f Nd neodymium 144.2	61 4f Pm promethium 145	62 4f Sm samarium 150.4	63 4f Eu europium 152.0	64 4f Gd gadolinium 157.3	65 4f Tb terbium 158.9	66 4f Dy dysprosium 162.5	67 4f Ho holmium 164.9	68 4f Er erbium 167.3	69 4f Tm thulium 168.9	70 4f Yb ytterbium 173.0	71 5d Lu lutetium 175.0	72 5d Hf hafnium 178.5	73 5d Ta tantalum 180.9	74 5d W tungsten 183.8	75 5d Re rhenium 186.2	76 5d Os osmium 190.2	77 5d Ir iridium 192.2	78 5d Pt platinum 195.1	79 5d Au gold 197.0	80 5d Hg mercury 200.6	81 6p Tl thallium 204.4	82 6p Pb lead 207.2	83 6p Bi bismuth 209.0	84 6p Po polonium 209	85 6p At astatine 210	86 6p Rn radon 222	87 7s Fr francium 223	88 7s Ra radium 226	89 5f Ac actinium 227	90 5f Th thorium 232.0	91 5f Pa protactinium 231.0	92 5f U uranium 238.0	93 5f Np neptunium 237	94 5f Pu plutonium 239	95 5f Am americium 243	96 5f Cm curium 247	97 5f Bk berkelium 247	98 5f Cf californium 251	99 5f Es einsteinium 252	100 5f Fm fermium 257	101 5f Md mendelevium 258	102 5f No nobelium 259
7 7s	87 Fr francium 223	88 Ra radium 226	89 5f Ac actinium 227	90 5f Th thorium 232.0	91 5f Pa protactinium 231.0	92 5f U uranium 238.0	93 5f Np neptunium 237	94 5f Pu plutonium 239	95 5f Am americium 243	96 5f Cm curium 247	97 5f Bk berkelium 247	98 5f Cf californium 251	99 5f Es einsteinium 252	100 5f Fm fermium 257	101 5f Md mendelevium 258	102 5f No nobelium 259	103 6d Lr lawrencium 262	104 6d Rf rutherfordium 261	105 6d Db dubnium 262	106 6d Sg seaborgium 266	107 6d Bh bohrium 264	108 6d Hs hassium 277	109 6d Mt meitnerium 268	110 6d Ds darmstadtium 281	111 6d Rg roentgenium 272	112 6d Cn copernicium 285	113 7p Uut ununtrium 284	114 7p Fl flerovium 289	115 7p Uup ununpentium 288	116 7p Lv livermorium 292	117 7p Uus ununseptium 293	118 7p Uuo ununoctium 294																

Figure 2 Periodic Table with metals, rare-earths, and transition metals highlighted

2.1. Metallic Germanides

In 2005, Hiroshi Fukuoka et. al. [9] synthesised a new binary germanium rich germanide, $\text{SrGe}_{6-\delta}$ ($\delta = 0.5$) using the High-pressure synthesis technique. This synthesis was performed in two steps, with first step being, reacting flakes of Strontium and Germanium with high purity and with molar ratios varying between 1:5 to 1:6 in an Ar-filled arc furnace and grinding them inside an Ar-filled glove box to prevent oxidation of Germanium. The products obtained in the

first step was found to be a mixture of SrGe₂ and Ge. In the subsequent step, they subjected this mixture to a high pressure of 5 GPa and were heated at 1200 °C for 30 min.

The samples obtained were each characterized using an X-Ray diffractometer, and an electron probe analyzer was used on 12 single crystals to determine the composition of the obtained germanide. The analysis performed on these 12 single crystals showed that the Ge composition ranged from 5.43 to 5.86 and hence the compound was described as SrGe_{6-δ}. X-ray single crystal structure analysis was performed on a suitable single crystal, and the structure was solved using CrystalStructure crystallography software package, and the composition was determined to be SrGe_{5.6}. The structure of this compound was found to be a cage-like structure with a Ge covalent network having each Sr atom surrounded by 14 Ge atoms.

They performed physical property measurements such as temperature dependence of electrical conductivity on a disk-shaped sample from room temperature to 2K using Van der Pauw method and on a bar-shaped sample which as in **Figure 3(a)** showed that the electrical resistivity of the obtained sample decreased with decreasing temperature with small amount of residual resistance ~ 0.28 mΩ cm and the resistivity ratio between 300K, and 2K temperature was found to be approximately 4, thermoelectric power measurements were performed using MMR Seebeck effect measurement technique and this revealed positive thermoelectric power indicating that the primary charge carriers are Holes. The thermoelectric power is shown in **Figure 3(b)** of this compound at room temperature was found to be 13 μV/K, not high enough for thermoelectric applications.

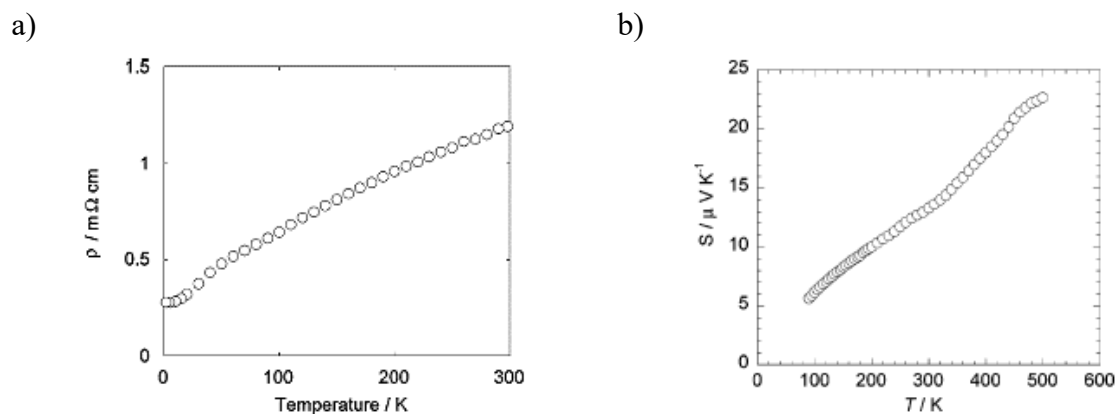


Figure 3 Temperature dependence a) electrical resistivity and b) thermoelectric power measured from 500 to 90K of SrGe_{5.6} [9]

This low conductivity was assumed to be due to Ge vacancy. The electron count of this compound SrGe_{5.6} (as determined by single crystal analysis) was approximated to be such that the two electrons donated by the Sr atom to the Ge network are consumed by 0.5Ge vacancy

per Sr atom to from four lone pairs of neighboring four Ge atoms. This was assumed to be the possible reason for SrGe_{5.6} showing low conductivity.

2.2. Transition metal Germanides

In 1966, I. Mayer et al. [10] synthesized silicides and germanides of various metals at relatively low temperatures using Amalgam method. Although some metals are not readily soluble in mercury including Germanium being sparsely soluble, with an increase in temperature the solubility could be improved. Also, for the formation of desired compounds, the elemental metals should not only dissolve in mercury to form amalgams but also be able to dissociate from it. They studied the optimum conditions for synthesizing silicides and germanides by this method varying several parameters.

They started with filings of metals namely Mn, Fe, Ni and Pt (chemically pure) and rare earth metals with 99.9% purity along with powders of Germanium and Silicon also 99.9% pure. The blend of these metal filings and Germanium/Silicon were placed inside a Pyrex tube. The tube was then filled with mercury such that the blend is 1% of mercury and was sealed after purging 3-4 times with Argon. This tube is then heated in an electric furnace for 10-15 hrs between 450-500 °C followed by cooling over 2-3 hrs. This process was desirable to improve solubility of blend in mercury. The amalgam so obtained was then distilled to separate out volatilized mercury and amalgam. The residual amalgam was then heated for 10-15 hr at 500-600 °C. This treatment decomposed the amalgams and the reactions required to form the desired compound occurred, i.e., reactions between metal and the germanium or silicon.

They performed X-ray analysis on the obtained silicides and germanides. It showed that they were free from any metal-mercury compounds although some germanium and silicon lines were observed, this could be because of non-stoichiometric silicides and germanides formation.

The preparation conditions and crystal type of all the silicides and germanides prepared by this method are shown in **Table 3** below in which the first stage represents the formation of amalgams, the second stage is the distillation of mercury, and the third stage is decomposition of the metal-mercury compounds.

Table 3 Preparation conditions and crystal type of Rare-Earth Disilicides, Digermanides, and Transition-metal silicides and germanides [10]

Disilicide of	First stage		Second Stage		Third stage		Crystal type
	Temp (°C)	Duration of Heating (h)	Temp (°C)	Duration of Heating (h)	Temp (°C)	Duration of Heating (h)	
La	550	18	180	3	550	25	GdSi ₂
Ce	550	18	180	3	550	6	ThSi ₂
Pr	445	8	180	8	500	5	GdSi ₂
Nd	450	8	180	8	500	5	GdSi ₂
Gd	450	10	200	2	550	10	AlB ₂
Tb	450	16	210	3	550	10	AlB ₂
Dy	450	16	200	3	550	10	AlB ₂
Ho	450	16	200	3	550	10	AlB ₂
Er	450	8	200	3	550	10	AlB ₂
Tm	450	16	180	3	550	12	AlB ₂
Yb	450	20	210	3	550	10	AlB ₂
Lu	450	20	190	3	550	10	AlB ₂
Y	450	10	200	3	550	10	AlB ₂
Digermanide of	Temp (°C)	Duration of Heating (h)	Temp (°C)	Duration of Heating (h)	Temp (°C)	Duration of Heating (h)	
La, Ce	450	15	190	5	550	10	GdSi ₂
Pr-Dy, y	450	15	190	5	550	10	ThSi ₂
Ho-Lu	450	15	190	5	550	10	Mixed Phase
Compound	First stage		Second Stage		Third stage		Crystal type
	Temp (°C)	Duration of Heating (h)	Temp (°C)	Duration of Heating (h)	Temp (°C)	Duration of Heating (h)	
Mn ₅ Si ₃	450	15	190	10	550	20	Mn ₅ Si ₃
Mn ₅ Ge ₃	500	15	240	1	700-800	5	Mn ₅ Si ₃
Ni ₂ Si	450	15	200	10	500	10	PbCl ₂
Pt ₂ Si	450	12	190	5	500	10	_____

They concluded that even if only one of the component metals are reactive to mercury, intermetallic compounds can still be formed using Amalgam method as the metal powder

obtained after amalgam formation, and dissociation is highly reactive and will immediately start reaction by interdiffusion with other metals at slightly elevated temperatures and in some cases even at room temperatures.

In 1981, V. M. Agoshkov et al. [11] synthesized/Crystallized both α and β phases of WGe_2 and $MoGe_2$ using High pressure and High-temperature synthesis technique. They prepared the sample from powdered molybdenum, tungsten and germanium with purity >99.9%. The blend of these powders Mo-Ge and W-Ge were placed in the heater inside a high-pressure chamber and were treated with high pressure and temperature over a period from 10-40 min.

Each sample obtained after those specific treatments were studied at room temperature and pressure conditions. X-ray powder photography was performed on the samples to determine the phases present, and they found that both α and β phases of WGe_2 in W-Ge system and $MoGe_2$ in Mo-Ge system were present.

Tungsten digermanides crystallized at 870 K with molybdenum digermanides close to 800 K. α - $MoGe_2$ was obtained at 20 Kbar whereas the β - $MoGe_2$ was obtained at high pressure and similarly in W-Ge system α - WGe_2 was obtained at pressures < 30 Kbar compared to high pressures for obtaining β - WGe_2 . To determine the unit cell dimension of the phases obtained, they used a mixture with NaCl. X-ray microanalysis was used to determine the composition of the alloys obtained, and they concluded that all the phases were prepared in pure form with a stoichiometric composition. For the obtained samples, they determined the dependence of resistivity on temperature between 4.2 and 270 K range using a four-contact scheme and an alternating current of frequency 30 Hz. On annealing, the samples for 5 h at 1000 °C at atmospheric pressure in an evacuated quartz tube, the α - WGe_2 and β - WGe_2 decomposed into elements whereas β - $MoGe_2$ got converted to α - $MoGe_2$.

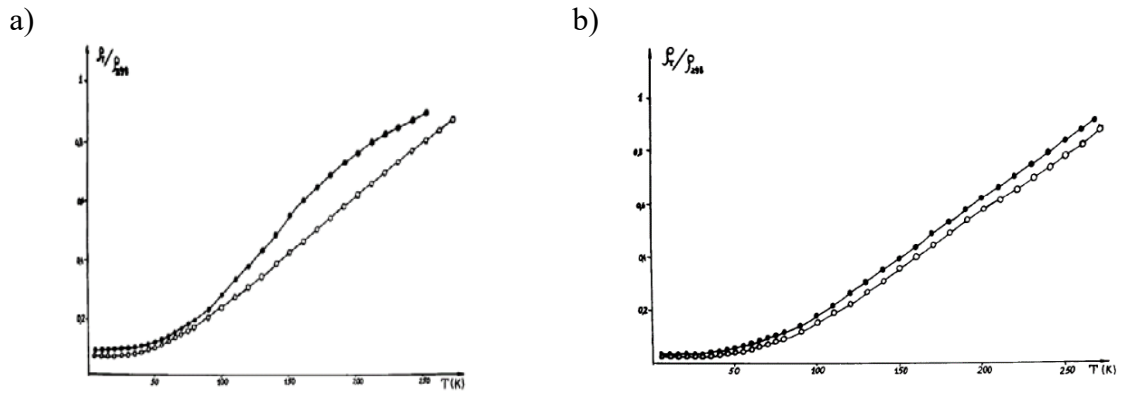


Figure 4 Electrical resistivity vs. temperature for a) α -MoGe₂ and β -MoGe₂ and b) α -WGe₂ and β -WGe₂ [11]

They concluded from the electrical resistivity measurements performed on these samples as shown in **Figures 4 (a) and (b)** that these samples show conductivity like metals at low temperatures.

In 1987, H. Takizawa et al. [12] synthesized Mn₃Ge₅, a germanium-rich manganese germanide using High Pressure and High-temperature synthesis technique. In the phase diagram as shown in **Figure 5**, in Mn-Ge system there exists five intermetallic compounds, Mn_{3.25}Ge, Mn₅Ge₂, Mn₂Ge, Mn₅Ge₃, and Mn₁₁Ge₈, under equilibrium conditions. By the time of their study, germanium-rich germanides were not synthesized. In this study, they were aiming to prepare a Germanium-rich Manganese germanides, i.e., Mn₃Ge₅ which was expected to be a semiconductor.

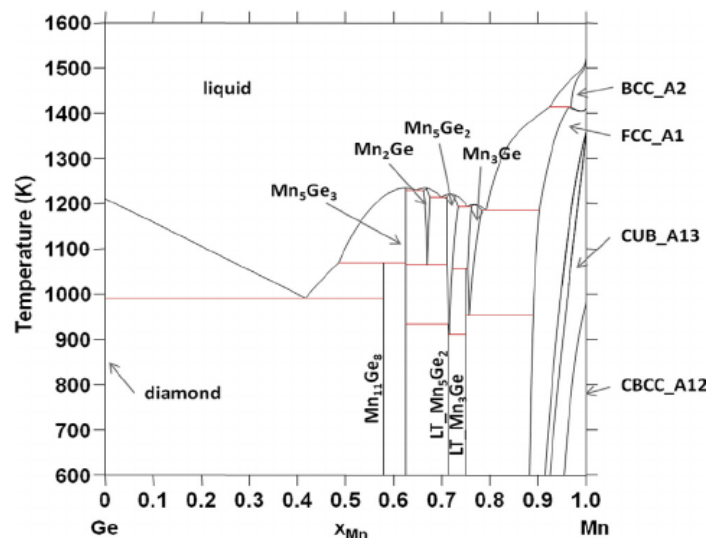


Figure 5 Mn-Ge phase diagram [13]

They started with powders of Manganese and germanium with purities > 99% in case of manganese and > 99.99% in case of germanium. A blend of these powders with varying atomic ratios from 1.5 to 2.0 was prepared and pressed to form pellets of dimensions 5mm diameter by 3mm thickness. These pellets were placed into a cylindrical BN capsule which was then placed in a carbon heater. This entire assembly was placed in a cell filled with NaCl and was subjected to a high pressure of 4GPa and a varying temperature between 600 -1000°C using Belt-Type apparatus as shown in **Figure 6**. The duration of these reactions was varied from 1-8 hr followed by quenching to room temperature. The detailed experimental procedure is mention in their paper [12].

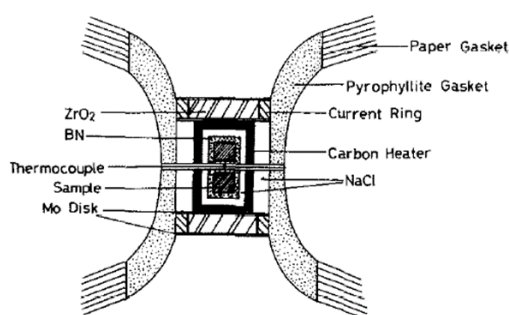


Figure 6 Belt type apparatus arrangement [12]

At 900 °C, they obtained $Mn_{11}Ge_8$ while at 600-100 °C and 4GPa, two new phases were observed which had mixed phases of $Mn_{11}Si_{19}$ type and FeSi type structures. At 800 °C and 4 GPa for 8 hr, they obtained single phase containing $Mn_{11}Si_{19}$ structure type along with some residual germanium. The structure type was determined by leaching out the residual germanium using HNO_3 solution. X-ray powder diffraction analysis was performed on the obtained sample. The analytical results they obtained were in good agreement with the calculated values for the chemical formula Mn_3Ge_5 as shown in **Table 6** below and the crystallographic parameters of this is shown in **Table 7**

Thermal analysis of Mn_3Ge_5 was performed along with the study of temperature dependence of electrical resistivity and thermoelectric power as shown in **Figures 7 (a) and (b)**. They found that the compound Mn_3Ge_5 was stable up to 300 °C, between 300-350 °C it decomposed to MnGe, $Mn_{11}Ge_8$ and Ge under atmospheric pressure.

They observed that the electrical resistivity increased with increasing temperature in the range of 80-200 K and was almost constant above 200 K. Over the range of 80-300 K, 50-70 $\mu V/K$ thermoelectric power was observed with a positive sign which was relatively large.

From these results, they concluded that the Mn_3Ge_5 compound is a p-type degenerate semiconductor or a semimetal.

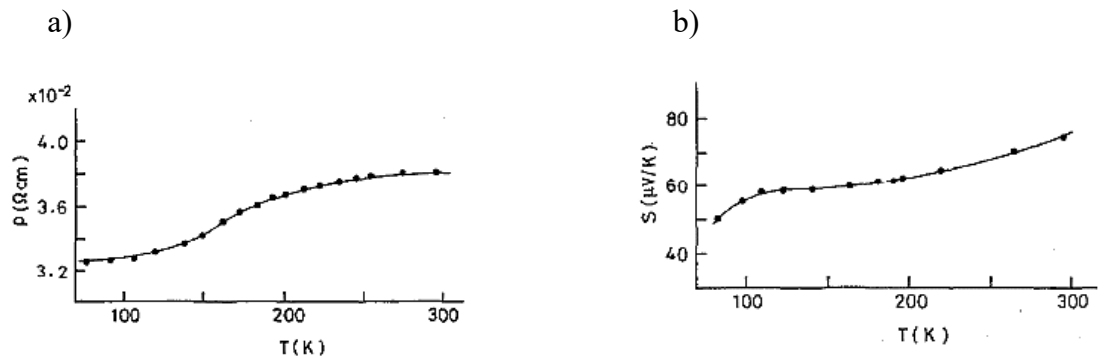


Figure 7 Temperature dependence of a) electrical resistivity and b) thermoelectric power of Mn_3Ge_5 [9]

Table 4 Chemical compositions of Mn_3Ge_5 [12]

	Found (at. %)	Calculated (at. %)
Mn	31.2 ± 0.1	31.2
Ge	68.8 ± 0.1	68.8

Table 5 Crystallographic parameters of Mn_3Ge_5 [12]

Compound	Lattice parameters (nm)			
	<i>a</i>	<i>c</i>	<i>c'</i>	<i>c'/a</i>
Mn_3Ge_5	0.5745	1.38	0.46	0.806

In 1988, H. Takizawa et al. [14] synthesized another metastable MnGe phase alongside CoGe both with the cubic B20 structure using High-pressure synthesis technique. In this synthesis, a blend of Manganese and cobalt powders with >99.9% purity and germanium powder >99.99% purity was prepared with desirable molar ratios and pellets were formed out of them at room temperature using agate mortar, by uniaxially pressing at 100MPa.

The pellets of Mn-Ge so obtained were subjected to similar High pressure and temperature treatment as explained above [12] (Synthesis of Mn_3Ge_5) with pressure varying between 4-5.5 GPa and between 600-1000 °C for 1-3 hr. Before releasing the applied pressure, the samples were quenched to room temperature.

X-ray powder diffraction was performed on the obtained sample to determine the phases obtained, and least squares method was used to determine the lattice parameters. All the diffraction patterns were indexed as FeSi structure type cubic B20 structure, and the lattice constant of $a = 0.4795$ nm was determined from calculations.

Based on thermal analysis on the sample, they determined that MnGe is metastable at room temperature and by annealing at 600 °C, it decomposed to Mn₁₁Ge₈ and Ge. The temperature dependence of electrical resistivity and thermoelectric power were studied using suitable setups between 80-300K, and the results are as shown in **Figures 8 (a) and (b)**.

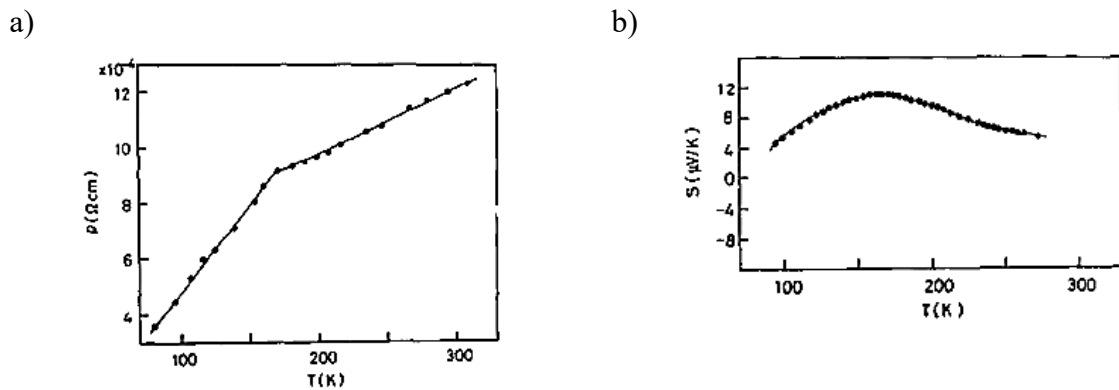


Figure 8 Temperature dependence of a) electrical resistivity and b) thermoelectric power of MnGe [10]

The electrical resistivity increased linearly up to 170K which is an indication of metallic behavior. The slope change was observed at 170K in resistivity vs. temperature curve at which the thermoelectric power was observed to be maximum. Magnetic susceptibility measurements with varying temperature between 80-300K were carried out, and the results are shown in **Figure 9**. The results indicated that MnGe is antiferromagnetic with Neel temperature of 197K.

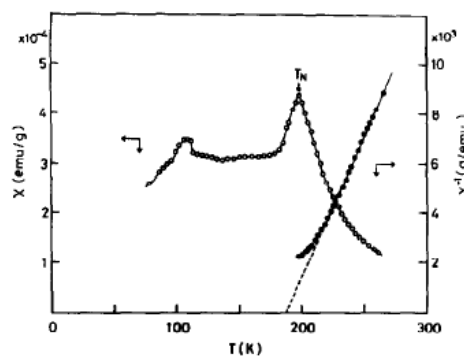


Figure 9 Temperature dependence of magnetic susceptibility and reciprocal magnetic susceptibility of MnGe [14]

χ_g obeyed Curie-Wiess type relation of $M\chi_g = M\chi_p + C/(T-\theta_p)$, In the paramagnetic region of the curve. The Pauli paramagnetic susceptibility was calculated to be $2.17 \cdot 10^{-6}$ emu/g at

paramagnetic Curie temperature, θ_p of 187 K with Curie constant, C of 1.138 emu. K/mol. The larger θ_p value indicated that Mn-Mn ferromagnetic exchange interactions exist in MnGe, the first nearest magnetic exchange interactions. They mentioned that the small hump in magnetic susceptibility curve could be due to a few impurities which X-ray powder diffraction could not detect.

The pellets of Co-Ge were subjected to a high pressure of 4 Gpa and temperature between 800-1000 °C for 1-3 hr to obtain CoGe phase. The lattice constant was calculated to be $a = 0.4631$ nm and was in good agreement with the one reported previously by Larchev and Popova [15]. The CoGe high-pressure phase obtained with cubic B20 structure was metastable at room temperature and pressure and transformed to stable monoclinic phase by annealing to 600 °C in an evacuated silica tube. The electric resistivity, thermoelectric power, and magnetic susceptibility measurements were performed on the cubic B20 structure type CoGe over the range of 80-300K, and the results are shown in the **Figures 10 (a), (b) and 11 respectively**.

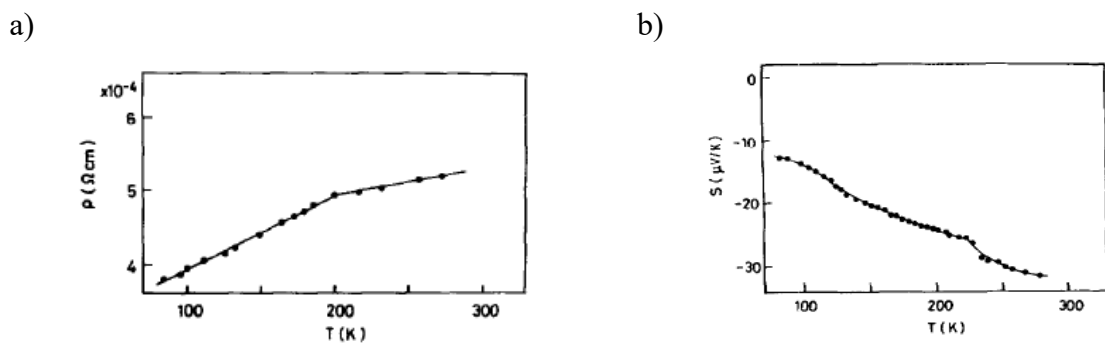


Figure 10 Temperature dependence of a) electrical resistivity and b) thermoelectric power of CoGe [10]

Monoclinic CoGe phase showed metallic behavior with an electrical resistivity of $5.1 \times 10^{-5} \Omega \text{ cm}$ at 80K and $1.6 \times 10^{-4} \Omega \text{ cm}$ at 300K. It was observed that the cubic B20 structure type CoGe although showed metallic behavior, had noticeably higher electrical resistivity than the monoclinic phase and the thermoelectric power relatively larger. Similar to MnGe, the change in slope was observed in resistivity curve at $\sim 200\text{K}$ at which an anomalous change in thermoelectric power was observed.

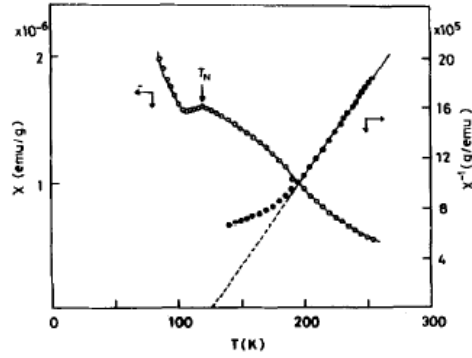


Figure 11 Temperature dependence of magnetic susceptibility and reciprocal of magnetic susceptibility of CoGe with B20 structure [14]

The magnetic susceptibility curve showed that the high-pressure B20 type CoGe phase was antiferromagnetic with Neel temperature of 120K. Also, the material showed Pauli paramagnetism with a magnetic susceptibility of 1.3×10^{-6} emu/g. At elevated temperatures, χ_g obeyed Curie-Weiss type relation with paramagnetic susceptibility of 1.02×10^{-7} emu/g, $C = 0.0082$ emu. K/mol and θ_p of 132 K. They concluded from this value of θ_p that ferromagnetic exchange interactions are dominant similar to MnGe. In the paramagnetic region, below 200K the deviation from Curie-Weiss law was observed which is where the anomalous change in electrical resistivity and thermoelectric power was observed.

The 3d-electrons in intermetallic compounds show essentially an itinerant character. The spin fluctuation in the narrow d-band plays an important role in magnetic and transport behaviors [16]. The spin fluctuation observed in weakly ferromagnetic or nearly ferromagnetic metals is small and variable, but in a localized moment system, it is large and fixed [16][17]. The 3d-electrons in the B20 monogermanides are expected to have localized character, and larger amplitude of spin fluctuation as the large distances between the metal atoms increase the localization of 3-d electrons. Moriya [17] reported cases where the spin fluctuation is highly dependent on temperature and reaches saturation at a finite temperature. Above this point, the spin fluctuation is considered as a set of local moments in Heisenberg model. The anomalies found above in magnetic behaviors of MnGe and CoGe were considered to be the effect of “temperature-induced local moment” (TILM) model. From the magnetic susceptibility measurements of CoGe, the saturation point is considered to be at 200K as the change in transport behaviors occur at this point. In case of MnGe, this occurred at 170K which was observed from a change in resistivity and thermoelectric power measurements.

The effective moment of MnGe and CoGe along with CrGe₆ and FeGe₆ values reported previously are shown in **Figure 12**.

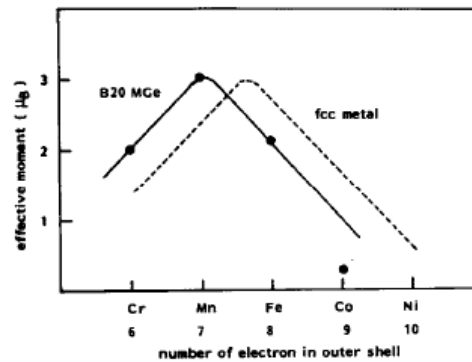


Figure 12 Effective moment per first-row transition metal atom as a function of the number of electron in the outer shell of B20 germanides [14]

From this, they concluded that the effective moments of B20 mono germanides changed by $1\mu_B$ in the series CrGe-MnGe-FeGe like the fcc metals represented by a dotted line in **Figure 12**. Also, the value of CoGe is smaller compared to other mono germanides. The plot shows the shift of B20 germanides from the fcc metals to the left and this shift magnitude is equivalent to 0.7 d-electron. This indicated that each Germanium atom donated 0.7 electrons to the d-band of the transition metal.

The antiferromagnetic MnGe and CoGe are considered to have a helical spin structure as all the B20 compounds are reported to have helical magnetic structure [18][19][20][21] due to Dzyaloshinsky-Moriya interaction as the B20 structure is noncentrosymmetric [21][22].

It is known that the magnetic interaction in alloys or intermetallics containing Mn is closely related to nearest Mn-Mn distance. The nearest Mn-Mn distance in MnGe was found to be 0.294 nm. They concluded that this long distance of 0.294 nm and the increase in the number of electrons in 3d obtained from germanium atom might lead to ferromagnetic exchange interaction between Mn atoms in MnGe with B20 structure.

In 1990, H. Takizawa et al. [23] synthesized another metastable germanium rich Mn-Ge phase, MnGe₄ along with CoGe₄ by high-pressure synthesis technique. Manganese and Cobalt powders with >99.9% purity and Germanium powder with >99.99% purity were used as the starting materials. The blend of these powders Mn-Ge, Co-Ge was prepared varying the atomic ratios Ge/T (T- Mn, Co) from 4.0 to 5.0 using agate mortar. The synthesis process is similar to

what they adapted for synthesizing MnGe, CoGe as well as Mn₃Ge₅ [12][14]. Solid state reactions were induced by subjecting the samples to high pressures of 5.5-6 GPa and temperatures of 600-700 °C for 2hr using Belt type apparatus followed by quenching to room temperature. The samples obtained had residual germanium which was then leached out with 5 N NaOH + 3% H₂O₂ solution at room temperature.

The synthesis condition for MnGe₄ was 5.5 GPa at temperatures between 600-700 °C and keeping there for 2 hr. The products obtained were analyzed using ICP emission spectrochemical analysis. XRD analysis was performed on each sample obtained after varying the synthesizing conditions, and they found that the product obtained with starting composition of Ge/Mn = 4 was a mixed phase of MnGe₄, Mn₃Ge₅ and MnGe₂ with the other two being of low intensity. Single phase MnGe₄ was obtained by starting out with Ge/Mn ratio of 4.8 and leaching out the residual germanium. The germanium wt.% in the obtained single-phase composition after leaching out residual germanium was found to be 85.8±0.1 which was slightly higher than the calculated value of 84.1 wt.% in MnGe₄. The exact chemical composition was determined to be Mn_{0.875}Ge₄. MnGe₄ synthesized using this method was metastable under ambient pressure condition which decomposed Mn₅Ge₃ and elemental Ge between 270-300 °C.

All the diffraction peaks were precisely indexed in the tetragonal structure with lattice constants, $a = 1.103 \pm 0.001$ and $c = 0.5598 \pm 0.0003$ nm, respectively. Since $h+k+l = 2n$ condition was satisfied, they expected the space group to be one of I4/m, I422, I4mm, I4m2, I42m, or I4/mmm.

Change in magnetization with the magnetic field as well as a change in magnetization and magnetic susceptibility over the temperature range of 77-450 K were measured using a magnetic torsion balance with an applied field of up to 10 KOe. The results are shown in **Figures 13, 14 (a) and (b)** respectively.

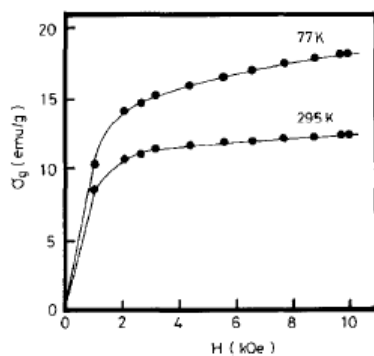


Figure 13 Magnetic field dependence of magnetization of MnGe₄ [2]

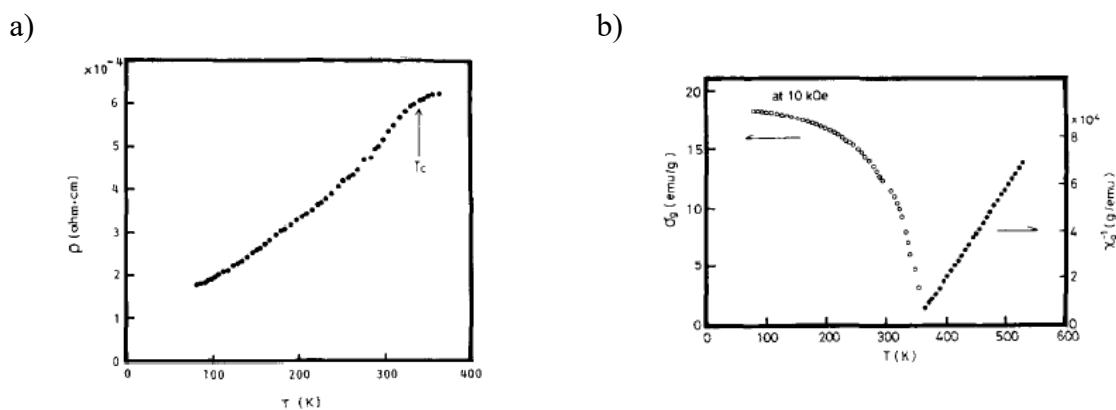


Figure 14 Temperature dependence of a) electrical resistivity and b) magnetization as well as the reciprocal magnetic susceptibility of MnGe₄ [2]

MnGe₄ showed ferromagnetic behavior with curie temperature of 340 K. The magnetic moment at saturation point μ_s for Mn atom was calculated to be $1.2 \pm 0.1 \mu_B$. Above curie temperature, magnetic susceptibility followed Curie-Weiss law. The effective Bohr magnetons P_{eff} was calculated to be $2.83 \pm 0.03 \mu_B$ with paramagnetic curie temperature θ_p of 349 ± 3 K. From the electrical resistivity vs. temperature curve, they concluded that MnGe₄ exhibits metallic behavior although there was a slight change in slope of the curve near the Curie temperature.

Synthesis of CoGe₄ was carried out by subjecting Co-Ge blends to 6 GPa between temperatures of 600-700 °C for 2hr. It was metastable at ambient pressure conditions and decomposed to CoGe₂ and Ge at 380-400 °C. Like MnGe₄ a single phase wasn't obtained when started with the stoichiometric ratio. Hence, they started with the composition of Ge/Co = 4.2 and leached out the residual germanium. Upon analysis, the Ge wt.% in the single-phase

obtained was found to be 83.5 ± 0.1 wt.% which is slightly higher than the calculated value of 83.1 wt.% of Ge in CoGe_4 . The exact composition was determined as $\text{Co}_{0.975}\text{Ge}_4$.

X-Ray powder diffraction was performed on the samples with single phase CoGe . All the diffraction peaks were perfectly indexed with cubic structure with a lattice constant of $a = 1.099 \pm 0.001$ nm. As the reflections observed satisfied the $h+k+l = 2n$ condition, they expected the space group to be one of $I23$, $I213$, $Im3$, $I432$, $I43m$, $Ia3$, or $Im3m$.

They studied the variation of electrical resistivity with temperature in the range of 80-300 K which is shown in **Figure 15**

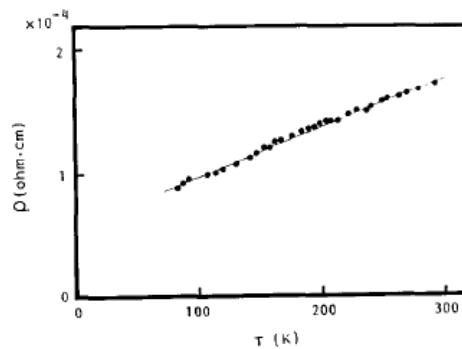


Figure 15 Temperature dependence of electrical resistivity of CoGe_4 [23]

From the resistivity vs. temperature curve, they concluded that the material exhibits metallic behavior. The magnetic susceptibility measurement showed that CoGe_4 was Pauli paramagnetic with a magnetic susceptibility of 5×10^{-7} emu/g.

In 2000, H. Takizawa et al. [24] synthesized a metastable phase of Ni-Ge system, NiGe_2 using the same high-pressure synthesis technique. In the binary Ni-Ge system, nine intermediate phases, $\beta\text{-Ni}_3\text{Ge}$, $\gamma\text{-Ni}_3\text{Ge}$, $\delta\text{-Ni}_5\text{Ge}_2$, Ni_2Ge , $\epsilon\text{-Ni}_5\text{Ge}_3$, $\acute{\epsilon}\text{-Ni}_5\text{Ge}_3$, $\text{Ni}_{19}\text{Ge}_{12}$, Ni_3Ge_2 , and NiGe , are known to exist in the equilibrium phase diagram. The Ge rich portion (≥ 50 at.% Ge) of the phase diagram (NiGe-Ge) is a simple eutectic type with the eutectic point of 762 °C at 67 at.% Ge shown in **Figure 16** No intermediate phases exist in this region.

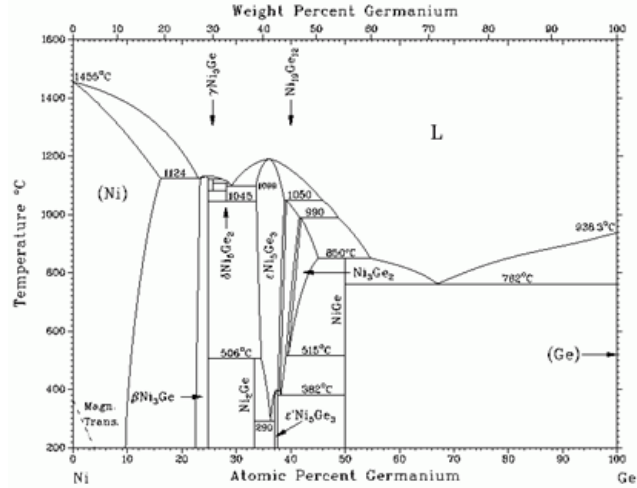


Figure 16 Ni-Ge phase diagram [24]

A blend of Ni and Germanium powders were encapsulated in an h-BN cell and were subjected to a high pressure of 5.5 GPa at a temperature of 700 °C for 30 min. The samples obtained were ground to powder state again, and the procedure of subjecting them to high pressure and temperature in h-BN cells was repeated several times. The samples thus obtained were then quenched to room temperature before releasing the applied pressure.

X-ray diffraction technique was used to analyze the obtained samples, and the crystal structure was refined using Rietveld analysis of powder diffraction data using RIETAN program.

NiGe₂ obtained was metastable at room temperature and pressure conditions which decomposed to NiGe and Ge upon heating it above 300 °C. They were able to index the diffraction pattern completely to a tetragonal unit cell with lattice parameters $a = 5.762(2) \text{ \AA}$ and $c = 10.83(1) \text{ \AA}$, although the diffraction pattern was similar to that of orthorhombic CoGe₂ [25][26] which indicated a possible orthorhombic unit cell. The structural refinement was carried out by Rietveld analysis of X-ray diffraction data. The refinement revealed that NiGe₂ crystallizes into an orthorhombic structure with lattice parameters $a = 10.830(5) \text{ \AA}$, $b = 5.763(3) \text{ \AA}$, and $c = 5.762(3) \text{ \AA}$.

The change in electrical resistivity and thermoelectric power with temperature over the range of 77-300 K were measured by standard d. c. methods. Their results are shown in **Figures 17 (a) and (b)**.

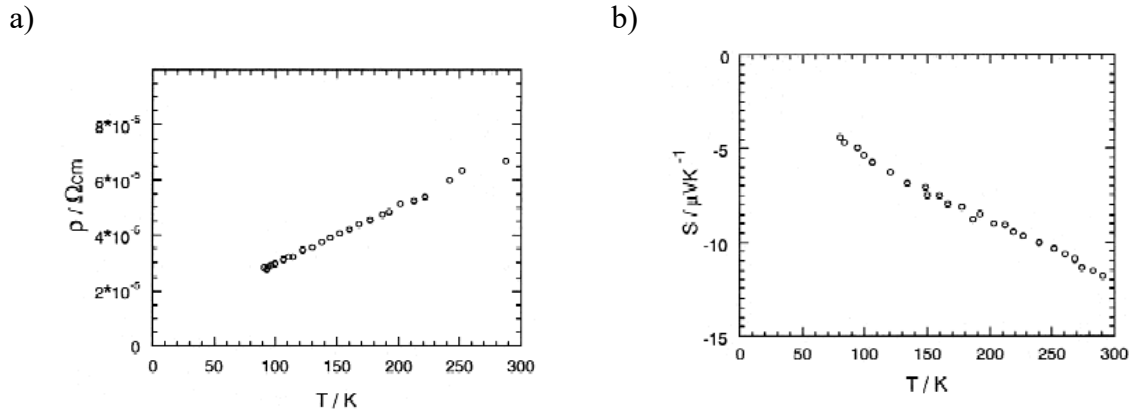


Figure 17 Temperature dependence of a) electrical resistivity and b) thermoelectric power of NiGe₂ [33]

From these, they concluded that NiGe₂ exhibits metallic behavior with high carrier concentration.

Magnetic susceptibility measurements were also performed which revealed that the material is Pauli paramagnetic, i.e., the susceptibility was independent of temperature, and its value was determined to be 2.4×10^{-7} emu/g which indicated no magnetic moment on Ni atom. This was explained for by assuming that an electron was transferred from Ge atom, i.e., the 3d band of NiGe₂ is filled by the formation of short Ni-Ge bonds.

In 2004, L. J. Jin et al. [27] synthesized NiGe, Ni₃Ge₂ alongside NiSi, Ni₃Si₂ and NiSiGe using Thin film deposition technique (in-situ annealing and rapid thermal annealing techniques). They started out with relaxed (100) Si_{0.75}Ge_{0.25}, (111) Ge and (100) Si wafers by cleaning first two with piranha (H₂O₂/H₂SO₄ =1:3) and the Si wafers with standard RCA solution. All the samples were dipped in a dilute HF to remove any residual oxide layers prior to the Ni depositions. Once this is done, the sample was immediately transferred to sputtering chamber. A thin film of Ni with 100 Å thickness was deposited onto wafers at room temperature by sputtering at a deposition rate of 2 Å/s. The base pressure was maintained at below 5×10^{-7} Torr, and the deposition pressure was at about 3×10^{-3} Torr.

Two different annealing methods were used to get different compositions. One was rapid thermal annealing at 400 °C for 60 seconds in an N₂ ambient with temperature ramping at a rate of 30 °C /s, whereas the other method was in-situ annealing process at 400 °C for 30 min inside the sputtering chamber in a vacuum. In in-situ annealing, the heating rate was as low as 0.2 °C /s. The films/ samples obtained were examined using 2D area X-ray diffraction with CuKα radiation and micro-Raman spectroscopy. The XRD results revealed that NiGe was

formed in both the annealing techniques at 400 °C with some residual germanium in case of Ni deposited on Ge and where Ni was deposited on Si and SiGe, both the technique resulted in the formation of low resistivity NiSi and NiSiGe. The XRD spectra of all these films formed using both techniques are shown in **Figures 18 (a), (b) and (c)**.

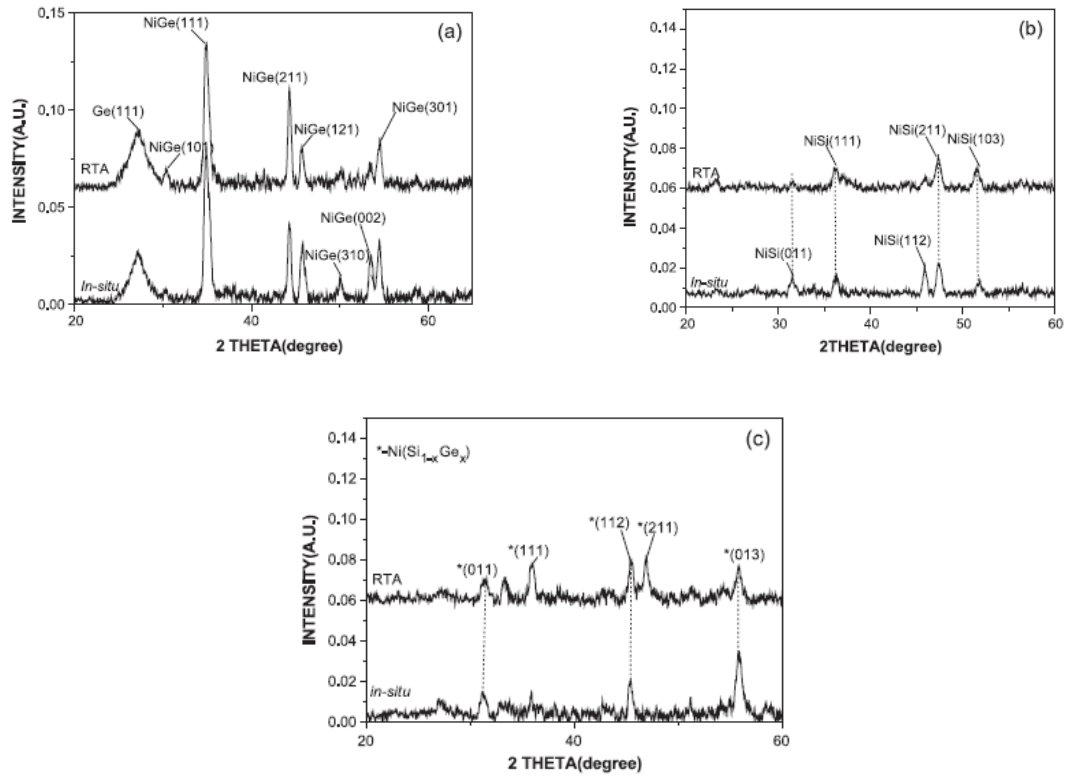


Figure 18 XRD spectra of (a) 10 nm Ni germanide Ge, (b) 10 nm Ni silicide Si and (c) 10 nm Ni germanosilicide Si_{0.75}Ge_{0.25} by RTA method and in-situ annealing method at 400 °C [27]

The surface morphology and the corresponding elemental information was studied using Cross-sectional Transmission electron microscope (TEM) and energy dispersive X-ray spectrometry (EDS) technique in TEM respectively. The sheet resistance of these films of 10nm Ni on Si, Si_{0.75}Ge_{0.25} and Ge substrates was measured using a 4-point probe method, and the results are shown in **Figure 19**.

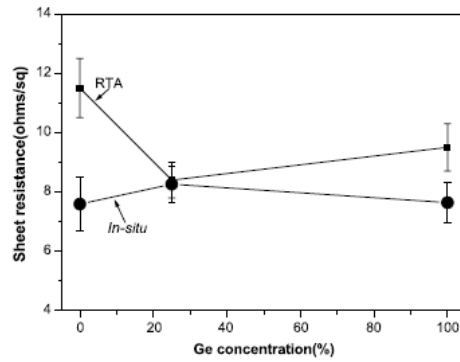


Figure 19 Sheet resistance of 10 nm Ni on Si, Si_{0.75}Ge_{0.25} and Ge using a rapid thermal annealing and an in-situ annealing method at 400 °C, respectively [35]

From the above graph, they concluded that the sheet resistance values of the in-situ annealed samples were lower than the ones annealed by RTA technique. This was assumed to be because of variation in thickness as a result of different annealing methods. In the case of in-situ annealing, Ni has more time to diffuse into Si, Ge and SiGe layers when compared to RTA thus forming Ni silicide, Ni germanide and Ni germanosilicide respectively and hence the thickness would be more in case of in-situ annealed films than RTA annealed ones.

The micro-Raman spectra collected for these films at room temperature are shown in **Figure 20**.

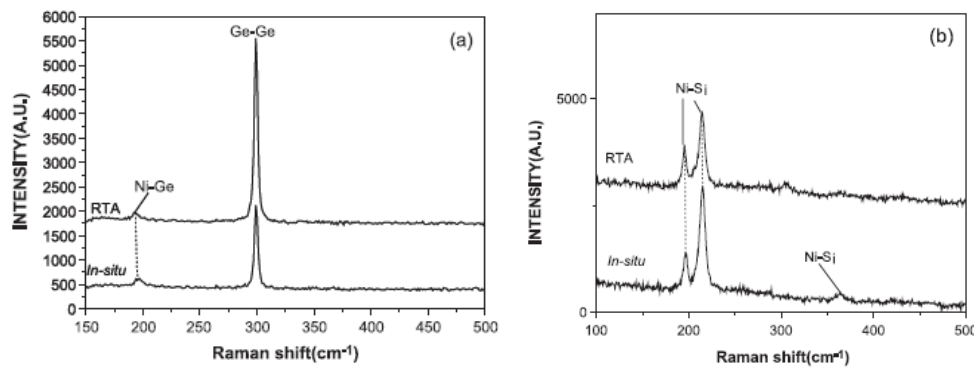


Figure 20 Raman spectra of (a) 10nm Ni on Ge and (b) 10nm Ni on Si annealed at 400 °C by RTA and the in-situ annealing [27]

In these results, they observed a peak at 193 cm⁻¹ in Ni-Ge system in both RTA and in-situ annealing techniques. Before this, there was no report of Raman peaks for Ni_xGe_y and hence from their XRD results and the Raman spectroscopy results, they attributed that peak at 193

cm^{-1} to NiGe phase. In Ni-Si system, they observed Raman peaks corresponding to NiSi phase at 199, 217 and 367 cm^{-1} .

The EDS analysis in TEM showed two phases in Ni-Ge system annealed by RTA method, i.e., NiGe as well as Ni_3Ge_2 although the one annealed by in-situ method had only one phase, i.e., NiGe. This was assumed to be another supporting reason for obtaining lower sheet resistance in in-situ annealed samples. The EDS analysis of Ni-Si system revealed that by annealing using RTA method they were able to obtain a uniform layer of NiSi whereas, in case of annealing by the in-situ method, two phases were found, i.e., NiSi and Ni_3Si_2 . Similarly, in Ni-SiGe system, EDS analysis revealed that using RTA annealing method they were able to obtain almost uniform $\text{Ni}(\text{Si}_{0.78}\text{Ge}_{0.22})$ phase whereas in in-situ annealing method, two phases were obtained which were $\text{Ni}(\text{Si}_{1-x}\text{Ge}_x)$ ($x=0.17$) and $\text{Ni}_3(\text{Si}_{1-y}\text{Ge}_y)_2$ ($y=0.20$). The presence of $\text{Ni}_3(\text{Si}_{1-y}\text{Ge}_y)_2$ phase similar to the one in Ni-Si system was assumed to be due to the reaction of $\text{Ni}_2(\text{Si}_{1-y}\text{Ge}_y)$ with $\text{Ni}(\text{Si}_{1-y}\text{Ge}_y)$ as a result of long annealing time.

In 2006, Matthieu Jamet et al. [28] reported the synthesis of a high Curie temperature ferromagnetic phase of Mn-Ge epitaxial layer using a molecular beam epitaxy growth technique. Standard Ge and Mn effusion cells were used and a low deposition rate of 0.22 \AA s^{-1} . Epi-ready Ge (001) wafers with n-type doping residual ($n \approx 10^{15} \text{ cm}^{-3}$, $\rho \approx 5 \text{ } \Omega \text{ cm}$) were used as a substrate. Once the thermal desorption of surface oxide was done, a 40-nm thick Ge layer was grown as a buffer layer at $250 \text{ }^\circ\text{C}$ which resulted in a perfect 2×1 reconstruction which was confirmed by reflection high-energy electron diffraction. Due to the low solubility of Mn in Ge, an 80-nm thick layer of $\text{Ge}_{1-x}\text{Mn}_x$ was grown subsequently at low temperatures of $70\text{-}130 \text{ }^\circ\text{C}$. Preliminary magnetic measurements on the obtained samples showed that the ones obtained in a very narrow temperature region at around $130 \text{ }^\circ\text{C}$ were of High Curie temperature ferromagnetic samples which had a high Mn content of 6%. They observed that the nanocolumns grown below $100 \text{ }^\circ\text{C}$ had a different structure and a very low Curie temperature. In case of those grown at above $200 \text{ }^\circ\text{C}$, they observed that a secondary phase Ge_3Mn_5 crystallites which was shown in the reflection high energy electron diffraction pattern. Between $100 \text{ }^\circ\text{C}$ and $200 \text{ }^\circ\text{C}$, they observed that upon continuously increasing the growth temperature, pure high-Tc nanocolumns were formed in the beginning and later a mixture of High Tc nanocolumns and Ge_3Mn_5 crystallites were formed.

The morphology of the grown layers was investigated using transmission electron microscopy (TEM). X-Ray fluorescence was used to determine the Mn content in the obtained

thick samples and Rutherford backscattering on Ge-Mn films grown on Silicon. These two techniques showed that the Mn concentrations varied between 5 to 7%. They mentioned that the Mn contents and the magnetic moments they observed had the uncertainty of the order of 17%. The TEM analysis showed self-assembled nanocolumns extending throughout the thickness of GeMn layer. The nanoscale chemical analysis performed on these using electron energy-loss spectroscopy (EELS) showed that chemical maps revealing that the columns were Mn-rich whereas in the matrix was below detection limit (~1%). The cross-section images at high resolution revealed that the epitaxy layer is fully coherent on the Ge buffer layer and no defects or other phases were observed. The high-resolution X-ray diffraction scans performed on epitaxial layers showed only germanium (004) diffraction peak in the range $15^\circ < 2\theta < 150^\circ$. The thickness fringes observed beside the (004) peak showed a 120-nm thick layer which is the total thickness of the film $\text{Ge}_{1-x}\text{Mn}_x$ including Ge buffer. Thus, they confirmed from the XRD data, the high-quality interface between Ge buffer and the $\text{Ge}_{1-x}\text{Mn}_x$ film as there are no secondary phases present. X-ray diffraction performed on the same layers but after annealing at 650 °C for 15 min showed (002) and (004) diffraction lines of Ge_3Mn_5 . This heat treatment activates volume diffusion of Mn atoms resulting in collapsing of nanocolumns into nanoparticles of Ge_3Mn_5 . These were observed in the TEM images at the bottom of GeMn layer. The average diameter of these particles was derived from XRD data and TEM which was 10-12 nm. The EELS performed on these particles showed that they comprised high Mn content.

Magnetic property measurements were carried out using a SQUID magnetometer, and the results are shown in **Figures 21**. The temperature dependence of magnetization was studied at 2 T. The magnetic moment per Mn atom was $4.7 \mu_B$ at 3 K which was close to $5 \mu_B$ expected for Mn^{2+} ions according to Hund's rule. The observed large magnetization was consistent with high ferromagnetic phase with $T_c > 400$ K. From the ZFC_FC study performed on these, it is observed that the curves from 3 K to 300 K superimpose which suggested that there were no nanoparticles except if their blocking temperature exceeds 300 K.

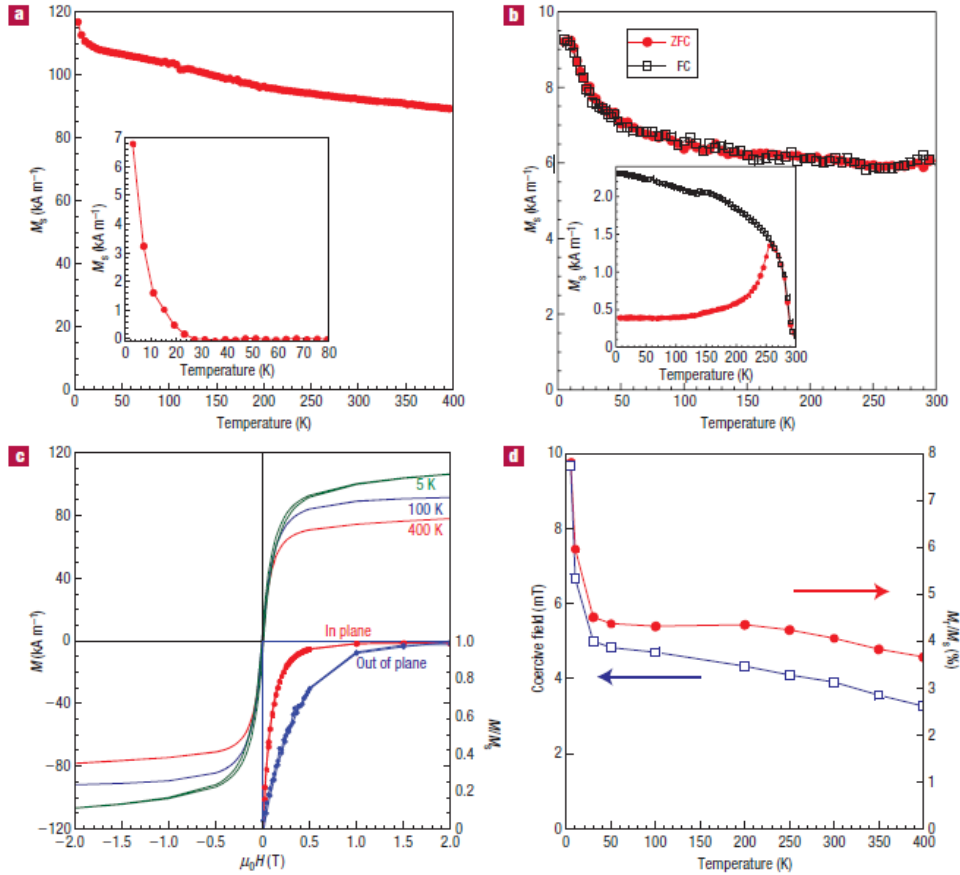


Figure 21 Magnetic measurements using a SQUID magnetometer. Magnetic fields are applied in the plane along the (100) direction. a) Temperature dependence of the saturation magnetization measured at 2 T. The inset shows extrapolated matrix signal at low temperature after subtracting the nanocolumns magnetic signal, b) ZFC_FC measurement carried out at 0.01 T. Both curves superimpose. Inset: ZFC_FC curves after 15 min annealing at 650 °C, c) Magnetization loops at 5, 100 and 400 K, after subtracting the diamagnetic contribution from the substrate. The inset demonstrates the easier saturation in-plane at 250 K. d) Coercive field (μ_0H_C) and remnant magnetization (M_r/M_s) versus temperature. μ_0H_C and M_r/M_s are given with a precision of the order of 10% [28]

In case of the annealed layer, the Curie temperature was ~ 300 K corresponding to Ge_3Mn_5 metallic phase with ZFC_FC curve exhibiting a block temperature of 250 K which agreed with the nanoparticles observed in TEM images. This high T_c phase was attributed to nanocolumns after considering the Mn distribution in GeMn films. In the low-temperature range, the magnetization increased with decreasing temperature and the related saturation

magnetization observed was small ($\sim 9 \text{ kAm}^{-1}$). The additional susceptibility was described by Curie-Weiss law temperature between 10 and 15 K. All the magnetization loops had low remnant magnetization and low coercive field.

In 2012, A. V. Tsvyashchenko et al. [29] synthesized MnGe and CoGe with the cubic B20 structure using high pressure and high-temperature synthesis technique similar to the one used by H. Takizawa et al. [14] for the synthesis of MnGe and CoGe with same crystal structure but using a different setup. In this case, they synthesized MnGe and CoGe at a pressure of 8 GPa by melting the constituent elements by passing current directly through the mixture. They obtained a uniform polycrystal by employing such method.

They performed powder X-ray diffraction using a STOE diffractometer, and they found that the material consisted of a single phase with cubic B20 structure in both MnGe and CoGe. The lattice parameters they obtained were 0.4806 nm for MnGe and 0.4633 nm for CoGe which were found to be close to previous reports. All the magnetic characterization along with determining the specific heat were performed on quantum design MPMS and PPMS instruments. Temperature dependence of magnetic susceptibility was measured for both MnGe and CoGe which is shown in **Figures 22 (a) and (b)** respectively. From these measurements, they observed that CoGe was Pauli paramagnetic whereas for MnGe, shows antiferromagnetic behavior with Neel temperature of $\sim 175 \text{ K}$ which were in good agreement with the one reported by Takizawa et al. [14]. In CoGe, the upturn in susceptibility curve at low temperature was assumed to be due to a small amount of magnetic impurities (less than 0.1% of free cobalt). These results were found to be in contradiction with the one reported by Takizawa et al. [14] which states this material to be antiferromagnetic below 120 K and Curie-Weiss like susceptibility between 200-250 K. The anomalies observed in the magnetic measurements reported by Takizawa et al. [14] were assumed to be due to the presence of magnetic phases as impurities.

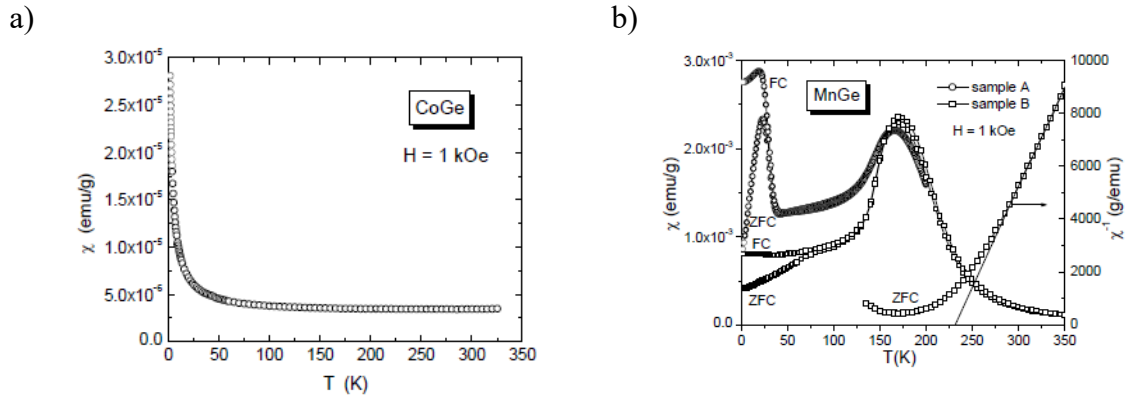


Figure 22 Temperature dependence of magnetic susceptibility of a) CoGe and b) MnGe (samples A and B are from different preparations) [11]

The magnetic susceptibility of MnGe was observed to be following Curie-Weiss law above 300 K with an effective magnetic moment of $\mu_{\text{eff}} = 3.68 \mu_{\text{B}}/\text{f.u.}$ and $\theta_{\text{p}} = +231 \text{ K}$. A strong ferromagnetic response was confirmed from this large θ_{p} . The value of effective magnetic moment was observed to be close to free Mn^{4+} ion value $3.87 \mu_{\text{B}}/\text{f.u.}$ Zero-field-cooled and field cooled hysteresis were observed at very low temperatures $< \sim 50 \text{ K}$ as shown in **Figure 22(b)** above, which was assumed to be due to the possible formation of ferromagnetic-like domains. The change in magnetization with a temperature between 2-350 K and with the applied field between 50-60 KOe was measured for both the samples A and B of MnGe and with two different MPMS instruments. Although they observed the difference in susceptibility behavior in both samples, the magnetic moment at high field and magnetization were in good agreement for both samples. The figure below shows magnetization of sample B in fields up to 60 KOe at different temperatures between 2-350 K. It was observed that the magnetization tends to saturate as it reaches higher fields which indicated the formation of field polarized ferromagnetic state. Small hysteresis was observed in the magnetization curves at low temperatures which gradually decreased and disappeared above 100 K. From the measurements of magnetization of MnGe in field up to 60 KOe at different temperatures as shown in **Figure 23 (a)**, they constructed its T-H magnetic phase diagram which is shown in **Figure 23 (b)**. This was observed to be like that proposed for MnSi-type compounds with the helical magnetic order.

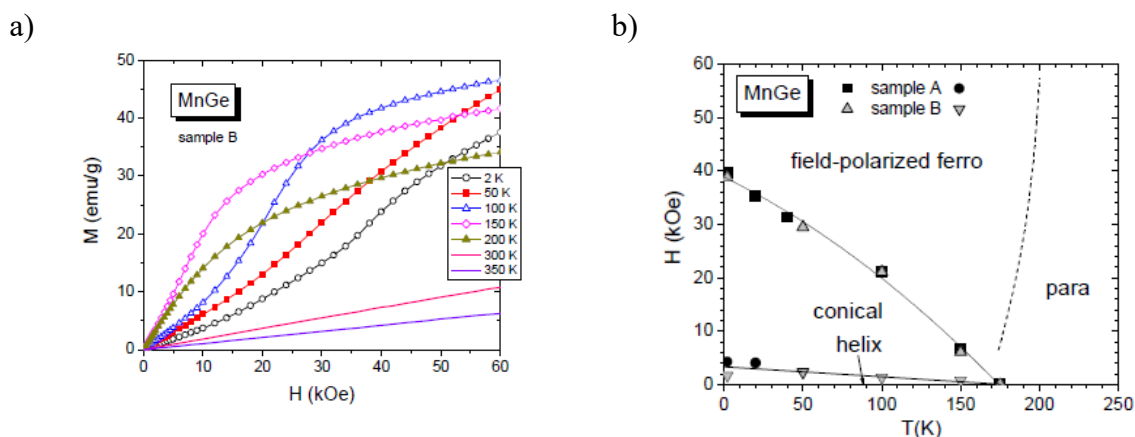


Figure 23 a) Magnetization curves of MnGe at different temperatures and b) The magnetic T-H diagram of MnGe [11]

The specific heat measurements of MnGe and CoGe performed as shown in **Figure 24** between 2-300 K reveal that the total magnetic entropy of MnGe relative to non-magnetic CoGe is equal to 3.55 J/mole-K ($0.62R\ln 2$) and 93% of this value was released below $T_N = 175$ K.

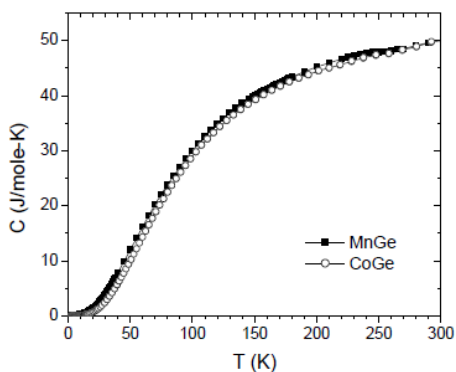


Figure 24 Temperature dependence of the specific heat of MnGe and CoGe [29]

The remaining entropy was found to be in the temperature range of 175-250 K. Near 175 K, no sharp peak was observed in $C(T)$ while the magnetic susceptibility showed a broad maximum in contrary to MnSi. For CoGe, the C/T at 2 K was found to be ~ 4 mJ/mole-K² which is typical for a magnetic metal whereas for MnGe it was found to be close to 20 mJ/mole-K².

In 2013, Dimitri D. Vaughn II et al. [30] synthesized Fe-Ge nanostructures by hot injection of an oleylamine solution of $\text{Fe}(\text{CO})_5$ into a solution containing GeI_4 , oleylamine, oleic acid, and hexamethyldisilazane. They claimed that this approach was a combination of recent advances in the synthesis of colloidal Ge nanocrystals with methods that are used to synthesize metal and alloy nanoparticles. Germanium(IV) iodide (GeI_4 , 99.99+%), hexamethyldisilazane (HMDS, >99%), and iron (0) pentacarbonyl [$\text{Fe}(\text{CO})_5$, >99.99%] were used for this synthesis process. Oleylamine (>50% tech.) and oleic acid (90% tech.) were degassed before use, and all other chemicals were used as received without further purification. All syntheses were carried out under Argon atmosphere using standard Schlenk techniques, and the workup procedures were performed in air.

A solution of $\text{Fe}(\text{CO})_5$ in oleylamine (OAm-Fe) was prepared in the glovebox by mixing 15 μL (~ 0.1 mmol) of $\text{Fe}(\text{CO})_5$ with 2 mL of oleylamine. This solution was stored in an airtight vial. For the synthesis of Fe_3Ge_2 nanocrystals, 60 mg (~ 0.1 mmol) of GeI_4 was placed into a 20 mL scintillation vial along with 10 mL of oleylamine and 0.75 mL of oleic acid. This vial was sonicated for ~ 10 min until a colorless solution was obtained. The solution thus obtained was transferred to a 100 mL three-necked round-bottomed flask which was fitted with a condenser, thermometer with its adapter, and a rubber septum, in which it was degassed under vacuum at 120 $^\circ\text{C}$ for ~ 5 –10 min. The solution was then cooled to approximately 80 $^\circ\text{C}$ and was exposed to argon. Under a constant flow of argon gas, 1 mL of HMDS was injected directly into the reaction flask. The mixture was then slowly heated to 200 $^\circ\text{C}$ at ~ 10 $^\circ\text{C}/\text{min}$, and the previously prepared OAm-Fe solution was injected immediately which resulted in the formation of a light-brown colored solution. The final reaction mixture was then treated in two different ways to get two different products one being Fe_3Ge_2 nanocrystals and the other was FeGe nanowires. To obtain Fe_3Ge_2 nanocrystal, the mixture was heated to 260 $^\circ\text{C}$ at ~ 2 $^\circ\text{C}/\text{min}$ and held for ~ 30 min, forming a black solution followed by cooling, by removing the flask from the heating mantle. To get FeGe nanowires, they heated the mixture at 300 $^\circ\text{C}$ for 30 min. In both the cases, a black solid was precipitated by adding 20 mL of ethanol and then centrifuging at 12,000 rpm for 10 min. The as-synthesized nanocrystals, nanowires were washed three times using a 1:1 toluene/ethanol mixture (with centrifugation in between washes) and then suspended in hexanes, toluene, or ethanol to form a colloidal suspension for further characterization.

Powder X-ray diffraction (XRD) was performed on the obtained samples using a Bruker D8 Advance X-ray diffractometer with $\text{Cu K}\alpha$ radiation, and the refined lattice

constants for Fe_3Ge_2 were found to be $a = 3.958(6) \text{ \AA}$ and $c = 4.965(3) \text{ \AA}$. Transmission electron microscopy (TEM) images and selected-area electron diffraction (SAED) patterns were obtained. They observed from XRD as well as SAED that the nanocrystal obtained showed hexagonal diffraction patterns. Upon analyzing multiple EDS spectra, they concluded that the nanocrystals obtained had Fe:Ge ratio between 50:50 and 60:40. From these results, they assumed that the obtained nanoparticles were close to Fe_3Ge_2 . Scanning transmission electron microscopy coupled with energy-dispersive X-ray spectroscopy (STEM-EDS) was performed along with collecting High-resolution TEM images. These confirmed the crystal structure and the composition for Fe_3Ge_2 nanocrystals.

For FeGe nanowires, the XRD pattern revealed that the product obtained had a structure which was similar to monoclinic CoGe along with small impurity of GeO_2 . Scanning electron microscopy (SEM) and energy-dispersive X-ray spectroscopy (EDS) data were collected. The EDS element mapping confirmed that the Fe and Ge were homogeneously distributed throughout the nanowires. The morphology of the nanowires was confirmed from TEM images.

Temperature dependence of magnetization for the obtained Fe-Ge nanostructures was performed using a Quantum Design superconducting quantum interference device (SQUID) magnetometer, and the results of Fe_3Ge_2 are shown in **Figure 25**.

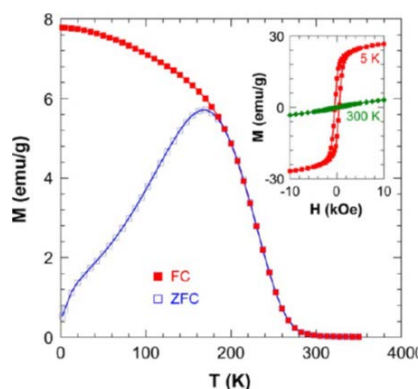


Figure 25 Temperature-dependent (FC and ZFC) magnetization data for the Fe_3Ge_2 nanocrystals, indicating ferromagnetic behavior with a T_c of $\sim 265 \text{ K}$. Consistent with this, the inset shows a plot of M vs H , which indicates magnetic hysteresis at 5 K but not at 300 K [30]

The figure above shows a plot of magnetization measured at 100 Oe field as a function of temperature. Both Zero-field and field cooled measurements were performed on a

representative sample of Fe₃Ge₂ nanocrystals. From these magnetic measurements, they concluded that Fe₃Ge₂ nanocrystals obeyed Curie-Wiess law above ~280K and magnetization rises sharply above Curie-Wiess behavior below that temperature. These results were found to be consistent with the Fe₃Ge₂ nanocrystal which is ferromagnetic with Curie temperature of $T_C \approx 265$ °C. Subsequent MvH loops performed at 5 K revealed that the crystal consisted of single magnetic phase consistent with MvT curves. The MvH curves also revealed the saturation magnetization of 24 emu/g, remnant magnetization of 12.2 emu/g and coercivity of 460 Oe. From the MvH runs performed at 300K which is slightly above T_C they confirmed that the samples obtained were free from Fe₃O₄, Fe₂O₃ or Fe impurities as there was no magnetic response and these phases have T_C greater than 300K which would have shown up in MvH curve obtained at 300K.

In 2014, V. G. Myagkov et al. [31] synthesized ferromagnetic germanides of Mn by solid-state reactions in 20Ge/80Mn films. The initial bilayers of 20Ge/80Mn were obtained by thermal deposition of Mn and Ge layers onto a glass substrate under vacuum and residual pressure of 10⁻⁶ Pa. These substrates were degassed at 350 °C before deposition of Mn layers at 200 °C. The deposition of Ge layers was performed at room temperature to prevent any reaction between Mn and Ge during the process. The samples are made with 20Ge:80Mn atomic composition with a total thickness of 0.5 μm. These samples were annealed in vacuum at a residual pressure of 10⁻⁴ Pa from temperatures 50 to 500 °C in steps of 50 °C and keeping the sample at that temperature for 30 minutes. The samples thus obtained were characterized using MPMS-XL SQUID magnetometer and SPECS photoelectron spectrometer.

From the X-ray diffraction performed on initial 20Ge/80Mn films as shown in **Figure 26**, they observed that it showed α Mn reflections. They assumed that the top Ge layer grew with fine grains as they did not observe Ge reflection in the diffraction patterns. On annealing, at 150 °C, the Mn reflections disappeared, and reflections of ferromagnetic Mn₅Ge₃ phase were observed, and this phase became dominant after annealing at 250 °C. Above 250 °C, the Mn₅Ge₃ phase disappeared and new reflections corresponding to weakly ferromagnetic k -Mn₅Ge₂ [ICDD PDF35-1409] and ϵ -Mn₃Ge [ICDD PDF65-6715] were observed which then became dominant upon further annealing at 400 °C. It was observed that upon increasing the annealing temperature above 400 °C, some X-ray patterns contained peaks of ϵ_1 -Mn₃Ge that formed due to transition from ϵ to ϵ_1 [32]. The unindexed peaks were assumed to be belonging to metastable Mn_xGe_{1-x} phases with high Mn content, or to nonequilibrium Mn₃Ge structure

[33][34][35]. On further annealing it at 500 °C, they observed that the peaks of κ -Mn₅Ge₂, ϵ -Mn₃Ge, and ϵ_1 -Mn₃Ge phases remained along with rise in peaks of weak MnO and Mn₅Ge₃ phase.

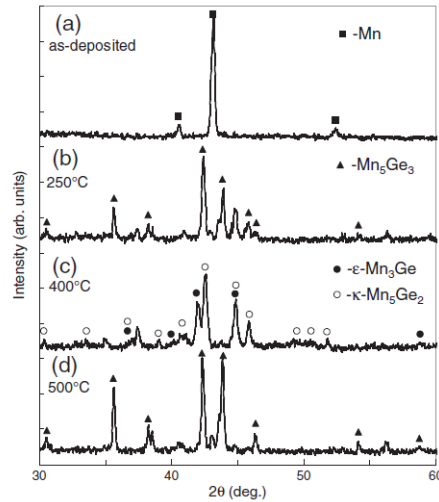


Figure 26 X-ray diffraction patterns of the 20Ge/80Mn film system: (a) initial sample, (b) sample annealed at 250 °C, (c) 350 °C, and (d) 500 °C [31]

The annealing temperature dependence on saturation magnetization M_s and resistance R for the initial 20Ge/80Mn films were studied, and the results are shown in **Figure 27**.

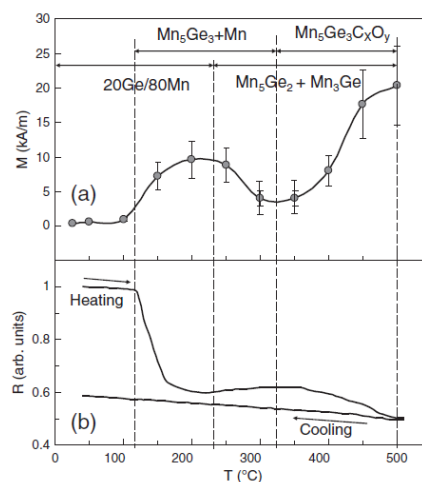


Figure 27 Annealing temperature dependences of (a) saturation magnetization M_s , and (b) resistance R of the 20Ge/80Mn bilayer. The top of the figure shows the temperature boundaries of the existence of the 20Ge/80Mn film system and the Mn₅Ge₃ and Mn₅Ge₃C_xO_y phases [31]

They observed that the magnetization reaches a maximum at an annealing temperature of 250 °C, 350 °C and 500 °C. The experimental values of magnetization were observed to be scattered which was assumed to be due to the formation of the metastable Mn-rich phase of Mn-Ge system. They observed that the samples obtained after annealing at 120 °C were nonmagnetic. After annealing it at 250 °C, Magnetization showed a strong increase. This trend indicated that the intermixing of Ge and Mn layers started with initiation temperature of $T_0^1 = \sim 120$ °C resulting in solid state synthesis of ferromagnetic phase. Upon annealing at 300 °C, they observed the decrease in saturation magnetization which was assumed to be due to the formation of weak magnetic compounds with initiation temperature of $T_0^2 = \sim 300$ °C. Further annealing it at $T_0^3 = \sim 400$ °C caused the saturation magnetization to increase sharply and reaches its maximum value of 14-25 kA/m at 500 °C which is shown in **Figure 27**. They found that this evolution of saturation magnetization with varying annealing temperatures was consistent with the formation of ferromagnetic Mn_5Ge_3 phase at ~ 120 °C and the weak magnetic k - Mn_5Ge_2 and ϵ - Mn_3Ge phases at ~ 300 °C.

For the resistance dependence on annealing temperature which is shown in **Figure 27**, the resistance change was insignificant until ~ 120 °C, and it decreased rapidly above ~ 120 °C. This indicated that there were no significant changes at Ge/Mn interface before ~ 120 °C. The intense mixing of Mn and Ge layers started above ~ 120 °C resulting in the formation of Mn_5Ge_3 which was confirmed from X-ray diffraction patterns. The resistance was at its maximum when the annealing temperature was between 150-200 °C and weakly varies in the range of 270-370 °C. They concluded that this was due to the formation of Mn_5Ge_2 and Mn_3Ge phases. The resistance dropped above ~ 370 °C because of formation of Mn_5Ge_3 again. The resistance smoothly increased with decreasing temperature from 500 °C which is a typical feature of a semiconductor.

They also studied the temperature dependence of saturation magnetization as shown in **Figure 28**. From this, they confirmed the sequential formation of Mn_5Ge_3 , Mn_5Ge_2 and Mn_3Ge phases in the 20Ge/80Mn films after annealing at 250 °C and 400 °C respectively. In the samples annealed at 250 °C, the shape of saturation magnetization indicated the presence of only magnetic phase with Curie temperature ~ 300 K which is close to the reported value of Mn_5Ge_3 [36].

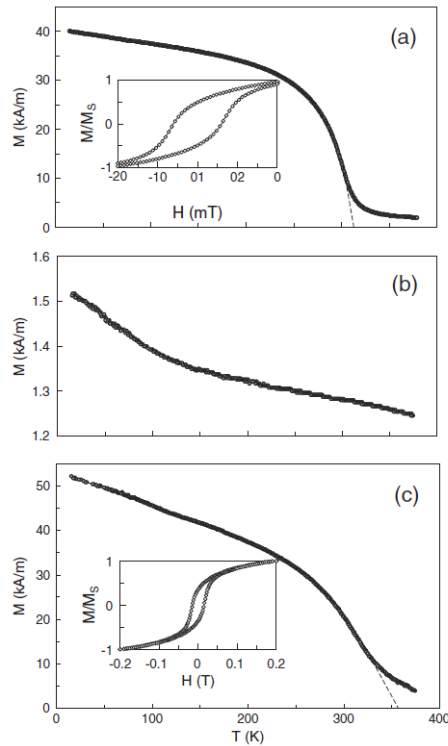


Figure 28 Temperature dependences of saturation magnetization M_S measured in a magnetic field of 0.5 T for the 20Ge/80Mn film system after annealing at (a) 250 °C, (b) 350 °C, and (c) 500 °C. Insets show in-plane M – H hysteresis loops for Mn_5Ge_3 and $Mn_5Ge_3C_xO_y$ phases [31]

In samples annealed at 400 °C, the insignificant magnetization is observed which was due to the presence of small amounts of Mn_5Ge_3 phase along with the formation of weakly magnetic phases, i.e., ϵ - Mn_3Ge , ϵ_1 - Mn_3Ge and k - Mn_5Ge_2 phases. Upon annealing at 500 °C, the samples with high magnetization showed Curie temperature $T_C \sim 350$ – 360 K.

They have studied the composition and chemical state of the Mn, Ge, O, and C over the film depth by applying XPS coupled with Ar + sputtering. The study performed on initial 20Ge/80Mn bilayers revealed the presence of Ge layers and the absence of Mn layers after etching the sample to a depth of 20–30 nm. The relative concentration of Mn, Ge, O, and C as a function of sputtering time of 20Ge/80Mn samples after annealing at 500 °C is shown in **Figure 29**.

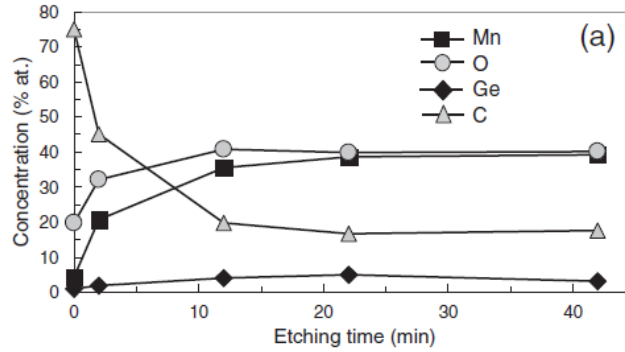


Figure 29 Relative concentration of Mn, Ge, C, and O in 20Ge/80Mn films as a function of sputtering time [31]

After decontamination, the distribution of Mn, Ge, O, and C were found to be almost homogenous to a depth of 50-60 nm. For the samples annealed at 400 °C, the carbon and oxygen were found localized on the surface only. The change in elemental spectra with depth was found insignificant. These results along with magnetic measurements indicated the migration of C and O into Mn₃Ge lattice and the formation of Nowotny phase Mn₅Ge₃C_xO_y with Curie temperature of T_C~350-360 K and with a high saturation magnetization of M_S~14-25 kA/m at room temperature.

In 2015, Fang Yuan et al. [7] synthesized Cr₅B₃-type Ta₅Si₃ by arc melting method along with Cr₅B₃-type Ta₅Ge₃ by sintering at 1000 °C. For the synthesis of Ta₅Si₃, pieces of Ta with 99.999 wt% and Si with 99.9999 wt. % were taken such that final sample mass close to 1 g. These pieces were arc melted under a pure argon atmosphere, and the resulting mixture was remelted thrice to improve the homogeneity. The melting point of Ta (T_m=3017 °C) being close to the boiling point of Si (T_b = 3265 °C) had led loss of Si and to compensate for this, they added excess 30% Si. For the synthesis of Ta₅Ge₃, Ta powder with 99.9999 wt. % and Ge pieces with 99.9999 wt% were taken. The Ge pieces were ground and then mixed with Ta powder such that the molar ratio was close to 3:5. This was all performed in an Ar-filled glove box. This mixture was then pressed and sealed in an evacuated silica tube and heated to 600 °C at a rate of 20 °C /hour. The mixture was kept at this temperature for 24 hr and then heated to 100 °C at 100 °C /hour rate. The samples were left at this temperature for 1 week and were then quenched to room temperature using cold water. They have noticed that there was no weight loss during the sintering process.

The X-Ray diffraction analysis was performed on the samples Ta_5Si_3 and Ta_5Ge_3 obtained after the arc melting and sintering processes respectively using a PANalytical X'Pert Pro diffractometer with linear X'Celerator detector, $CuK\alpha_1$ radiation in the 2θ range of 20° to 70° or 80° . The determination of lattice parameters was performed by a full-profile Rietveld refinement. They observed that the Ta_5Si_3 and the Ta_5Ge_3 phases both adopt Cr_5B_3 structure type with space group $I4/mcm$. They concluded positions of the atoms in these phases as describes; Ta atoms sit on the $16l$ and $4c$ sites while Si and Ge atoms were on $4a$ and $8h$ sites. The crystallographic data of these samples from the refined XRD patterns shown in **Figures 30 and 31** are shown **Table 13**.

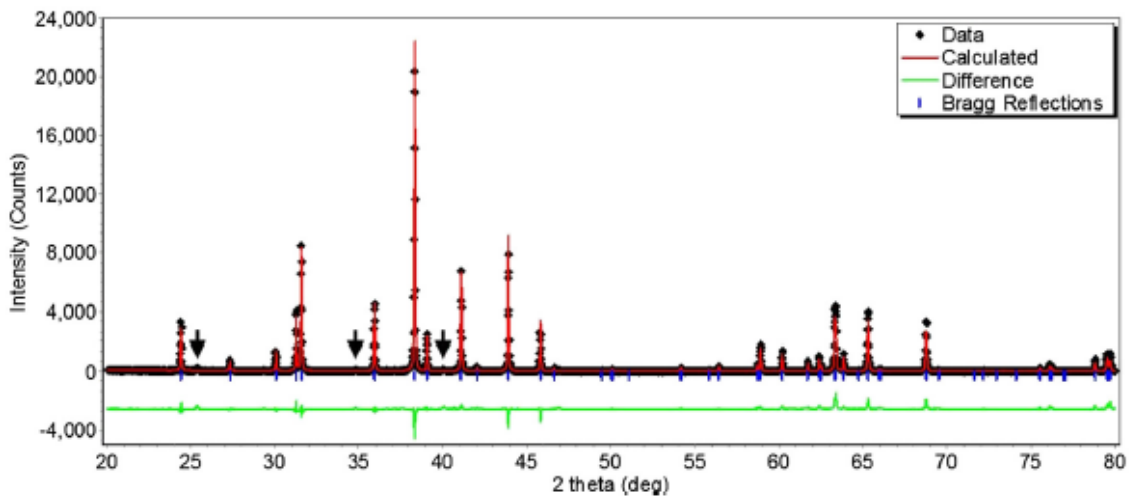


Figure 30 Powder X-ray diffraction patterns and Rietveld refinements of Cr_5B_3 -type Ta_5Si_3 . The $TaSi_2$ impurity is indicated with arrows [7]

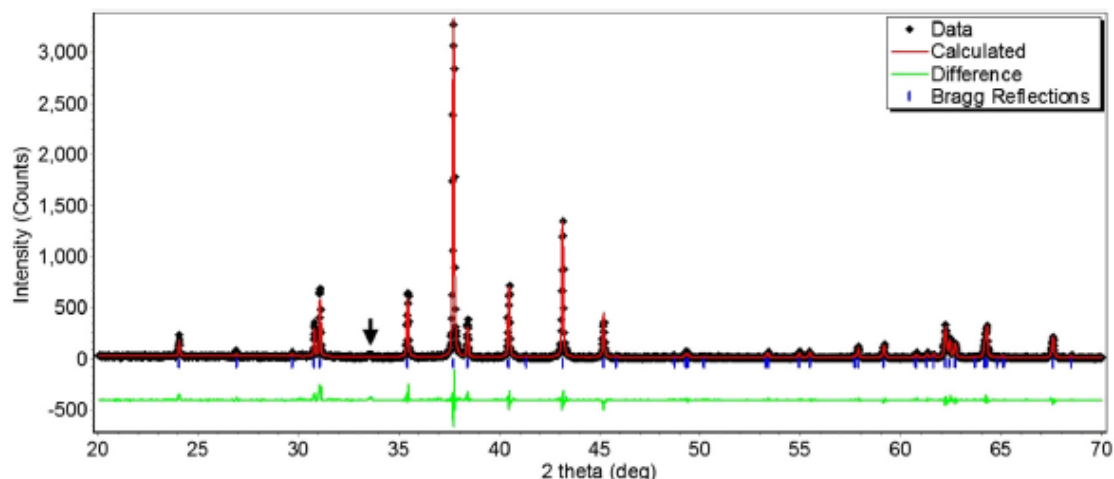


Figure 31 Powder X-ray diffraction patterns and Rietveld refinements of Cr₅B₃-type Ta₅Ge₃. The Ta impurity is indicated with an arrow [7]

Table 6 Crystallographic data for the Ta₅Si₃ and Ta₅Ge₃ samples determined from the powder X-ray diffraction [7]

Composition	Treatment	Str. Type	<i>a</i> , Å	<i>c</i> , Å	<i>V</i> , Å ³
Ta ₅ Si ₃	Cast	Cr ₅ B ₃	6.51718 (8)	11.8765 (2)	504.44 (1)
Ta ₅ Ge ₃	Annealed	Cr ₅ B ₃	6.62144 (6)	12.0284 (2)	527.37 (1)

It was noticed that some weak peaks corresponding to TaSi₂ were observed along with Ta₅Si₃ which was an impurity where in the Ta₅Ge₃, the small, weak peaks observed were of pure unreacted Ta phase. In both cases, the weight percent of impurities was close 1%.

They analyzed single crystal extracted from the samples using a STOE IPDS II diffractometer with MoK α radiation. Numerical absorption corrections were made based on crystal shapes derived from optical face indexing. These were later optimized against equivalent reflections using STOE X-Shape software. The structural solution and refinement were performed using SHELXS and SHELXL software packages respectively. They observed that the obtained data from single crystals were in good agreement with those from the X-ray powder diffraction. They assumed that Ta₅Si₃ and Ta₅Ge₃ were stoichiometric as they did not observe any deficiencies on the crystallographic sites.

Also, they observed that the sample obtained were stable in the air after a long exposure and no decomposition was observed.

Magnetization dependence on temperature and electrical resistivity dependence on temperature were studied for each of these samples using Superconducting Quantum Interference Device (SQUID) on the magnetic property measurement system (MPMS)

magnetometer and Quantum design's physical property measurement system (PPMS) equipped with an ac transport controller (Model 7100) respectively.

Since both the Ta_5Si_3 and Ta_5Ge_3 samples contain no active magnetic elements, they predicted Pauli paramagnetic response. This was true in case of Ta_5Si_3 which was confirmed from the MvT data shown in **Figure 32**. However, Ta_5Ge_3 showed a much complex behaviour with three distinct regions; (1) a steep increase in M below 50 K; (2) almost temperature dependent behaviour between 100 and 250 K; (3) a decrease of M with temperature above 250 K. They assumed that all three regions could be attributed to the variable filling of the spin subbands with temperature. Although they observed small Ta impurity in Ta_5Ge_3 , they doubted that it would have any significant effect on the magnetic behavior of the sample.

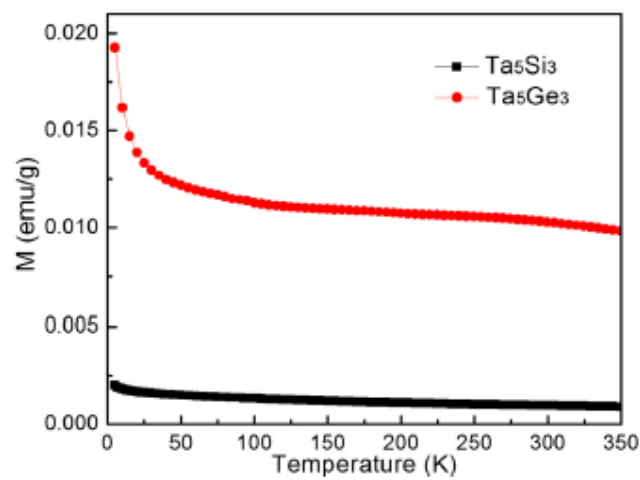


Figure 32 Magnetization vs. temperature for Ta_5Si_3 and Ta_5Ge_3 [7]

Based on previous reports [37][38] Ta_5Si_3 and Ta_5Ge_3 show metallic behavior. The electrical resistivity they measure on these samples showed small values between 2 and 300 K. They observed a positive temperature coefficient from 20-300 K which is shown in **Figure 33**.

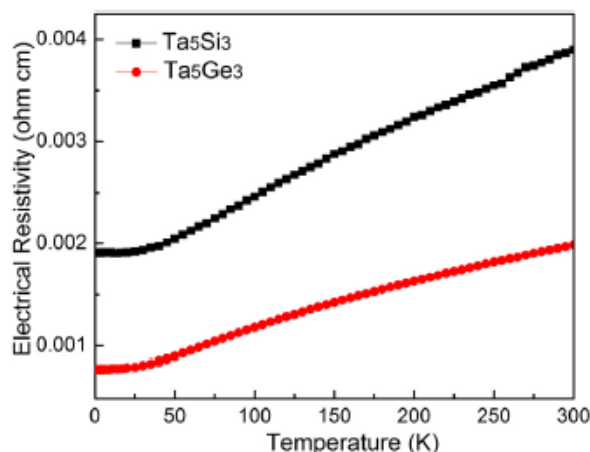


Figure 33 Electrical resistivity of the Ta₅Si₃ and Ta₅Ge₃ samples [7]

From this, they deduced that the Cr₅B₃-type Ta₅Si₃ and Ta₅Ge₃ are metallic which agreed with LMTO calculation. They also observed that the resistivity of Ta₅Si₃ was higher than Ta₅Ge₃ and their individual values were almost constant between 2-20 K which was attributed to impurity scattering.

In 2015, Ahmed A. Al-Joubori, C. Suryanarayana [6] synthesized NiGe₂, a metastable phase of Ni-Ge system by the mechanical alloying process. Ni and Ge powder with greater than 99.9% purity were mixed such that they form a nominal composition of Ni-67 at. % Ge. This powder blend was then milled/Alloyed for several hours in a high-energy SPEX 8000D mill. A small amount of process control agent, i.e., ~2 wt.% stearic acid was added when required, to the powder mixture to prevent cold welding between powder particles and the walls of the container. A number of experiments were conducted and for each of them, 10 g of blended powder in stoichiometric ratio along with 100 grams of grinding media (stainless steel balls) such that the Ball to powder ratio was close to 10:1. In each case, about 50% of the vial space was left empty to provide enough space for balls and powder particles to move around freely. Since the Ge is highly prone to oxidation and to reduce any contamination, they conducted all the sample handling inside the glove box in Ar atmosphere. The actual milling was performed for different times up to 75 hours in steps of 2 hrs of milling and 30 minutes of break. They observed that at the early stages of milling, the powder got stuck to the walls of the vial which prevented proper alloying. To minimize this, they opened the vial inside the glove box at regular intervals and scraped the powder off the vials.

A small amount of sample was removed at selected time intervals and was used to test the constitution, morphology and the chemical composition of the phase formed. The X-ray diffraction studies on these samples were performed using Rigaku-DXR 300 diffractometer using CuK α radiation ($\lambda = 0.154056$ nm) at 40 kV and 30 mA settings. The XRD patterns of Ni-67 at. % Ge powder mixture after milling for different time intervals are shown in **Figure 34**. They presented the XRD pattern of the initial blend, i.e., with 0 hours of milling to indicate the presence of pure crystalline Ni and Ge. Upon milling for 1 hr, they noticed that the peaks of Ni and Ge became broader and their intensities decreased. Also, the shift in Ni diffraction peaks towards lower angles was observed with simultaneous formation of NiGe phase which suggested that solid solubility of Ge in Ni occurred at this stage.

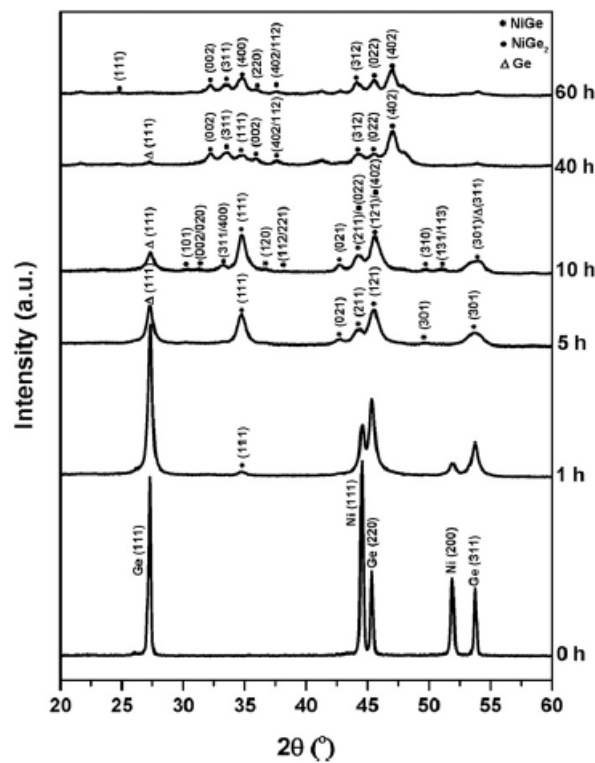


Figure 34 XRD patterns of the Ni-67 at.% Ge powder blend milled for different times. While the Ni and Ge peaks are seen in the unmilled powder (0 h), the formation of a solid solution started to occur on milling for 1 h. Simultaneously, the equilibrium NiGe intermetallic also started to form, and its amount increased with milling time. On milling the powder for 10 h, a new metastable phase, identified as the metastable NiGe₂ phase, started to form. An almost homogeneous NiGe₂ phase had formed on milling the powder for 60 h [6]

Upon increasing the milling time, the trend of increasing peak broadening, decreasing intensities of Ni and Ge peaks along with an increase in NiGe peaks continued. The lattice parameter of Ni(Ge) solid solution was calculated from 111Ni peak position as a function of milling time, and they observed an increase in lattice parameter from 0.3522 nm of pure Ni from as blended powder to 0.3529 nm after 2 hr of milling. This indicated that more germanium is getting incorporated into Ni lattice upon continuous milling. Based on the variation in lattice parameter of Ni(Ge) solid solution with Ge content [39][40][41] as shown in **Figure 35**, they estimated the Ge content in the solid solution to be ~ 11.9 at.% which is greater than what is observed under equilibrium conditions which is 10 at.%. From this, they concluded that the solid solubility of Ge in Ni has increased in this alloy system by mechanical alloying.

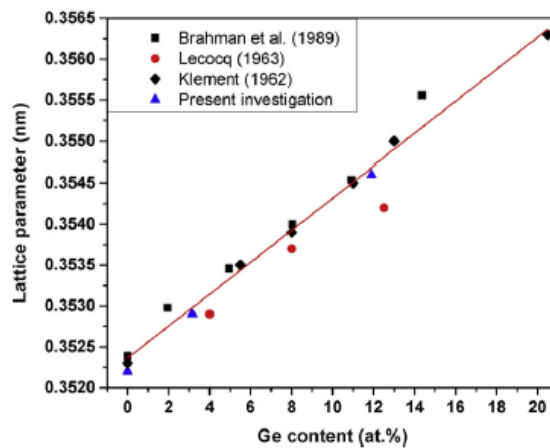


Figure 35 Variation of the lattice parameter of the Ni(Ge) solid solution with Ge content based on ref [6]

It was noticed that upon milling for 5 hr, all the Ni peaks disappeared completely and only NiGe and Ge peaks were visible. At 10 hours of milling time, the 111NiGe peak became more intense along with small Ge peaks and this XRD of 10 hr milled sample is shown separately in **Figure 36**.

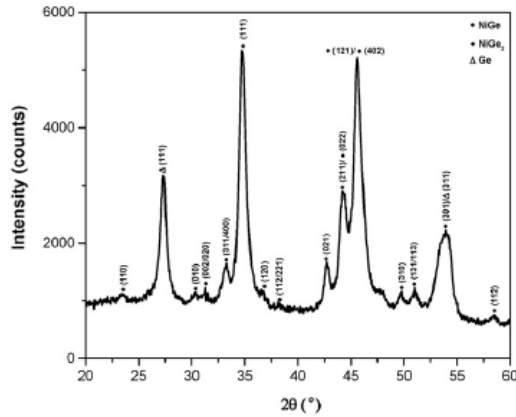


Figure 36 XRD pattern of the Ni–67 at.% Ge powder blend milled for 10 h showing the formation of the equilibrium NiGe intermetallic phase. Note that a small amount of Ge, and even a smaller amount of NiGe₂, are also present in the powder at this stage [6]

They concluded that the crystal structure of obtained NiGe was orthorhombic with lattice parameters $a = 0.581$ nm, $b = 0.538$ nm and $c = 0.343$ nm. Upon increasing the milling time furthermore by 10 hr, they observed new peaks that were the result of the formation of a new phase which was then determined to be NiGe₂. This metastable phase formed as a result of the reaction between equilibrium phase NiGe and Ge as they observed a sharp decrease in Ge content as the intensity in NiGe₂ peaks increased. The peaks of NiGe₂ phase became more prominent upon milling till 60 hrs which are shown in **Figure 37**.

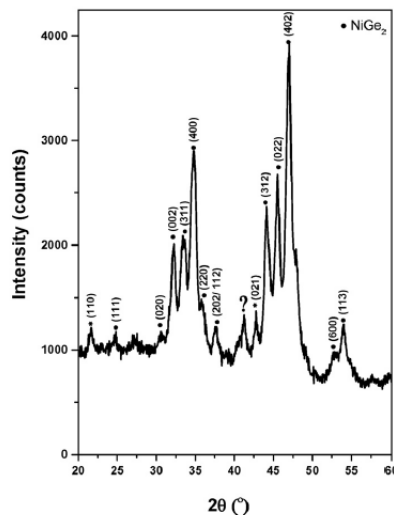


Figure 37 XRD patterns of the Ni–67 at.% Ge powder blend milled for 60 h showing an almost homogeneous formation of the metastable NiGe₂ phase [6]

They calculated the lattice parameter of the NiGe₂ phase obtained after milling for 60 hr and noticed a difference in lattice parameters from the NiGe₂ phase obtained in the early stages. In the early stages, the lattice parameters were $a = 1.0830$ nm, $b = 0.5763$, and $c = 0.5762$ nm and in the later stages, the lattice parameters were $a = 1.0303$ nm, $b = 0.5829$ nm, and $c = 0.5402$ nm.

Table 7 Crystal structures and lattice parameters of stable and metastable phases in the Ni–Ge system [6]

Phase	Crystal structure	Pearson symbol	Structure type	Lattice parameters			
				a (nm)	b (nm)	c (nm)	c/a or β (°)
(Ni)	Cubic	cF4	Cu	0.3523	-	-	-
β -Ni ₃ Ge	Cubic	cP4	Cu ₃ Au	0.357	-	-	-
γ -Ni ₃ Ge	Cubic	cP4	NaTl	0.35731	-	-	-
δ -Ni ₅ Ge ₂	Hexagonal	hP84	Pd ₅ Sb ₂	0.6827	-	1.2395	1.816
Ni ₂ Ge	Orthorhombic	oP12	Co ₂ Si	0.7264	0.511	0.383	-
ε -Ni ₅ Ge ₃	Hexagonal	hP4	NiAs	0.3622	-	0.5013	1.384
ε' -Ni ₅ Ge ₃	Monoclinic	mC32	Ni ₅ Ge ₃	1.1682	0.6737	0.6364	52.1 °
Ni ₁₉ Ge ₁₂	Monoclinic	mC62	Ni ₁₉ Ge ₁₂	1.1638	0.6715	1.0048	90 °
Ni ₃ Ge ₂	Hexagonal	hP4	NiAs	0.386	-	0.5	1.295
NiGe	Orthorhombic	oP8	MnP	0.581	0.538	0.343	-
Ge	Cubic	cF8	C	0.56575	-	-	-
Metastable phase							
NiGe ₂	Orthorhombic	oP24	CoGe ₂	1.083	0.5763	0.5762	-

The SEM analysis and EDS spectra were performed on the samples that were taken out at certain intervals, and the results are shown in **Figures 38 (a, b), (c, d), (e, f)**.

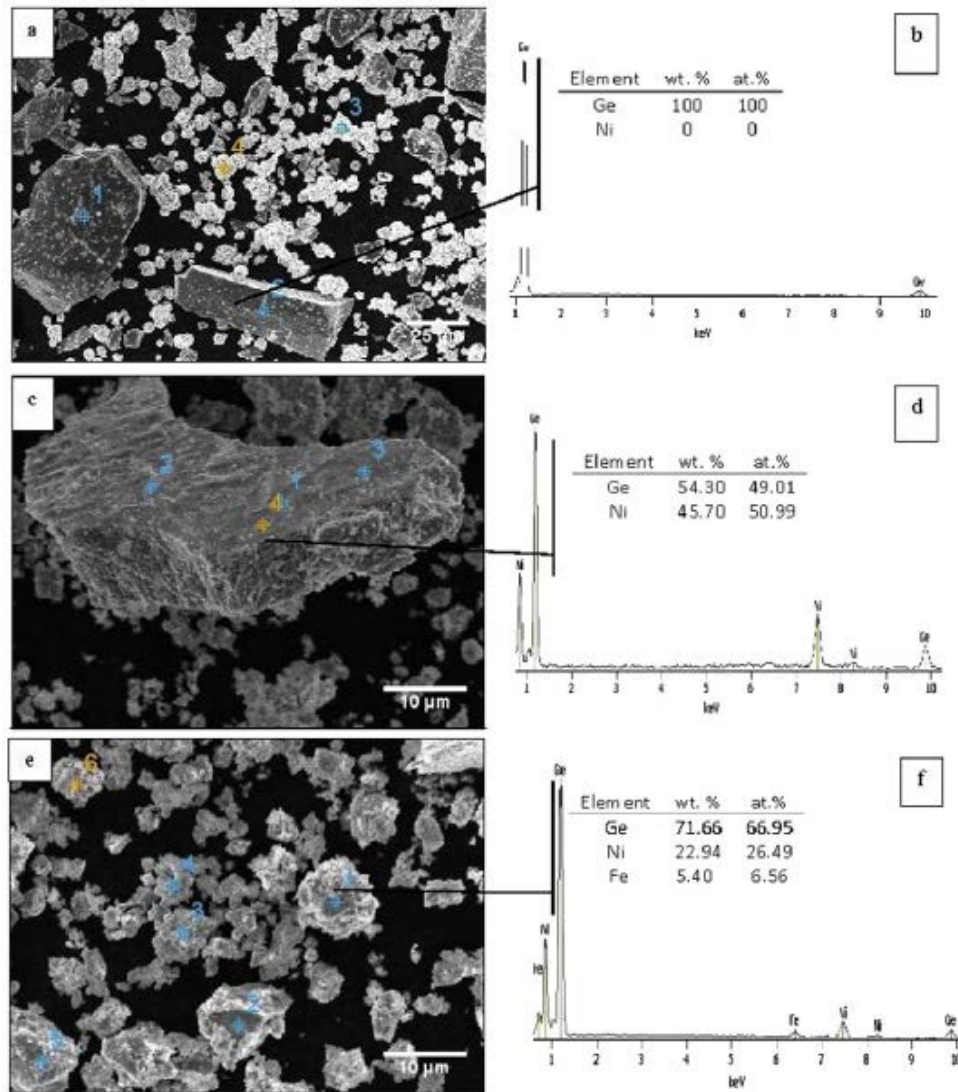


Figure 38 SEM images and EDS spectra of the Ni-67 at. % Ge powder blend milled for (a and b) 0 h, (c and d) 5 h and (e and f) 60 h. Whereas Ni and Ge are present in the unmilled powder (0 h), the powder contains predominantly the equilibrium NiGe phase on milling the powder for 5 h, and the metastable NiGe₂ phase on milling for 60 h [6]

From the images above, it was observed that at 5 hr of milling, equilibrium NiGe phase was predominant and at 60 hours of milling, the metastable NiGe₂ was formed along with some Iron contamination. This was a result of prolonged milling as in literature on mechanical alloying/milling, upon milling for more than ~50 hr, the chances of iron contamination increase gradually when using a steel vial. Upon increasing the milling time to 75 hours, the iron contamination increases significantly along with the reversible reaction of NiGe₂ to form NiGe and Ge [42].

In 2017, Adam S. Ahmed et al., [43] synthesized B20 superlattices [CrGe/MnGe/FeGe] out of single crystal MnGe, CrGe and FeGe thin films using molecular beam epitaxy method. These films were grown in an ultrahigh vacuum (UHV) chamber with a base pressure of 2×10^{-10} torr. They first prepared the Si substrates by cleaning the Si substrates and loaded them immediately into a growth chamber. Pre-annealing was done on these substrates at 800 °C for 20 minutes to desorb hydrogen and obtain a 7×7 reconstruction simultaneously. For the growth of FeGe films, they maintained the substrate temperature at 300 °C and deposited the Fe and Ge elemental flux in the ratio of 1:1 onto the substrate. The pressure during the deposition was maintained at 1×10^{-9} Torr. For the growth of MnGe and CrGe films, the substrate temperature was maintained at 250 °C and deposition were performed in ratios 1:1 of Mn and Ge, Cr, and Ge respectively.

They obtained qualitative information about in-plane crystallinity of the samples by characterization with in situ RHEED. X-ray diffraction was performed on the sample to obtain out-of-plane lattice constants, and for the superlattice, they performed cross-sectional STEM and XEDS for mapping of the composition of individual layers.

Starting out with FeGe, the RHEED patterns of Si (111) surface were taken along [112] and [110] in-plane directions as shown in **Figure 39**, and they observed a clear 7×7 reconstruction pattern after annealing at 800 °C. This indicated that the substrate was clean and well-ordered for further growth of B20 materials.

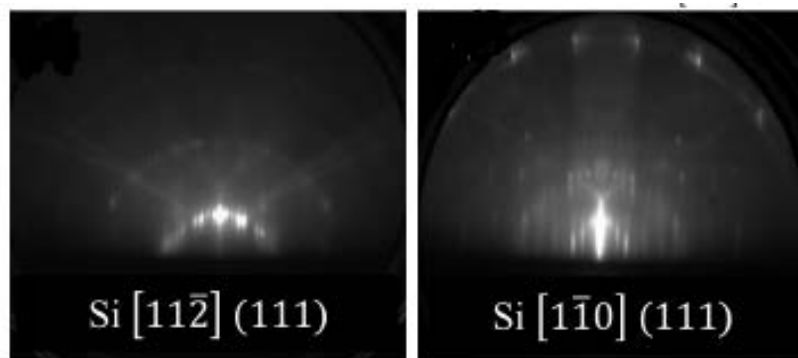


Figure 39 RHEED images of a 7×7 reconstructed Si(111) surface shown for in-plane directions of 112 and 110, respectively [43]

After the deposition of FeGe films, RHEED patterns were obtained for these ~ 40 nm FeGe films which are shown in **Figure 40**. The FeGe lattice was rotated relative to the Si(111) lattice

in order to minimize the lattice mismatch thereby having the [110] axes of FeGe aligned with [112] axes of Si(111), and the [112] axes of FeGe align with the [110] axes of Si(111).

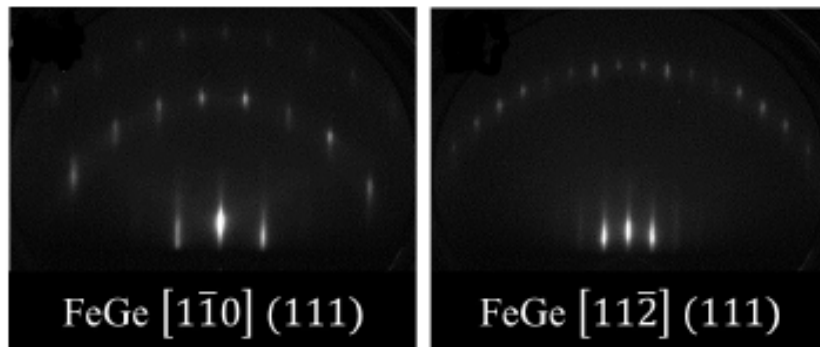


Figure 40 RHEED patterns measured along the 110 and 112 in-plane directions of the ~40 nm FeGe film, respectively [43]

They concluded that the sharp streaks observed in the RHEED pattern indicate flat terraces and that the distinct patterns observed along 110 and 112 directions indicated in-plane single crystal order.

They also performed X-ray diffraction on the FeGe films which are shown in **Figure 41**. They noticed the peaks of Si(111) and (222) from the substrate alongside FeGe(111) peaks and no other peaks were observed indicating a single phase of FeGe was present. From this, they calculated the QL period to be 2.703 Å which was observed to be larger than the bulk value by ~0.065%. They attributed this difference to the in-plane compressive strain on FeGe film due to the lattice mismatch between FeGe(111) and Si(111) by 0.05%.

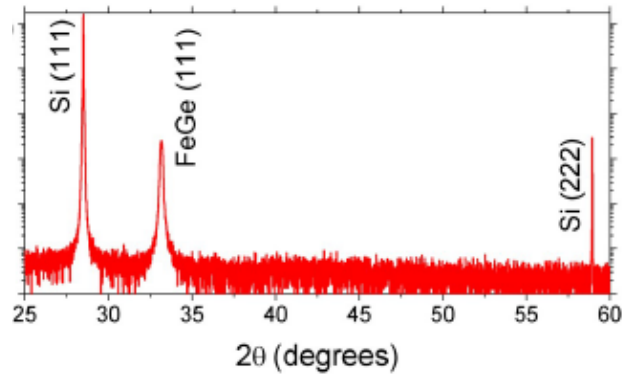


Figure 41 XRD scan of the FeGe film. Single-phase, single crystal FeGe is shown amongst the Si substrate peaks [43]

After establishing this FeGe single crystal growth on Si(111), they utilized this as a template for subsequent growth of B20 overlayers of MnGe and CrGe superlattices.

For the deposition of MnGe, thin films of MnGe were grown over FeGe/Si(111) for determining a suitable growth condition for the formation of MnGe/FeGe superlattices. ~40 nm MnGe layer was deposited from elemental Mn and Ge over a ~5 nm base layer of FeGe grown over Si(111). The flux ratio was maintained at 1:1 and the substrate temperature, in this case, was maintained at 250 °C during the growth. RHEED images were taken for the MnGe film along the [110] and [112] directions, and these are shown in **Figure 42**. These images indicated flat terrace growth of MnGe on the FeGe base layer.

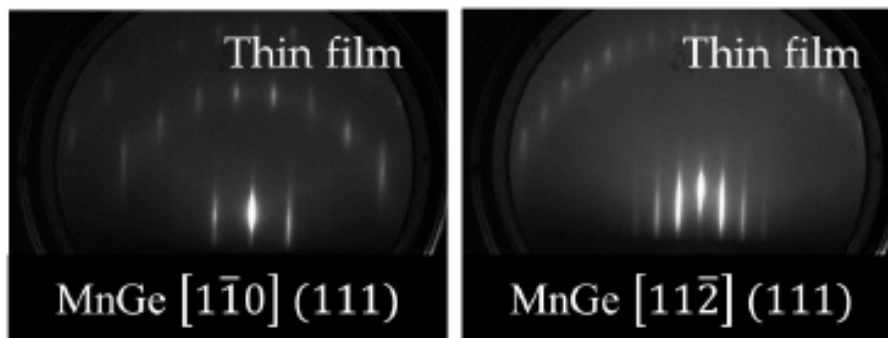


Figure 42 RHEED for MnGe thin film grown on FeGe buffer layers is shown along the 110 and 112 directions respectively [43]

X-ray diffraction was performed to quantify the out-of-plane constant. They observed from the XRD which is shown in **Figure 43** that there are no other phases of Mn_xGe_y except

MnGe and the (111) peak of MnGe appeared at 2θ of 32.41° . The corresponding QL period was found to be 2.759 \AA which was observed to be less than the bulk value by 0.33% . They compared this value to 2.5% lattice mismatch between MnGe and FeGe and suggested that the $\sim 40 \text{ nm}$ MnGe film has relaxed to its bulk like lattice structure. They attributed the additional peak observed to the $\sim 5 \text{ nm}$ FeGe base layer. From the RHEED and XRD data, they concluded that the MnGe grows in a single crystalline form over the FeGe(111) template.

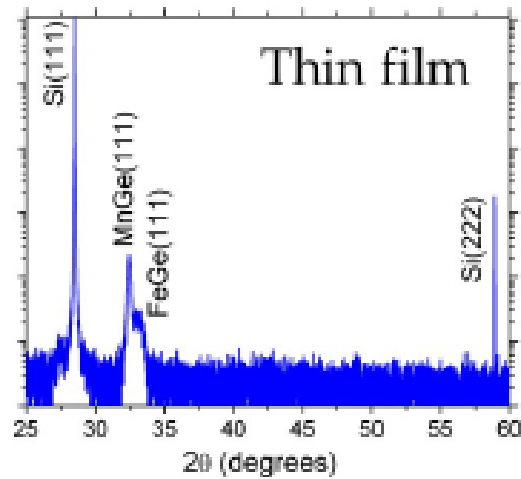


Figure 43 XRD for a $\sim 40 \text{ nm}$ thick MnGe film. The MnGe(111) peak is shown alongside the $\sim 5 \text{ nm}$ FeGe buffer layer [43]

Once they were able to synthesize the MnGe/FeGe/Si (111) sublayers, they successfully synthesized two-component superlattice comprised of $\sim 2 \text{ nm}$ thick MnGe and $\sim 2 \text{ nm}$ thick FeGe. They grew FeGe/Si (111) at first at which the substrate temperature was maintained at 300°C . RHEED images of FeGe were taken at this point, and the substrate was cooled to 250°C followed by growth of MnGe over FeGe to form the superlattice. RHEED images of the final FeGe and MnGe layers are shown in **Figure 44** respectively. They observed that both the images were qualitatively similar and during the growth, and very little change was observed in the RHEED images of different layers. The XRD of the superlattice $[\text{MnGe/FeGe}]_8/\text{Si}(111)$ obtained is shown in **Figure 45**, and they observed that instead of two peaks of MnGe and FeGe, a single peak of the superlattice was present at 2θ of 32.72° which corresponds to QL period of 2.734 \AA . This QL value was observed to be between the measured QL periods of thick FeGe films which was 2.703 \AA and MnGe films which was 2.759 \AA . Upon closer look at the

XRD pattern of the superlattice, a weak satellite peak was observed which was indicated by the arrow in the inset of the **Figure 45**.

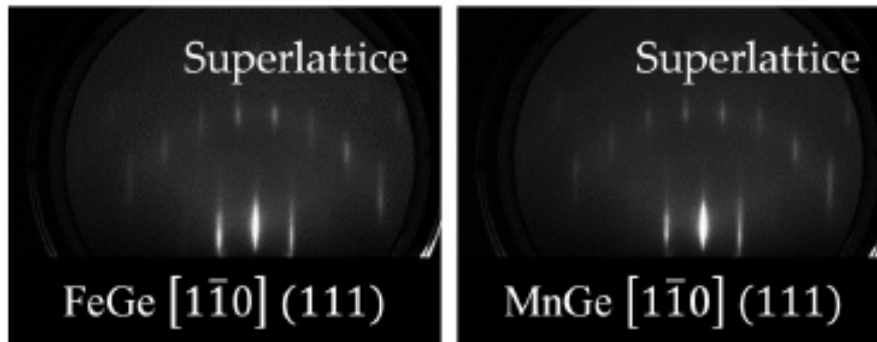


Figure 44 RHEED patterns are shown for the final topmost layers in a $[\text{MnGe}/\text{FeGe}]_8$ superlattice for FeGe 110 (111) and CrGe 110 (111), respectively [43]

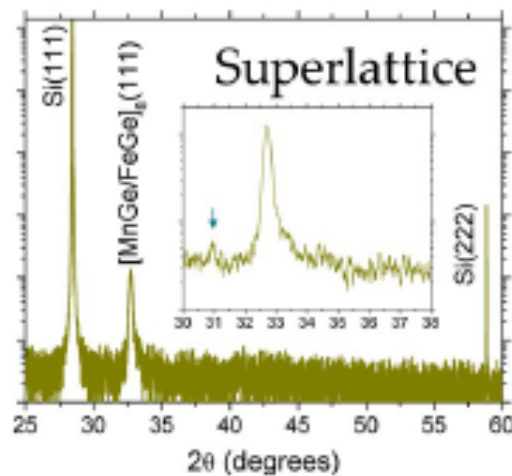


Figure 45 XRD for the superlattice structure shows a single (111) peak. Inset: a weak satellite peak (arrow) due to superlattice structure is observed [43]

For the growth of CrGe layer, they grew a base layer of FeGe with ~ 5 nm thickness on a 7×7 reconstructed Si(111) substrate at 300°C before the growth of CrGe layer. The elemental Cr and Ge were co-deposited on this FeGe base layer maintained at 250°C forming a ~ 30 nm thick film of CrGe. The RHEED images of this CrGe are shown in **Figure 46**. They observed that the images were qualitatively similar to MnGe, and FeGe layers but the streaks had bright spots and arrowhead-like features which are indicative of onset faceting and 3 D growth [44].

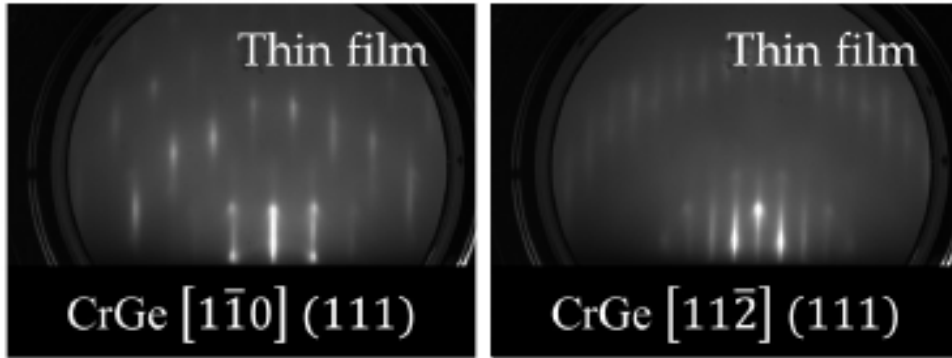


Figure 46 RHEED for the CrGe thin film grown on FeGe buffer layers is shown along the 110 and 112 directions respectively [43]

They performed X-ray diffraction of this layer in spite of these features, to calculate the out of plane lattice constant of CrGe which is shown in **Figure 47**. They observed CrGe peak at a 2-theta of 32.38 ° alongside FeGe(111) peak of the buffer layer. The corresponding QL period was calculated to be 2.761 Å which was less than that observed in bulk by 0.15% which suggested that the ~30 nm CrGe film relaxed to its bulk-like lattice structure.

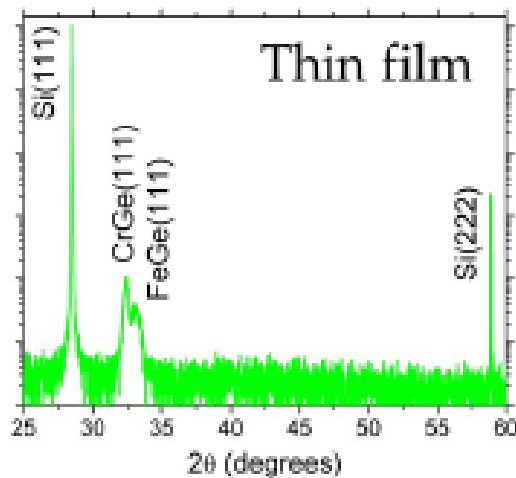


Figure 47 XRD for a ~30 nm thick CrGe film. The CrGe(111) peak is shown alongside the ~5 nm FeGe buffer layer [43]

After the successful growth of CrGe thin films, they applied a similar technique to grow two-component superlattice. The [CrGe/FeGe]₁₀ superlattices were grown on Si(111) maintained at 250 °C. Each layer thickness was maintained at ~ 2 nm. The RHEED patterns during the growth are shown in **Figure 48**. They notice that unlike the RHEED patterns observed in CrGe,

these patterns were streaky and arrowheads features were absent. The XRD pattern of this superlattice revealed a peak at 2-theta of 32.68 ° with corresponding QL period of 2.737 Å. The presence of a satellite peak was observed upon closer investigation of the XRD pattern which is shown in the inset in **Figure 49**.

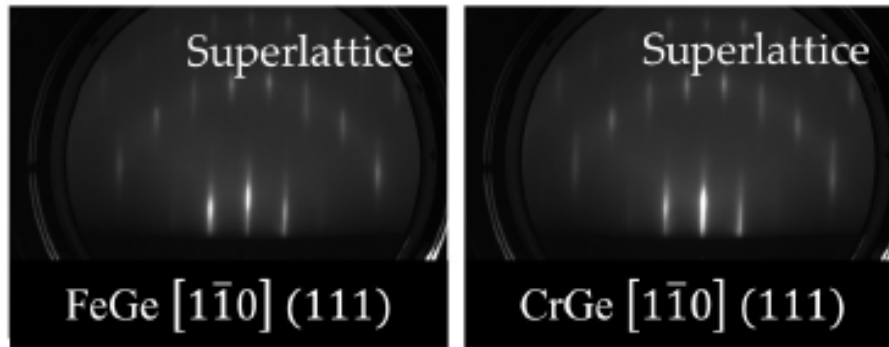


Figure 48 RHEED patterns are shown for the final topmost layers in a $[\text{CrGe}/\text{FeGe}]_{10}$ superlattice for FeGe 110 (111) and CrGe 110 (111), respectively [43]

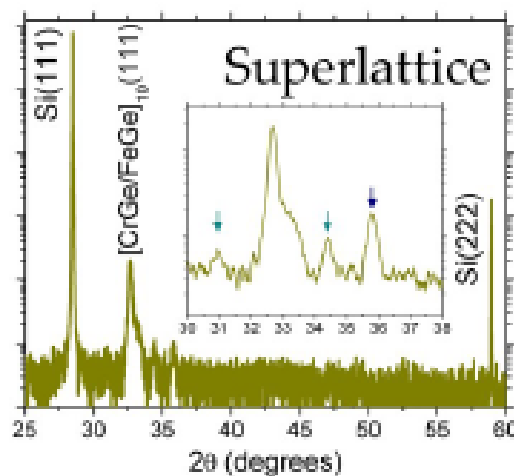


Figure 49 XRD for the superlattice structure shows a single (111) peak. Inset: satellite peaks (arrows) are observed due to the superlattice structure [43]

The stronger satellite peaks they observed in this case compared to MnGe suggested sharper interfaces. They confirmed that the spacing of satellite peaks observed was corresponding a superlattice period of ~5 nm which was observed to be consistent with the design period of ~4 nm. With this, they have established that the B20 CrGe layers are suitable for artificial heterostructures.

For the growth of the trilayer superlattice], the $[\text{CrGe}/\text{MnGe}/\text{FeGe}]_8$ superlattice structure was grown at 250 °C on a 7×7 reconstructed Si(111) surface. Each layer was grown to a thickness of ~ 2 nm. The RHEED patterns of this superlattice in the $[110]$ direction with the topmost layer being FeGe, followed by MnGe and CrGe layers are shown in **Figure 50 (a), (b), (c)**. They observed that the RHEED patterns were streaky indicating smooth 2 D surfaces and that all the three layers had similar patterns. The X-ray diffraction performed on this showed a peak at 2-theta of 32.65 ° which is shown in **Figure 50 (d)** and the corresponding QL period was calculated to be 2.740 Å. They also observed the satellite peaks corresponding to a superlattice period of ~ 7 nm which was consistent with the design period of ~ 6 nm.

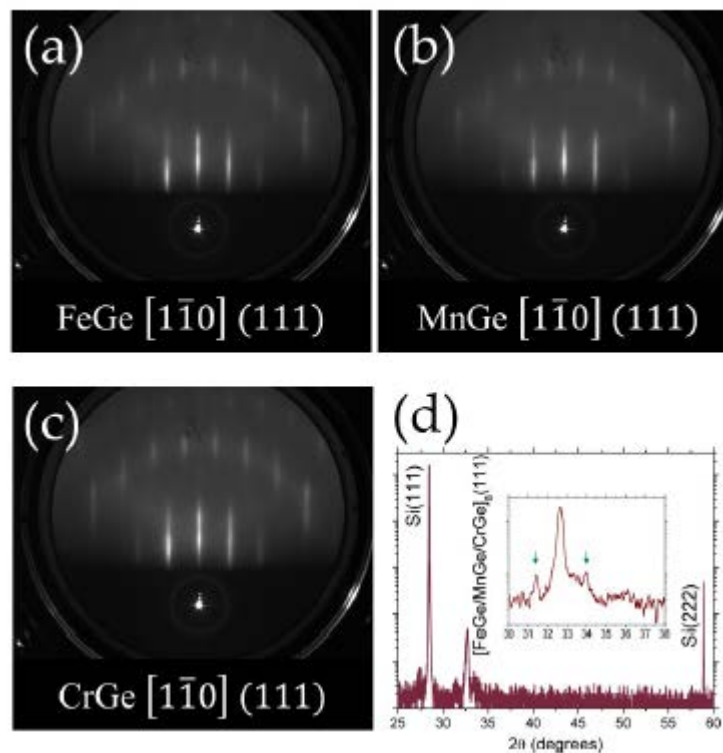


Figure 50 RHEED and XRD characterization of a three-component superlattice $[\text{CrGe}/\text{MnGe}/\text{FeGe}]_8$. (a-c) RHEED patterns are shown for the topmost layers FeGe, MnGe, and CrGe layers, respectively. The patterns are measured along the 110 in-plane directions of the films. Qualitatively, the RHEED images are very similar to each layer. (d) XRD scan of the trilayer superlattice shows a single (111) peak with satellite peaks from the superlattice structure (arrows in the inset) [43]

For further insight into the structural and compositional quality of this superlattice, they performed cross-sectional STEM and XEDS and found that the crystalline quality was high with relatively low interdiffusion between layers.

2.3. Rare Earth Germanides

In 2009, Hiroshi Fukuoka et al. [45], prepared a series of lanthanide penta-germanides LnGe_5 ($\text{Ln} = \text{Ce}, \text{Pr}, \text{Nd}, \text{and Sm}$) using the high-pressure and high-temperature synthesis technique with a pressure ranging from 3-13 GPa and temperature ranging from 500-1600°C. Synthesis procedure followed was like the one implemented for synthesis of SrGe_{6-8} [9] except for in this case, LnGe_2 was obtained from the arc furnace with starting materials of Ce, Pr, Nd and Sm being 99.9% pure and was mixed with the 99.99% pure Ge in various molar ratios from 1:3 to 1:8 and were placed in an h-BN cell and reacted at 3-13 GPa and 500-1600 °C to obtain the final LnGe_5 composite.

MacScience M18XHF diffractometer with graphite-monochromated $\text{CuK}\alpha$ radiation and a Bruker AXSD8 Advance diffractometer were used to perform powder X-Ray diffraction measurements and to perform single-crystal X-Ray analysis, Rigaku R-Axis diffractometer equipped with an imaging plate area detector with graphite-monochromated $\text{MoK}\alpha$ radiation was used. SHELX-97 crystallographic software package was used to perform Single-crystal structure analysis. Chemical compositions of the products were determined with an electron probe microanalyzer (EPMA) (JEOLJCMS-733).

They observed that CeGe_5 crystallized in associate orthorhombic unit cell (S.G. *Immm* (71)) with $a = 4.000(5) \text{ \AA}$, $b = 6.192(5) \text{ \AA}$, $c = 9.86(1) \text{ \AA}$, and $V=244.1(5) \text{ \AA}^3$ also the new germanides were isotypic with LaGe_5 consisting of a Ge valency network with tunnels wherever guest ions Ln^{3+} were settled. The network consisted of sublayers with edge-sharing Ge six-membered rings with solely boat configuration. They also observed that the sublayers were connected by sparse eight-coordinated Ge atoms. The cell volume of the compounds consistently decreased from La to Sm compounds, aside from CeGe_5 , because of the lanthanide contraction. The lattice constants of CeGe_5 were smaller than those of the Pr compound as it contains Ce^{4+} ions.

They have studied the magnetic properties of the obtained LaGe_5 -type compounds. It was difficult to prepare single phases of LnGe_5 , $\text{Ln} = \text{Ce}, \text{Pr}, \text{Nd}, \text{and Sm}$ and to avoid the influence of other binary germanides in magnetic susceptibility measurements, they used samples containing parts of LnGe_5 phase and Ge because Ge does not show any magnetic

transitions. Corrections were made on overall data considering the amount of Ge in each sample, and the results are summarized and shown in **Table 17**. Magnetic susceptibility measurements were performed with a SQUID magnetometer (Quantum Design MPMS-5) in a 5000-Oe field which is shown in **Figures 51 (a), (b), (c) and (d)**.

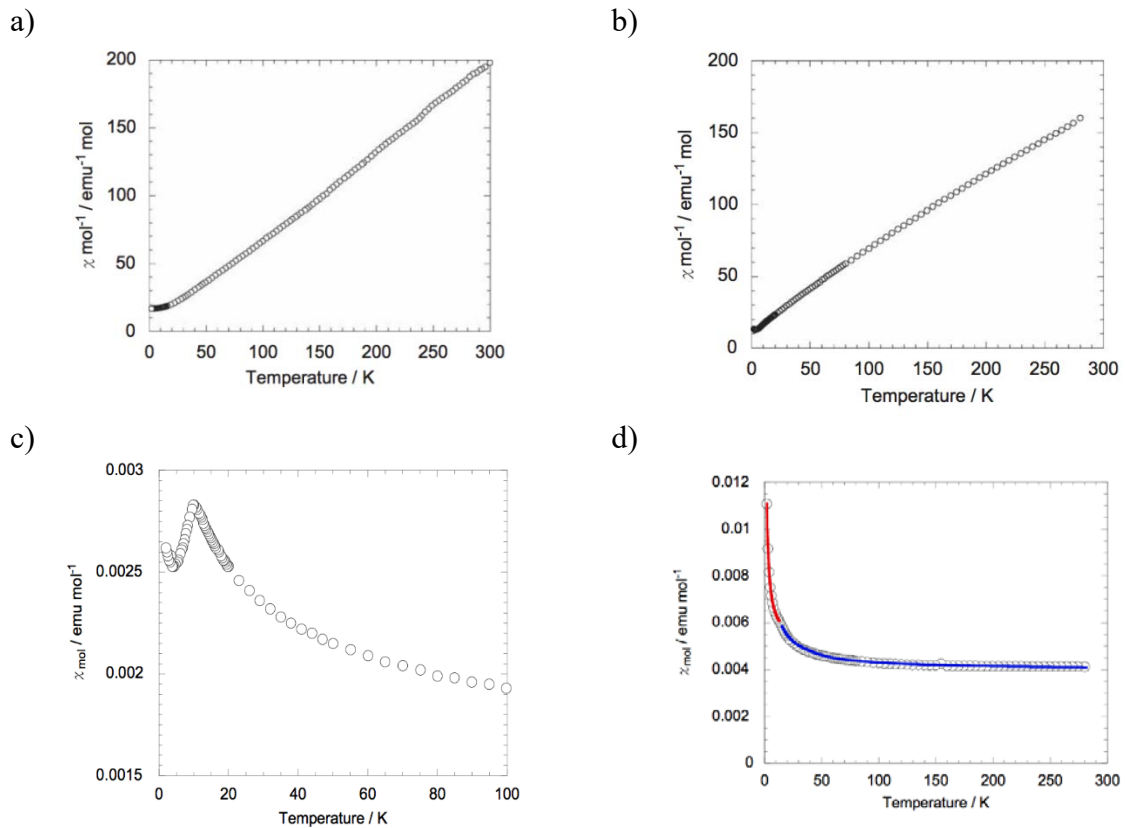


Figure 51 Temperature dependence of magnetic susceptibility of a) PrGe₅ and b) NdGe₅ c) SmGe₅ and d) CeGe₅ [46]

They observed that the magnetic properties of the obtained composites as CeGe₅ is paramagnetic above 2K, however, doesn't confirm the Curie–Weiss law, PrGe₅ and NdGe₅ are Curie–Weiss type paramagnets with Weiss temperatures of $\theta = -3.3$ K and -18.4 K respectively, also that SmGe₅ showed an antiferromagnetic transition at 10.4 K. They observed that the SmGe₅ did not obey the Curie–Weiss law, due to contributions from first and Second-Zeeman effects of Sm ions[46]. Effective magnetic moments μ_{eff} of 3.50 and $3.64\mu_{\text{B}}$ were

observed for the Pr and Nd compounds, respectively, which correspond well to the theoretical values of 3.58 (Pr³⁺) and 3.62 (Nd³⁺) μ_B .

Table 8 Magnetic properties of LaGe₅-type compounds [45]

LaGe ₅	Superconductor	T _c = 6.8 K
CeGe ₅	Paramagnetic	————
PrGe ₅	Paramagnetic	$\theta = -3.3$ K
NdGe ₅	Paramagnetic	$\theta = -18.4$ k
SmGe ₅	Antiferromagnetic	T _N = 10.4 k

In the temperature dependence of magnetic susceptibility for CeGe₅, an anomaly was observed at 14K. They applied a modified Curie-Weiss equation $\chi_{mol} = \chi_0 + C/(T - \theta)$, where χ_0 is a constant, C is curie constant and θ is, the wiess temperature separately to the for the temperature ranges from 300 to 15 k and from 14 to 2 k. Deduced fit parameters were $\chi_0 = 0.0052$ emu/mol, C = 0.0121 emu K/mol, and $\theta = 0.04$ K for the lower temperature region, and for the higher, $\chi_0 = 0.0040$ emu/mol, C = 0.0308 emu K/mol, and $\theta = 1.48$ K . The effective magnetic moment was observed to be $\mu_{eff} = 0.31$ and $0.50\mu_B$ for lower and higher regions, respectively. They observed that these values were too small for Ce³⁺ compounds because the theoretical moment for Ce³⁺ is $2.54\mu_B$. They assumed that therefore, some Ce ions are possibly in a 4+ oxidation state and suggested that more detailed study was necessary to determine the valence of Ce in CeGe₅.

In 2011, Hiroshi Fukuoka et al. [47], synthesized a new binary lanthanum germanide, LaGe₃ using the high-pressure synthesis technique with pressures ranging from 3-12 GPa and temperatures ranging from 500-1600 °C. A mixture of La (Furu-Uchi Chemical 99.9%) and Ge (Mitsuwa Pure Chemical 99.999%) in 1:3 atomic ratios were reacted in an Ar-filled arc furnace to obtain a mixture of LaGe₂ and Ge. The obtained mixture is then ground in an Agate mortar and placed in an h-BN cell. The reactions were carried out using Kawai-type high-pressure system varying both pressure and temperature between 3-13 GPa and 500-1600 °C.

Bruker AXS D8 Advance diffractometer with Ni-filtered CuK α radiation was used to perform X-Ray powder diffraction and for characterization of samples obtained. The data for

structural analysis were collected using the step-scan mode (0.00741°) from 24° to 100° and to reduce the background a nonreflecting Si plate was used as a sample holder. At 5 GPa and 500°C , they observed small peaks of LaGe_5 and LaGe_2 alongside other huge peaks which could not be identified with any known phases. These peaks were indexed using a hexagonal cell with $a = 6.381(1) \text{ \AA}$ and $c = 22.290(3) \text{ \AA}$. With increase in pressure and temperature to 12 GPa and 1100°C , they observed that the crystallinity of the unknown phase increased but also the amount of LaGe_5 increased which is shown in **Figure 52**

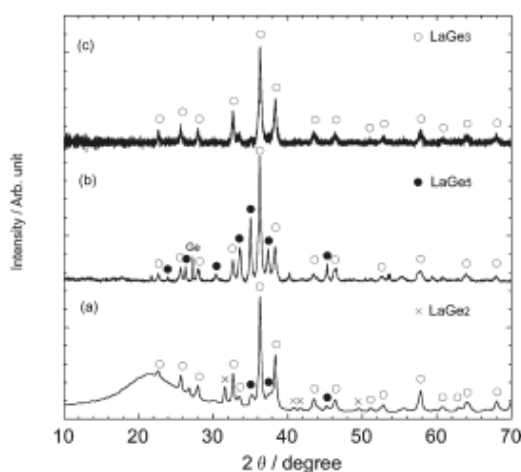


Figure 52 X-ray powder diffraction patterns of La Ge samples: (a) 5 GPa, 500°C ; (b) 12 GPa, 1100°C ; (c) 10 GPa, 850°C . Cross marks show diffractions from LaGe_2 . Filled and open circles show XRD patterns of LaGe_5 and LaGe_3 , respectively [47]

The final and best sample containing almost only LaGe_5 was obtained by performing reactions at 10 GPa and 850°C . The obtained sample was analyzed using EPMA, and the composition was determined to be $\text{La}:\text{Ge} = 1:2.91(3)$. From this, they confirmed the synthesis of a new lanthanum germanide, LaGe_3 . This compound was tested for stability by leaving it in the open air, and they found that this phase was very stable in air and moisture under ambient pressure.

The samples obtained were observed to have crystallized in the BaPb_3 structure (the space group $R3m$) with lattice constants of $a = 6.376(1) \text{ \AA}$, $c = 22.272(3) \text{ \AA}$, and $V = 784.1(2) \text{ \AA}^3$. They refined the structure using Rietveld analysis from X-ray powder data and found that the structure is composed of two types of close-packed atom layers. In one layer, every La atom is surrounded solely by Ge atoms with the same distance of 3.188 \AA and the other layer contained Ge_3 regular, triangular cluster units with a Ge-Ge distance of 2.634 \AA . Their

conclusion from the electron localization function and crystal orbital Hamilton population calculations were that the triangular cluster was composed of three Ge-Ge covalent bonds and that each Ge atom has a lone pair.

The temperature dependence of the magnetic susceptibility and electrical conductivity measurements were performed on the obtained samples which are shown in **Figures 53**. They observed that the resistivity of LaGe_3 decreased with decreasing temperature up to 8 K and slight increase after that followed by zero resistivity below 7.4 K. From this they concluded that LaGe_3 is metallic and shows superconductivity with a transition temperature of $T_C = 7.4$ K.

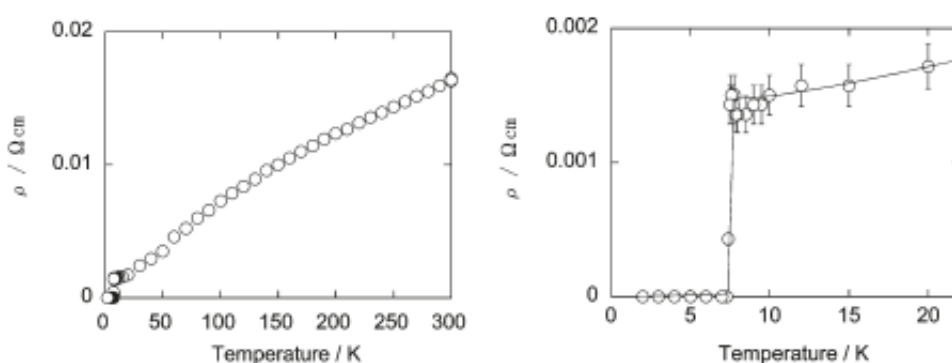


Figure 53 Temperature dependence of the electrical resistivity for LaGe_3 for (a) wide temperature range and (b) lower temperature range [47]

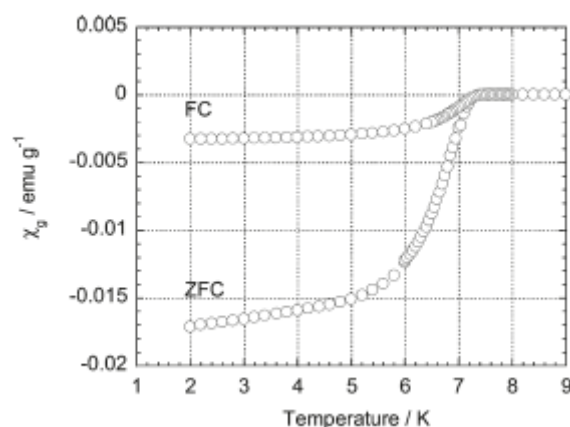


Figure 54 Temperature dependence of the magnetic susceptibility of LaGe_3 [47]

From the temperature versus magnetic susceptibility curve shown in **Figure 54**, the curve passed through zero magnetization at 7.4 K and then showed a sudden decrease to

negative values which agreed with the results of the resistivity measurements. From the magnetic susceptibility curve, they calculated the superconducting volume fraction which was more than 100% at 2 K, and from this, they concluded that the transition was due to LaGe₃. This critical temperature is highest for the La-Ge system.

In 2012, Jiliang Zhang et al. [48] used the Bi-flux technique to synthesize single-crystals of the novel rare-earth metal-bismuth digermanides with idealized formula RE[Bi_xGe_{1-x}]₂ (RE=Y, Pr, Nd, Sm, Gd–Tm, Lu; x<0.16). All starting elements used for synthesis were purchased from Alfa or Aldrich with purity greater than 99.9 wt.%. The starting materials were loaded into a 2cm³ alumina crucibles with molar ratio RE:Ge:Bi = 1:2:8 (RE= La-Sm, Gd-Lu). The crucibles were then encapsulated inside the fused silica tubes, which were then flame-sealed under vacuum and heated for the reactions to take place, inside a box furnace. The process followed was a three-step process in which temperature was ramped up to 1273 K at a rate of 200 K/h, kept at that temperature for homogenization for 20 h, followed by cooling down to 873 K at a rate of 10 K/h. The flux formed was removed at that temperature by decanting it, and the crystals were grown were isolated. They reported that the Bi-flux technique produced best results regarding yield and crystal quality. Due to the vastly different melting temperatures of the starting elements and the evaporative loss of bismuth, the REBiGe phase could not be reliably made via arc-melting. Induction melting in sealed tubes worked, but they found that the method was unsuccessful in producing phase-pure material even after a long time(1–2weeks) annealing, the induction melted products were multi-phase mixtures and the size/quality of the single-crystals from induction melting was found to be inferior to that of the flux-produced samples.

The samples obtained were characterized using single-crystal X-ray diffraction using Bruker SMART CCD-based diffractometer. The structure solution and refinement were performed using SHELXTL package. Also, the X-ray powder diffraction data were collected using Rigaku Miniflex powder diffractometer. The experimental powder X-ray diffraction patterns were well matched with those obtained from single-crystal work calculations. The single-crystal data and the structure refinement parameters are summarized in tables [48].

The field cooled magnetization measurements as shown in **Figures 55 and 56**, were performed in the temperature range of 5 K to 300 K on the single crystal samples, in the direction parallel to the basal plane in an applied field of 500 Oe. The temperature dependence of magnetization and resistivity were also measured for these single crystal samples.

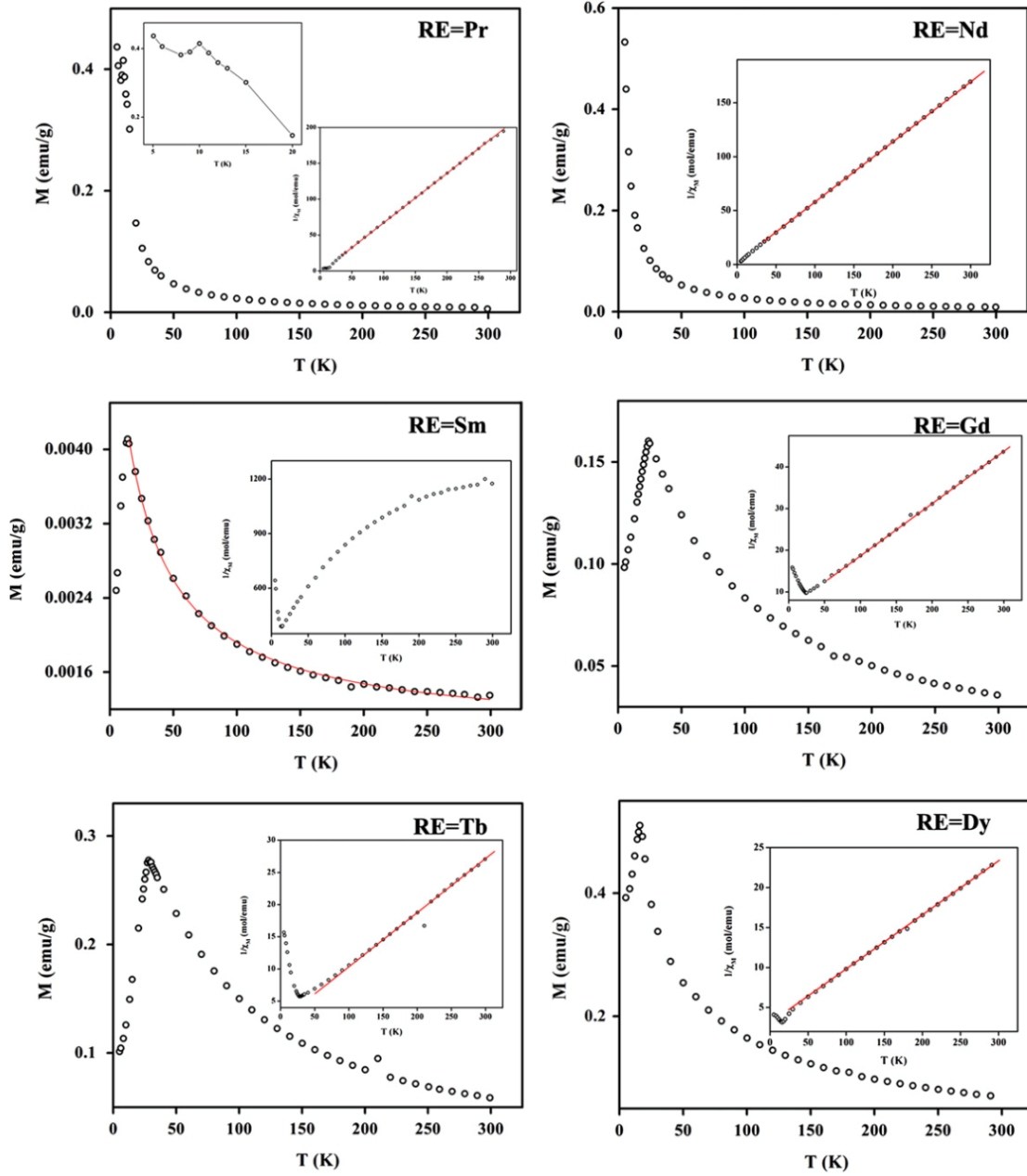


Figure 55 Field cooled magnetization data gathered under an applied field of 500 Oe for the REBiGe compounds with structures I and II [48]

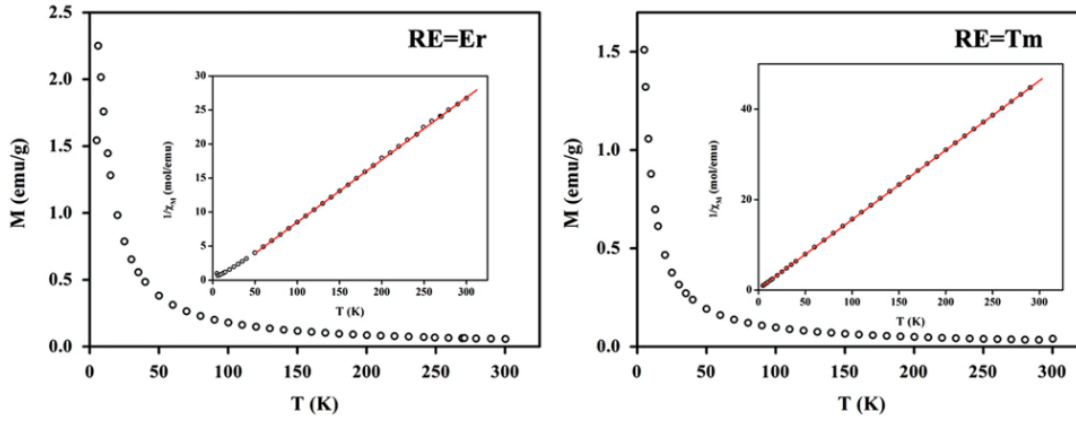


Figure 56 Field cooled magnetization data gather under an applied field of 500 Oe for the REBiGe compounds with structure II [48]

They concluded that all the samples exhibited antiferromagnetic behavior excluding NdBiGe and TmBiGe. Upon closer investigation at lower temperatures regions, they observed that a two-stage transition existed in PrBiGe compound.

From the inverse molar susceptibility measurements against temperature which are shown in the inset plots, it was concluded that all the samples follow Curie-Wiess law in the paramagnetic region except SmBiGe. Upon fitting these data using Curie-Wiess law, effective moment p_{eff} and paramagnetic Curie temperature θ were obtained (Table 18).

Table 9 Magnetic parameter of RE[Bi_xGe_{1-x}]₂ [48]

Compounds	Ordering	$g\sqrt{J(J+1)}$	$P_{eff}(\mu_B)$	$\theta(K)$	$T_N(K)$	$J(O)_\rho$	$J_{ff}/k(K)^a$
PrBiGe	AFM	3.58	3.43	-0.3	10	0.0816	-0.62
NdBiGe	AFM	3.62	3.78	-2.8	≤ 5	-0.0571	-2.24
SmBiGe	AFM	0.85	0.76	-21.4	12	0.0350	-7.39
GdBiGe	AFM	7.94	7.88	-38.8	23	-0.0075	-3.69
TbBiGe	AFM	9.72	9.79	-24.9	12	0.0105	-2.55
DyBiGe	AFM	10.63	10.86	-43.6	16	0.0434	-9.25
HoBiGe	AFM(\perp^b)	10.6	10.34	-24.7	13	-0.0625	-8.22
HoBiGe	AFM(\parallel^b)	10.6	10.42	-10.9	13	-0.0417	-3.65
ErBiGe	AFM	9.58	9.34	7.08	6	-0.0763	4.16
TmBiGe	AFM	7.56	7.23	7.23	≤ 5	-0.1536	-2.72

^a J_{ff}/k (K) is the exchange constant.

^b Single-crystal in two orientations with respect to the basal plane.

They observed that SmBiGe showed a much smaller magnetic susceptibility value at high temperature compared to other compounds and its value was determined to be $\sim 10^{-5}$ - 10^{-6} emu/g. It was observed that the value was close to diamagnetic susceptibility and Van Vleck paramagnetic susceptibility terms [49]. These two terms which are neglected in Curie-Weiss law were taken into consideration for SmBiGe. They concluded from the mean field approximation that the paramagnetic susceptibility of metallic samarium compound should be in the form below room temperature.

$$\chi(T) = \chi_0 + D/(T - \theta)$$

where χ_0 is the temperature-independent susceptibility and D is the effective Curie constant. The susceptibility of SmBiGe shown in **Figure 55** can be well fitted using the above equation. With parameters $\chi_0 = 1.89 * 10^{-6}$ emu/g, $\theta = -21.4$ K and $D = 235 * 10^{-6}$ emu/g. The determined effective moment P_{eff} from the D was $0.76 \mu_B$.

In 2014, Nian-Tzu Suen, et al. [50] reported the synthesis of an extended family of rare-earth metal–germanides with a general formula $\text{RE}_{5-x}\text{Ca}_x\text{Ge}_3$ (RE=Y, Ce–Nd, Sm, Gd–Tm and Lu; $x < 2$) and the study of their structural characterization. All the starting materials, rare-earth metals (ingots, from Ames Laboratory or Alfa), Ca (dendritic, from Alfa), and Ge (powder, from Acros), used to prepare the $\text{RE}_{5-x}\text{Ca}_x\text{Ge}_3$ (RE= Y, Ce–Nd, Sm, Gd–Tm, and Lu) were of >99.99% purity. All these materials were stored and handled inside an argon-filled glovebox to prevent any contamination. The materials in their elemental form were loaded into the Nb - tubes, which was then sealed shut by arc-welding in an argon atmosphere. The tubes were placed in the silica tubes which were then heated to red rod and flame sealed under vacuum. The reactions were carried out by heating to 1100 °C at a rate of 200 °C/h; homogenization at 1100 °C for 20 h; followed by cooling to room temperature at a rate of 50 °C/h. Of all the series of experiments they conducted, only the La-reaction proceeded as intended and La_2CaGe_2 with Mo_2FeB_2 structure type, space group $P4/mbm$; $a = 7.858(2)$ Å and $c = 4.526(2)$ Å was obtained whereas the other reactions containing Ce and heavier rare-earth metals produced different phases far from the required RE_2CaGe_2 phase.

The X-ray diffraction analysis and single-crystal analysis they performed revealed that the products were $\text{RE}_{5-x}\text{Ca}_x\text{Ge}_3$, adopting the Mn_5Si_3 structure type (space group $P63/mcm$), where Ca partially replaces the RE atoms with refined compositions $\text{RE}_{5-x}\text{Ca}_x\text{Ge}_3$ ($x=1-2$).

New reactions with the “correct” stoichiometric RE:Ca:Ge ratios were carried out after

determining the composition of obtained samples. The new synthesis process included the following three heat treatment steps: (1) increasing the temperature to 1085 °C at a rate of 200 °C/h; (2) equilibration at 1085 °C for 24h; (3) followed by slow (10 °C/h) cooling to 400–600 °C. After that, the ampoules were taken out of the furnace and quenched in air. They observed that the samples produced were homogeneous, containing numerous small, shiny crystals with dark-metallic luster. The materials were brittle, and they were able to ground them with a mortar and pestle. After this method, from the X-ray diffraction patterns they concluded that they were able to obtain single phase in the early rare-earth metal samples(Ce–Nd), whereas for the mid and late rare-earth metals (Gd–Tm, Lu, and Y) samples, the final product was a mixture of $RE_{5-x}Ca_xGe_3$, $REGe_{2-x}$ and some CaGe.

They speculated that the higher melting temperature of the lanthanides beyond Gd might be the problem and attempted using finely ground rare-earth metals, which made no difference. Increasing the reaction temperature from 1085 °C to 1250 °C also did not work. Higher temperature favored different major phase, the orthorhombic $RE_{5-x}Ca_xGe_4$ with Gd_5Si_4 structure type and Pnma space group. They also attempted using induction heating and arc-melting but proved to be unsuccessful for obtaining phase-pure samples and/or increasing crystal size. The nominally divalent Eu and Yb does not appear to form compounds with this structure type. Under the given synthesis conditions, the products obtained from the reactions containing Eu and Ca were the solid solutions $Eu_{1-x}Ca_xGe_2$ (A_1B_2 structure type), while the reactions involving Yb and Ca produced major product $Yb_{2-x}Ca_xGe$ (MgSrSi structure type), respectively.

They have performed a field cooled direct current magnetic susceptibility measurement using a conventional physical property measurement system (PPMS). These measurements were carried out in 5 to 300k interval in a magnetic field (H) of 5000 Oe as shown in **Figure 57**. The raw magnetization data were converted to molar susceptibility ($\chi_m = M/H$). The net effective moments (μ_{eff}) and Weiss temperatures (θ_p) were calculated from the linear fits of the inverse magnetic susceptibility versus temperature.

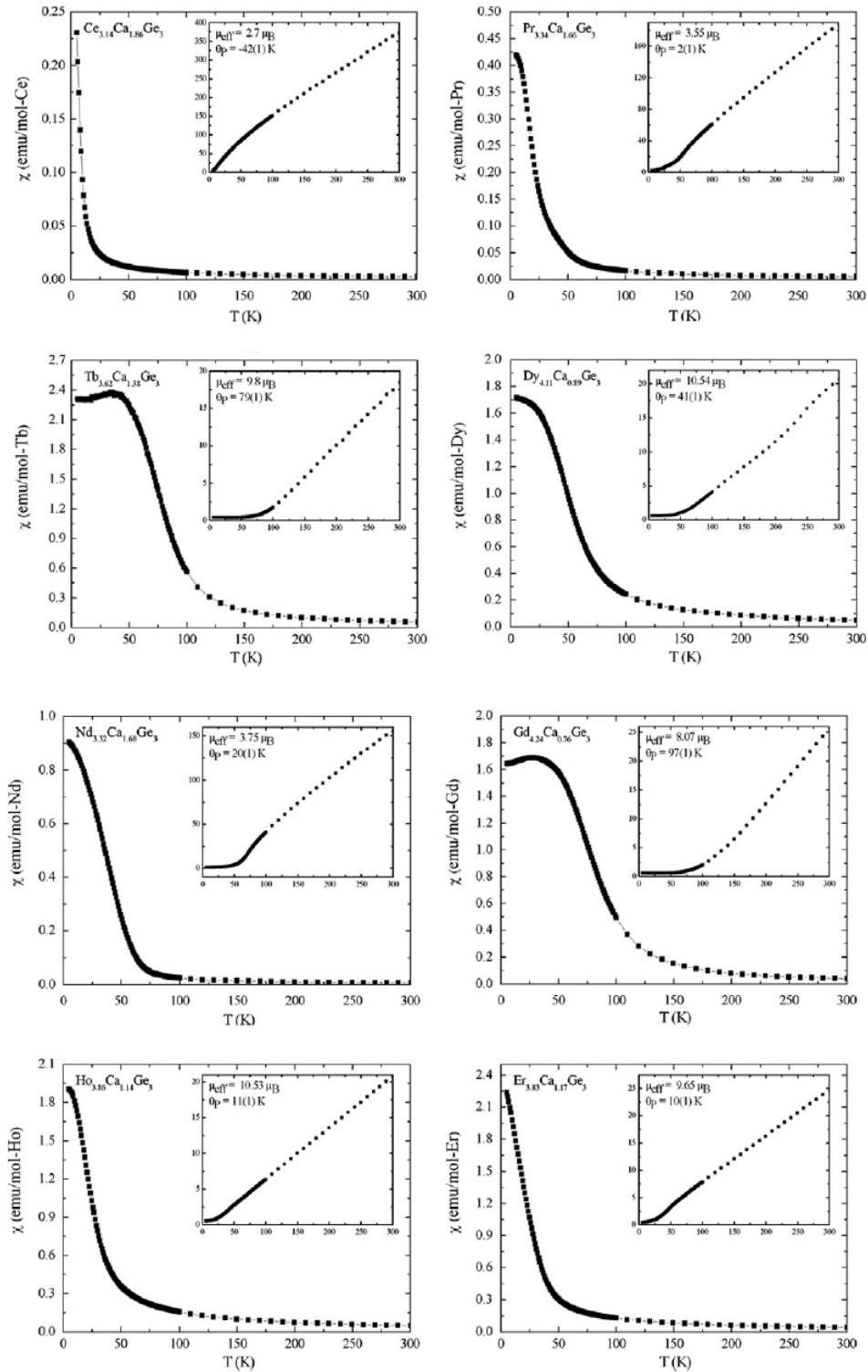


Figure 57 Field-cooled magnetic susceptibility versus temperature of RE_{5-x}Ca_xGe₃ (RE = Ce–Nd and Gd–Er). The insets show the temperature dependence of the inverse magnetic susceptibility [50]

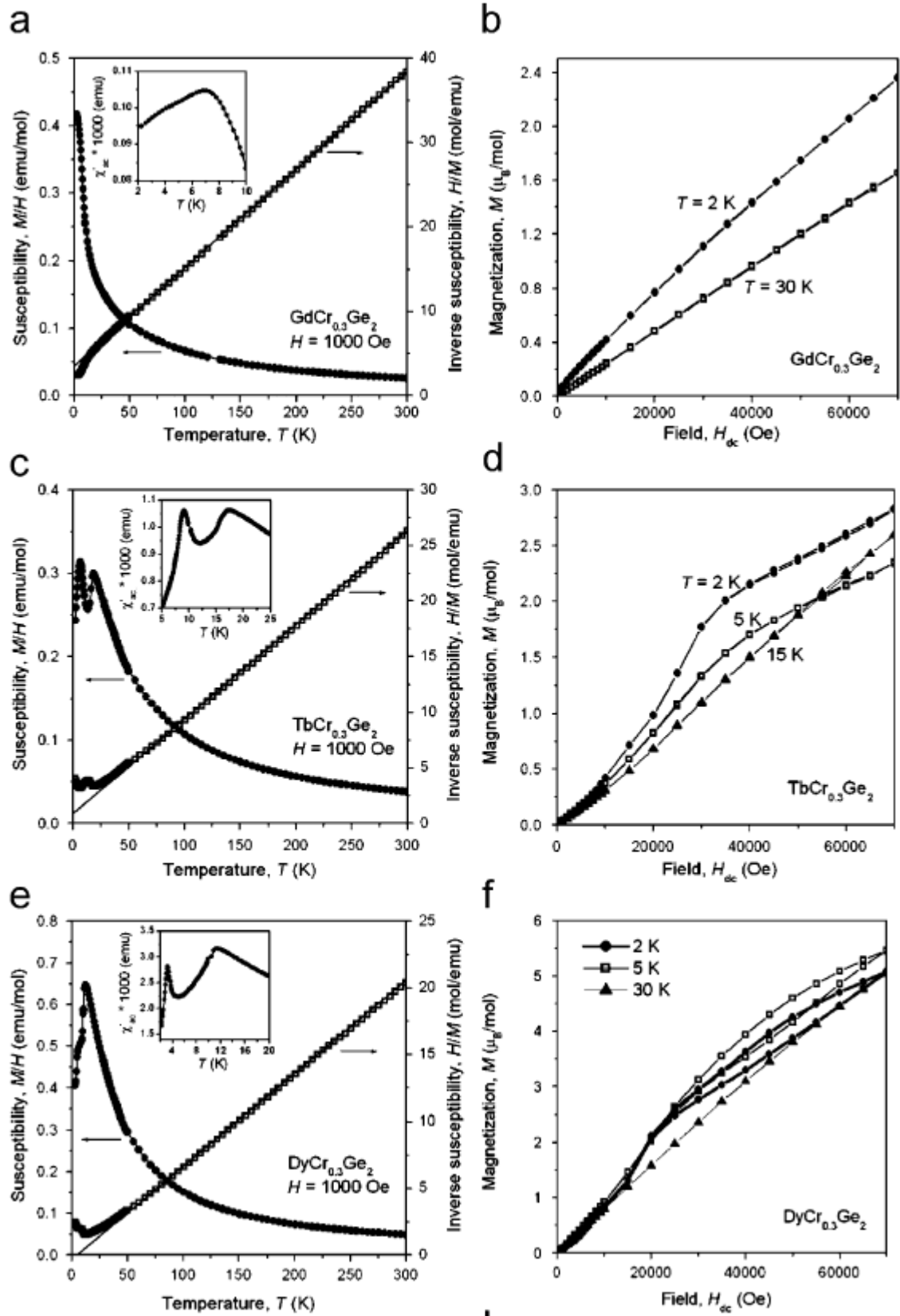
For the Lu- and Y-compounds, they performed these measurements at a lower magnetic field (50 Oe) to test if there was a possibility of superconductivity. They did not observe any signs of the expulsion of magnetic field down to 5 k, though there was a possibility that the samples would become superconducting at lower temperatures. The magnetic measurements of Sm- and Tm-samples were not performed as they were not phase-pure based on their powder X-ray diffraction patterns.

2.4. Rare Earth-Transition Metal Germanides

In 2009, Haiying Bie, et al. [51] synthesized rare-earth chromium germanides $RECr_xGe_2$ (RE = Sm, Gd-Er) using different synthesis techniques such as reacting the elements in the presence of tin or indium flux, or by arc-melting followed by annealing at 800 °C. Pieces of Rare-earths with 99.9% purity, Cr powder with 99.8% purity and Ge powder with 99.999% purity were used for this synthesis processes. For the synthesis of $SmCr_xGe_3$, the elements in the stoichiometric ratio of Sm:Cr:Ge = 1:1:3 were loaded into an alumina crucible jacketed by a fused silica tube in the presence of 0.5g Sn as flux. The tube has been heated to 800 °C slowly over 2 days and was kept at that temperature for 4 days followed by slow cooling to 500 °C at a rate of 3 °C per hour. The liquid tin flux is centrifuged at this temperature. Similarly, $GdCr_xGe_2$ and $DyCr_xGe_2$ were synthesized by reacting the elements in stoichiometric ratios RE:Cr:Ge = 1:1:2 in the presence of a ten-fold molar excess of Indium instead of tin placed inside the alumina crucibles jacketed with fused-silica tubes. These tubes were then heated to 1000 °C over 10 hours, cooled to 850 °C at the rate of 2 °C per hour and kept at this temperature for 2 days. The samples were then cooled to 300 °C over 2 days at which the liquid indium flux was centrifuged.

Single crystal x-ray diffraction data were collected for the samples $SmCr_xGe_2$, $GdCr_xGe_2$ and $DyCr_xGe_2$ using a Bruker Platform/SMART 1000 CCD diffractometer. The composition of $RECr_{0.3}Ge_2$ (RE = Gd-Er) was confirmed to be phase pure without any impurities of flux material. EDX analysis was performed on all these samples, and they noticed the presence of all the elements in the ratios 31-35% of RE, 7-10% of Cr and 60-63% of Ge.

Magnetic susceptibility measurements were performed using a Quantum Design 9T-PPMS dc magnetometer/ac susceptometer on the powder samples with nominal composition $RECr_{0.3}Ge_2$ (RE = Gd-Er), which was confirmed to be phase pure by X-ray diffraction analysis. The magnetic data of these samples are shown in **Figures 58 (a, b, c, d, e, f, g, h, i and j)** and is summarized in **Table 19**.



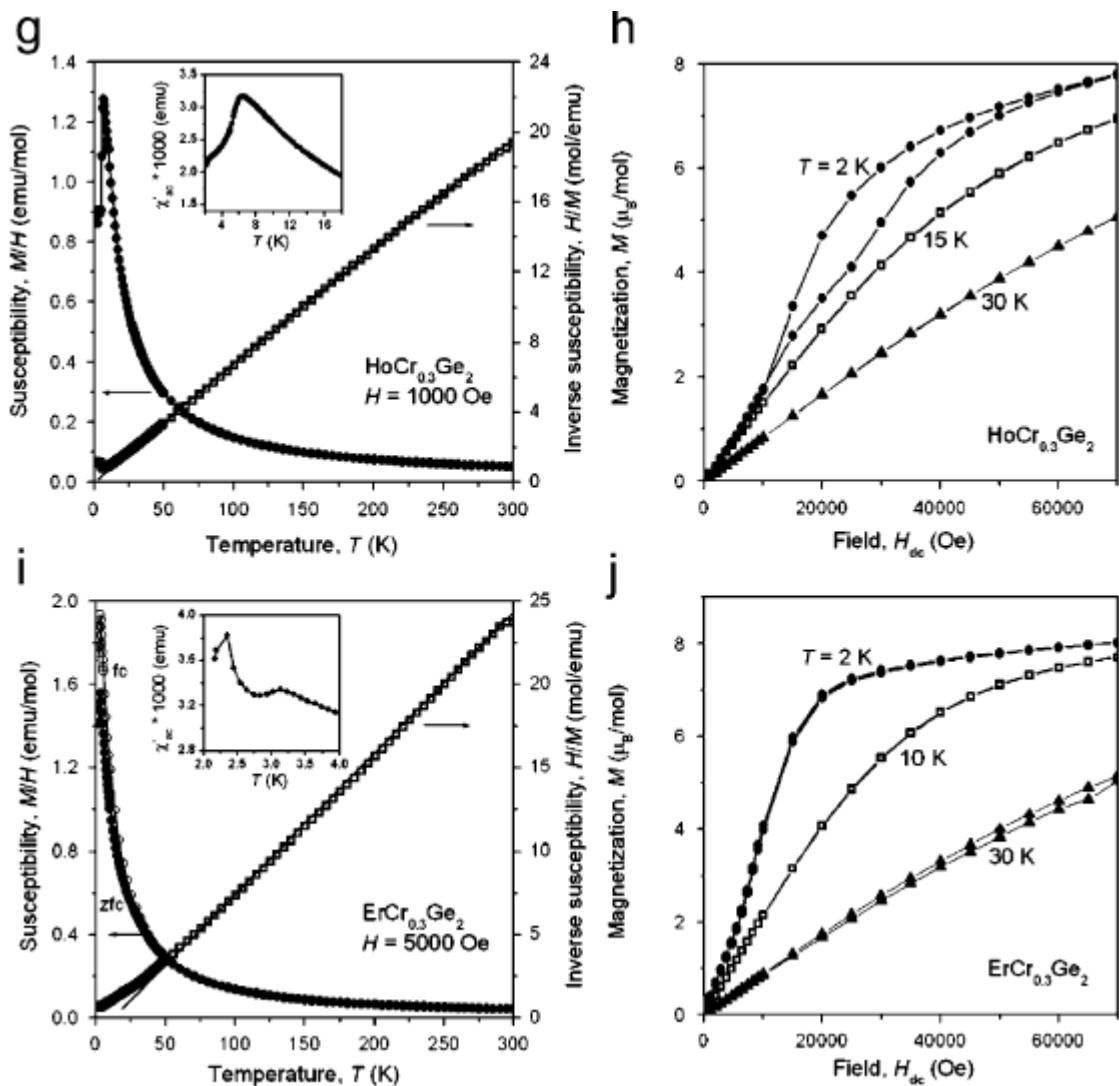


Figure 58 Magnetic data for $\text{RECr}_{0.3}\text{Ge}_2$ (RE = Gd-Er). The left panels show the zero-field-cooled dc magnetic susceptibility and its inverse as a function of temperature (with the insets highlighting low-temperature transitions in the ac magnetic susceptibility), and the right panels show isothermal magnetization curves at various temperatures. The field-cooled susceptibility is also shown in the case of $\text{ErCr}_{0.3}\text{Ge}_2$

[51]

Table 10 Summary of magnetic data for RECr_{0.3}Ge₂ (RE = Gd–Er) [51]

	GdCr _{0.3} Ge ₂	TbCr _{0.3} Ge ₂	DyCr _{0.3} Ge ₂	HoCr _{0.3} Ge ₂	ErCr _{0.3} Ge ₂
T _N (K) from:					
d(χ ^T)/dT vs T plot	10.2	4.3,16.1	4.0,9.9	5.5	2.5
χ' ac vs T plot	7	9.1,17.4	3.2,11.2	6.4	3.1
θ _P (K)	-28.4(2)	-9.9(2)	4.5(2)	-2.3(2)	16.6(3)
μ _{eff} , meas (μ _B /f.u.)	8.26(1)	9.73(1)	10.76(1)	11.08(1)	9.67(1)
μ _{eff} , theor for RE ³⁺ (μ _B)	7.94	9.72	10.65	10.61	9.58

A paramagnetic behavior was observed in all the samples below 300 K down to 20 K when the zero-field magnetic susceptibility measurement were performed with low applied magnetic fields of $H = 1000$ Oe for RE = Gd–Ho and 5000 Oe for RE = Er. The Neel temperatures of the samples were identified from plots of $d(\chi^T)/dT$ or from the ac susceptibility curves and are summarized in **Table 19**. Below 20 K, the downturns in the curves was observed which suggested the onset of antiferromagnetic ordering. They observed that in case of Tb and Dy samples, a second transition was visible at lower temperatures in both dc and ac magnetic susceptibility curves. These transitions and the change in magnetic susceptibility below 20 K are explained in the paper [51].

In 2009, Fumiko Ohtsu et al. [52] synthesized samarium platinum germanides: SmPtGe₂ and Sm₂Pt₃Ge₅ using high pressure and high-temperature synthesis technique. The mixture of Sm, Pt, and Ge with varying atomic ratios were melted in an Ar-filled arc furnace. The purity of metals they used were greater than 99.9%. The starting mixtures of SmGe₂ and Ge with appropriate ratios were placed into h-BN containers, and these containers were placed inside an octahedral-shaped MgO cell and were reacted at high pressures of 10-13 GPa and high temperatures using a Kawai-type high-pressure system.

SmPtGe₂ was obtained by arc-melting of Sm:Pt:Ge in the ratio 1:1:2 mixture. The samples obtained by this method were not suitable for obtaining single crystals suitable for structure analysis. Hence, they used the high pressure of 13 GPa and 1200 °C with materials in the ratio Sm:Pt:Ge = 1:1:3 were used for the preparation of good single crystals of SmPtGe₂. The excess Ge was assumed to have acted as a flux for the crystal growth of SmPtGe₂.

Single crystals of Sm₂Pt₃Ge₅ were synthesized from the elements Sm, Pt, and Ge taken in the ratio 1:1:3. This mixture was reacted at a high pressure of 13 GPa. The temperature was

maintained at 1000 °C for 1 hour and decreased to 850 °C over 1 hour. The samples were then slowly cooled to room temperature, and the pressure was released.

The samples obtained were characterized using Rigaku R-Axis diffractometer, and SHELX-97 crystallographic software package was used to analyze the single-crystal structure. The chemical composition was determined using an electron probe microanalyzer (EPMA). Dark single crystal of SmPtGe₂ with dimensions of 0.02*0.02*0.04 mm³ and of Sm₂Pt₃Ge₅ with dimensions 0.01*0.01*0.02 mm³ were used for the structure analysis. The details on crystallographic data, atomic parameters, and atomic displacement are shown in the paper [52].

They observed that the SmPtGe₂ crystallizes in the space group Immm with lattice constants $a = 4.3679(9)$ Å, $b = 8.728(2)$ Å, $c = 16.378(4)$ Å and $v = 624.4(2)$ Å³. The composition was analyzed by EPMA and was found to be in the ratio Sm:Pt:Ge = 1:1:2. Similarly, for Sm₂Pt₃Ge₅, they observed that this compound was isotypic with U₂Co₃Si₅.

Electrical resistivity measurements as shown in **Figure 59 (a)** and the magnetic susceptibility measurements are shown in **Figure 59 (b)** were performed on the SmPtGe₂ samples obtained by arc melting method using a typical four-probe method using dc from 2 to 300 K and a Squid magnetometer respectively.

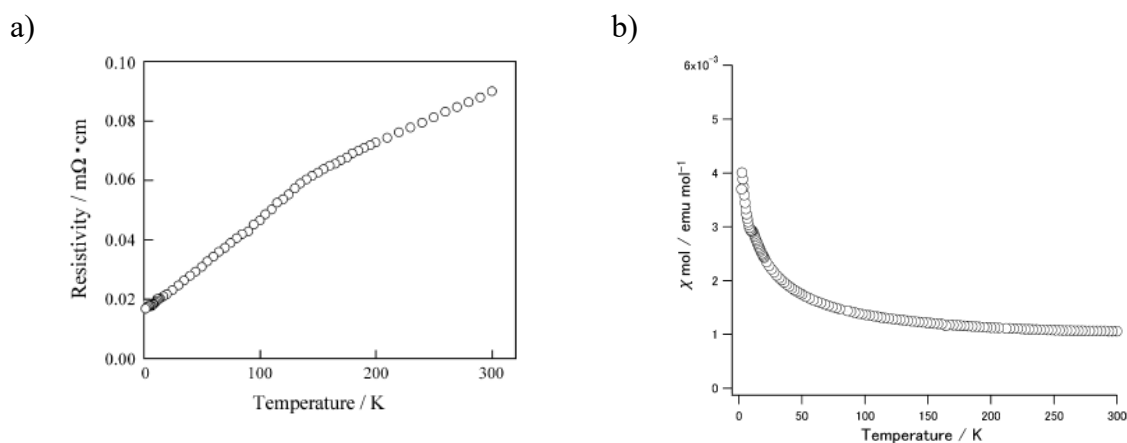


Figure 59 Temperature dependence of a) electrical resistivity and b) Magnetic susceptibility of SmPtGe₂ [52]

They observed that the electrical resistivity decreases with temperature which indicated that the material is metallic. From the magnetic susceptibility curve, they observed that it does not obey Curie-Weiss law which they assumed to be because of the first and second order Zeeman effects of Sm³⁺. The small anomaly observed at 11 K was assumed to be due to an impurity.

In 2013, Anton O. Oliynyk et al., [53] Synthesized rare earth manganese germanides $RE_{2+x}MnGe_{2+y}$ (RE = La, Ce) by arc-melting elements and annealing at 800 °C. Freshly filed RE pieces (RE = La-Nd, Sm, Gd-Tm, Lu, 99.9%, Hefa), Mn powder with 99.96% purity and Ge powder with 99.9999% purity were used for the synthesis process. The mixture was prepared from these materials with various loading conditions within 1% of $RE_{40}Mn_{20}Ge_{40}$ in the RE-Mn-Ge phase diagram within the total mass of 0.3 grams. These were pressed into pellets which were arc-melted in argon atmosphere twice using a Centorr 5TA tri-arc furnace. The arc melted ingots were then annealed at 800 °C for 2 weeks sealed inside the fused-silica tubes. The samples were then quenched to room temperature using cold water. Although they attempted to synthesize the compounds for many RE components, only those containing La and Ce were successful.

Powder X-ray diffraction was performed on the samples using the Inel diffractometer. They observed that the highest yield was obtained in a sample containing La whereas a small amount of other phases (Ce-Ge binaries/impurities) were observed in compounds containing Ce. The refinement of structural parameters was performed using CSD suite and the refined parameters were found to be $a = 16.061(2)$ Å, $c = 8.169(1)$ Å, $v = 2107.2(8)$ Å³ for $La_{2+x}MnGe_{2+y}$ and $a = 15.769(3)$ Å, $c = 8.048(2)$ Å and $v = 2001(1)$ Å³ for $Ce_{2+x}MnGe_{2+y}$. The chemical composition of the samples obtained were determined using energy dispersive X-ray spectroscopy (EDX) analysis on JEOL JSM-6010LA scanning electron microscope. From these they observed that the single crystal of $La_{2+x}MnGe_{2+y}$ extracted from La-containing sample had composition of 43(2) % La, 18(1) % Mn, 39(2) % Ge which was close to the loading composition which was 40%La, 20%Mn and 40%Ge. For Ce-containing samples, polished surfaces were used for EDX, and they found that the composition was comprised of the required ternary phase 43(2) % Ce, 18(1) % Mn, 39(2) % Ge along with Ce_3Ge and another ternary phase with different composition (40(2) % Ce, 25(1) % Mn, 35(2) % Ge). They claimed that this later ternary phase with composition close to $RE_{40}Mn_{25}Ge_{35}$ was observed for a wide range of RE metal (RE = Ce-Nd, Sm, Gd-Dy)

The electrical resistivity, the magnetic susceptibility and the magnetization curves which are shown in **Figures 60 (a), (b) and (c)** for the obtained single-phase ternary compound i.e. $La_{40}Mn_{20}Ge_{40}$ sample were measured on Quantum Design physical property measurement system (PPMS) equipped with ac transport controller (Model 7100) and Quantum Design 9 T-PPMS magnetometer respectively. The single crystals of $La_{2+x}MnGe_{2+y}$ were used for these measurements.

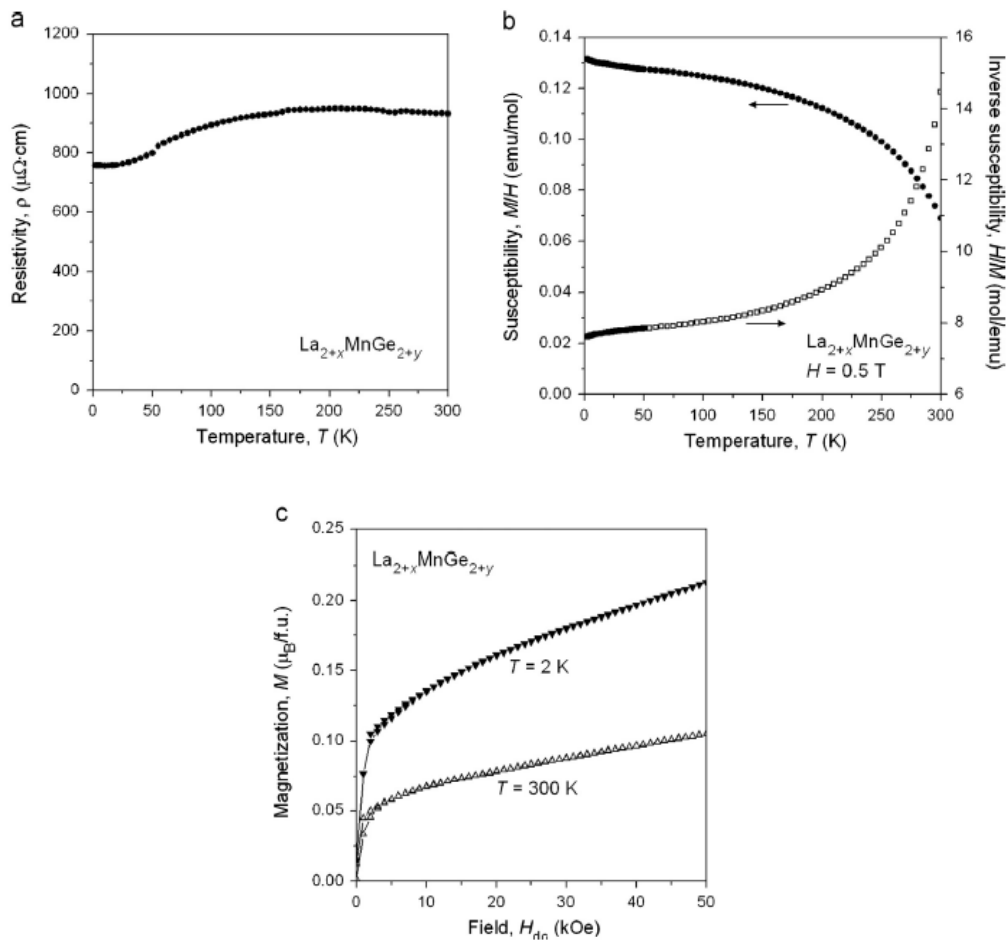


Figure 60 Plots of (a) electrical resistivity, (b) magnetic susceptibility and its inverse as a function of temperature, and (c) magnetization as a function of the field at 2 and 300K for $\text{La}_{2.1}\text{MnGe}_{2.2}$ [54]

They observed that, although the temperature dependence of electrical resistivity was low, the measurements confirmed the metallic behavior of the compound which was expected for $\text{La}_{2.1}\text{MnGe}_{2.2}$. The absolute resistivity obtained by testing four crystals were observed to be high ($\rho_{2\text{k}} = 750\text{-}950 \mu \Omega \text{ cm}$) and the relative resistivity ratios were observed to be small ($\rho_{300\text{k}} / \rho_{2\text{k}} = \sim 1.2$) which was consistent with the disorder present in the crystal structure. From the magnetic susceptibility vs. temperature curve which does not obey Curie-Weiss law and from the approach to magnetization observed in the magnetization vs. field between 2 k and 300 K, they suggested that the $\text{La}_{2.1}\text{MnGe}_{2.2}$ undergoes ferro- or ferrimagnetic ordering with a Curie temperature above 300 K. Since this compound contains nonmagnetic RE component, they assumed that the magnetization observed was the contribution from Mn moments alone.

2.5. Mechanical Alloying

This technique has been known as a ‘mechanochemical synthesis’ technique, ‘solid-state processing’ technique, ‘far from equilibrium’ or a ‘Non-equilibrium’ synthesis technique because of the way it functions. It involves continual deformation of materials/powders by repeated fracturing and rewelding of powder particles. This deformation is carried out by extremely energetic collisions of grinding media (balls) moving with high KE and the powders with themselves and the inner walls of the vial.

A blend of initial powders is taken in required composition and is added into a suitable vial. A suitable grinding media mostly steel balls, are used provide the required energy transfer. Whenever these two steel balls collide, some quantity of powder is captured in between them. The force of the impact plastically distorts the powder particles resulting in work hardening and fracture. The new surfaces created alter the particles to weld along, and this results in a rise in particle size as in the early stages of the milling process, the particles are soft, and hence their tendency to weld along and form massive particles is high. The process schematic is shown in **Figures 61 and 62**.

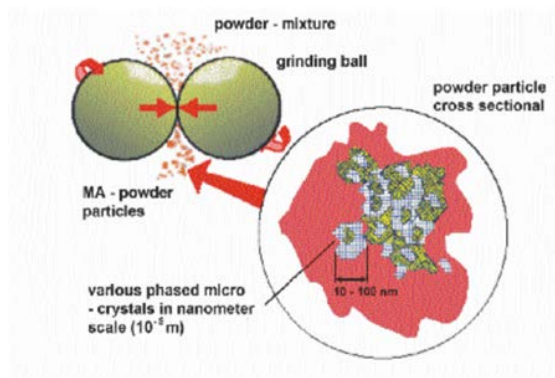


Figure 61 Schematic of collision as the main event of energy transfer [55]

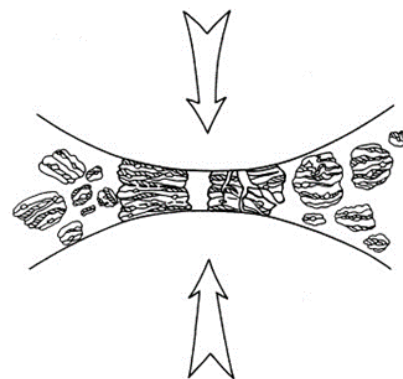


Figure 62 Particles getting trapped between the grinding media [3]

This milling process is carried out until the desired steady state composition is achieved, i.e., every powder particle has the same proportion as of starting elements taken in powder form. The obtained powder is subjected to heat treatment if necessary to obtain a required compound with desired microstructure and properties. Although the process appears simple, there are several variables/parameters that can be or need to be adjusted to obtain desired compound/microstructure without or with least contamination. Some of the parameters that affect the final product we obtain are:

1. Type of Mill
2. Milling Container
3. Milling Speed
4. Milling Time
5. Type, Size and size distribution of grinding medium
6. Ball to powder ratio
7. Extent to filling the vial
8. Milling atmosphere
9. Process control agent
10. Temperature of Milling

Some of these parameters are interrelated as the Milling speed is mostly specific to Type of mill. Also, the optimum milling time depends on the type of mill, ball to powder ratio, type, size and size distribution of grinding medium and the extent to filling the vial. It also depends on the type, and the amount of process control agent used.

2.5.1. Type of Mill

For the processing of materials using high kinetic energy techniques, equipment like Conventional Horizontal Ball Mills, Horizontal ball mill controlled by magnetic force, Vertical mill, Attritor mill and shaker ball mill have been in use for the past decade as they can induce high energy compressive impact forces, each being modified and upgraded to process different types of materials. In some cases, Tumbler mills with large diameter have also been used by reducing the operating speed just below the critical rotational speed, so the balls don't stay pinned to the walls of the chamber. Before a decade, for some large-scale production of commercial alloys, Tumbler mills were used instead of Attrition mills [4].

In mechanical alloying, the powder mixture which may contain either the elemental particles or the alloying particles is loaded into the container of the ball mill which is also known as the vial or the bowl or the jar alongside some steel or ceramic balls. The powder particles are subjected to high energy collisions from the balls when the vials are rotated or shaken with high kinetic energy. Hence the basic equipment for mechanical alloying is a Ball mill.

The alloying process can be done in various equipment namely Attritor mill, SPEX shaker mill, Planetary ball mill or a horizontal mill, whichever equipment is used, the principle behind the mechanical alloying is the same. The particles are repeatedly fractured, and cold

welded during the process and hence is important to maintain a balance between the two to alloy successfully. It is believed that the key to successful synthesis is to select appropriate impact energy for the milling process. The high impact energy and frequency in the SPEX, Attritor and the planetary ball mills enable the mechanical alloying duration to be shortened. Compared to gravitational and centrifugal ball mills, SPEX, Attritor, and planetary ball mills can achieve a significantly higher collision energy [4].

The well-known Planetary ball mill, the shaker mill, the vertical Attritor or the modern Simoloyer are often used to produce mechanically alloyed powders for laboratory purpose. To process a small quantity of powder mixture for use in laboratory, Shaker ball mills are often used as it may take one or more times longer to attain a given structure in a Tumbler or vibrating mill when compared to high energy small shaker mills. A typical example of such shaker mill is SPEX 8000 is shown in **Figure 63** which was originally developed to pulverize spectrographic samples.



Figure 63 SPEX 8000 mixer/mill [1]

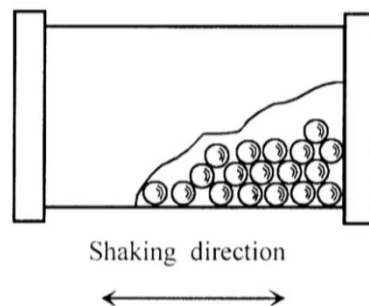


Figure 64 Vial of a Shaker ball mill and the shaking direction [1]

This type of mill, which is suitable for research purposes, is most widely used in U.S.A. [56]. It agitates the charge of powder and the balls in three mutually perpendicular directions at approximately 1200 rpm. The container/vial may have a capacity of up to $55 \times 10^{-6} \text{m}^3$. Compared to attrition and vibratory ball mills, it is highly energetic, and this can be obtained by using high frequencies and large amplitude of vibration. The table below shows the number of impacts for a different number of balls and the resulting kinetic energy occurring over 0.5 or 1.0 second of milling [4]. It was observed that most of the impact occurs in the 10^{-3} to 10^{-2} Joules range.

Table 11 Table showing number of impacts for a different number of balls and the resultant values of kinetic energy [4]

Number of balls used (2g each)	Mill operating for 0.50 seconds				
	Kinetic energy of impact (J)				
	10^{-7} - 10^{-4}	10^{-4} - 10^{-3}	10^{-3} - 10^{-2}	10^{-2} - 10^{-1}	10^{-1} -1.0
5	0	43	297	3	0
10	0	78	505	13	1
15	4	124	928	24	0
Mill operating for 1.0 seconds					
5	0	78	612	3	0
10	0	148	1201	13	2
15	4	229	1873	24	0

2.5.2. Milling Container

In mechanical alloying, the vial or the milling container undergoes very high energy impacts continuously. This container acts as a boundary with which all the energy transfer takes place except for the loss of some energy as heat from the walls of the container. These impacts may lead to one of the two possibilities, i.e., either powder gets continuously embedded into the walls of the vial until it finally reaches a stagnation point and starts coming out of the vial along with some amounts of vial surface material which then gets alloyed/ mixed with the powders present inside, or the balls when hit the inner surface of the vial, dislodge some material from the it which then gets mixed/alloyed with the sample. If the material of the container/vessel is different from the powder being milled/alloyed, then the final sample would be contaminated. On the other hand, if the container and the powder are of the same material, the chemistry or the stoichiometry might change resulting in different phases than expected unless proper precautions are taken to compensate for the additional amount of elements incorporated into the powder. Hardened steel, tool steel, hardened chromium steel, tempered steel, stainless steel, WC-Co, WC-lined steel and bearing steel were the most commonly used types of materials for containers/vials. There are some specific vial materials like copper, Titanium sintered corundum, yttria-stabilized zirconia, partially stabilized zirconia + yttria, sapphire, agate, hard porcelain, Si_3N_4 , and Cu-Be that have been used where it was observed that those materials

wouldn't react with the powders or where it was acceptable to have a little to no contamination [1].

2.5.3. Milling Speed

It is often assumed that the faster the mill rotates/operates, the higher is the energy input or the energy transfer. This might be true in some cases/types of mills but for those that depend directly on rotational speed such as conventional ball mill, if the speed reaches the critical speed, the balls/grinding media get pinned to the wall of the container, hence reducing energy transfer to powders that need to be alloyed, through impact to ~ 0 . Thus, the effectiveness of the actual mechanical alloying process is reduced drastically. Hence, the maximum speed must be limited to just below the critical speed.

2.5.4. Milling Time

The time up to which the milling is continued to obtain a steady state of fracturing and welding without any change in particle size [1] is considered as milling time. It is an important parameter which is highly dependent on other parameters like the type of mill being used, type of powders being milled/alloyed, Ball to powder ratio being used and if any size distribution in grinding medium. Milling for a longer time causes severe contamination from its environment which must be kept at a minimum in most cases. In different types of mills, the intensity of milling is varying as the energy input is different and this directly affects the time the milling has to be performed to obtain that steady state of fracturing and welding. In case of alloying, it depends on the type of materials being alloyed and the ease of their formation. Alloys that can be obtained at a lower temperature using other techniques can be obtained at very low milling/alloying times and for those which need more energy need to be milled for a longer time. If the Ball to powder ratio is high, it requires less time to mill/alloy powder, and if it low, it might take longer. If using a varying balls sizes, increasing the milling time might result in breaking of the smaller balls due to the impact from bigger one if the size variation is significant.

2.5.5. Type, Size and Size Distribution of Grinding Medium

Many different types of materials have been used for grinding medium like Hardened steel, stainless steel, tool steel tempered steel, hardened chromium steel WC-Co and bearing steel. It is desirable to use grinding media of same material as the powders being milled or alloyed to

avoid cross-contamination [1]. The size of the balls/grinding media has a huge impact on how effective the milling is in a given time. Bigger balls certainly have higher impact resulting in faster milling/alloying as the energy transfer in each impact is very high. On the other hand, when using small balls, more number of balls will be used to attain a certain ball to powder ratio, and this means more number of impacts but with significantly lower impact energy. It was observed that amorphous phases formed when using smaller balls as they produce intense frictional action whereas when using bigger balls, more stable and crystalline compounds were obtained.

Even though in most cases only one size of balls/grinding media are used, there were some instances where different sized balls have been used together [1]. Previous reports stated that using a combination of large and small balls for milling reduces the amount of cold welding [1]. Also when using a set of same-sized balls in the vial, they tend to produce tracks which indicates that the motion is not random and they move along a defined trajectory whereas when using a mixture of balls of different sizes, it was noticed that the motion was random [1].

2.5.6. Ball to Powder Ratio

The Ball to powder ratio which sometimes is also referred as charge ratio is the ratio of the mass of balls to the mass of powder being milled or alloyed excluding the mass of Process control agent being added. Although the most common used charge ratio is 10:1 in laboratory purpose small-scale mills, this value has been varied from as low as 1:1 [1] to as high as 220:1 [1] in large capacity mills such as attritor.

The ball to powder ratio has a direct impact on how fast the required phase is obtained. Lower the ball to powder ratio, longer it takes to reach the required phase and vice versa. Having very high ball to powder ratio might lead to problems like not having enough space for proper milling or powders not getting hit by balls and instead balls hit each other.

2.5.7. Extent to Which the Vial Is Filled

For milling to be effective, there should be enough space left inside the vial to help the movement of the balls/ grinding media and the powders freely. The longer the ball travels, the more impact energy it supplies, and thus each impact is highly effective. Filling the vial space for more than 50 % would lead to a significant decrease in energy being supplied to powders thus taking longer time to obtain the required phases [1]. If the very small amount is taken such that greater than 70% of the vial is left empty, the production rate would be very low. Hence

the extent to which the vial is being filled must be considered carefully to have an effective process.

2.5.8. Milling Atmosphere

Milling atmosphere plays a vital role when handling materials in a powder state. Most material/metals although not very reactive in solid form, are highly reactive when they are ground to a powder form; ex: Mn. There are chances that with a small amount of Oxygen present inside the vial, the powder blend or the elemental powder may get oxidized resulting in oxide contamination. Hence in most cases, the powder handling is performed inside a glove box filled with suitable inert gas. High purity Argon gas is most commonly used [1]. This atmosphere is also dependent on the type of material being synthesized/milled for example; if one is trying to produce nitrides, they could use Nitrogen or ammonia atmosphere, or if they are trying for hydrides, they may use Hydrogen atmosphere [1]. This atmosphere is also known to have a significant effect on the nature of the final phase produced [1].

2.5.9. Process Control Agent

During mechanical alloying, the powder undergoes repeated cold welding and fracturing and the balance between these two is necessary for the milling/alloying to be effective. The powder particles undergo a heavy plastic deformation during the process especially if they are ductile. This results in excessive cold welding thereby affecting the balance between the welding and fracturing. To reduce/prevent this excessive cold welding, a process control agent (PCA) also called as a surfactant or a lubricant is used. These PCA's can be in solid, liquid or gaseous form. Most of the PCA's are organic compounds which act as surface-active agents [1]. Different types of PCA's such as ethanol, methanol, hexane, Oxalic acid, Benzene, ethyl acetate, Heptane, polyethylene glycol, naphthalene, cyclopentane, Toluene and stearic acid have been used depending on the level and type of contamination they would induce and also their effectiveness on milling process [1]. If the powder yield is high, it means that the PCA is effective. If the yield isn't high enough, it probably means that the PCA was not sufficient or the type of PCA is not right for those materials being milled [1]. The type of PCA and the quantity of it being added determines the final size, shape, and purity of the powder particles after milling/alloying. Increasing the amount of PCA helps reduce the particle size exponentially for a given milling time [1].

2.5.10. Temperature of Milling

The vial temperature during the milling process is another significant parameter which directly affects the final composition of the powders milled/alloyed. In the formation of alloys phases, diffusion process occurs irrespective of whether the final phase is a solid solution, intermetallic, nanostructure, or an amorphous phase and temperature of milling has a significant effect in this process [1].

There have been few investigations where the temperature of the milling was varied intentionally. They were performed to study the effect of temperature of milling on solid solubility levels and the formation of either amorphous or crystalline phases at different temperatures [1]. To obtain lower temperatures, the milling vial was dripped on with liquid nitrogen and to obtain higher temperatures, the vial heated electrically [1].

2.6. Contaminations in Mechanical Alloying

There are several factors leading to contamination in this synthesis process of which major contamination was observed to be from three different sources which are explained below.

2.6.1. Contamination from Milling Tools

One of the most common contaminations in mechanically alloyed powders is Fe and Cr elements from the milling vial and balls since most milling tools are made from those types of elements. During mechanical alloying, the balls impact onto the powder mixture, the vial as well as onto each other. The powder particles are therefore not only cold welded with powder particles themselves but also with the milling tools under high energy collision. The cold-welded powder will sooner or later be fractured from the balls and the vial by direct collision and relative friction, leading to transfer of atoms from the milling tool to the powder particles. It appears that contamination from milling tool is unavoidable especially at high impact intensity and long milling duration. It is a serious problem in the mechanical alloying, and several methods have been suggested to reduce this sort of contamination:

- a. Using hardened milling tools;
- b. Employ milling tools with similar composition as the powder mixture so that the contamination will have the same composition as the milled materials.
- c. Increase cold welding so that the milling tools may be covered with the powder mixture.

2.6.2. Contamination from Atmosphere

Although inert gases such as argon, nitrogen, and helium are usually employed to prevent oxidation, they may themselves react with the powder mixtures being mechanically alloyed. Depending on different material systems, sometimes this reaction can be very serious.

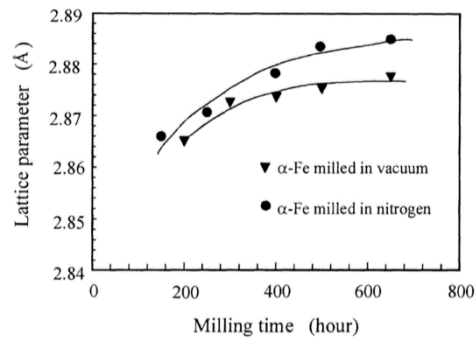


Figure 65 Influence of vacuum and nitrogen environments on the change in average lattice parameter of Fe [57]

The figure above shows the average lattice parameter of Fe powder ball milled under two milling environments, namely, vacuum and nitrogen protection [57]. The lattice parameters change under both conditions: there is a large increment when the Fe powder is milled in a nitrogen atmosphere, but only a little increase in the latter case. About 0.8% increase in lattice parameter in the former case is attributed to the absorption of nitrogen and a corresponding expansion of the lattice. In the latter case, the lack of gases leads to a slower increase in lattice expansion; about 0.4% increase in lattice parameter is associated with the residual gases.

For materials that will readily form nitrides, the use of nitrogen to provide an inert atmosphere should be avoided. Research shows that nitrides may be formed if Ti, Ta, Zr, Mo, and Si are milled in a molecular nitrogen atmosphere.

2.6.3. Contamination from Process Control Agents

Decomposition of process control agents during mechanical alloying cannot be avoided. As these process control agents normally contain carbon, oxygen, and hydrogen, their decomposition may cause carbon, oxygen and hydrogen contamination. Use of stearic acid has been found to give contamination of 1.1wt.% carbon and 0.8wt.% oxygen [57]. Direct formation of hydride in mechanical alloying of Al-Zr has also been reported [57], indicating the decomposition of the process control agent. It has been explained that the process control agent decomposes into hydrogen, oxygen, and carbon due to rise in temperature in the

mechanical alloying process. Repeated cold welding and fracturing result in the formation of very fine powder particles. Because of large surface area to volume fraction, the surface energy of the mechanically alloyed powder particles increases with the increase in milling duration. The fresh surface created by the fracturing process promotes diffusion. In comparison to oxygen and carbon, the diffusion rate of hydrogen is much faster than that of oxygen [57]. The table below gives the amount of H₂, O₂ and C contents of different types of process control agent.

Table 12 Amount of H₂, O₂ and C percentage in each process control agent which could lead to contamination [57]

Generic name	Chemical formula	H ₂ (%)	O ₂ (%)	C (%)
Stearic acid	CH ₃ (CH ₂) ₁₆ CO ₂ H	13	11	76
Heptane	CH ₃ (CH ₂) ₅ CH ₃	16	0	84
Ethyl acetate	CCH ₃ CO ₂ C ₂ H ₅	9	36	55
Ethylenebidisteramide	C ₂ H ₂ -2(C ₁₈ H ₃₆ ON)	13	5	77
Dodecane	CH ₃ (CH ₂) ₁₀ CH ₃	15	0	85
Hexanes	C ₆ H ₁₄	16	0	84
Methyl alcohol	CH ₃ OH	13	50	37
Ethyl alcohol	C ₂ H ₅ OH	13	35	52

The degree to which the Hydrogen, Oxygen or Carbon gets absorbed into the material being synthesized depends upon the materials that are being milled/alloyed.

2.7. Key Points from Literature Review:

- In most cases, the starting elemental materials were of purity > 99.9% and for this transition metals are relative inexpensive when compared to rare-earth metals especially in powder form.
- Studying the phase evolution during the synthesis process when following the techniques mentioned in the literature is almost impossible as most of them are multistep process and involve extreme conditions.
- Almost all metallic germanides were synthesized under extreme conditions which could reduce the purity of the elemental materials being used.
- Most of these synthesis techniques involved impurities making the process non-reproducible.

- Mechanical Alloying is most suitable, and inexpensive non-equilibrium processing technique that could produce metastable phases with relatively high yield and purity.
- Removing samples during the synthesis process is much easier and hence studying the phase evolution.

CHAPTER 3. MOTIVATION

The limitations in the ability to study phase evolution in previously adopted synthesis processes and the challenges faced in the synthesis of germanium-rich and/or equi-atomic phases of manganese germanides, were the motivation of this research work. Although some of the metastable phases of Mn-Ge system have been synthesised before, they were synthesised under extreme conditions viz. very high pressure and/or temperatures where the elemental materials may deteriorate, in the form of solid chunks, and/or by various thin film techniques. The yield in these techniques were extremely low. Mechanical alloying (MA) a widely used non-equilibrium processing technique is known for making nanostructured powders. The powder processing technique involves continual deformation, fracturing and welding of powder particles as they are subjected to extremely high energy collisions from the grinding media. The phase evolution can be studied with ease by taking out powder samples at regular time intervals during the alloying process.

CHAPTER 4. EXPERIMENTAL PROCEDURE

4.1. Material Synthesis

The synthesis of the metastable phases of Mn—Ge system were carried out in two different ways using mechanical alloying varying different parameters. The two techniques are mentioned below and are explained in detail in the results section.

- a) Prevalent technique: alloying of powders with the intermediate addition of process control agent and removal of the sample (powders).
- b) Ideal technique: alloying of powders with addition of stearic acid only at the beginning of the alloying process and no intermittent removal of sample

It was observed that the best results were obtained when the ideal technique, was followed which is explained as the experimental procedure below.

Elemental powders of 99.95% purity Mn with a mesh size of -325 and 99.999% purity Ge with mesh size -100 were procured from Alfa Aesar and Acros Organics respectively which are shown in **Figures 66 (a) and (b)**.

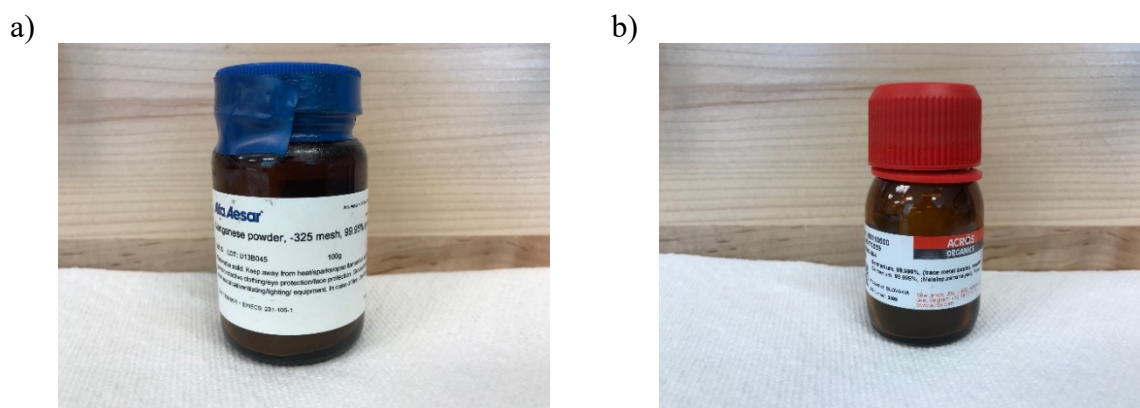


Figure 66 Elemental powders a) Manganese with 99.99% purity and b) Germanium with 99.999% purity

A blend of these powders was taken such that their composition corresponds to the stoichiometric ratio of the desired alloy, i.e., Mn-50 at. % Ge ($Mn_{50}Ge_{50}$). Each mechanical alloying run consisted of 5 g of blended powder, stainless steel balls which act as a grinding

media (maintaining ball to powder ratio of 8:1), and ~ 2 wt.% stearic acid as a process control agent (PCA). The powder blend along with the balls were loaded into a SPEX 8007 stainless steel vial, filling about 20 to 30 % of the vial space; leaving ~70 % or more empty space for the mechanical alloying process to be effective. The vial was closed/sealed tight inside the glove box maintained under argon (Ar) atmosphere having oxygen level less than ~0.01 % to prevent oxidation during mechanical alloying. The alloying was performed in a SPEX 8000D, high energy ball mill shown in **Figure 67** and; the vial, as well as the stainless-steel balls, are shown in **Figures 68 and 69**.



Figure 67 SPEX Sample Prep 8000D high energy ball mill



Figure 68 SPEX 8007 Stainless steel vial

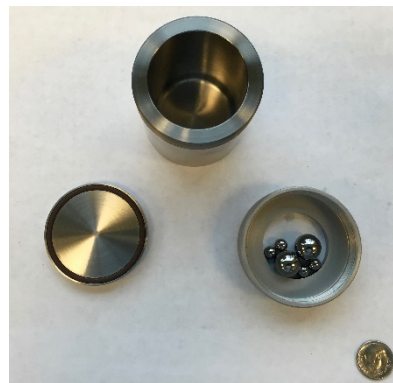


Figure 69 Components of vial and the stainless-steel balls spread out beside a Dollar coin for size reference

The addition of PCA was performed to help prevent: (i) welding of balls due to high impacts and (ii) cold welding between powder particles and the wall.

The vial once closed inside the glove box, was not opened until the stipulated mechanical alloying duration was complete, i.e., no intermediate scraping was performed. The process control agent was added only before the start of each alloying runs, (no intermediate addition of PCA was performed).

Alloying was performed in intervals such that the powder undergoes 3 hours (h) of continuous mechanical alloying and ~30 minutes of cooling of the vial in air. This not only helps the vial (and the powder) to cool down but also reduces the load on the SPEX Mill. The temperature of the vial was noted after every 3 hrs of continuous alloying. After mechanical alloying for the desired amount of time is complete, the vial was allowed to cool overnight and was opened inside the glovebox (Ar atmosphere, oxygen % < ~0.01). The powder stuck to the walls of the vial was scraped off and mixed well with the remaining powder in the vial. The samples were removed such that each was a representative of certain hours of alloying with no intermediate hindrance and hence multiple alloying runs were performed for different samples obtained after different hours of alloying. These powder samples were stored in a big and a small glass vial (inside glovebox). A representative powder sample approx. ~300 mg was stored in a big glass vial for phase analysis by x-ray diffraction where as a small amount of sample was stored in a smaller glass vial as a backup for the XRD analysis in case the sample inside the big glass vial gets oxidized. The typical big glass vial and the small glass vial is shown in **Figures 70**.



Figure 70 Samples after alloying are stored inside the bigger and smaller Glass vials as shown in left and right images respectively

4.2. Materials Characterization

Each of the mechanically alloyed powder samples obtained after continuous alloying were characterized by performing powder X-ray diffraction using a Rigaku-Miniflex600 X-Ray diffractometer with Ni-filtered CuK α radiation in the 2-theta range of 20° to 90°. The patterns obtained were analyzed using JADE 2016 software package to confirm the phase change is happening during the alloying process. The final samples that contained ~100 % MnGe phase were characterized using X-ray diffraction, and the obtained peaks were analyzed using ORIGIN PRO to obtain the accurate peak position, i.e., 2- θ value for each peak. The Lorentz curve fitting was used to obtain the 2- θ value. These values were used to determine lattice parameter of the obtained phase using Cohen's least square method [58]. The lattice parameter correction was performed using the analytical method, and the final value is obtained. The details of this method are mentioned in the results section.

Particle size and size distribution analysis along with the determination of composition analysis were performed on the final samples containing maximum MnGe phase using Philips XL30 SEM with EDAX setup and an Image-J software package.

Magnetization measurements such as a change in a magnetic moment with a change in the applied field as well as a change in the magnetic moment over the temperature range of 60-360K and 300-960K with an applied field of 100 Oe were performed on these samples using Quantum Design's Vibrating Sample Magnetometer. The equipment used are shown in **Images 71, 72 and 73**:



Figure 71 Rigaku Miniflex powder X-ray diffractometer



Figure 72 Philips XL30 SEM and EDAX setup



Figure 73 Quantum design's vibrating sample magnetometer setup

CHAPTER 5. RESULTS AND DISCUSSIONS

From the literature, it was observed that the mechanical alloying was performed in different ways varying different parameters. In this work, we have attempted few of them, and the results of each attempt are shown below.

5.1. Phase evolution during the synthesis of MnGe

Synthesis of MnGe was carried out in two different variations of mechanical alloying and each of them along with their results are explained below.

5.1.1. Adopting the Prevalent Technique

It was noticed that in the most popular approach of mechanical alloying, the mass of initial blend of powders was close to 10 g and that of the balls was ~100 g such that the ball to powder ratio was maintained at ~10:1. About 2 wt. % PCA was added at the beginning of the alloying process. Alloying was performed in steps of 3 hours of alloying and 1 hour of cool down period. A small amount of sample was removed at certain intervals (intermediate stages) for characterization. PCA was added at these stages if any cold welding was observed. Also, the powder was scraped off the walls of the vial if it was found sticking to the walls. If from the characterization, it was found that the required phases are obtained, alloying was stopped, and the entire powders from the vial are taken out and are analyzed thoroughly. If not, the alloying was continued with the remaining powders in the vial until the required compound or phase is obtained [6][1]. An attempt was made with the processing parameters similar to the one used in popular approach which are shown below in **Table 22**.

Table 13 Table of parameters used in the Prevalent technique

Time (hours)	Ball Material	Balls (Grinding Media)		Powder mass			PCA (Wt.%)	Ratio (B/P)
		Ball Size (mm)	Mass of 12 balls	Sample in Vial	Sample removed	Total mass		
				grams	grams	grams		
0	~	~		0.00	0.00		~	~
3	Stainless Steel	12.7	98.74	10.00	0.30	9.70	2	10.18
6	Stainless Steel	12.7	98.74	9.70	0.30	9.40	0	10.51
12	Stainless Steel	12.7	98.74	9.40	0.30	9.10	2	10.85
18	Stainless Steel	12.7	98.74	9.10	0.30	8.80	2	11.22
24	Stainless Steel	12.7	98.74	8.80	0.30	8.50	2	11.62

In this attempt, after alloying for certain time, the vial along with the powder inside was allowed to cool down to room temperature and was then opened in the air. A small amount of sample was removed at intermediate stages, and PCA was added every time the sample was removed to prevent any cold welding. As soon as the sample was taken out and exposed to air, it started a self-sustained reaction. This happened every time the sample was taken out in ambient atmosphere during the attempt for the synthesis of MnGe. The samples obtained were analyzed/characterized using powder X-ray diffraction, and the results are shown in **Figures 74 and 75**.

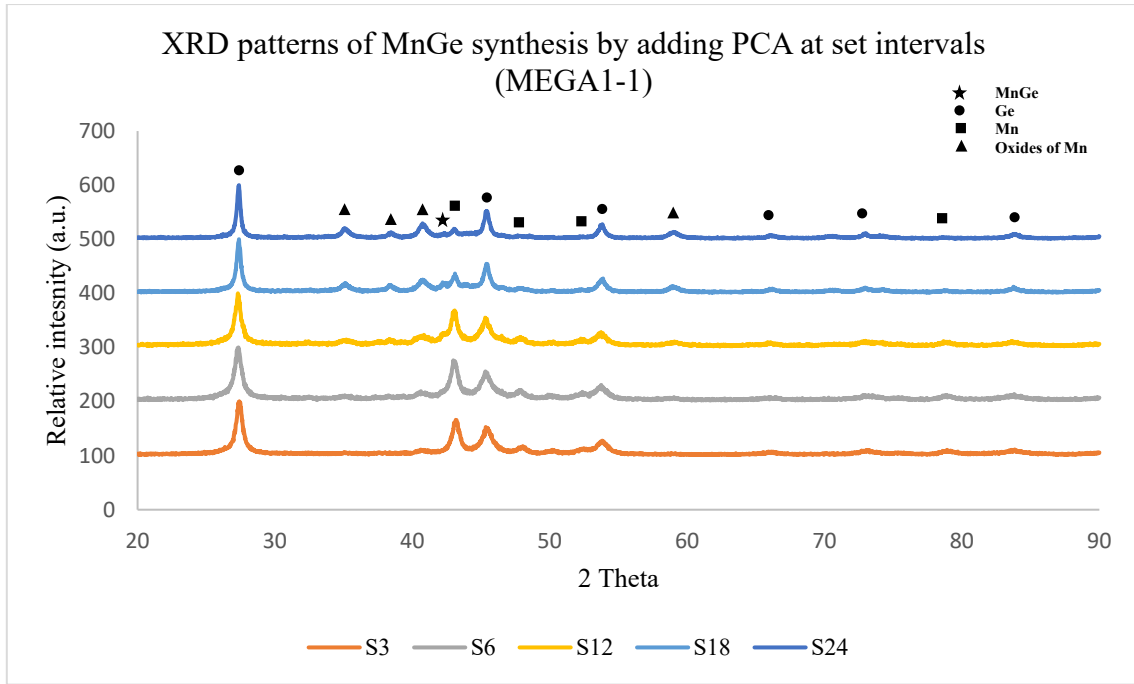


Figure 74 XRD Pattern of all the samples synthesized with intermediate addition of PCA and removal of sample

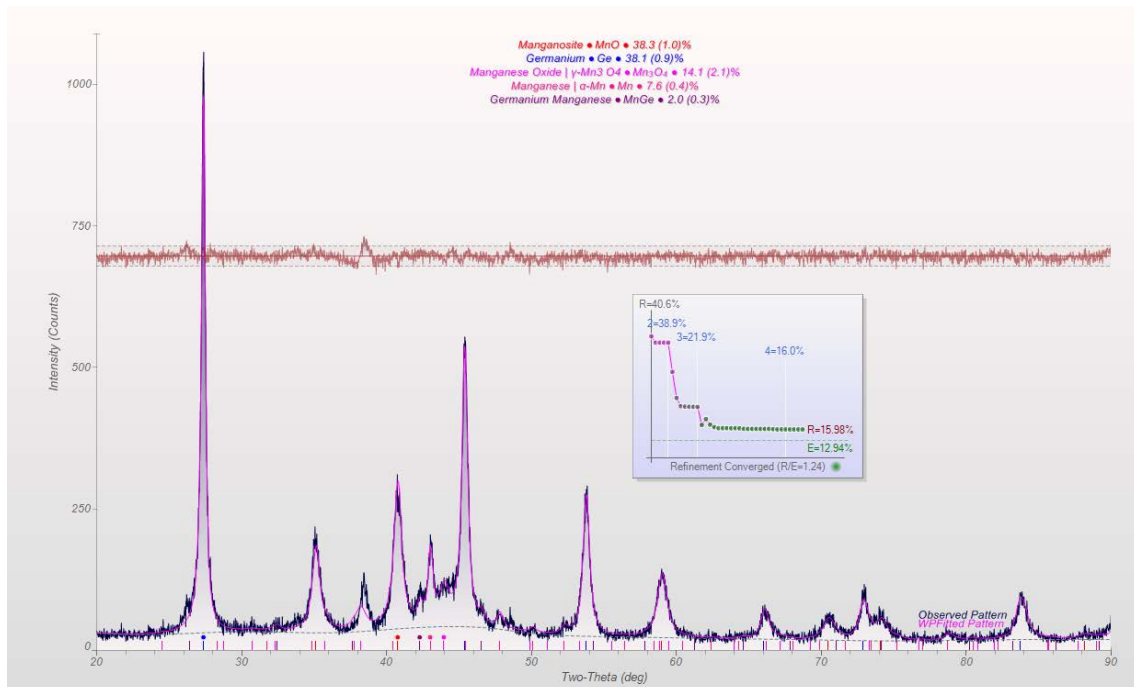


Figure 75 XRD pattern of sample S24 analyzed in JADE 2016 software package showing oxidation

The XRD patterns show high-intensity peaks of Ge regardless of how long they were alloyed along with the increase in the manganese oxide peaks. This was assumed to be due to the reactions that occurred when the sample was exposed to air. These reactions could be happening because of one or all the reasons mentioned below.

1. Presence of sub-micron size Mn powders that are highly reactive and also are subjected to such high energy, or
2. The phases formed after alloying are unstable at ambient conditions, or
3. The stearic acid is reacting with the sub-micron Mn powders or the already formed phases of Mn-Ge system.

The other drawback observed in this method was, removing sample at intermediate stages causes a change in a ball to powder ratio resulting in a gradual increase of B/P which is shown in **Table 22**.

To avoid or to minimize these drawbacks, a process with ideal processing parameters and sample handling techniques was established/used which is explained in detail below.

5.1.2. Adopting the Ideal Technique

In this Ideal case, the mass of powder blend taken was reduced to ~5 grams, and mass of balls taken was ~ 41g such that the ball to powder ratio was close to ~ 8:1, leaving enough space, i.e., ~70 % of the vial empty for the alloying to be effective. Stearic acid was added only at the beginning of the process, and no intermediate addition was performed to eliminate any chances of it reacting with Mn or the phases forming upon alloying. The detailed processing parameters are shown in **Table 23**.

Table 14 Table of parameters used in the mechanical alloying process without intermediate removal of sample or addition of PCA

Time (hours)	Ball Material	Balls (Grinding Media)		Elemental Powders			PCA (Wt%)	Ratio (B/P)
		Ball Size (mm)	Mass of 5 balls	Mn 43.06 wt%	Ge 56.94 wt%	Total mass in grams		
0	~	~					~	~
9	Stainless Steel	12.7	41.1126	2.153	2.8473	5.0003	2	8.2220
15	Stainless Steel	12.7	41.1101	2.1531	2.8472	5.0003	2	8.2215
18	Stainless Steel	12.7	41.1599	2.1532	2.8469	5.0001	2	8.2318
24	Stainless Steel	12.7	41.0762	2.153	2.8467	4.9997	2	8.2157
30	Stainless Steel	12.7	41.1603	2.153	2.8468	4.9998	2	8.2324
36	Stainless Steel	12.7	41.0906	2.1531	2.8468	4.9999	2	8.2183
30-2	Stainless Steel	12.7	41.1325	2.1531	2.8471	5.0002	2	8.2262

The temperature of the vial was measured every three hours when the alloying was stopped to allow the vial and the motor of the mill to cool down. The temperatures observed in each run are stacked one over the other which is shown in **figure 76**.

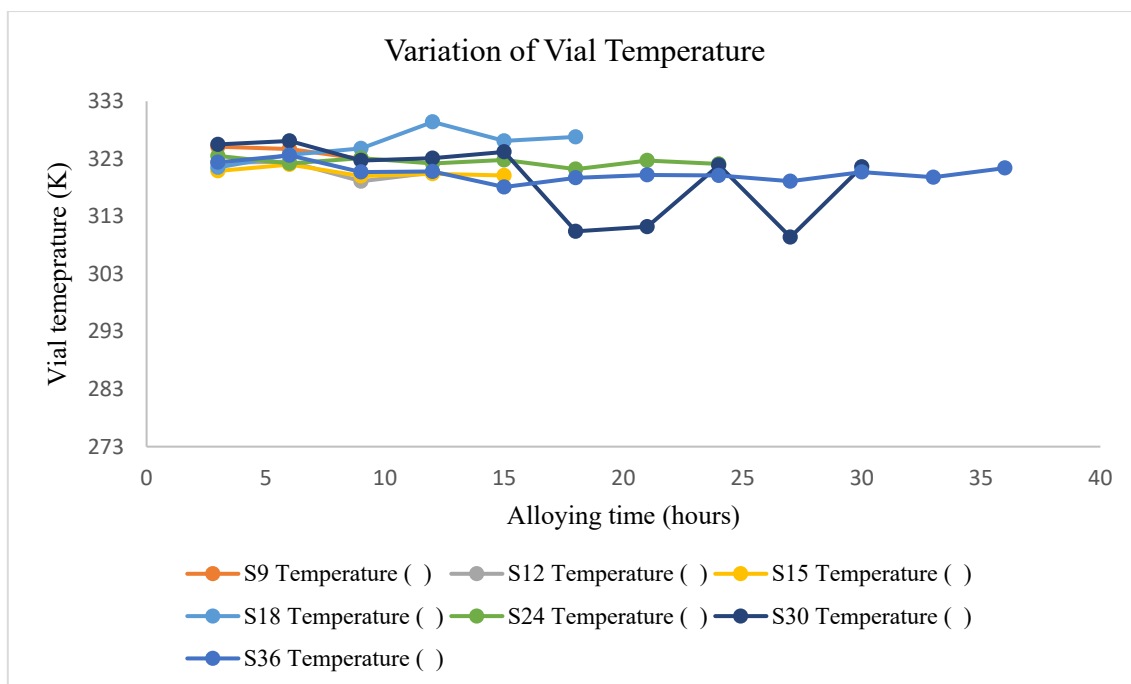


Figure 76 Temperature variation observed on the outside walls of the vial recorded every 3 hours during the alloying process

It was observed that the balls were getting welded or seized at or after 15 hours of alloying time which resulted in a slight or significant reduction in temperature depending on how long the balls stayed seized.

No intermittent removal of the sample was performed in this process, to avoid any change in the ball to powder ratio. The powder was scraped off the walls of the vial, and the entire powder was removed as a sample after alloying is performed for a certain time. All the powder/sample handling was performed inside the glove box to prevent any oxidation or degradation. Detailed characterization was performed on each such sample which are shown below, and if it was seen that further alloying was required, a new sample is prepared from the beginning taking a fresh blend of elemental powders.

Except for sample S3, when samples were exposed to air during the sample prep for XRD measurement, they were stable, without any observable reactions and from the XRD, it was clear that there was no oxidation.

From XRD patterns, the phase evolution could be seen from sample alloyed for 3 hours to the sample alloyed for 30 hours. All these patterns are compared with XRD of initial powder blend taken in a stoichiometric ratio.

In 3 hours alloyed sample, when the sample was taken out for XRD characterization, the sample that got exposed to air started a self-sustaining reaction similar to what was observed in previous cases, i.e., when following a prevalent technique. This was assumed to be happening because of one or both the reasons, i.e. 3 hours of alloying in the presence of stearic acid is not sufficient enough for stearic acid to spread out evenly without reacting with the phases forming at these stages causing the reactions observed, or the presence of high Mn content, when milled to sub-micron scale, is highly reactive which is reacting with the stearic acid and causing oxidation. The XRD pattern of this sample is **shown in Figure 77**.

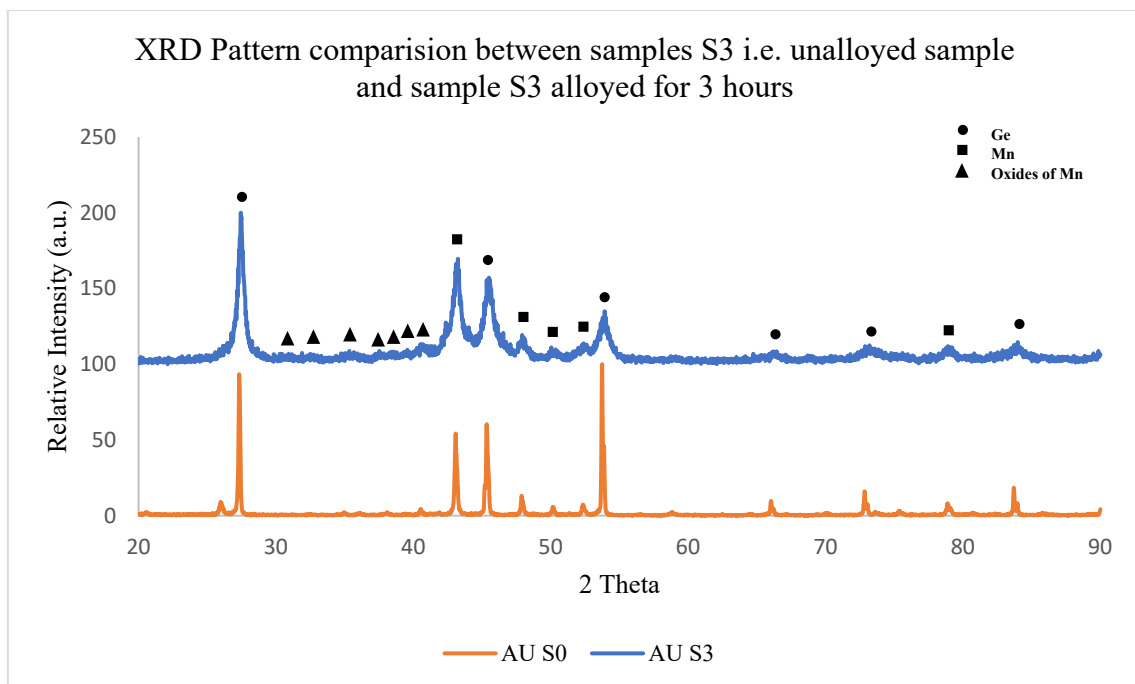


Figure 77 XRD patterns of sample alloyed for 3 hours compared with S0, i.e., just blended sample in stoichiometric ratio

In the sample alloyed continuously for 9 hours, a mixture of phases of Mn_3Ge_5 and $MnGe$ were observed along with small peaks of Ge and Mn. A steep decrease in Ge and Mn peaks was observed compared to samples S0 and S3.

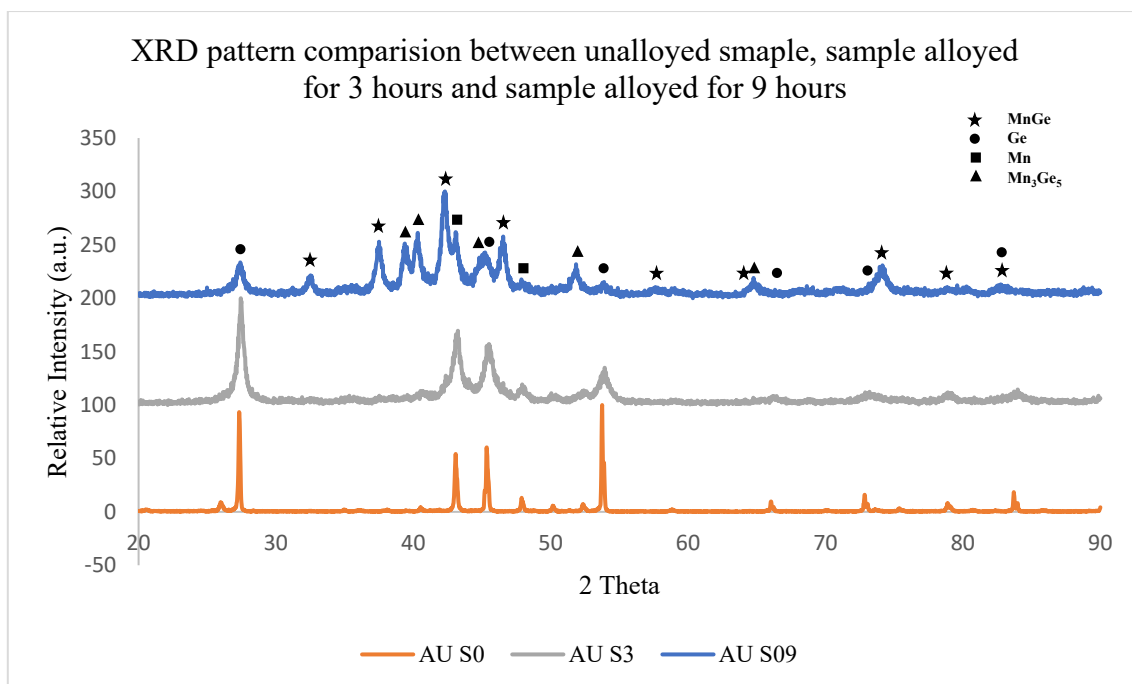


Figure 78 XRD patterns of samples alloyed for 3 hours and 9 hours compared with S0, i.e., just blended sample in stoichiometric ratio

Alloying was continued for different times, i.e., 12 hours, 15 hours, 18 hours, 24 hours, 30 hours at which a pure MnGe phase was obtained and 36 hours to check the stability of the formed phase.

To observe the phase evolution during the process, all the XRD patterns were stacked one over the other and are **shown in Figures 79 and 80**.

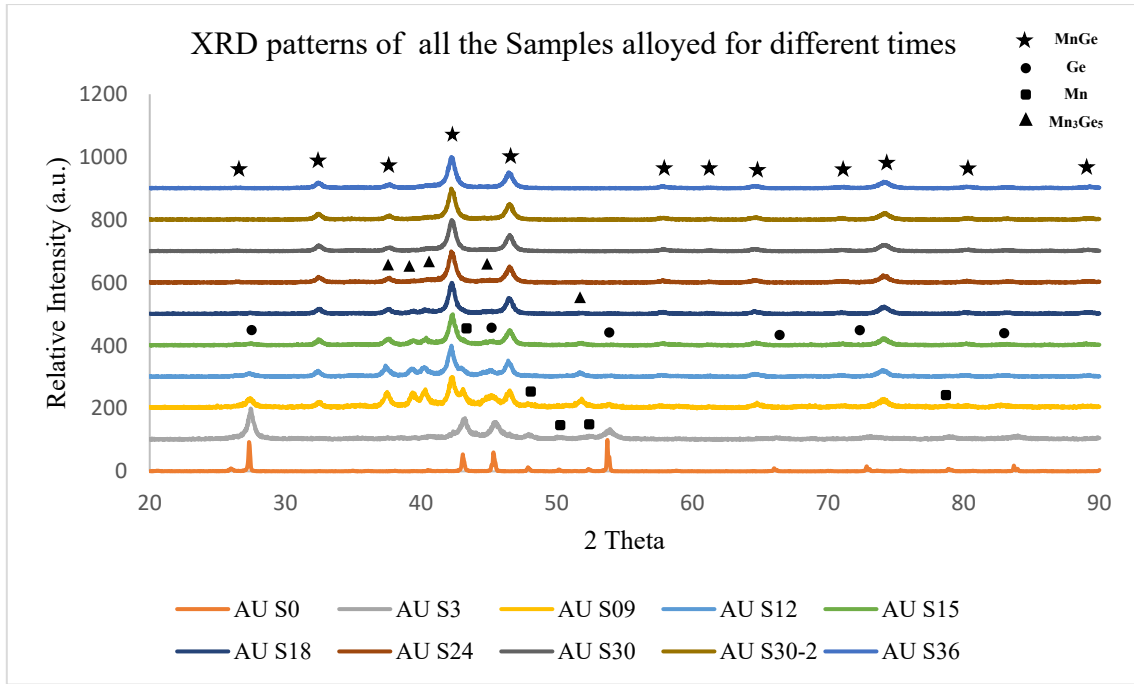


Figure 79 XRD patterns of all the samples obtained at different hours of alloying without the intermittent addition of PCA or removal of the sample

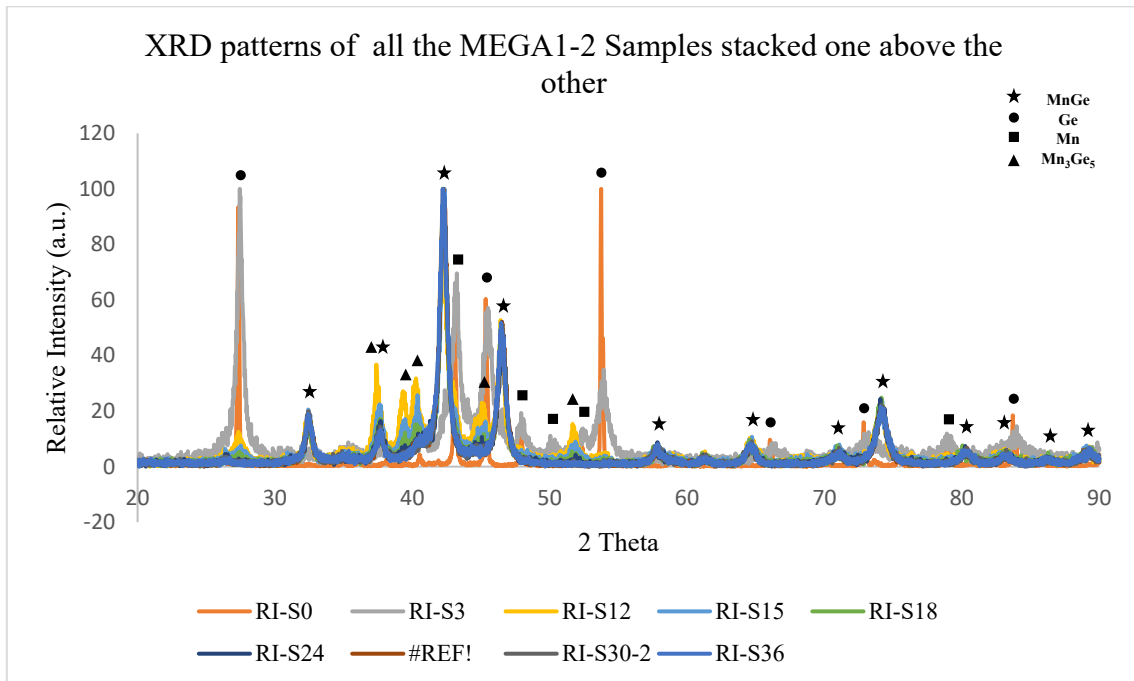


Figure 80 XRD patterns of all the samples obtained at different hours of alloying stacked one over the other

From these patterns, it is noticed that at the early hours of alloying interdiffusion between Mn and Ge peaks started, i.e., both Mn diffusing into Ge lattice and Ge diffusing into Mn lattice

are happening simultaneously. Along with this, compressive strain is being induced on the particles resulting in a decrease in lattice parameters which effectively increases the 2- θ value shifting the peaks of both Mn and Ge towards the right as **shown in Figures 81 and 82**.

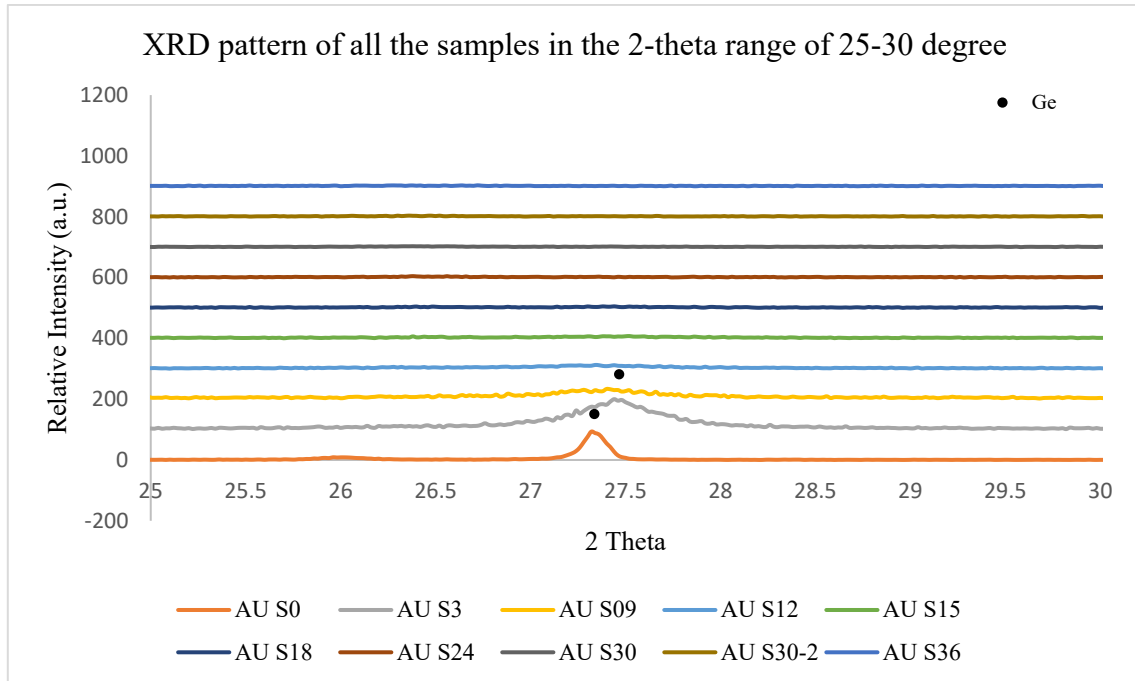


Figure 81 XRD of all the samples in the 2- θ range of 25-30 degree showing shift in Ge peak

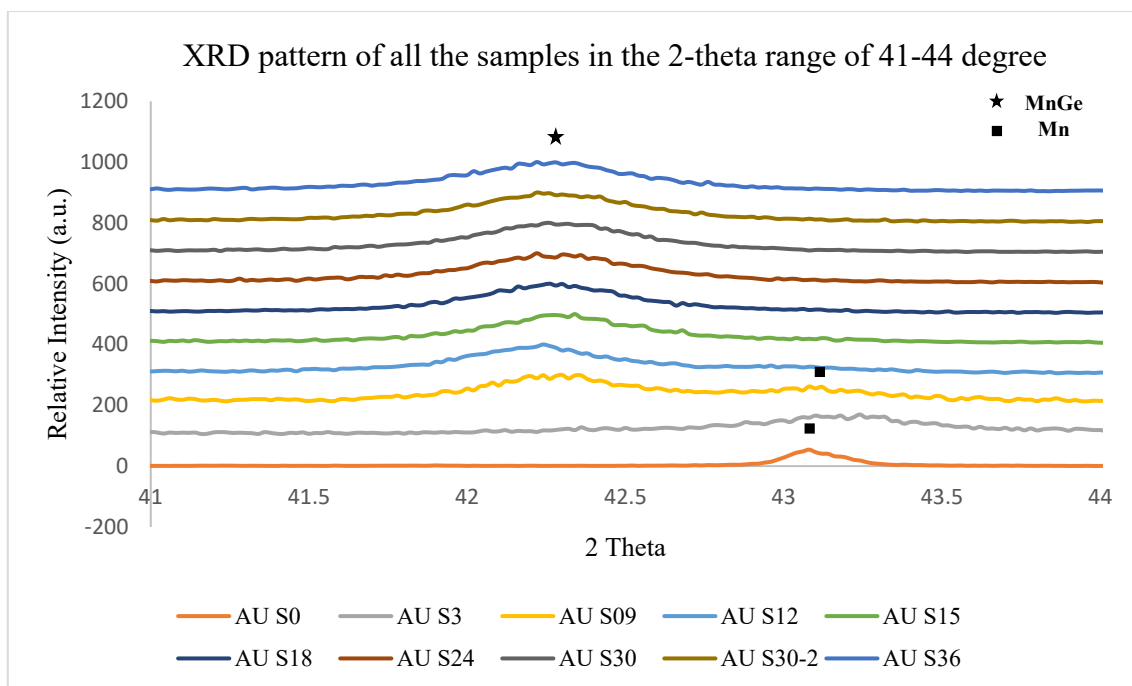


Figure 82 XRD of all the samples in the 2- θ range of 41-44 ° showing shift in Mn peak

From these patterns, it can be seen that the highest peak of Ge at 2- θ of $\sim 27.4^\circ$ is shifting towards the right and a similar pattern is observed in the highest peak of Mn, i.e., the peak at 2- θ of $\sim 43.1^\circ$. This shift towards the right was observed to be decreasing and moving left instead after 9 hours of alloying after which the Mn_3Ge_5 phase started decreasing. This interdiffusion resulted in the formation of two phases MnGe where Ge is going into Mn and Mn_3Ge_5 where Mn is going into Ge.

A steep increase in MnGe peaks and a decrease in Ge and Mn peaks alongside high-intensity Mn_3Ge_5 peaks were observed in the sample alloyed for 9 hours. It is noticeable that the Ge peaks are relatively smaller compared to Mn at 9 hours of alloying which is due to the formation of Ge rich Mn_3Ge_5 phase alongside MnGe.

The peaks of Mn_3Ge_5 phase started going down after alloying for 12 hours. It was noticed that after 12 hours of alloying, the decrease in Mn and Ge peak intensities was almost similar showing the predominance in the formation of MnGe and reduction in Mn_3Ge_5 . This was assumed to be associated with two things, as the amount of Ge decreased compared to Mn before 12 hours due to the formation of germanium rich phases at early stages, the probability of Mn going into Ge is greatly reduced at which point Ge going into Mn is dominated resulting in the formation of MnGe. Also as the alloying time is increased, the temperature inside the vial may reach above 300°C at which the Mn_3Ge_5 phase was reported to be unstable[12].

The increase in MnGe phase peaks was associated with a simultaneous decrease in Mn₃Ge₅ phase, Ge, and Mn peaks. At 18 hours of alloying, the elemental Mn and Ge peaks were barely visible. After 30 hours of alloying, the peaks present were only of pure MnGe phase which is shown in **Figure 83**.

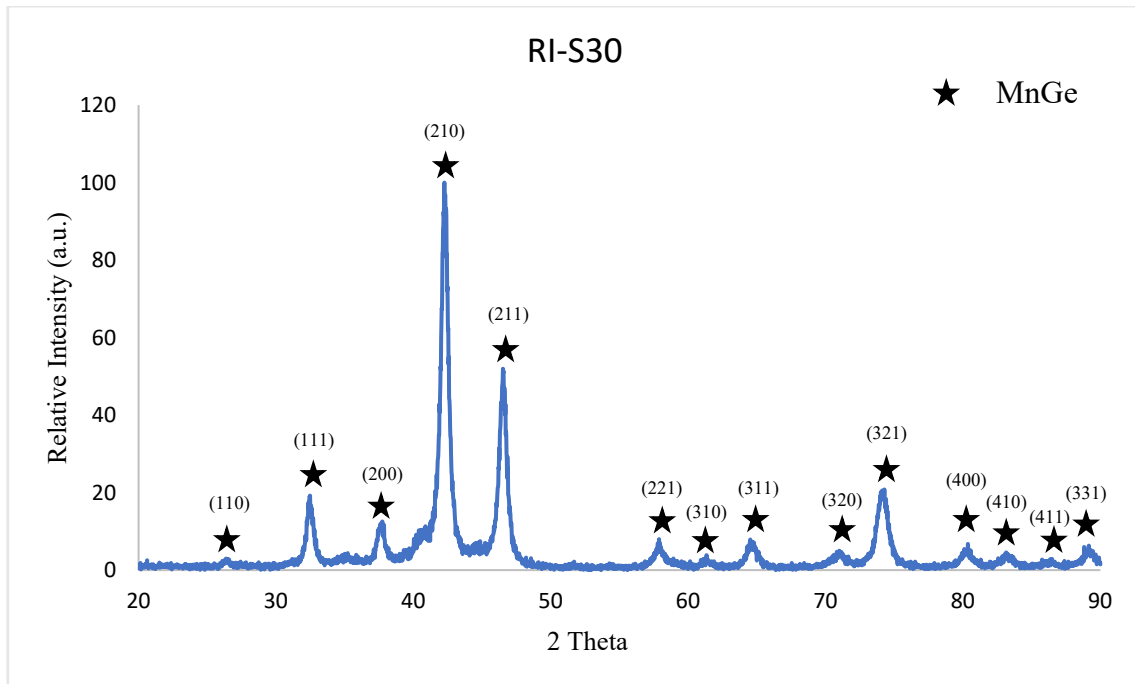


Figure 83 XRD pattern of sample alloyed for 30 hours continuously with MnGe peaks indexed.

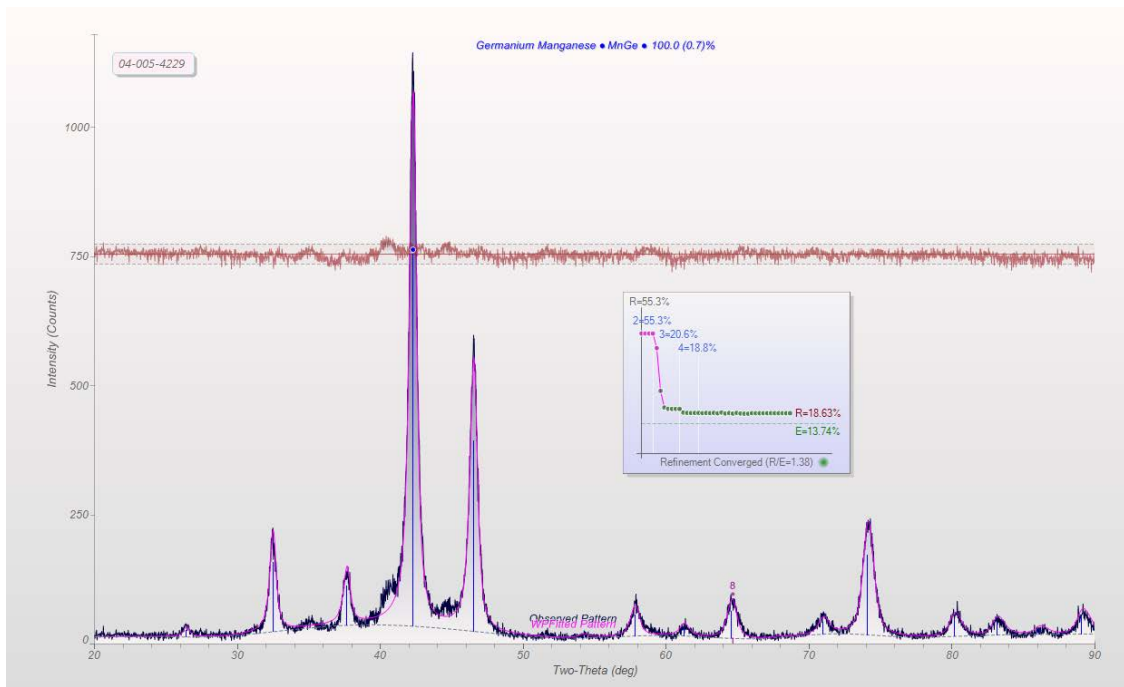


Figure 84 XRD pattern of sample alloyed for 30 hours continuously, analyzed in JADE 2016 software package showing 100% MnGe phase

At 30 hours of alloying time, the sample composition was confirmed to be of single phase MnGe from the XRD pattern analysis performed using JADE 2016 software package as shown above in **Figure 84**.

To check the reproducibility, a new sample was prepared and alloyed for 30 hours, and we were able to obtain pure MnGe phase confirming the reproducibility. The XRD of 30 hours alloyed sample prepared the second time is shown below and is compared with the previous 30 hours alloyed sample. The XRD patterns of both the samples look alike which is shown below.

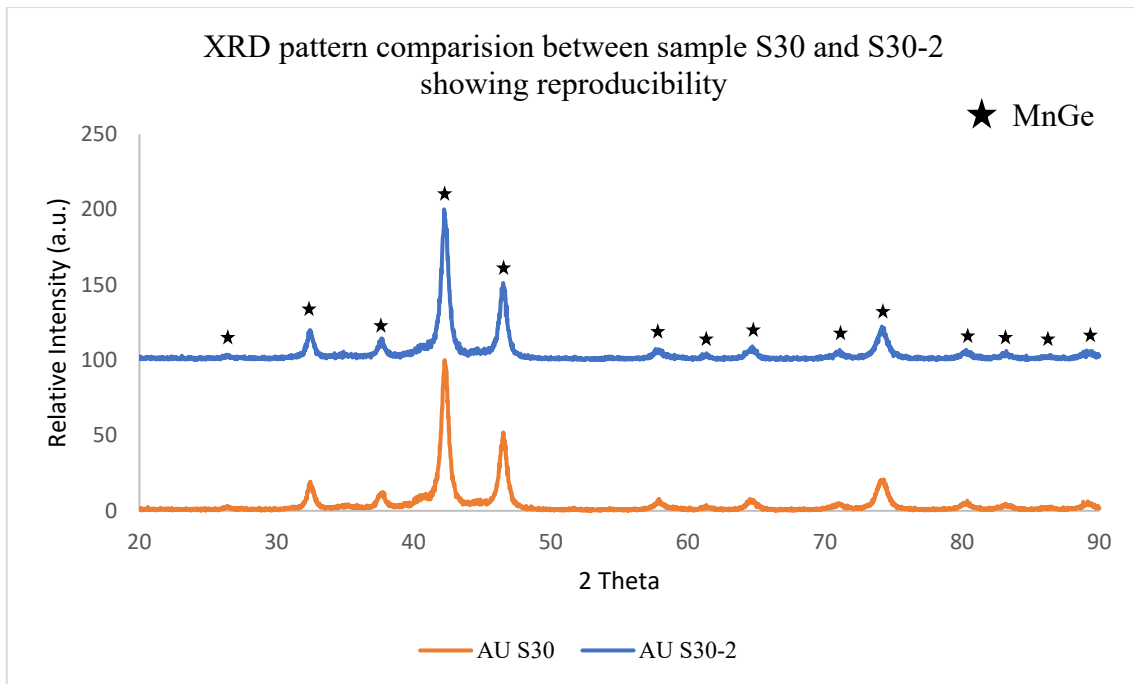


Figure 85 XRD patterns of Samples obtained from two different runs after 30 hours of alloying

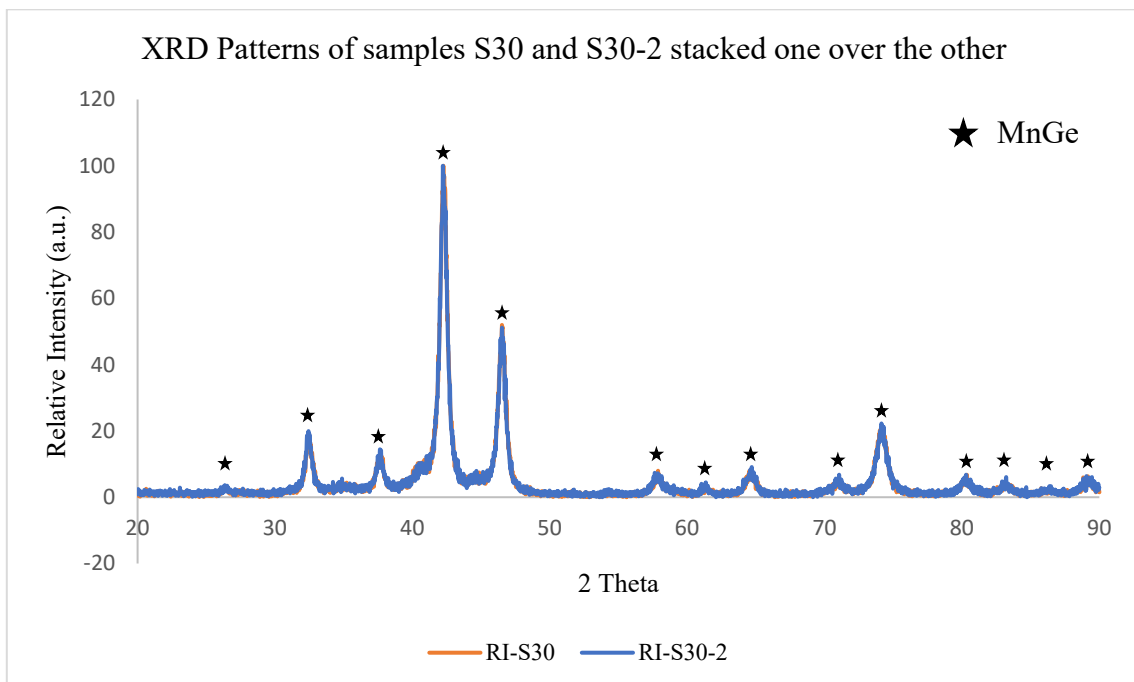


Figure 86 XRD patterns of Samples obtained from two different runs after 30 hours of alloying stacked one over the other to show similarity

Although pure MnGe phase was obtained at 30 hours of alloying, an attempt was made to check evolution on further increasing the alloying time to 36 hours. The X-ray characterization of this sample revealed that the phase is stable even after increasing the alloying time by 6 hours.

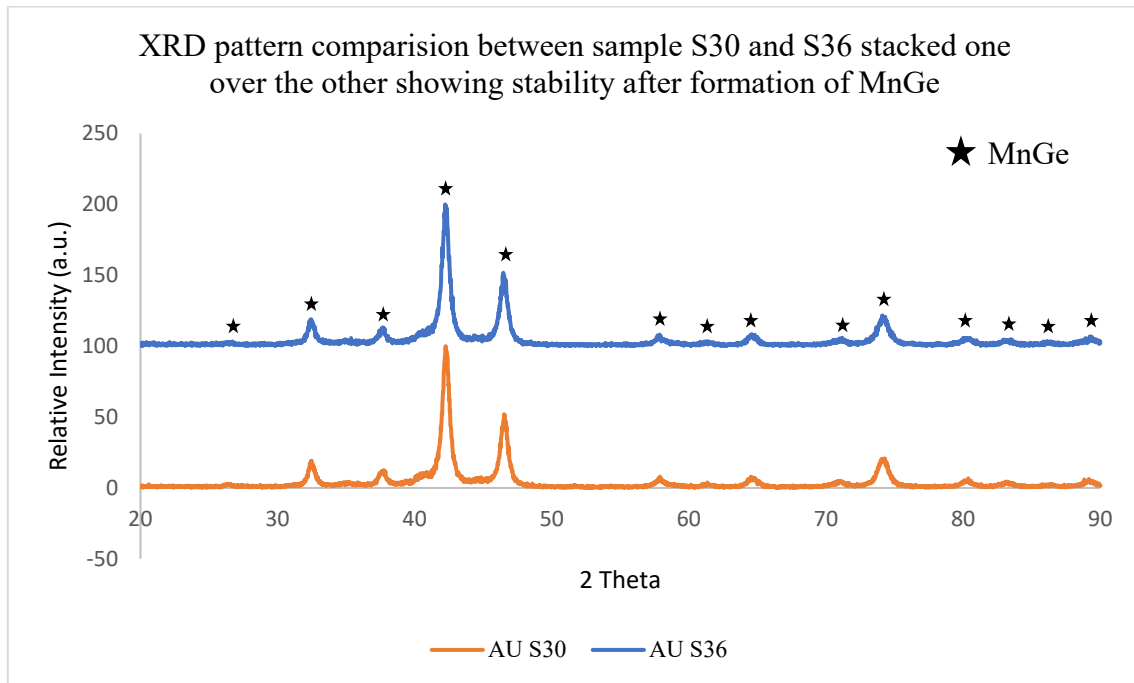


Figure 87 XRD pattern comparison between sample S30 and S36

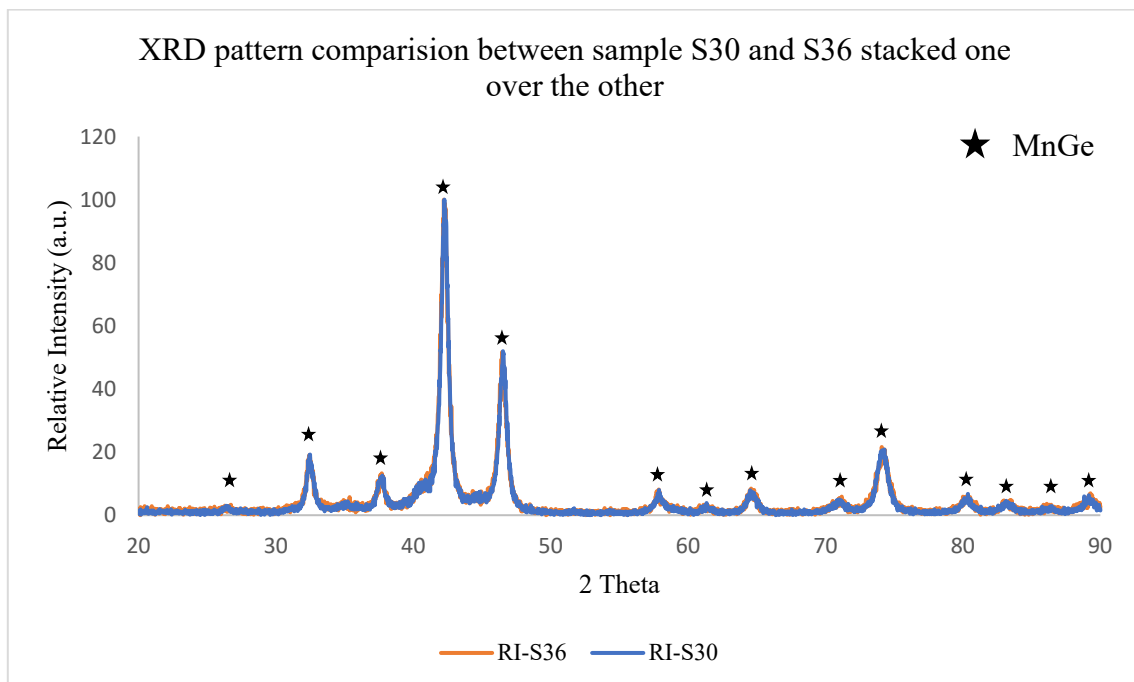


Figure 88 XRD pattern comparison between sample S30 and S36 stacked one over the other to show stability

Lattice parameters of the MnGe phase obtained after 30 hours of alloying were calculated from the XRD pattern using Cohen's method, i.e., least squares method. The peak locations were obtained using ORIGIN PRO software package with Pseudo Voigt 2 and Lorentz curve fitting functions. The lattice parameters are summarized in **Table 24**.

Table 15 Lattice parameter calculation of the obtained sample using Cohen's method

2 Theta	h	k	l	a
32.482	1	1	1	4.774400266
37.64878	2	0	0	4.778483156
42.27843	2	1	0	4.780063134
46.52638	2	1	1	4.781282859
57.89338	2	2	1	4.778555505
64.62952	3	1	1	4.783089627
71.01097	3	2	0	4.786038442
74.14748	3	2	1	4.784946332
80.26246	4	0	0	4.784390572
83.19699	4	1	0	4.787781456
89.19544	3	3	1	4.786073477

A slight shift/decrease in lattice parameter was observed from those reported previously. Lattice parameter correction was performed by analytical approach using the following equations **shown below** which is explain in the following book[58]

$$\begin{aligned}\sum \alpha \sin^2 \theta &= A \sum \alpha^2 + C \sum \alpha \delta \\ \sum \delta \sin^2 \theta &= A \sum \alpha \delta + C \sum \delta^2\end{aligned}$$

With, $\alpha = h^2 + k^2 + l^2$, $\delta = 10 \sin^2 2\theta$, $A = \frac{\lambda^2}{4a_0^2}$, $C = \frac{D}{10}$

Where λ was the average wavelength of both $K\alpha_1$ and $K\alpha_2$ radiations and 2θ is the corresponding value at each peak, a_0 is the corrected lattice parameter.

The corrected lattice parameter obtained was, $a_0 = 4.79738 \text{ \AA}$ which is much closer to the previously reported values i.e. $a = 4.795 \text{ \AA}$ in PDF # 00-041-1149 and $a = 4.7925 \text{ \AA}$ in PDF # 01-081-9919

A detailed SEM and EDAX analysis were performed on the obtained MnGe phase, i.e., samples obtained after alloying for 30 hours and 36 hours, and the results are shown in Figures 89, 90 and 91.

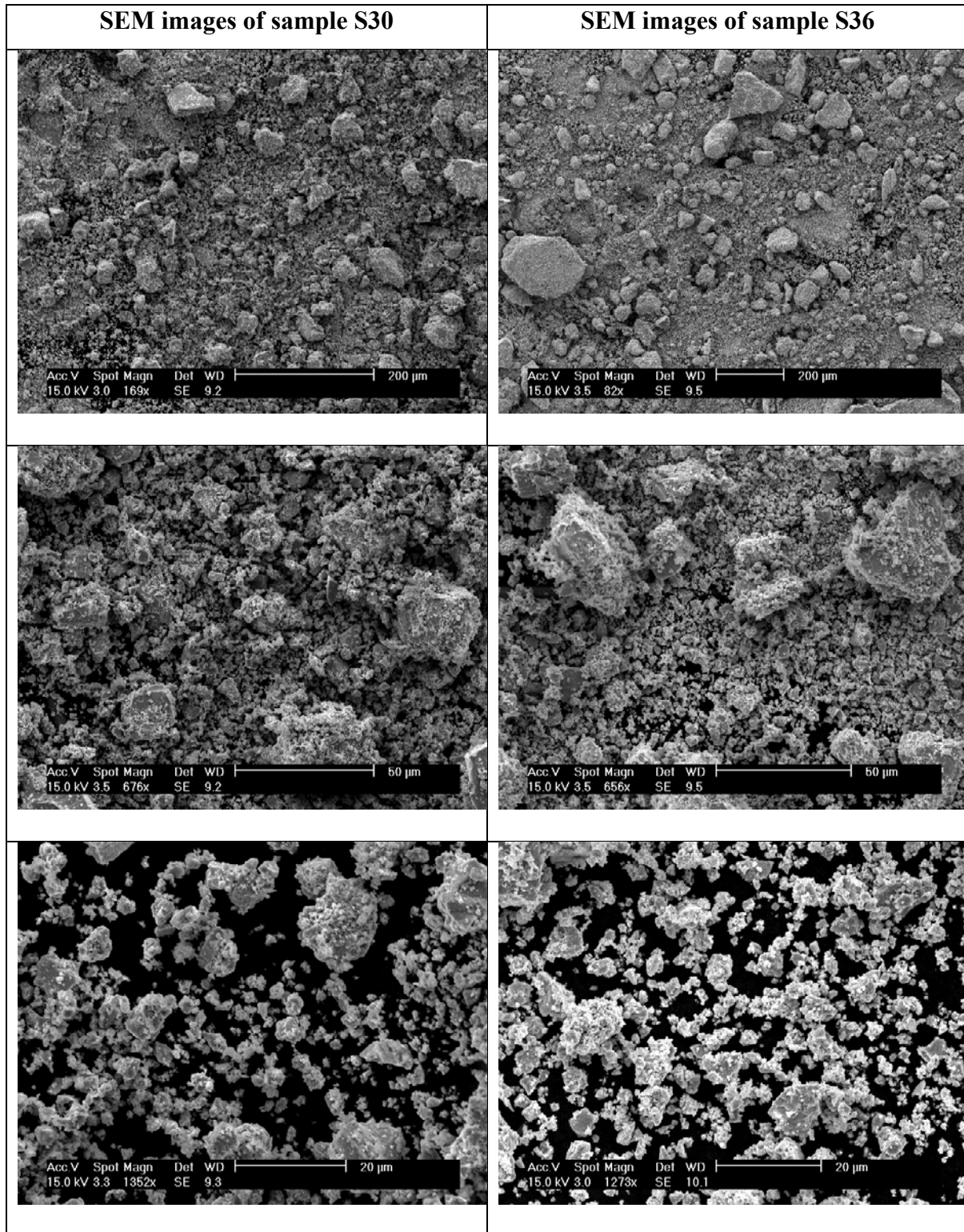


Figure 89 SEM images of sample alloyed for 30 hours are shown on the left and those of sample alloyed for 36 hours are shown on the right

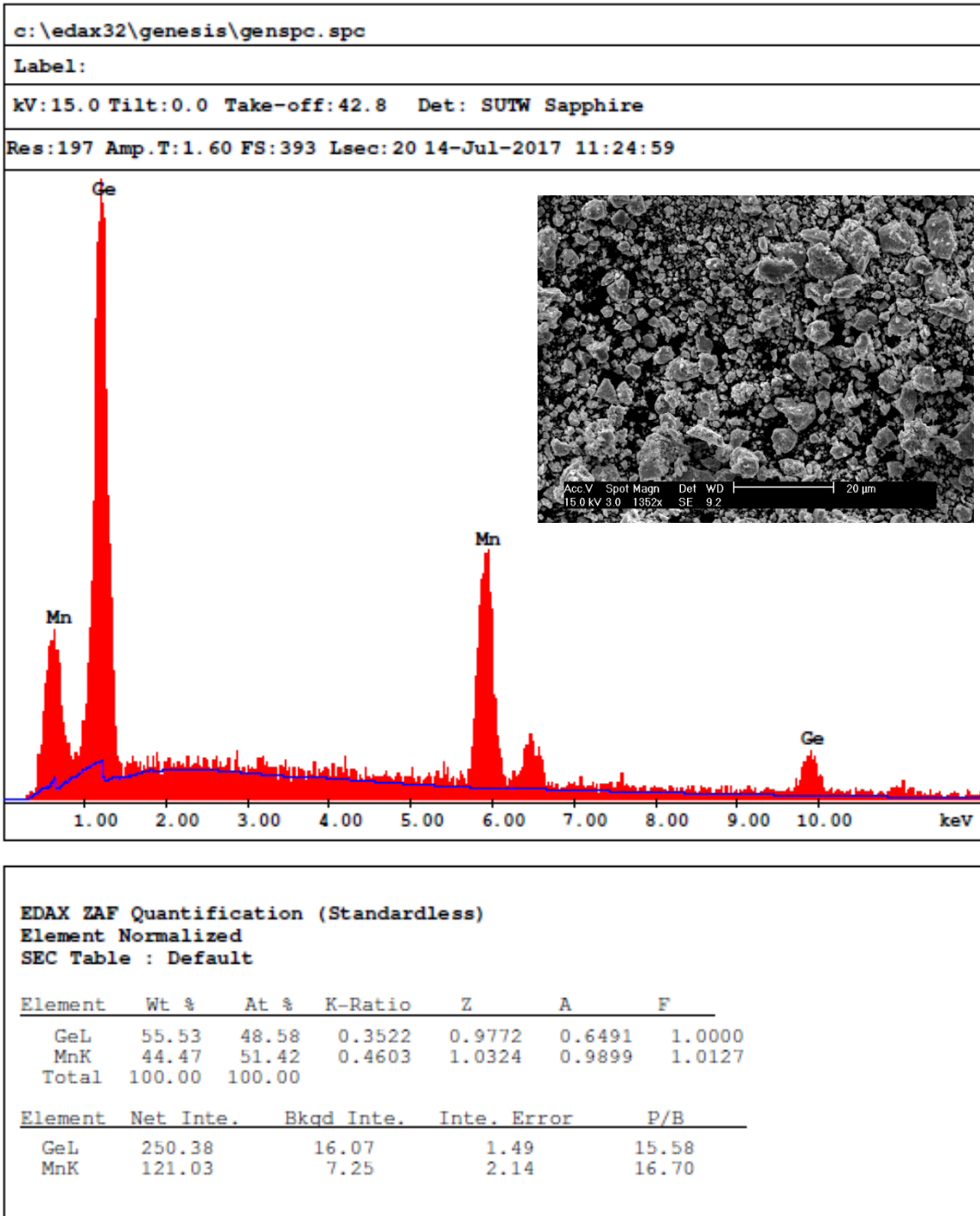


Figure 90 EDAX analysis of the sample S30 and the inset shows the corresponding image of the sample at 20 µm /1352x magnification

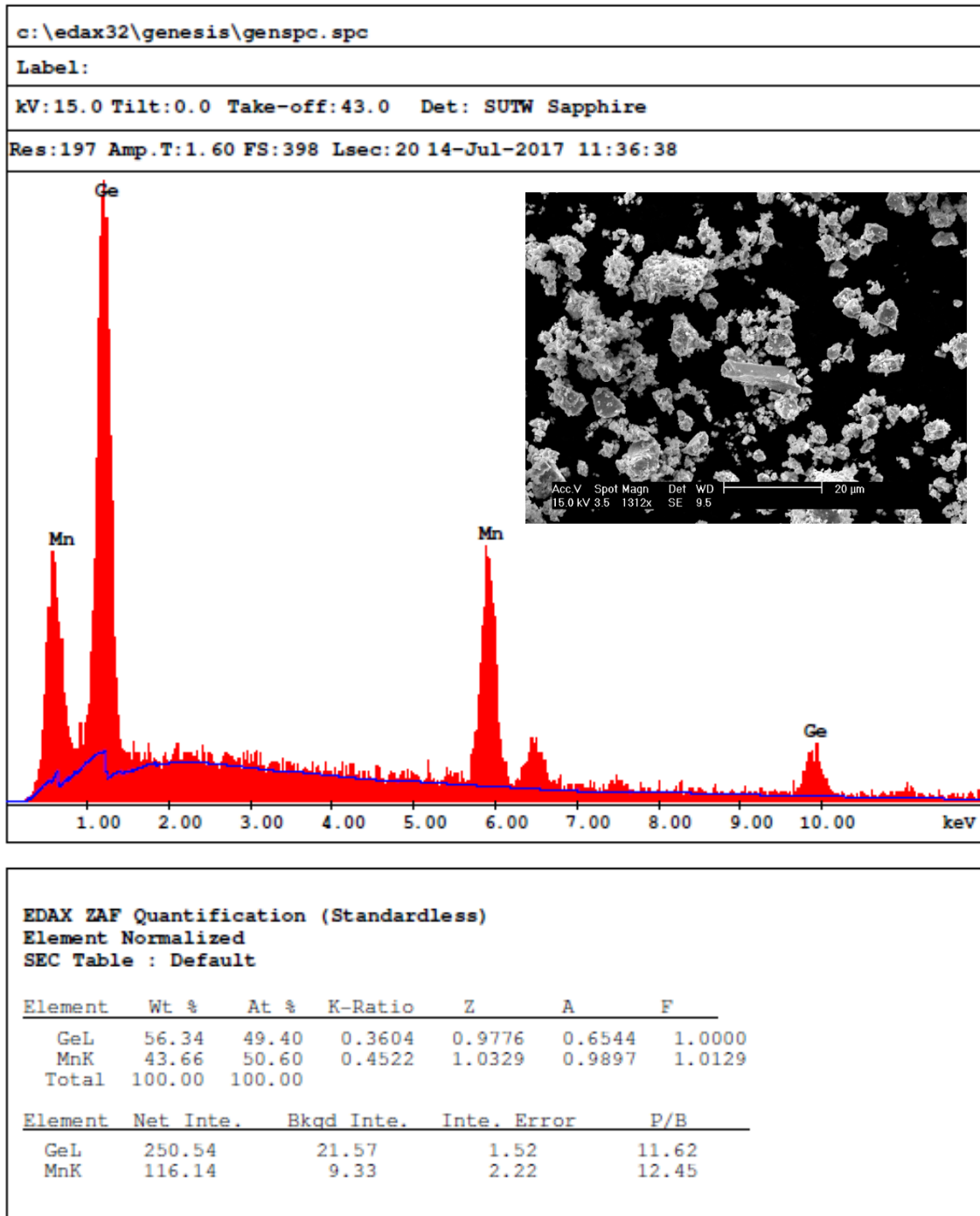


Figure 91 EDAX analysis of the sample alloyed for 36 hours and the inset shows corresponding image at 20 µm /1312x magnification

From the EDAX analysis performed on samples alloyed for 30 hours and 36 hours, it was noticed that the atomic ratios of Ge and Mn were close to 50:50 in both cases with confirms the presence of single phase MnGe and its homogeneity.

The particle size and distribution analysis were performed on multiple images obtained from SEM at various magnifications using Image-J software package and Minitab. The maximum particle size of sample S30, i.e., sample alloyed for 30 hours was found to be 10.1163 μm with a minimum of 0.1382 μm . The Size distribution of the particles is **shown in Figure 92** using a histogram.

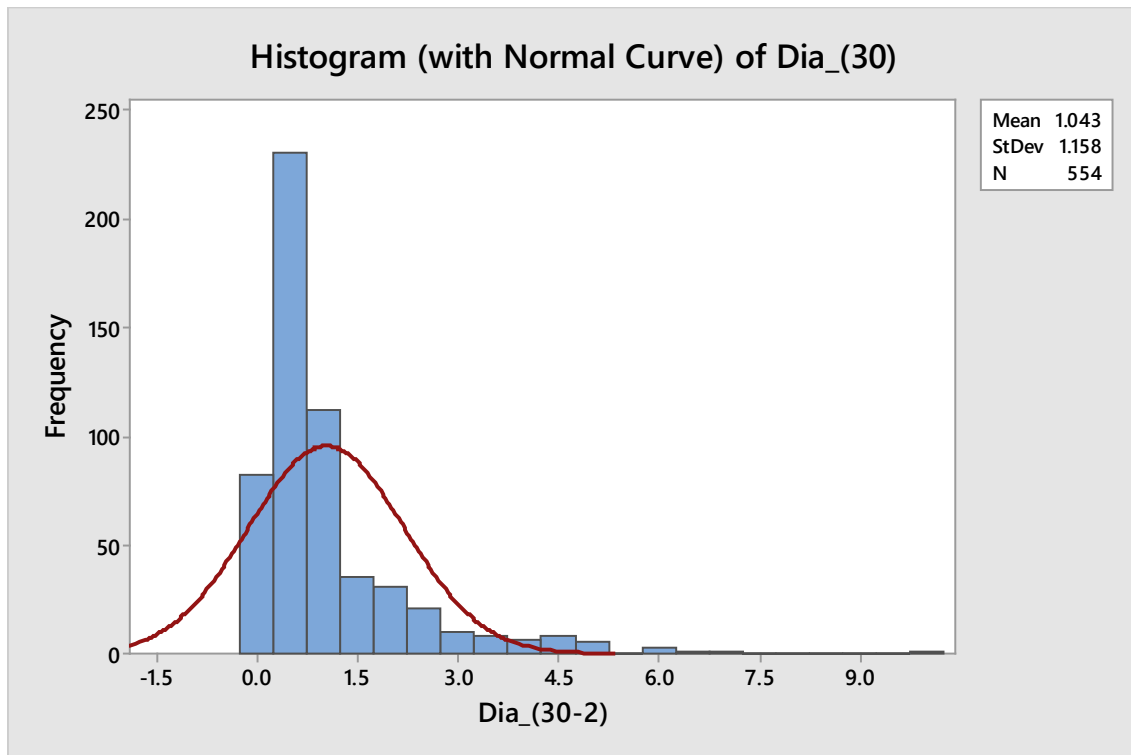


Figure 92 Particle size (μm) distribution in sample alloyed for 30 hours

Similarly, for S36, i.e., for sample alloyed for 36 hours, the maximum particle size was observed to be 12.5253 μm with a minimum of 0.1427 μm as **shown in Figure 93** which are similar to what was observed in sample alloyed for 30 hours.

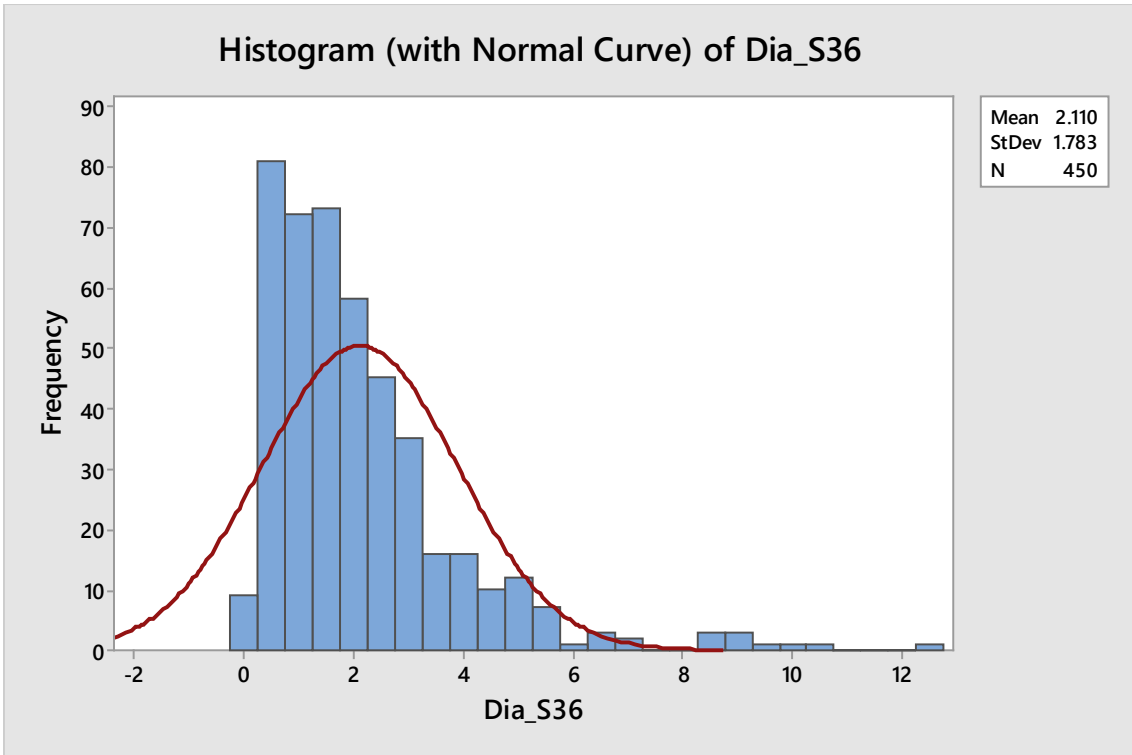


Figure 93 Particle size (μm) distribution in sample alloyed for 36 hours

The magnetic characterization was performed on the samples using Quantum design's vibrating sample magnetometer (VSM). The M vs. H curve, i.e., the change in magnetization with the applied field in the range of -28000 Oe to +28000 Oe for the sample S30 shown in **Figure 94** showed no hysteresis revealing that the sample was paramagnetic at room temperature.

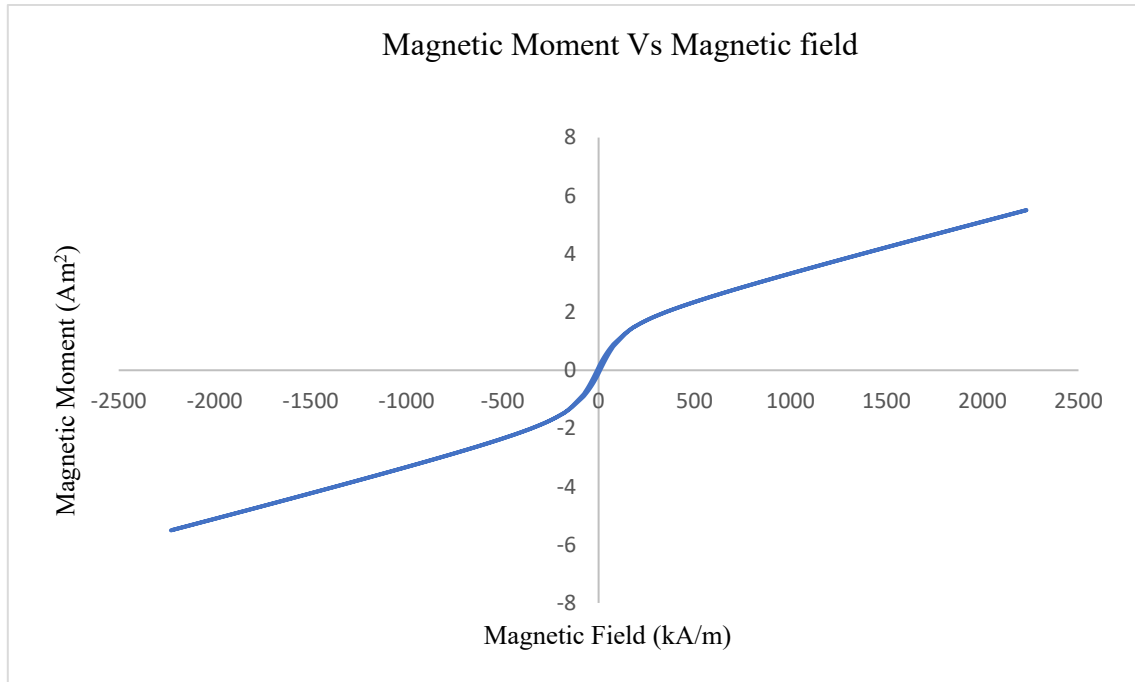


Figure 94 Change in Magnetic moment with applied field in MnGe

The temperature dependence of magnetization in Zero-field cooled and Field cooled conditions was measured for all the samples in the temperature range of 60 K to 360 K which are shown in **Figures 95, 96, 97, 98, 99, 100, 101 and 102**.

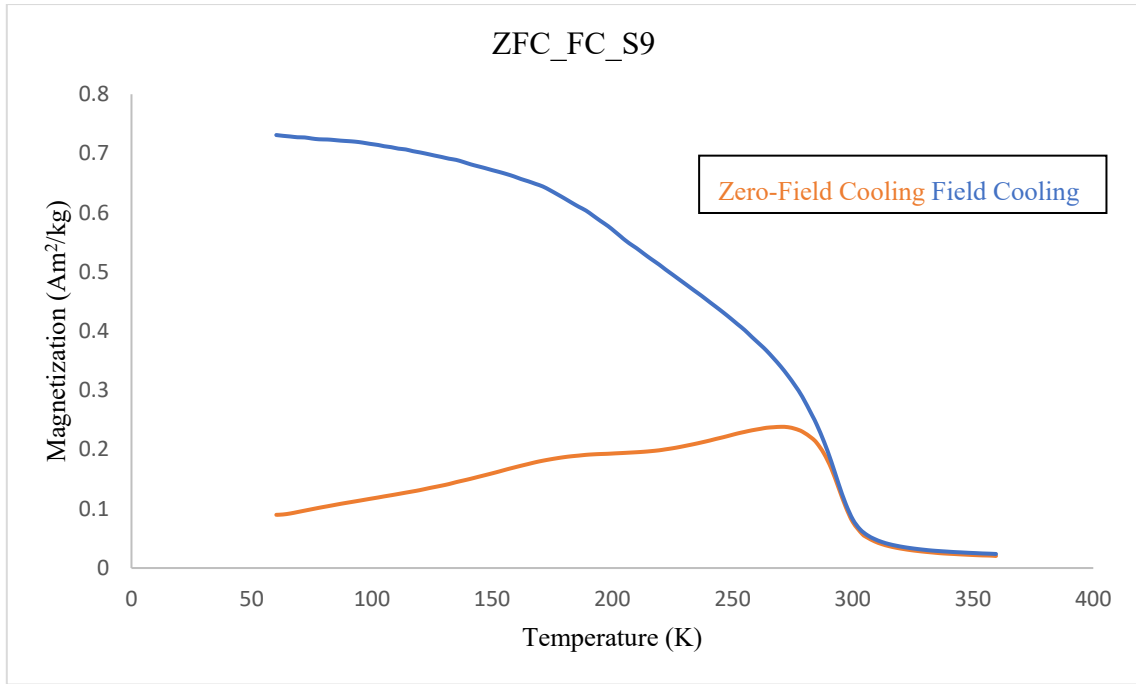


Figure 95 Change in Zero field and field cooled magnetization with temperature in sample alloyed for 9 hours

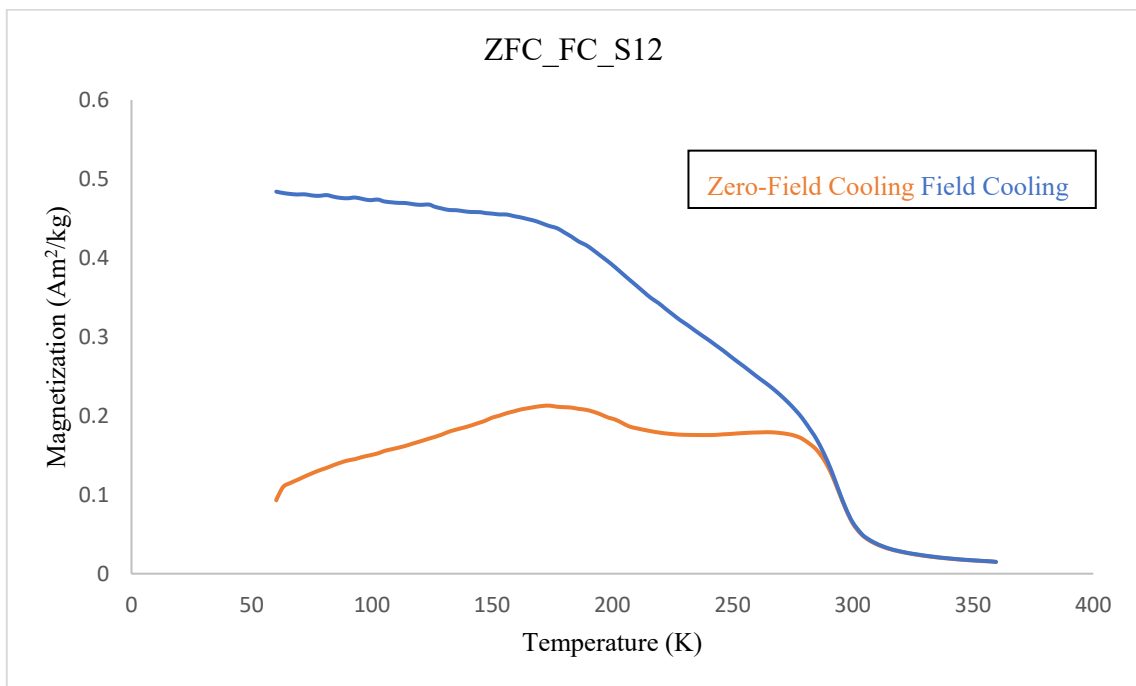


Figure 96 Change in Zero field and field cooled magnetization with temperature in sample alloyed for 12 hours

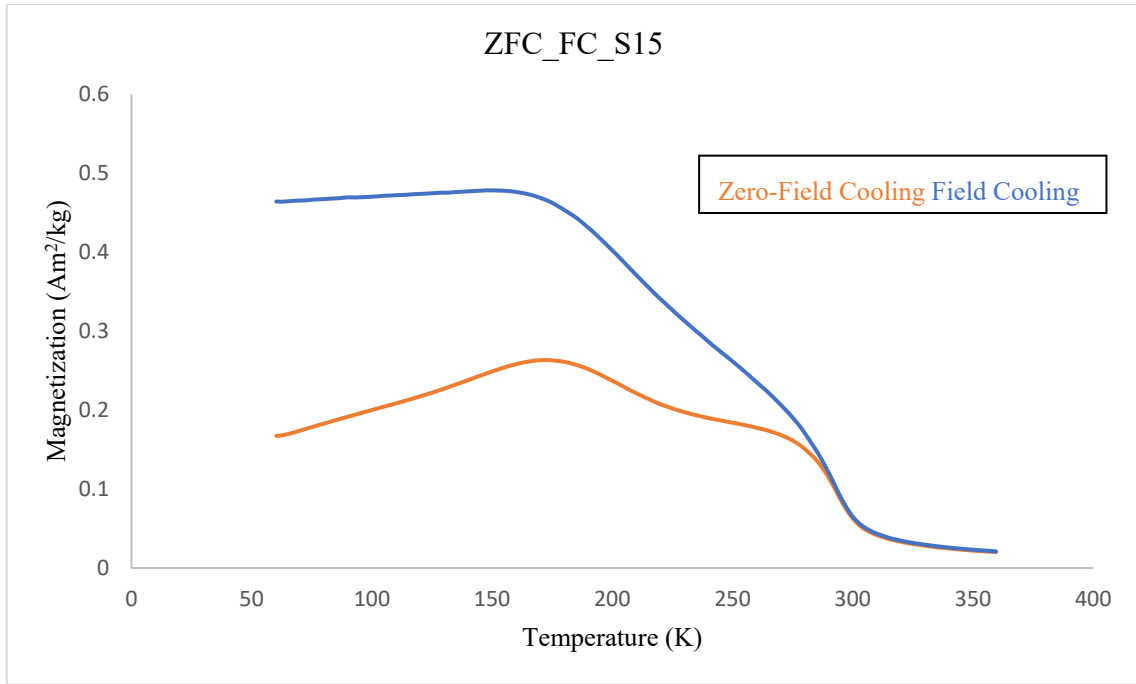


Figure 97 Change in Zero field and field cooled magnetization with temperature in sample alloyed for 15 hours

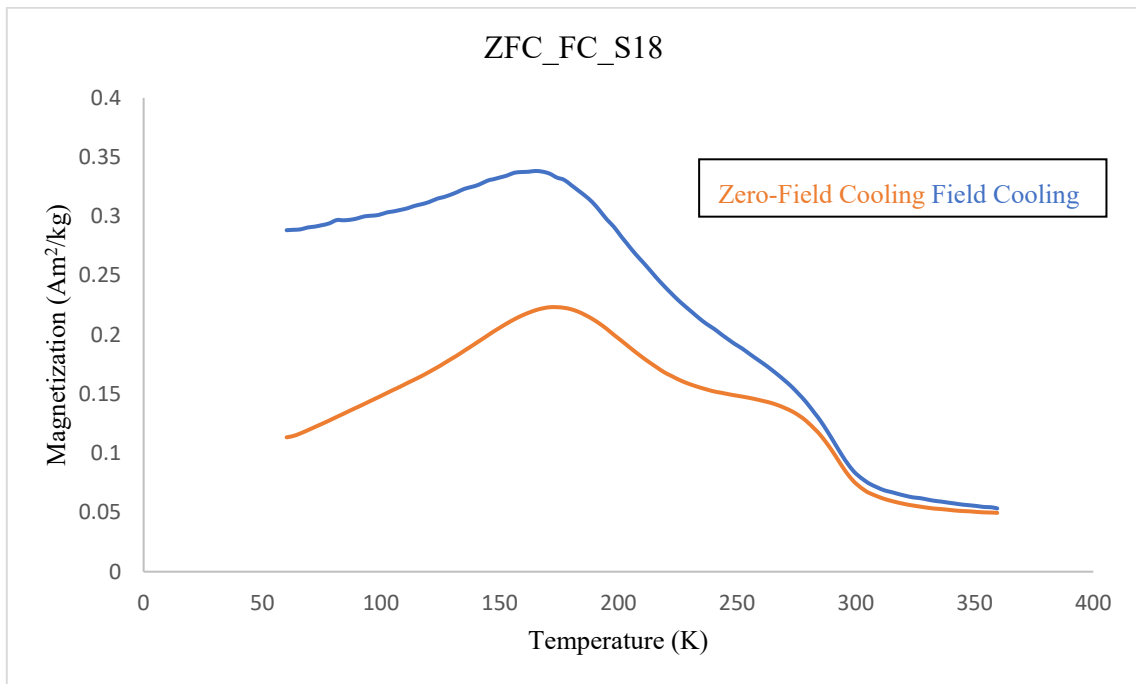


Figure 98 Change in Zero field and field cooled magnetization with temperature in sample alloyed for 18 hours

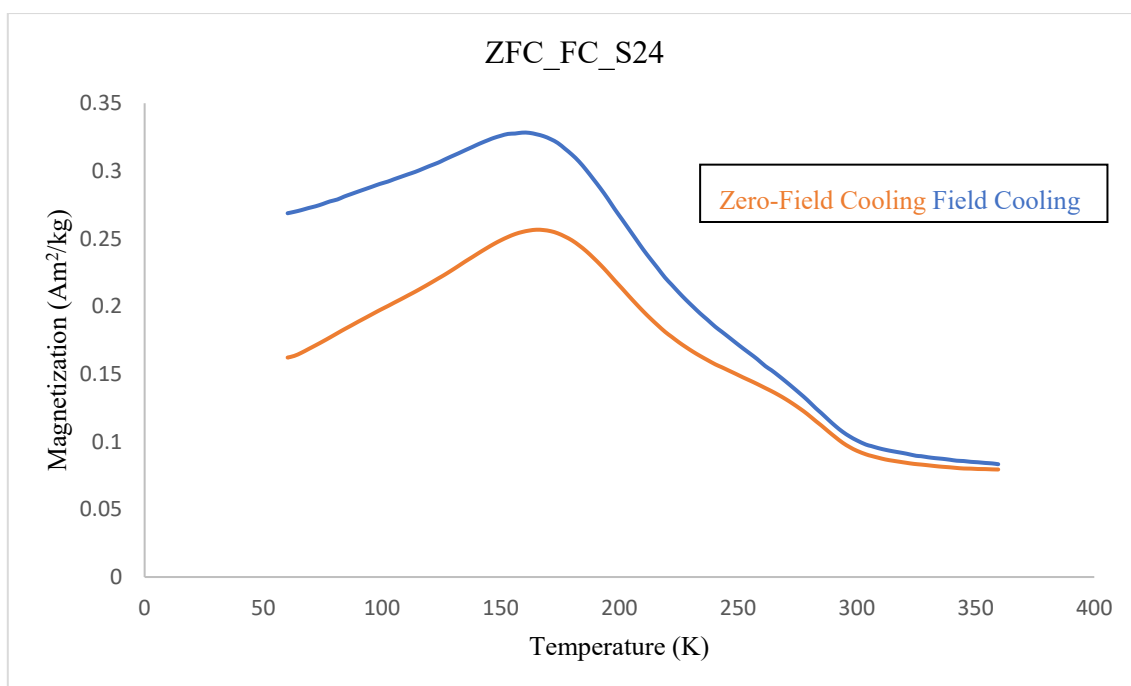


Figure 99 Change in Zero field and field cooled magnetization with temperature in sample alloyed for 24 hours

It was observed that at the early stages, i.e., at 9 hours of alloying, the difference between field cooled, and zero field cooled M vs. T curves was very high which revealed the formation of nanoparticles at the early stages of alloying. Also, there appears to be a drop in the magnetic moment at temperatures close to ~280 K. From the XRD of S9; it was observed that the sample has Mn₃Ge₅ alongside MnGe, Ge, and Mn. It was reported earlier that MnGe was Antiferromagnetic with Neel temperature close to 197 K [23] also it is known that Ge and Mn are diamagnetic and paramagnetic respectively. Hence this drop in the magnetic moment was assumed to be the Curie temperature for the ferromagnetic Mn₃Ge₅ phase present in the early stages. This assumption was confirmed as from the phase evolution upon increasing the alloying time. From XRD it can be noticed that the Mn₃Ge₅ started decreasing from S12, i.e., 12 hours of alloying and a similar pattern is observed in M vs. T ZFC_FC curves. This Curie point decreased gradually, and the almost pure antiferromagnetic MnGe phase was obtained at S30 with Neel temperature close to 170 K, which is shown in **Figures 100 and 101**.

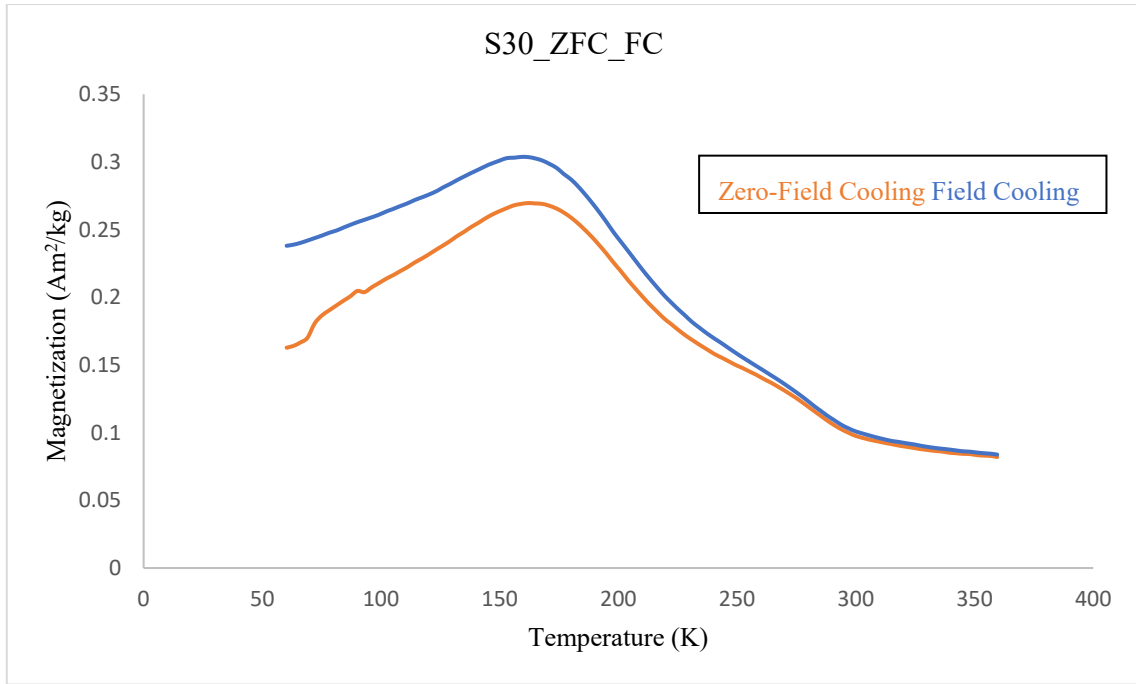


Figure 100 Change in Zero field and field cooled magnetization with temperature in sample alloyed for 30 hours

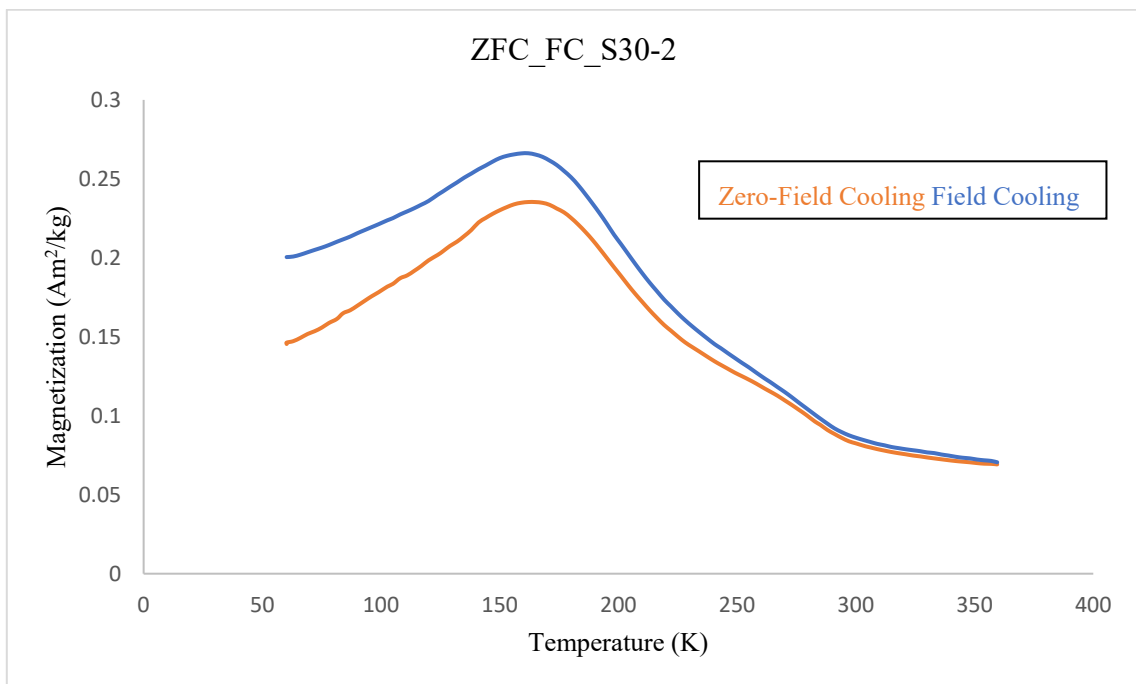


Figure 101 Change in Zero field and field cooled magnetization with temperature in sample alloyed for 30 hours for reproducibility check

Upon further increasing the alloying time to 36 hours, no significant changes were observed in both XRD and M vs. T ZFC_FC curves as shown in Figures 87 and 102 respectively showing the stability of the MnGe phase formed.

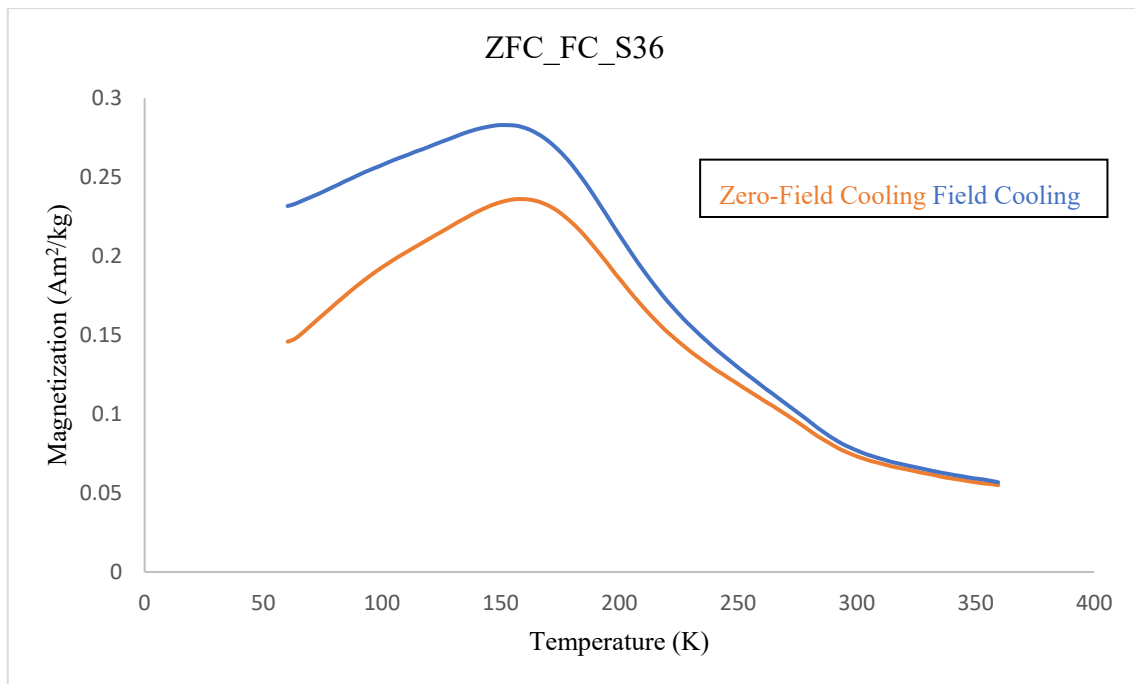


Figure 102 Change in Zero field and field cooled magnetization with temperature in sample alloyed for 36 hours

The magnetization dependence on temperature in the temperature range of 300 to 960 K was also performed on the MnGe phase obtained, i.e., on samples S30 and S36 which are shown in Figures 103 and 104.

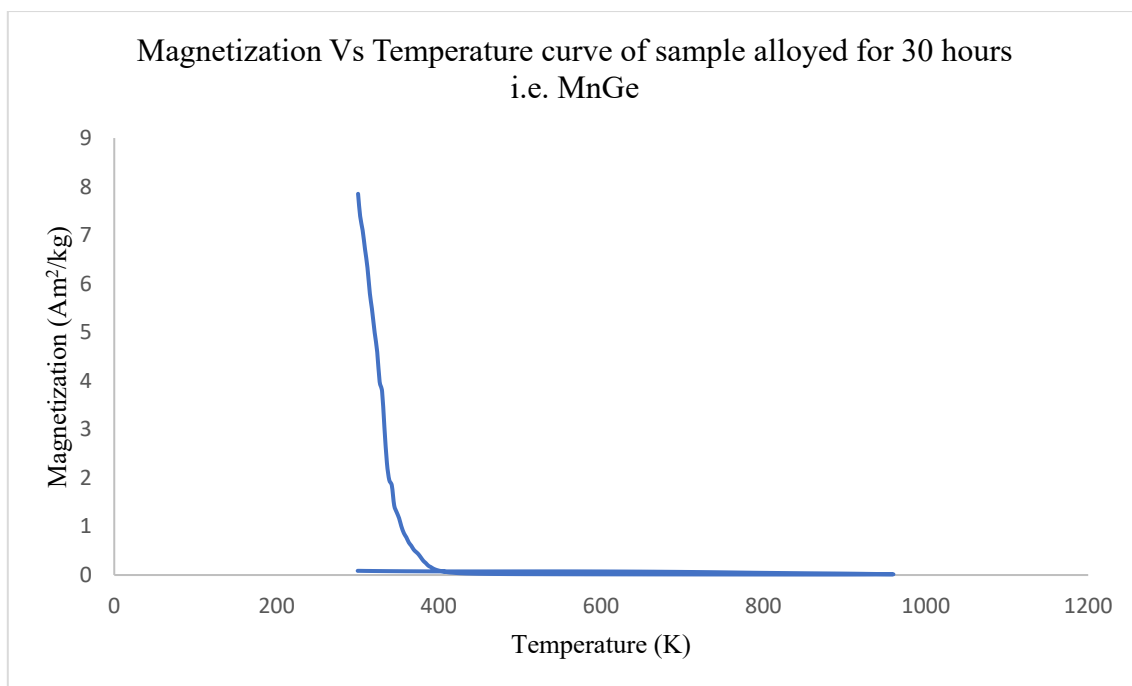


Figure 103 Change in magnetization with temperature in sample alloyed for 30 hours

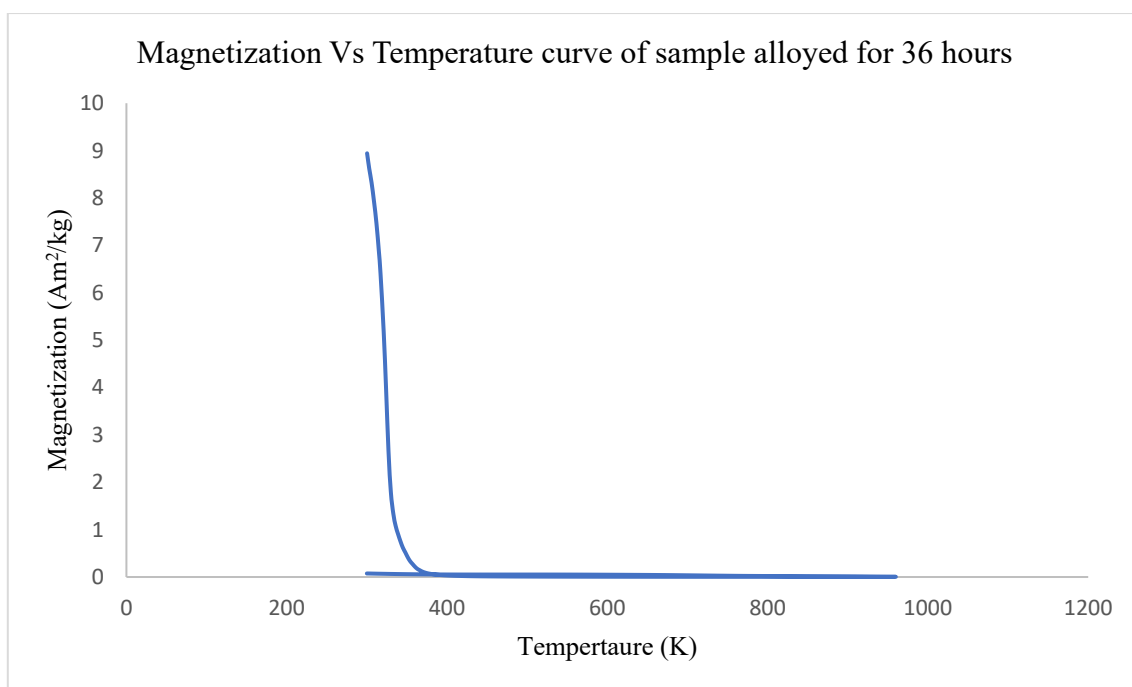


Figure 104 Change in magnetization with temperature in sample alloyed for 36 hours

It was observed that upon increasing the temperature, the sample, i.e., MnGe started dissociating at around ~600 K into possibly Mn₁₁Ge₈ and Ge which are reported to be paramagnetic and diamagnetic respectively at this temperature. This is clearly shown in **Figure 105**.

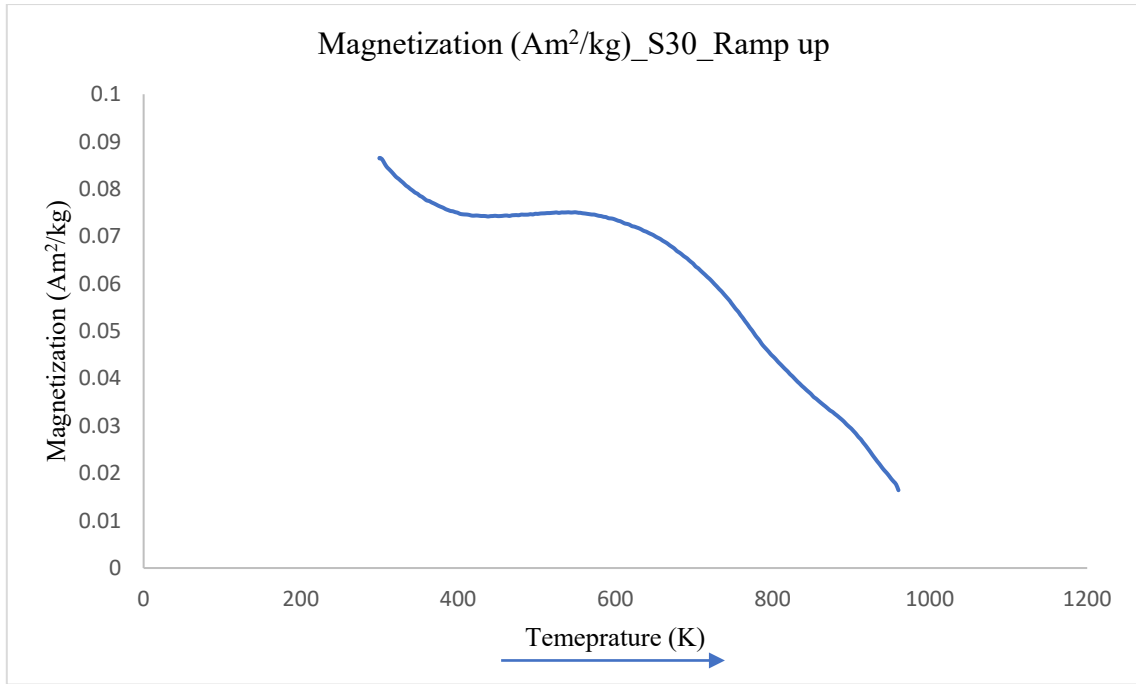


Figure 105 Change in magnetization with an increase in temperature in sample alloyed for 30 hours

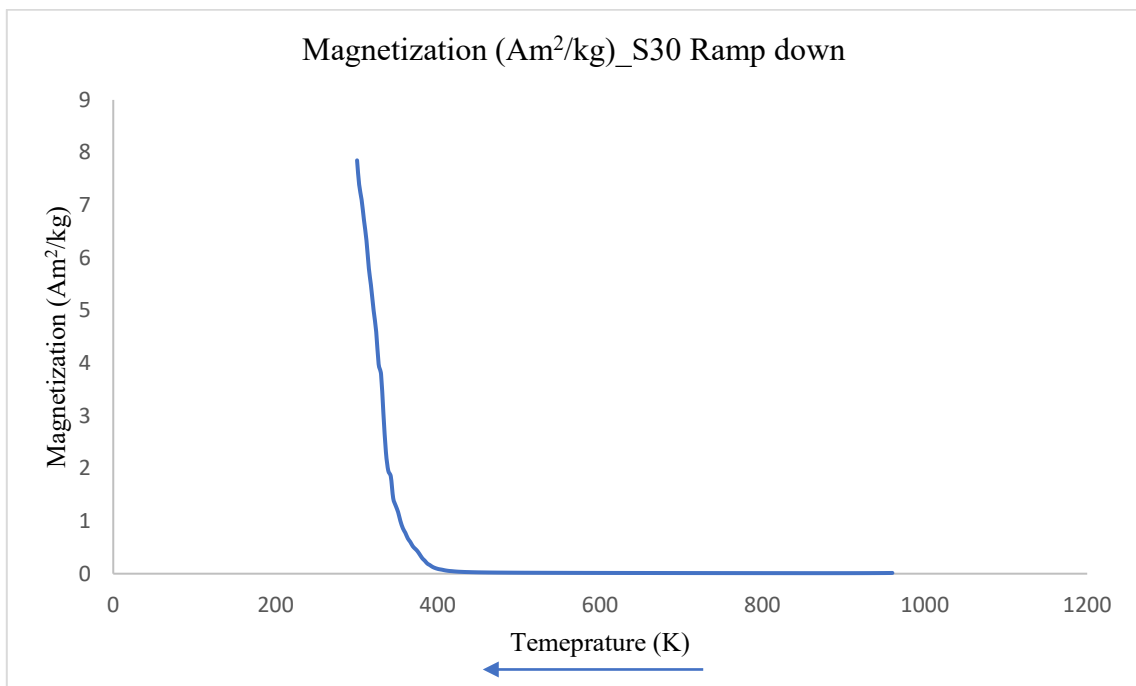


Figure 106 Change in magnetization with decrease in temperature in sample alloyed for 30 hours

The Mn₁₁Ge₈ phase was reported to be behaving as a ferromagnetic material close to room temperature, and this is observed in the Magnetization vs. Temperature curve during cooling the sample back to room temperature which is shown in **Figure 106**.

The huge variation in magnetization value from 0.016 emu/g at 960 K to as high as 7.85 emu/g at 300K shows the change in phase of the sample which changed its behavior from paramagnetic to ferromagnetic at room temperature.

5.1.3. Magnetization of MnGe

Several magnetic properties studies have been performed previously on MnGe, and no standard number was established to provide as a baseline number for verification of the phase purity. To obtain this base value, the magnetization of the phase pure MnGe was studied on multiple S30 samples at 10,000 Oe i.e., 1 Tesla and at room temperature 300 K. The results obtained are summarized in the table below.

Table 16 Table summarising the magnetization values of different MnGe samples measures at 10,000 Oe applied field

Sample and its condition	Moment (emu)	Mass (grams)	Magnetization (emu/g)
MnGe S30 as prepared	0.08	0.03	2.94
MnGe S30 reproduced, as prepared	0.10	0.03	2.91
MnGe S30 after 2 months exposed in air.	0.09	0.03	2.91
MnGe S30 alloyed in Air	0.09	0.04	2.51

The values of Magnetization for the sample alloyed for 30 hours in Argon was found to be between 2.94 and 2.91 emu/g. From the magnetization measurements, the sample appears to be stable even after 2 months stored in the air as it has similar values of magnetization even after 2 months, i.e., ~2.91 emu/g at 10000 Oe.

5.1.4. Synthesis Process Comparison:

Comparing the MnGe synthesized at room temperature and ambient pressure with those synthesized using high-pressure synthesis technique by H. Takizawa et al. [14] and by A. V. Tsvyashchenko et al. [29] as well as by thin film deposition technique by Adam S. Ahmed et

al. [43] reveals that the antiferromagnetic behavior observed in the samples prepared using mechanical alloying technique is in good agreement with those reported previously although there is slight variation in the Neel temperature observed. The Neel temperature of the sample synthesised using mechanical alloying is calculated to be at ~ 162 K in an applied field of 100 Oe whereas for those synthesised by high pressure and temperature synthesis were reported to be at 197 K [14] and 175 K [29] and for the one prepared by thin film deposition technique, it was reported to be close to 170 K [43].

The current synthesis technique is an easily scalable processing technique with high yield and has less number of steps for the preparation/synthesis of the materials whereas the high-pressure synthesis technique involves multi-step process where the pellets are to be prepared prior to the actual processing, then these pellets are subjected to high pressures and temperatures which are close to the degradation temperatures of Ge. In case of the thin-film deposition technique, a random and uncontrolled development of metallic nanoclusters were observed which resulted in poor reproducibility. In the current work, along with the study of phase evolution investigation was performed to reduce the time required for the synthesis process further increasing the efficiency of the process compared to the one's explained above. These investigations and their results are explained in detail in the process optimization section below.

5.2. Process Optimization for synthesis of MnGe

Once the phase pure MnGe was obtained using the Ideal processing parameters and handling techniques, attempts were made to reduce the time required for preparation of sample by varying few processing parameters or the powder handling techniques. Each of these attempts and their results are explained in detail below.

5.2.1. Using ideal technique with intermediate addition of stearic acid

In the attempt of synthesizing S30 directly without intermittent addition of PCA, it was observed that the balls were getting welded or seized due to the decrease in effectiveness of PCA which could be the reason for requiring 30 hours of alloying. To compensate for that, an attempt was made to add PCA at the intermediate stages where welding was noticed. It was noticed that in the 30 hours alloyed sample, the balls were getting welded after 15 hours and most significantly at 24 hours of alloying. Hence PCA was added after 24 hours of alloying. A small amount of sample was taken out at this point for X-ray characterization. The XRD pattern

comparison between samples S24 synthesized in this third attempt and the second attempt is shown below in **Figures 107 and 108**. The sample handling was performed inside the glove box except for when it was characterized using a powder X-ray diffractometer where the sample had to be mounted on a glass slide in air.

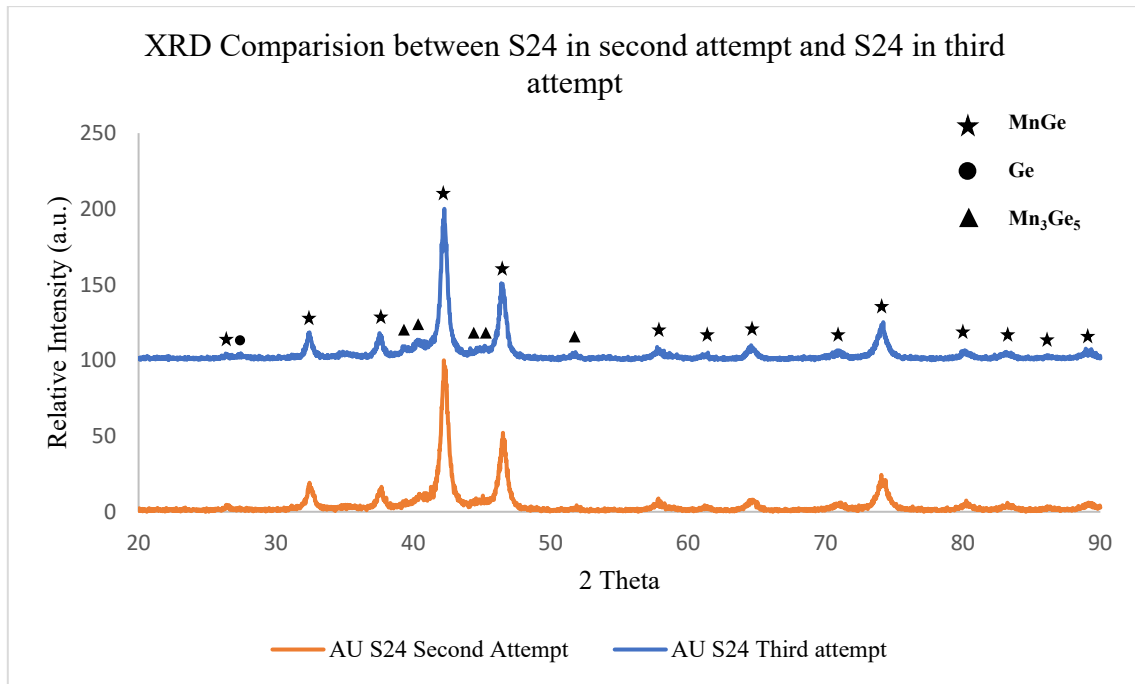


Figure 107 XRD patterns comparison between 24 hour alloyed samples using different alloying techniques

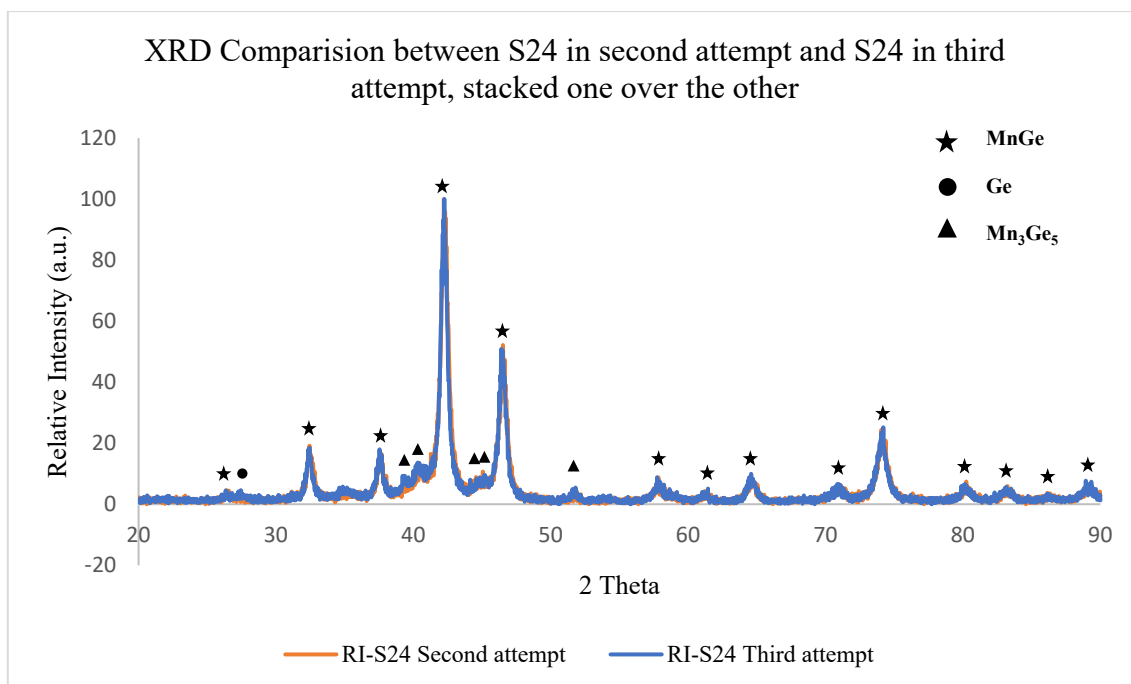


Figure 108 XRD patterns of 24 hour alloyed samples stacked one over the other

No drastic reactions were observed in this case, and hence the sample was kept back in the vial to maintain a constant ball to powder ratio. The alloying was continued for 6 more hours to obtain sample S30, i.e., 30 hours alloyed sample. The vial was opened inside the glove box, and a small amount of sample was taken out in a glass vial for XRD. From this sample, when a small amount of it was poured on a glass slide during sample preparation for XRD, it started a self-sustained reaction similar to what was observed in the previous case. The sample inside the glass vial appeared stable. The glass vial was left aside open for ~2 minutes allowing the air to flow through the sample and then the sample was mounted on the glass slide. No reactions were observed in this case and the XRD pattern of this sample in comparison to previous 30 hours alloyed sample is **shown in Figures 109 and 110.**

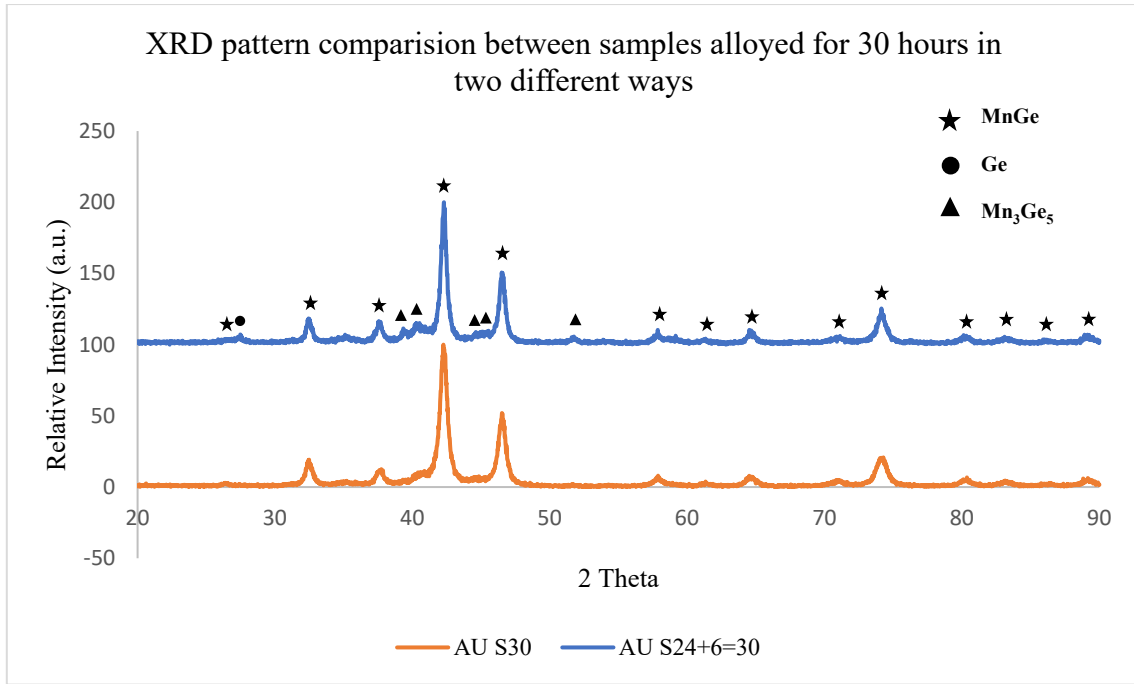


Figure 109 XRD patterns comparison between 30 hour alloyed samples using different alloying techniques

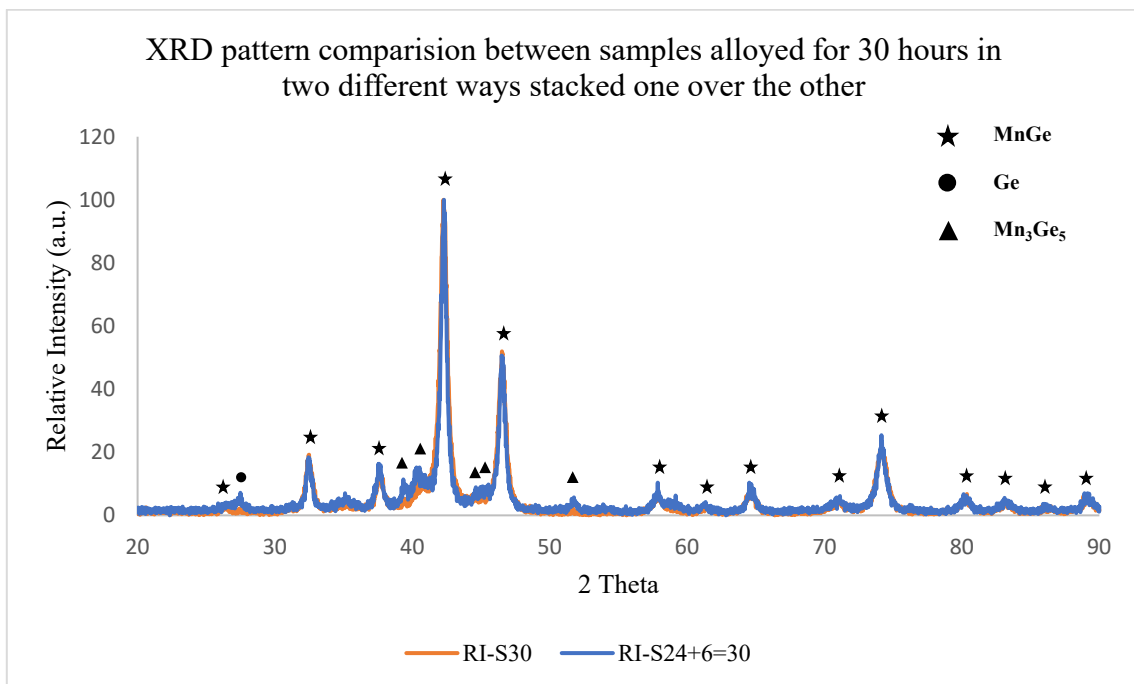


Figure 110 XRD patterns of 30-hour alloyed samples stacked one over the other

It is observed that in the case of 30 hours alloyed sample with the intermittent addition of stearic acid, i.e., at 24 hours, Mn₃Ge₅ and Ge peaks were still present.

These reactions were assumed to be because of the presence of unreacted stearic acid at the time alloyed after adding it, i.e., 6 hours was low, or because of the removal of some sample which was exposed to air and then was added back to the vial resulting in oxidation of the sample. To avoid such reactions, another attempt was made where PCA was added at 15 hours of alloying inside the glove box and continued alloying for 15 more hours without removing the sample. The entire sample was removed only after 30 hours. The sample behaved similarly to the one alloyed for 30 hours with the intermediate addition of stearic acid at 24 hours. The sample left in the glass vial was safe and the XRD of this in comparison to 30 hours alloyed samples from the second attempt are **shown in Figures 111 and 112.**

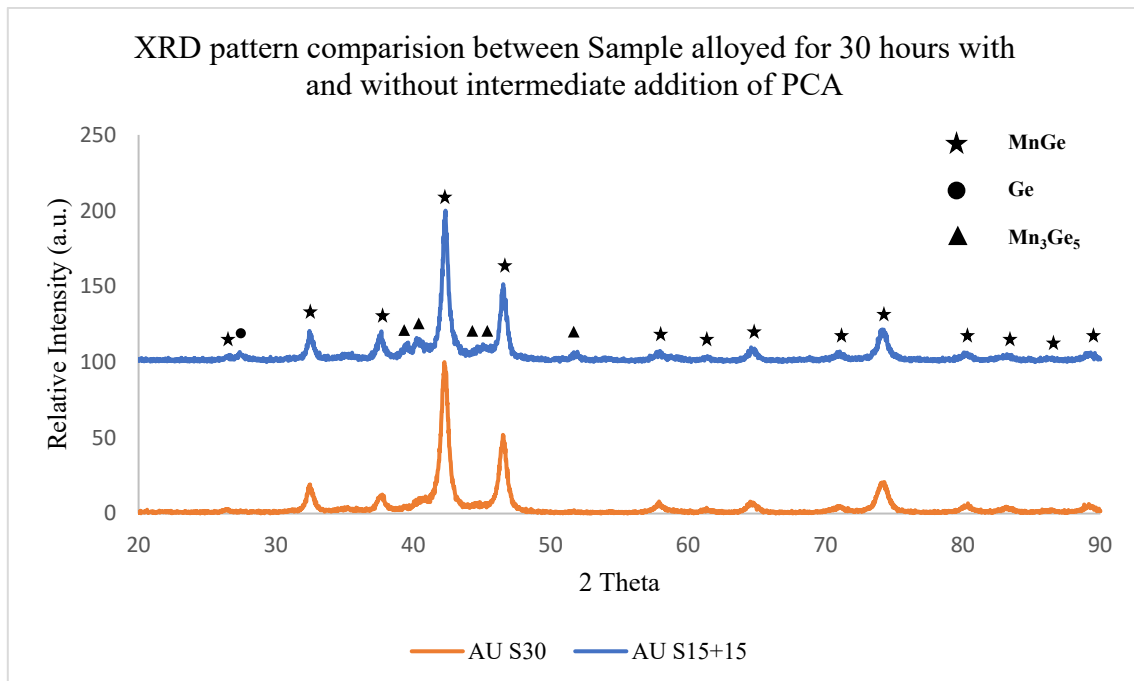


Figure 111 XRD patterns comparison between 30-hour alloyed samples using different alloying techniques

From these observations, it was assumed that the probable cause of such self-sustained reversible reactions is the addition of PCA at the intermediate stages. The PCA added after alloying for certain hours is reacting with one or more of the already formed phases of Mn-Ge system resulting in such violent reactions.

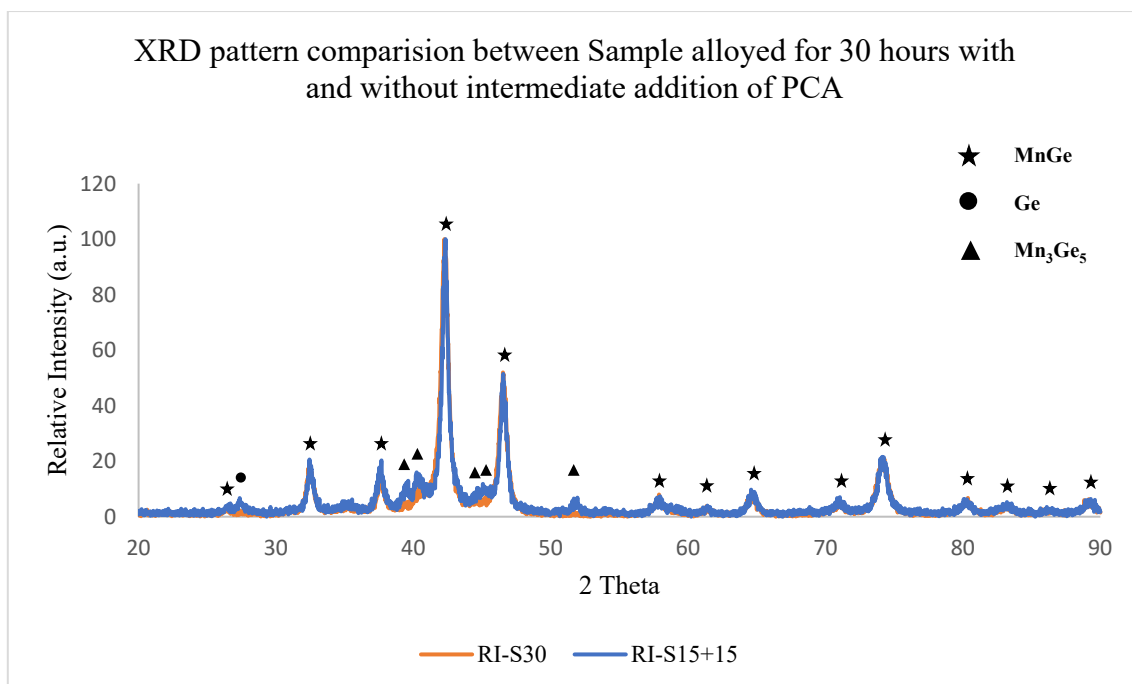


Figure 112 XRD patterns of 30-hour alloyed samples stacked one over the other

It can be seen that the peaks of Mn₃Ge₅ are still present, in spite of alloying for 30 hours (h) with the intermediate addition of PCA at 15 hours where continuous milling gave a pure MnGe phase by 30 hours (h) of alloying time.

5.2.2. Using Ideal technique, with increased ball to powder ratio

In this attempt, except for ball to powder ratio (B/P), all other parameters were kept the same such as the mass of powder blend is ~5 grams, ~2 wt% stearic acid as PCA, alloying continuously with the addition of PCA or removal of the sample at intermittent stages. The ball to powder ratio was increased to ~ 15 %, and the powders were alloyed for 24 hours.

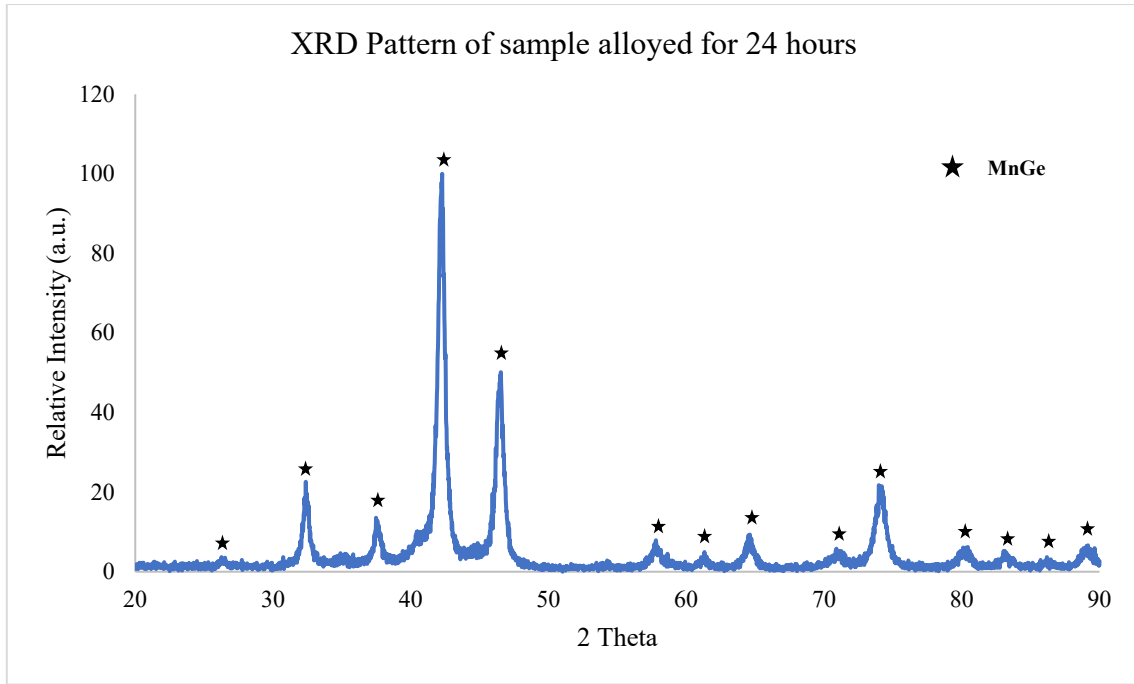


Figure 113 XRD Pattern of 24 hours alloyed sample with high ball to powder ratio showing pure MnGe phase

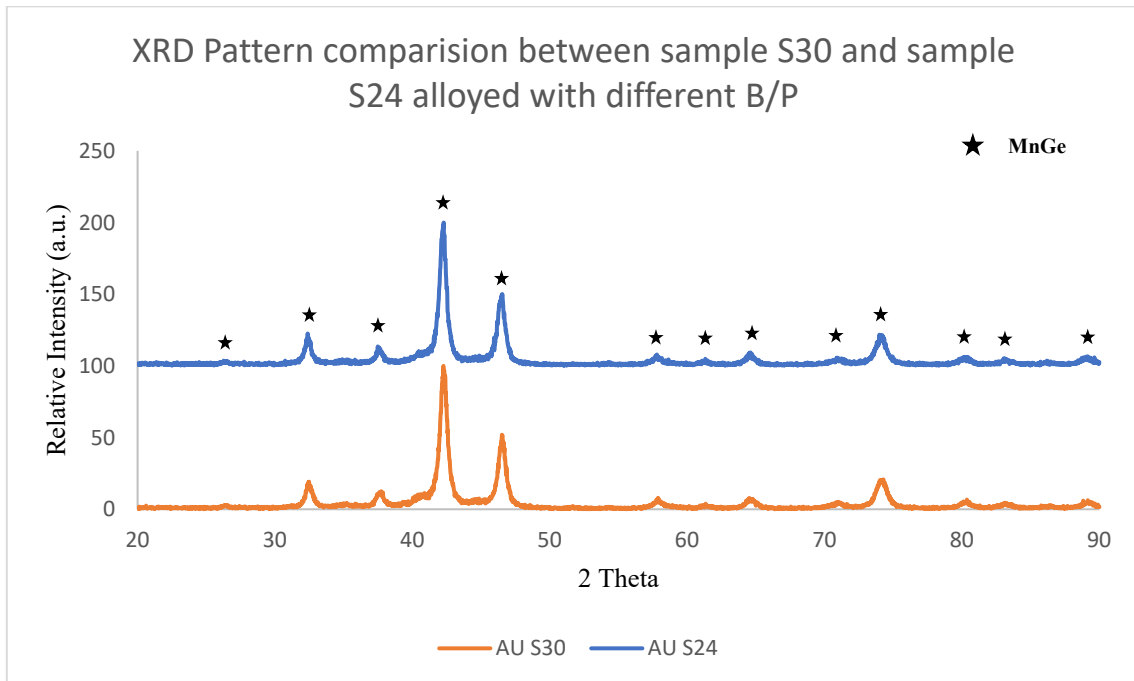


Figure 114 XRD patterns comparison between 30 hours alloyed sample with ~8:1 B/P and 24 hours alloyed sample with ~15:1 B/P

It can be seen that MnGe is obtained at 24 hours of alloying itself with the increased ball to powder ratio without any contamination from **Figures 113 and 114**.

The magnetization measurement performed on this sample is shown in Figure 115. The change in magnetization with a temperature below ambient were measured in zero field and field cooled conditions.

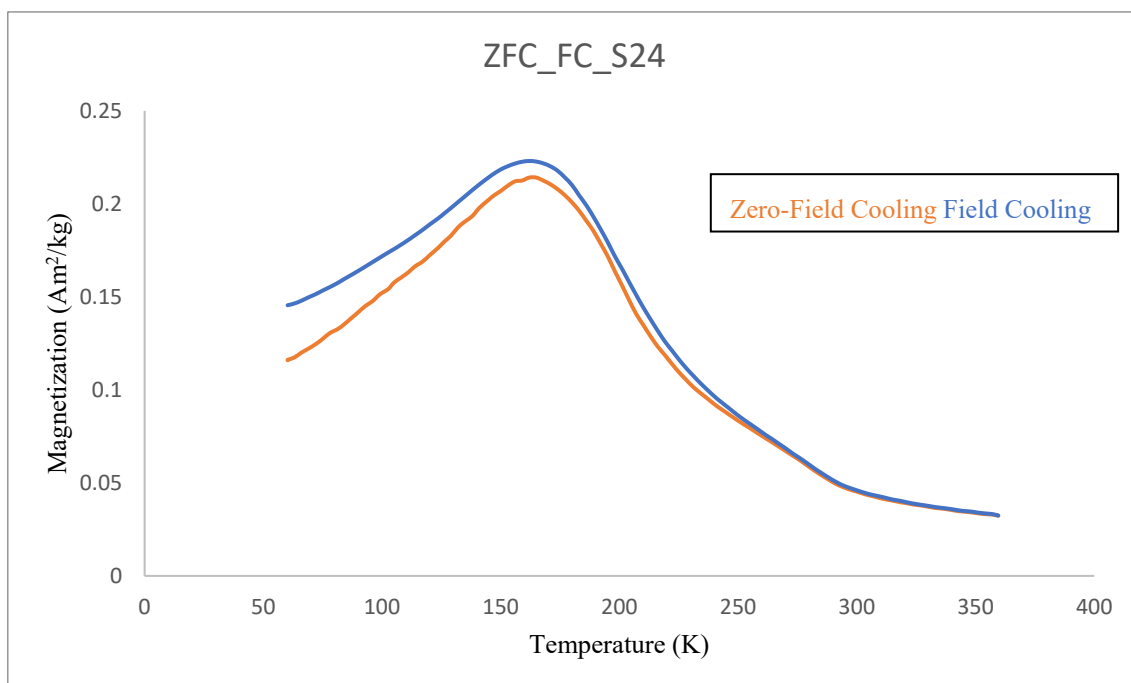


Figure 115 Change in Zero field and field cooled magnetization with temperature in sample alloyed for 24 hours with high ball to powder ratio

It was observed that the magnetization curve was similar to the one seen in sample alloyed for 36 hours proving that increasing the ball to powder ratio will greatly reduce the alloying time required. Similar synthesis technique was used in an attempt to synthesize other metastable phases of Mn-Ge system which are explained later below.

5.2.3. Synthesis of MnGe by alloying powders in atmosphere.

Once the phase pure MnGe was obtained, using the ideal alloying parameters, another attempt was made where the vial was closed in the air instead of in an argon-filled glove box and alloying was performed for 30 hours. All other alloying conditions such as the addition of 2 wt.% stearic acid only at the beginning of alloying, alloying for 3 hours and a cool down period of 30 min. The sample after alloying was opened in the air after allowing it to cool down overnight. The powder X-ray diffraction performed on this sample showed no significant oxidation, and the pattern looked similar to the 24 hour alloyed sample. Surprisingly, there was

no cold welding of balls observed in this case during the entire alloying process. The XRD results of this sample are shown in Figures 116 and 117.

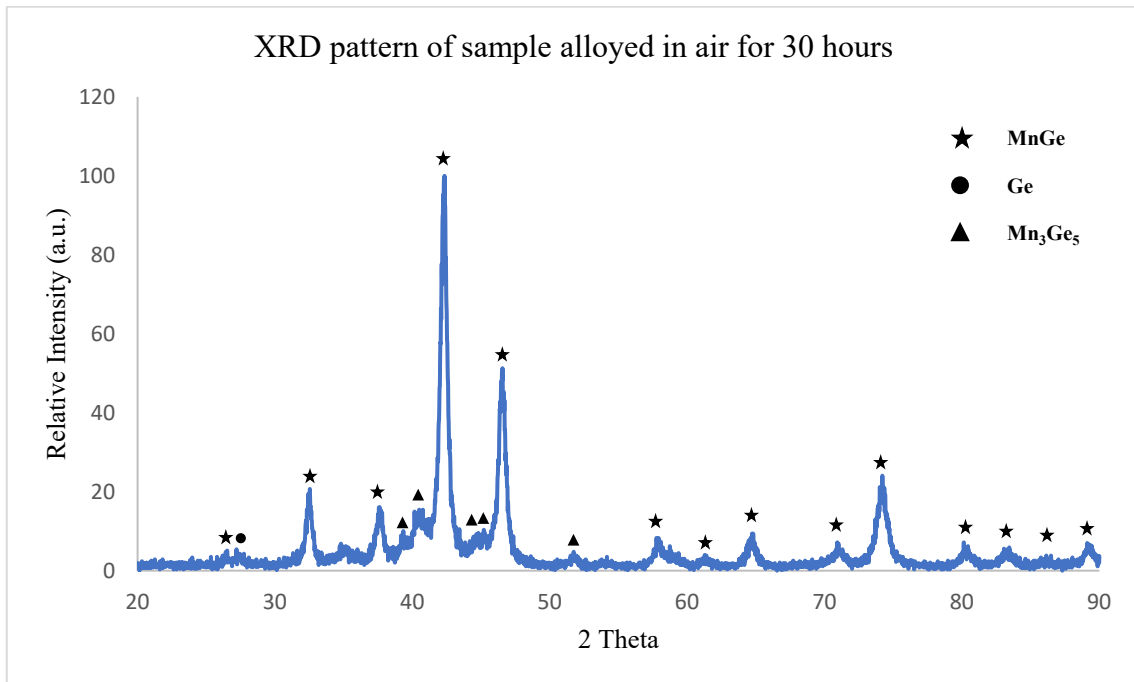


Figure 116 XRD pattern of sample alloyed in air for 30 hours using 8:1 B/P

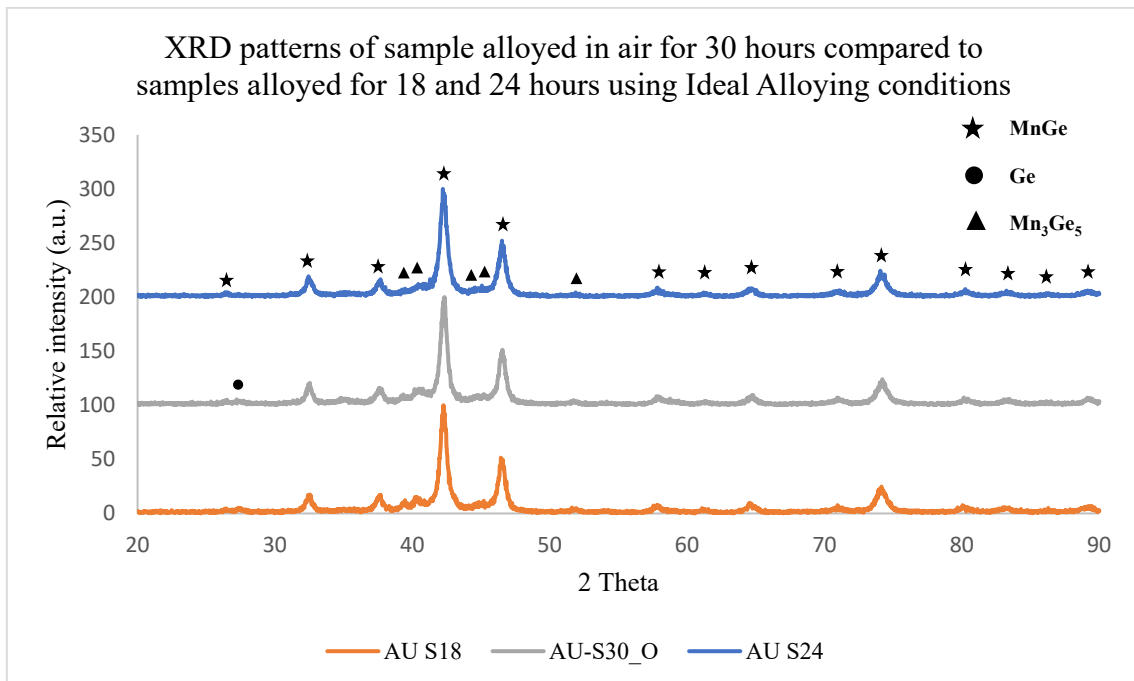


Figure 117 XRD pattern comparison between sample alloyed for 30 hours in air with those alloyed for 18 hours and 24 hours in argon atmosphere

It is to be noticed that there was no oxidation observed in the sample although it was alloyed in the presence of oxygen. Also, though there was no cold welding of balls observed, the sample appears to be between 18 hours alloyed and the 24 hours alloyed samples from the XRD pattern comparison.

5.2.4. Study of Effect of Different Types of PCA's

It was noticed when following the prevalent technique that the samples were undergoing drastic reactions when exposed to air resulting in oxidation. When following the ideal technique, the sample S3, i.e., the sample alloyed for 3 hours reacted in a similar way oxidizing almost entire sample. Based on these results multiple conclusions were drawn viz.

1. Reduction of Mn to sub-micron size which is highly reactive when exposed to air resulting in such reactions.
2. Stearic acid added was reacting with one of the elements most probably Mn resulting in these reactions.
3. Stearic acid is reacting with already formed phases resulting oxidation of Mn and bringing back Ge which was observed in the XRD peaks.

To eliminate the probability of stearic acid reacting with the elemental phases or with already formed phases of Mn-Ge system, three different attempts were made using oxalic acid, ethanol and Toluene as PCA's respectively and alloying for 3 hours. The samples when exposed to air showed a similar reaction in case of oxalic acid and ethanol whereas in case of Toluene no significant reactions were observed. Also, the sample when milled with 1 ml of ethanol appeared to have formed hard lumps instead of staying in powder form. The sample obtained using Toluene as PCA also formed lumps but was easily transformed into powder form.

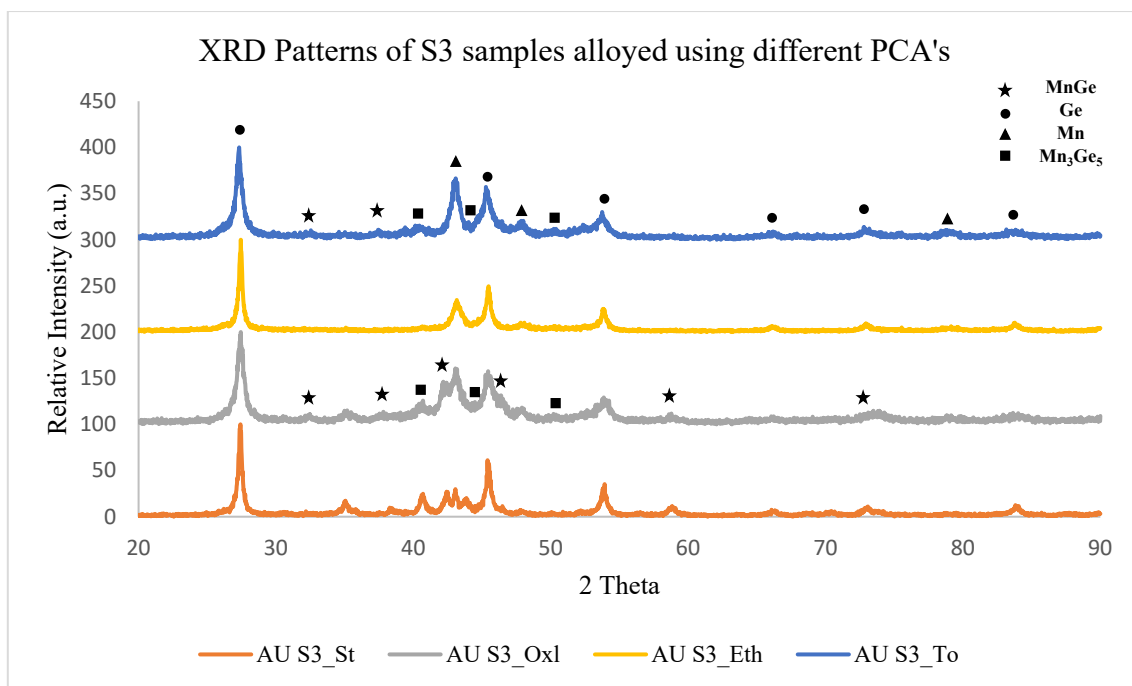


Figure 118 XRD pattern comparison of sample alloyed for 3 hours using different PCA's

Also, during the attempt to synthesize MnGe using the Ideal method, the presence of small amount of Mn was noticed at 15 hours and 24 hours but the samples did not react at these points when taken out for characterization. Although, when stearic acid was added at these stages and alloying was continued for 15 hours and 6 hours respectively, the sample showed such reaction but was very minuscule in scale. These results show that the stearic acid/PCA alone wasn't the reason for the reactions observed, but it was reacting with the large amounts of manganese in the initial stages and/or with the small/minuscule amount of manganese left unreacted in the samples alloyed in steps of 15 hr + 15 hr or 24 hr + 6 hr. From these observations, it is suggested not to add PCA during/in the middle of the alloying process and also not to open the vial at low hours of alloying such as 3 hrs and 6 hrs.

5.3. Phase evolution during the synthesis of Mn_3Ge_5

For the synthesis of Mn_3Ge_5 using ideal technique, the germanium and manganese with purity greater than 99.9% were mixed in a stoichiometric ratio of Ge:Mn = 5:3. Approximately 5 grams of this powder blend was loaded into a stainless-steel vial along with 2 wt. % stearic acid as a process control agent. Stainless steel balls (big balls with dia. = 12.7 mm) weighing close to ~41 grams were added to the vial which acts as a grinding media. The vial was then closed inside the glove box filled with Argon with <0.01% of oxygen. Alloying was performed for a certain number of hours in intervals of 3 hours of alloying and a half hour of cooldown period. Multiple samples were prepared using the same technique with each sample taken out after alloying for different hours. Powder X-ray diffraction was performed on each sample using Rigaku Miniflex-600 powder x-ray diffractometer, and the results are shown below. The X-ray diffraction study performed in all the samples obtained during the synthesis of Mn_3Ge_5 are shown below.

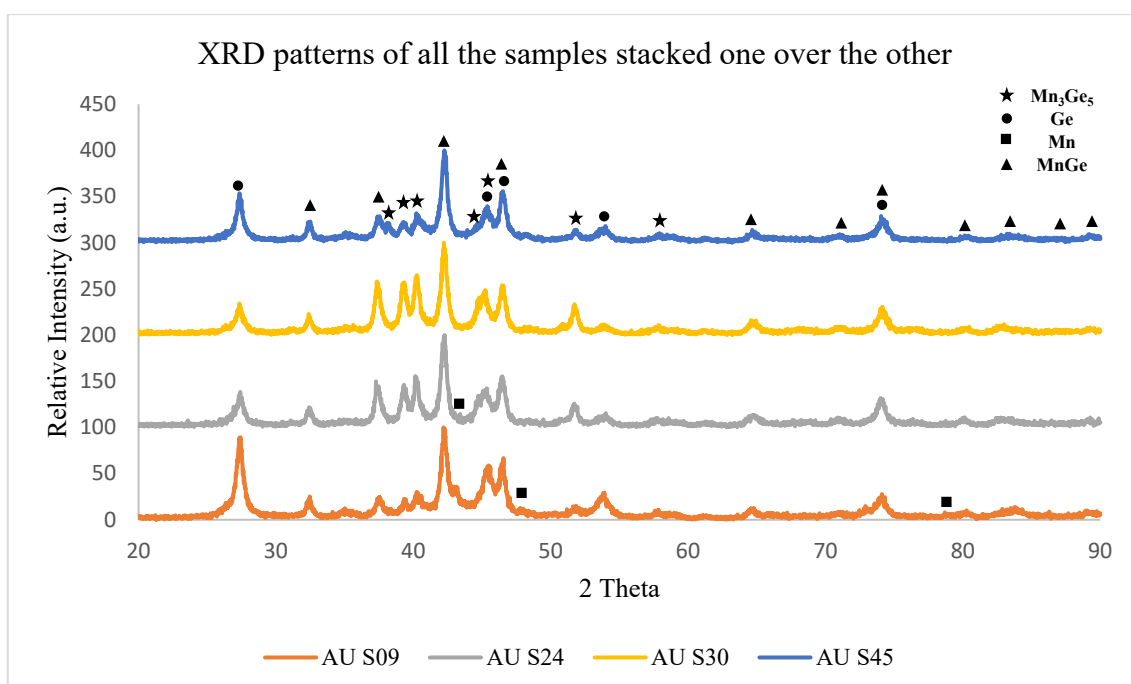


Figure 119 XRD pattern comparison of all the samples obtained during the synthesis process of Mn_3Ge_5

It was observed that the maximum Mn_3Ge_5 phase was obtained at 30 hours of alloying along with large amount of MnGe and a small amount of Ge. Upon increasing the alloying time to 45 hours, a decrease in Mn_3Ge_5 peaks was noticed (reversible reaction) leading to increase in

elemental Ge content. Further investigation is needed to find the ideal synthesis conditions for Mn_3Ge_5 phase using the mechanical alloying technique.

5.4. Phase evolution during the synthesis of $MnGe_2$

Synthesis of $MnGe_2$ was attempted using both the alloying techniques, i.e., Ideal technique as well as prevalent technique. Each process and its results are explained individually below.

5.4.1. Adopting Ideal alloying technique

In this attempt, the mass of powder blend taken was ~5 grams with 2 wt.% stearic acid and ~41 grams of balls with the ball to powder ratio close to 8:1. The vial was closed inside the glovebox, and it was alloyed for 36 hours continuously. The vial after alloying was opened inside the glove box, and the sample was taken into two separate vials one big and one small glass vial. Powder X-ray diffraction was performed on these samples, and the results are shown in the figure below.

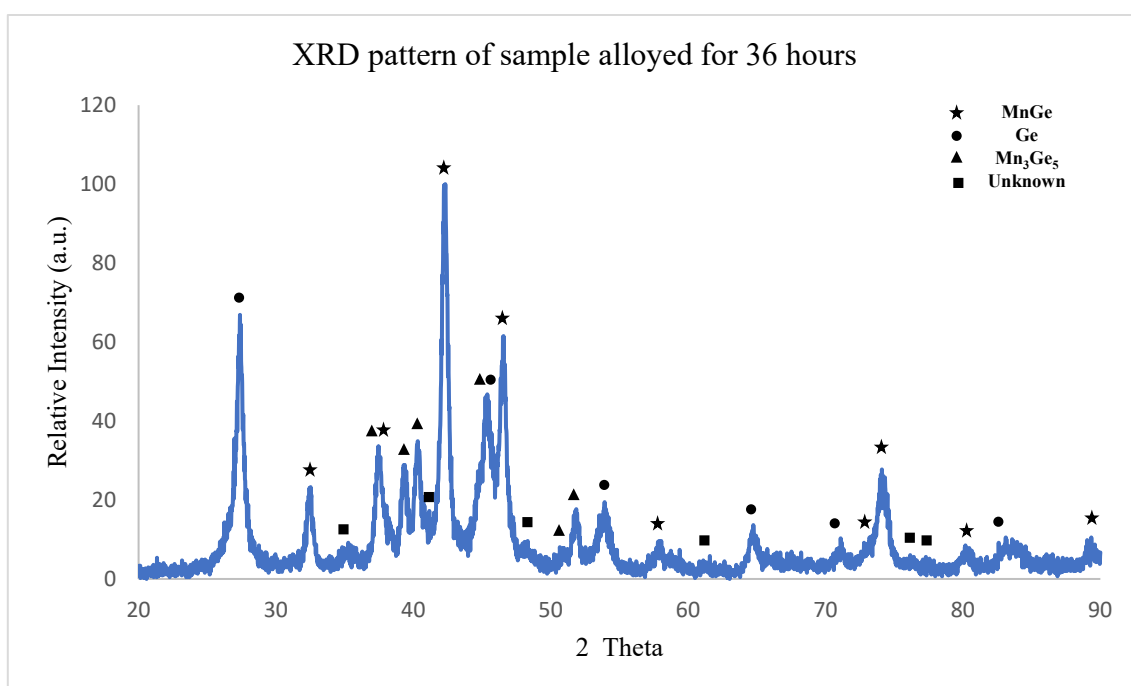


Figure 120 XRD pattern of sample during the attempt to synthesize $MnGe_2$ alloyed for 36 hours

It is observed that the sample is a mixture of $MnGe$, Mn_3Ge_5 and Ge . The presence of high amount of Ge even after 36 hours of alloying could probably mean that there is a reversible reaction happening at some point of the time which is resulting in reduction one or more of the

formed phases into Ge and the other phases. Further investigation is needed to find the suitable conditions for the synthesis of MnGe₂.

5.4.2. Adopting prevalent alloying technique

For the synthesis of MnGe₂, the powder of Mn and Ge with purity mentioned above were taken in stoichiometric ratio Ge:Mn = 2:1. The powders were loaded into a stainless-steel vial along with the grinding media, i.e., a mixture of big and small balls with diameters 12.7 mm and 6.35 mm respectively, which act as grinding media. The ball to powder ratio was maintained at 10:1 leaving abundant space to powders and the balls to move around freely for effective alloying. A small amount of stearic acid ~2 wt.% was added as a process control agent to prevent cold welding that might occur during the alloying process. The environment inside the vial during alloying was filled with Argon as the materials being alloyed were highly prone to oxidation in their powder state. Alloying was performed for 150 hours, and the sample was removed. The sample removal was performed in air, after allowing the vial to cooldown for 1 hour to room temperature. The sample obtained was characterized using XRD, SEM-EDAX and VSM analysis. The milling parameters are summarised in **Table 25 below**.

Table 17 Alloying parameters during synthesis of MnGe₂

Time in Hour	Vial and Balls Material	Number of Balls		Total Balls Mass (g)	PCA (Wt%)	Ratio (B/P)	Powder Mass (g)
		Big	Small				Total Mass
150	Stainless Steel	10	17	99.79	2	10.0	10.0003

The vial and the cap got seized after 45 hours of alloying due to excess heat build-up melting the aluminum vial cap threads or due to loosening of the vial cap leading to the accumulation of finer powder particles in the threads of the vial and the cap. The vial had to be opened forcefully to remove the sample, damaging the threads of the vial cap. It was observed that around 0.0420 g of powder was lost in the process as this was welded to the walls of the vial. It was noticed that the balls (both big and small) were severely deformed and some small balls were broken in the final hours of alloying which led to iron contamination. This was visible in the x-ray diffraction characterization performed on the sample. The results of the powder X-ray diffraction of sample S150, i.e., after alloying for 150 hours is shown below.

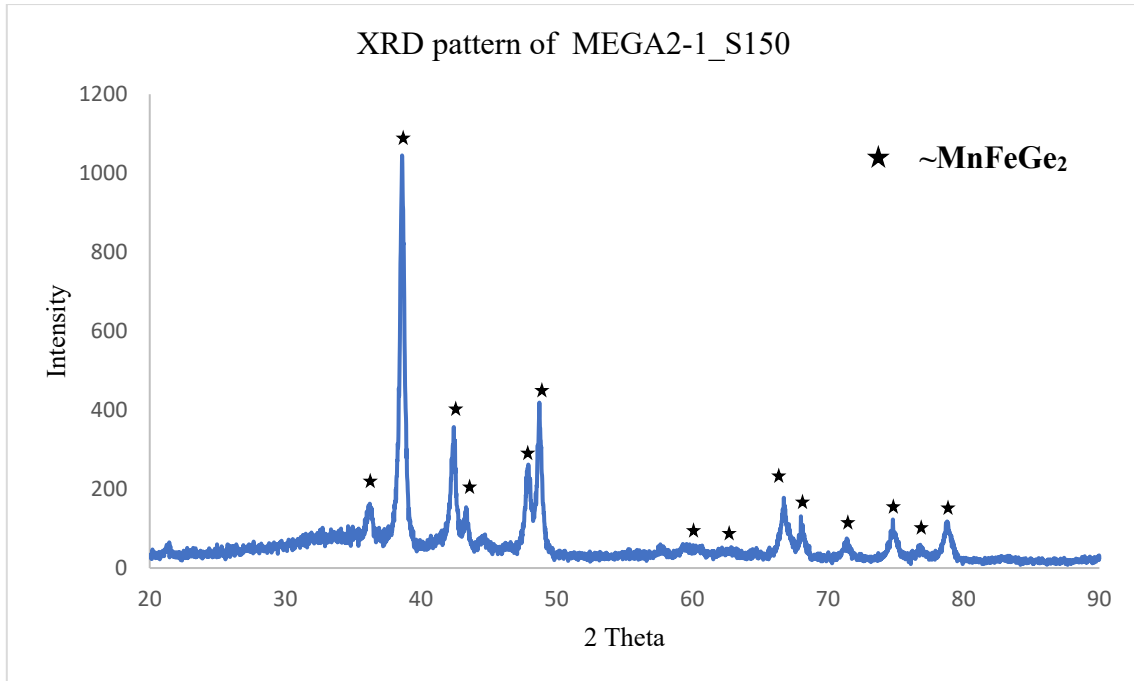


Figure 121 XRD pattern of sample $\sim\text{MnFeGe}_2$ alloyed for 150 hours with 10:1 B/P

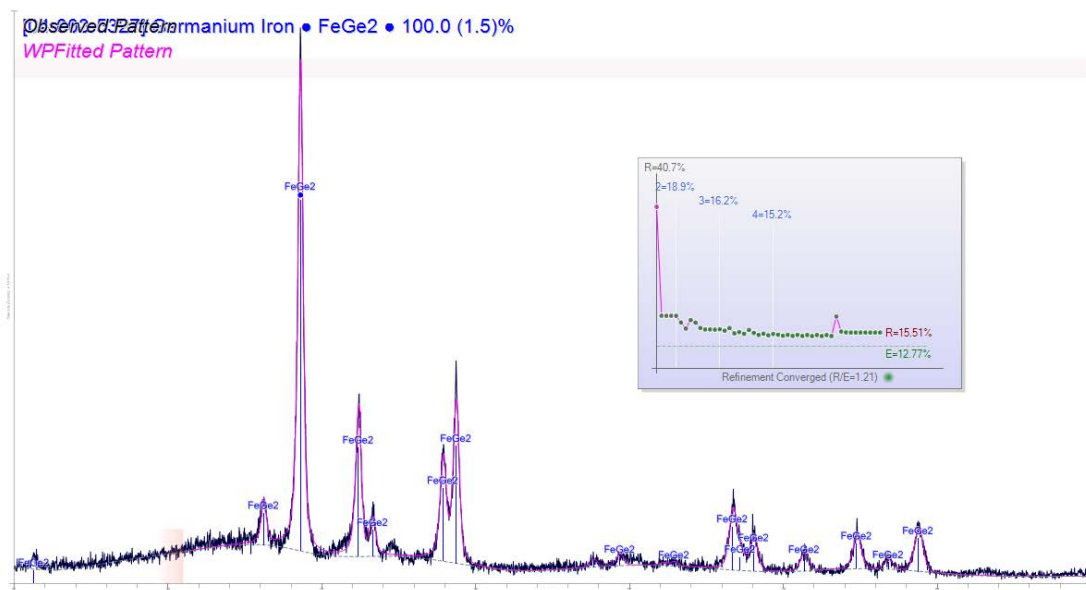


Figure 122 XRD pattern of sample alloyed for 150 hours analyzed in JADE software package

The EDAX analysis performed on this sample revealed that the sample had $\sim 56.93\text{wt. \% Ge}$, $\sim 20.81\text{wt. \% Mn}$ along with contamination of $\text{Fe} \sim 18.70\text{wt. \%}$ and $\text{Cr} \sim 3.57\text{wt. \%}$.

EDAX ZAF Quantification (Standardless)						
Element Normalized						
SEC Table : Default						
Element	Wt %	At %	K-Ratio	Z	A	F
CrK	3.57	4.38	0.0374	1.0363	0.9400	1.0775
MnK	20.81	24.18	0.2111	1.0193	0.9598	1.0371
FeK	18.70	21.37	0.1972	1.0409	0.9629	1.0520
GeK	56.93	50.07	0.5324	0.9745	0.9598	1.0000
Total	100.00	100.00				
Element	Net Inte.	Bkgd Inte.	Inte. Error	P/B		
CrK	22.32	4.20	5.56	5.31		
MnK	113.32	4.00	2.17	28.30		
FeK	94.65	3.75	2.39	25.21		
GeK	112.82	2.70	2.16	41.74		

Figure 123 EDAX analysis of the sample alloyed for 150 hours

Based on the results of XRD and EDAX analysis, the obtained sample was assumed to be a pure single-phase compound containing Mn, Fe and 2Ge and a relatively small amount of Cr.

Change in magnetization with magnetic field was performed on this sample to determine the behavior of the material. The results of this study are shown below.

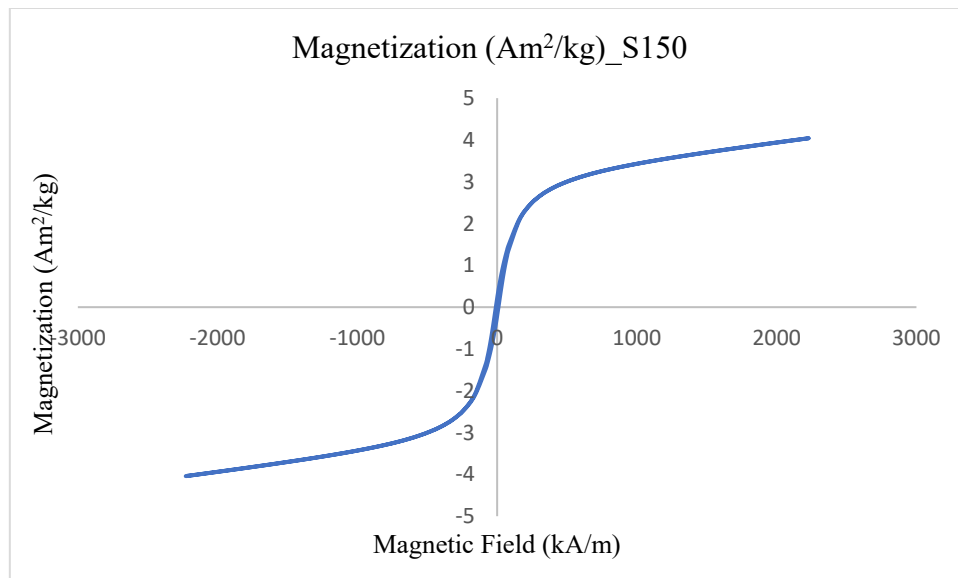


Figure 124 The magnetization versus applied magnetic field measurement performed on sample alloyed for 150 hours showing a hysteresis loop

The sample showed hysteresis when subjected to the varying magnetic field at room temperature, i.e., ~ 300 K revealing its ferromagnetic behavior. This ferromagnetism was assumed to be due to the presence of Iron content.

5.5. Phase evolution during the synthesis of MnGe₄.

For the synthesis of MnGe₄ ideal technique, with 8:1 ball to powder ratio, germanium and manganese with purity greater than 99.9% were mixed in a stoichiometric ratio of 4:1 respectively with the total powder blend mass approximating to 5 grams. 5 big stainless-steel balls weighing close to 41 grams were used as a grinding media. 2 wt.% stearic acid was used as a PCA and was added only before the start of the runs. The alloying was continued for 30 hours which gave the best results during the attempts for the synthesis of MnGe and Mn₃Ge₅. The sample obtained was characterized using powder X-ray diffractometer. The patterns obtained were analyzed using JADE 2010 software package. The results obtained are shown below.

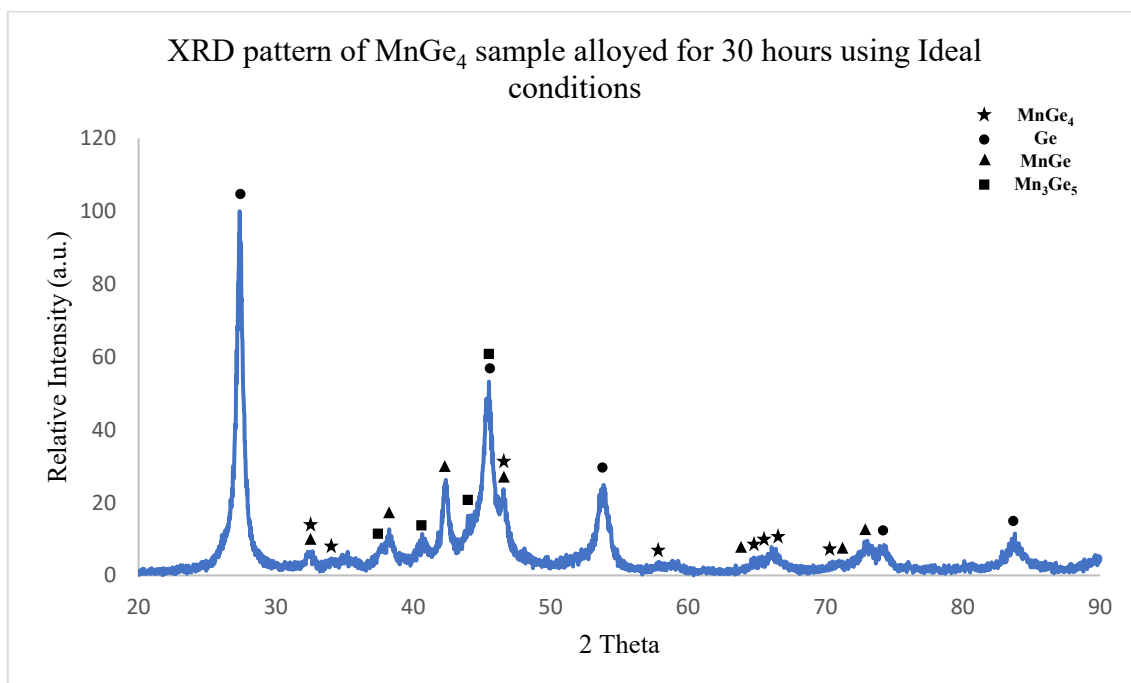


Figure 125 XRD pattern of the sample alloyed for 30 hours during the attempt to synthesize MnGe₄

It was noticed that even after 30 hours of alloying with ideal alloying conditions, the predominant phase was MnGe followed by Mn₃Ge₅ with MnGe₄ being the least amount. There is a large amount of unreacted Ge present. Further alloying may be required for the phase to evolve but increasing the alloying time beyond 50 hours would probably lead to iron contamination.

CHAPTER 6. CONCLUSION

The phase evolution during the synthesis of various metastable manganese germanides was investigated. In the case of the synthesis of MnGe, the metastable compound was synthesized successfully at ~30 hours of mechanical alloying. During the synthesis, the phase evolution involved the formation of both Mn₃Ge₅ and MnGe phases, while the former being predominant in the initial stages. After ~12 hours of mechanical alloying, the amount of Mn₃Ge₅ started to reduce accompanied with an increase in the amount of MnGe, which after 30 hours of alloying, resulted in 100% MnGe. The lattice parameter of the MnGe phase in powder form was estimated as 0.4798 ± 0.0008 nm, and the particle size distribution was found to be between ~1-3 μ m. The magnetic property measurement revealed that the MnGe phase was paramagnetic at room temperature, antiferromagnetic at sub-ambient temperature with Neel temperature estimated to be ~162 K and had a magnetization value (at 1 Tesla and 300 K) of ~ 3 emu/g.

In the case of the phase evolution during the synthesis of Mn₃Ge₅, it was observed that at the initial stages MnGe and Mn₃Ge₅ started going up, up to 30 hours of alloying after which Mn₃Ge₅ started disappearing with a simultaneous increase in MnGe phase. It is to be noticed that in the literature, MnGe was reported to be stable up to 600°C after which it dissociated to Mn₁₁Ge₈ and Ge whereas Mn₃Ge₅ was stable up to 300°C after which it dissociated into MnGe, Mn₁₁Ge₈, and Ge at atmospheric pressure. From these two reports, it can be concluded that it is easy for Mn₃Ge₅ to dissociate as it would require less energy whereas MnGe would require comparatively higher energy and at or after 30 hours of alloying, the energy supplied in the alloying process is crossing the dissociation energy required for Mn₃Ge₅ to dissociate into MnGe, Mn₁₁Ge₈, and Ge.

In the case of the phase evolution during the synthesis of MnGe₂, and MnGe₄, It was noticed that the formation of MnGe and Mn₃Ge₅ was hindering the further evolution of phases to the desired atomic ratio. Although Mn₃Ge₅ was dissociating after a certain hour of alloying, it is most certainly increasing the alloying time required to obtain the desired phase whereas MnGe is taking more than 50 hours of alloying time to dissociate at which, it is more than likely to get iron contamination.

Further investigation is in progress to hasten the synthesis of MnGe and to find the suitable processing parameters to suppress the formation of MnGe while synthesizing other Ge rich metastable Mn-Ge phases.

The metastable MnGe synthesized (in powder form), in this work, at ambient temperature and pressure conditions had a considerably high yield and reproducibility, unlike in the past synthesized by high-pressure/high-temperature technique (in bulk form) and thin-film deposition technique (thin film) available in the literature. Future study would involve the synthesis of other metastable compound by isolating MnGe during their evolution.

REFERENCES

- [1] C. Suryanarayana, "Mechanical alloying and milling," *Prog. Mater. Sci.*, vol. 46, no. 1, pp. 1–184, 2001.
- [2] D. Turnbull, "Metastable structures in metallurgy," *Metall. Trans. A*, vol. 12, no. 5, pp. 695–708, 1981.
- [3] F. H. (Sam)Froes, C. Suryanarayana, K. Russell, and C.-G. Li, "Synthesis of intermetallics by mechanical alloying," *Mater. Sci. Eng. A*, vol. 192–193, pp. 612–623, Feb. 1995.
- [4] C. C. Koch, "Materials Synthesis by Mechanical Alloying," *Annu. Rev. Mater. Sci.*, vol. 19, no. 1, pp. 121–143, Aug. 1989.
- [5] A. . Bhattacharya and E. Arzt, "Temperature rise during mechanical alloying," *Scr. Metall. Mater.*, vol. 27, no. 6, pp. 749–754, Sep. 1992.
- [6] A. A. Al-Joubori and C. Suryanarayana, "Synthesis of metastable NiGe₂ by mechanical alloying," *Mater. Des.*, vol. 87, pp. 520–526, 2015.
- [7] F. Yuan, S. Forbes, K. K. Ramachandran, and Y. Mozharivskyj, "Structure and physical properties of Cr₅B₃-type Ta₅Si₃ and Ta₅Ge₃," *J. Alloys Compd.*, vol. 650, pp. 712–717, 2015.
- [8] E. Arras, D. Caliste, T. Deutsch, F. Lan\ifmmode \mbox\cc\else ç\fi on, and P. Pochet, "Phase diagram, structure, and magnetic properties of the Ge-Mn system: A first-principles study," *Phys. Rev. B*, vol. 83, no. 17, p. 174103, May 2011.
- [9] H. Fukuoka, S. Yamanaka, E. Matsuoka, and T. Takabatake, "High-Pressure Synthesis and Transport Properties of a New Binary Germanide, SrGe_{6-δ} ($\delta \cong 0.5$), with a Cagelike Structure," *Inorg. Chem.*, vol. 44, no. 5, pp. 1460–1465, Mar. 2005.
- [10] I. Mayer, I. Shidlovsky, and E. Yanir, "Low-temperature synthesis of metallic silicides and germanides by an amalgam method," *J. Less Common Met.*, vol. 12, no. 1, pp. 46–50, Jan. 1967.
- [11] V. M. Agoshkov, V. D. Gorbatenkov, S. V. Popova, and L. N. Fomicheva, "Crystallization of MoGe₂ and WGe₂ at high pressure and some properties of these phases," *J. Less-Common Met.*, vol. 78, no. 2, pp. 235–243, Apr. 1981.
- [12] H. Takizawa, T. Sato, T. Endo, and M. Shimada, "High-pressure synthesis and electrical properties of Mn₃Ge₅ with Mn₁₁Si₁₉-type structure," *J. Solid State Chem.*, vol. 68, no. 2, pp. 234–238, Jun. 1987.
- [13] A. Berche, J. C. Tedenac, and P. Jund, "Thermodynamic modeling of the germanium–manganese system," *Intermetallics*, vol. 47, pp. 23–30, Apr. 2014.
- [14] H. Takizawa, T. Sato, T. Endo, and M. Shimada, "High-pressure synthesis and electrical

- and magnetic properties of MnGe and CoGe with the cubic B20 structure,” *J. Solid State Chem.*, vol. 73, no. 1, pp. 40–46, 1988.
- [15] V. I. Larchev and S. V. Popova, “The polymorphism of transition metal monogermanides at high pressures and temperatures,” *J. Less Common Met.*, vol. 87, no. 1, pp. 53–57, Sep. 1982.
- [16] T. Moriya, “No Title,” *J. Magn. Magn. Mater.*, vol. 77, pp. 31–34, 1983.
- [17] T. Moriya, “No Title,” *Solid State Commun.*, vol. 483, p. 26, 1978.
- [18] and M. R. Y. Ishikawa, K. Tajima, D. Bloch, “No Title,” *Solid State Commun.*, vol. 525, p. 19, 1976.
- [19] and M. K. Y. Ishikawa, G. Shirane, J. A. Tarvin, “No Title,” *Phys. Rev. B1*, vol. 4956, p. 16, 1977.
- [20] S. Haraldson and U. Smith, “No Title,” *J. Phys. Chem. Solids*, vol. 1237, p. 35, 1974.
- [21] and Z. Y. Z. J. Beille, J. Voiron, F. Towfig, M. Roth, “No Title,” *J. Phys. F*, vol. 2153, p. 11, 1981.
- [22] P. B. and M. H. Jensen, “No Title,” *J. Phys. C*, vol. L881, p. 13, 1980.
- [23] H. Takizawa, T. Sato, T. Endo, and M. Shimada, “High pressure synthesis and electrical and magnetic properties of MnGe₄ and CoGe₄,” *J. Solid State Chem.*, vol. 88, no. 2, pp. 384–390, 1990.
- [24] H. Takizawa, K. Uheda, and T. Endo, “NiGe₂: a new intermetallic compound synthesized under high-pressure,” *J. Alloys Compd.*, vol. 305, no. 1, pp. 306–310, 2000.
- [25] Z. M. K. Schubert, H. Pfisterer, “No Title,” vol. 41, p. 433, 1950.
- [26] K. Cenzual, L. M. Gelato, M. Penzo, and E. Parthé, “Inorganic structure types with revised space groups. I,” *Acta Crystallogr. Sect. B*, vol. 47, no. 4, pp. 433–439, Aug. 1991.
- [27] L. J. Jin *et al.*, “The interfacial reaction of Ni with (111)Ge, (100)Si_{0.75}Ge_{0.25} and (100)Si at 400 °C,” *Thin Solid Films*, vol. 462–463, no. 1, pp. 151–155, Sep. 2004.
- [28] M. Jamet *et al.*, “High-Curie-temperature ferromagnetism in self-organized Ge_{1-x}Mn_x nanocolumns,” *Nat Mater*, vol. 5, no. 8, pp. 653–659, Aug. 2006.
- [29] A. V Tsvyashchenko *et al.*, “High Pressure Synthesis and Magnetic Properties of Cubic B20 MnGe and CoGe,” *Solid State Phenom.*, vol. 190, pp. 225–228, 2012.
- [30] D. D. Vaughn II *et al.*, “Solution-Phase Synthesis and Magnetic Properties of Single-Crystal Iron Germanide Nanostructures,” *Chem. Mater.*, vol. 25, no. 21, pp. 4396–4401, Nov. 2013.
- [31] V. G. Myagkov *et al.*, “Formation of ferromagnetic germanides by solid-state reactions in 20Ge/80Mn films,” *Thin Solid Films*, vol. 552, pp. 86–91, Feb. 2014.
- [32] N. Yamada, H. Sakai, H. Mori, and T. Ohoyama, “Magnetic properties of ϵ -Mn₃Ge,” *Phys. B+C*, vol. 149, no. 1–3, pp. 311–315, Mar. 1988.
- [33] D. D. Dung, W. Feng, Y. Shin, and S. Cho, “Magnetism and transport properties of α -Mn structure Mn₃Ge thin film,” *J. Appl. Phys.*, vol. 109, no. 7, p. 07C310, Mar. 2011.

- [34] T. Matsui, M. Shigematsu, S. Mino, H. Tsuda, H. Mabuchi, and K. Morii, "Formation of unknown magnetic phase by solid state reaction of thin multilayered films of 75at% Mn–25at%Ge," *J. Magn. Magn. Mater.*, vol. 192, no. 2, pp. 247–252, Feb. 1999.
- [35] H. Kurt *et al.*, "Magnetic and electronic properties of D022-Mn₃Ge (001) films," *Appl. Phys. Lett.*, vol. 101, no. 13, p. 132410, Sep. 2012.
- [36] S. Olive-Mendez *et al.*, "Epitaxial growth of Mn₅Ge₃/Ge(111) heterostructures for spin injection," *Thin Solid Films*, vol. 517, no. 1, pp. 191–196, Nov. 2008.
- [37] G. V. S. V. S. Neshpor, "No Title," *Fiz. Tverd. Tela*, vol. 2, pp. 2202–2209, 1960.
- [38] A. A. K. V. N. Bondarev, V. A. Podergin, O. G. Grechko, V. P. Perminov, "No Title," *Nauka*, p. 65, 1972.
- [39] W. Klement, "No Title," *Can. J. Phys.*, vol. 40, no. 10, pp. 1397–1400, 1962.
- [40] I. Rama Brahman, A. K. Jena, and M. C. Chaturvedi, "On the nickel-rich nickel-germanium solid solution," *Scr. Metall.*, vol. 23, no. 8, pp. 1281–1284, Aug. 1989.
- [41] P. Le Cocq, "Etude magnétique et structurale des solutions solides de germanium dans le fer, dans le cobalt et dans le nickel et des germaniures du type M₃Ge et M₂Ge," *Ann. Chim.*, vol. 8, p. 85, 1963.
- [42] C. Suryanarayana and A. Al-Joubori, "Reversible transformation of NiGe in mechanically alloyed Ni–Ge powders," *J. Mater. Res.*, vol. 30, no. 13, pp. 2124–2132, Jul. 2015.
- [43] A. S. Ahmed, B. D. Esser, J. Rowland, D. W. McComb, and R. K. Kawakami, "Molecular beam epitaxy growth of [CrGe/MnGe/FeGe] superlattices: Toward artificial B20 skyrmion materials with tunable interactions," *J. Cryst. Growth*, vol. 467, pp. 38–46, Jun. 2017.
- [44] C. Heyn, A. Stemann, A. Schramm, H. Welsch, W. Hansen, and Á. Nemesics, "Faceting during GaAs quantum dot self-assembly by droplet epitaxy," *Appl. Phys. Lett.*, vol. 90, no. 20, p. 203105, May 2007.
- [45] H. Fukuoka E-mail: hfukuoka@hiroshima-u.ac.jp [Department of Applied Chemistry, Graduate School of Engineering, Hiroshima University, Higashi-Hiroshima 739-8527 (Japan)], K. Baba, M. Yoshikawa, F. Ohtsu, and S. [Department of A. C. Yamanaka Graduate School of Engineering, Hiroshima University, Higashi-Hiroshima 739-8527 (Japan)], "High-pressure synthesis and structures of lanthanide germanides of LnGe₅ (Ln=Ce, Pr, Nd, and Sm) isotypic with LaGe₅," 2009.
- [46] B. N. Figgis and M. A. Hitchman, *Ligand field theory and its applications*. New York : Wiley-VCH, 2000.
- [47] H. Fukuoka, K. Suekuni, T. Onimaru, and K. Inumaru, "High-Pressure Synthesis and Superconductivity of a New Binary Lanthanum Germanide LaGe₃ with Triangular Ge₃ Cluster Units," *Inorg. Chem.*, vol. 50, no. 9, pp. 3901–3906, May 2011.
- [48] J. Zhang *et al.*, "New rare-earth metal germanides with bismuth substitution. Synthesis, structural variations, and magnetism of the RE[BixGe_{1-x}]₂ (RE=Y, Pr, Nd, Sm, Gd–Tm, Lu) compounds," *J. Solid State Chem.*, vol. 196, pp. 586–595, Dec. 2012.
- [49] J. H. Van Vleck, *The Theory of Electric and Magnetic Susceptibilities*. London: Oxford

University Press, 1965.

- [50] N.-T. Suen, M. Broda, and S. Bobev, "Calcium substitution in rare-earth metal germanides with the hexagonal Mn_5Si_3 structure type. structural characterization of the extended series $RE_{5-x}Ca_xGe_3$ (RE=Rare-earth metal)," *J. Solid State Chem.*, vol. 217, pp. 142–149, Sep. 2014.
- [51] H. Bie, A. V. Tkachuk, and A. Mar, "Structure and magnetic properties of rare-earth chromium germanides $RECr_xGe_2$ (RE=Sm, Gd?Er)," *J. Solid State Chem.*, vol. 182, no. 1, pp. 122–128, Jan. 2009.
- [52] F. Ohtsu, H. Fukuoka, and S. Yamanaka, "Synthesis and structures of samarium platinum germanides: $SmPtGe_2$ and $Sm_2Pt_3Ge_5$," *J. Alloys Compd.*, vol. 487, no. 1, pp. 712–715, 2009.
- [53] A. O. Oliynyk and A. Mar, "Rare-earth manganese germanides $RE_{2+x}MnGe_{2+y}$ (RE=La, Ce) built from four-membered rings and stellae quadrangulae of Mn-centred tetrahedra," *J. Solid State Chem.*, vol. 206, pp. 60–65, 2013.
- [54] A. O. Oliynyk, S. S. Stoyko, and A. Mar, "Ternary rare-earth ruthenium and iridium germanides $RE_3M_2Ge_3$ (RE=Y, Gd?Tm, Lu; M=Ru, Ir)," *J. Solid State Chem.*, vol. 202, pp. 241–249, Jun. 2013.
- [55] H. Zoz, D. Ernst, and R. Reichardt, "High Energy Milling/Mechanical Alloying/Reactive Milling," in *3rd International Symposium of the school of chemical engineering, University of Mexico City*, 1998.
- [56] P. S. Gilman and W. D. Nix, "The structure and properties of aluminum alloys produced by mechanical alloying: Powder processing and resultant powder structures," *Metall. Trans. A*, vol. 12, no. 5, pp. 813–824, 1981.
- [57] L. Lü and M. O. Lai, *Mechanical Alloying*. Springer US, 2013.
- [58] D. L. Dorset, "X-ray Diffraction: A Practical Approach.," *Microsc. Microanal.*, vol. 4, no. 5, pp. 513–515, Oct. 1998.